Disease Markers

Identification of Novel Biomarkers in the Era of Precision Medicine

Lead Guest Editor: Jian-Xin Shi
Guest Editors: Chang Gu, Jun Yang, Xufeng Pan, Haoran Liu, and Dechen Zhang

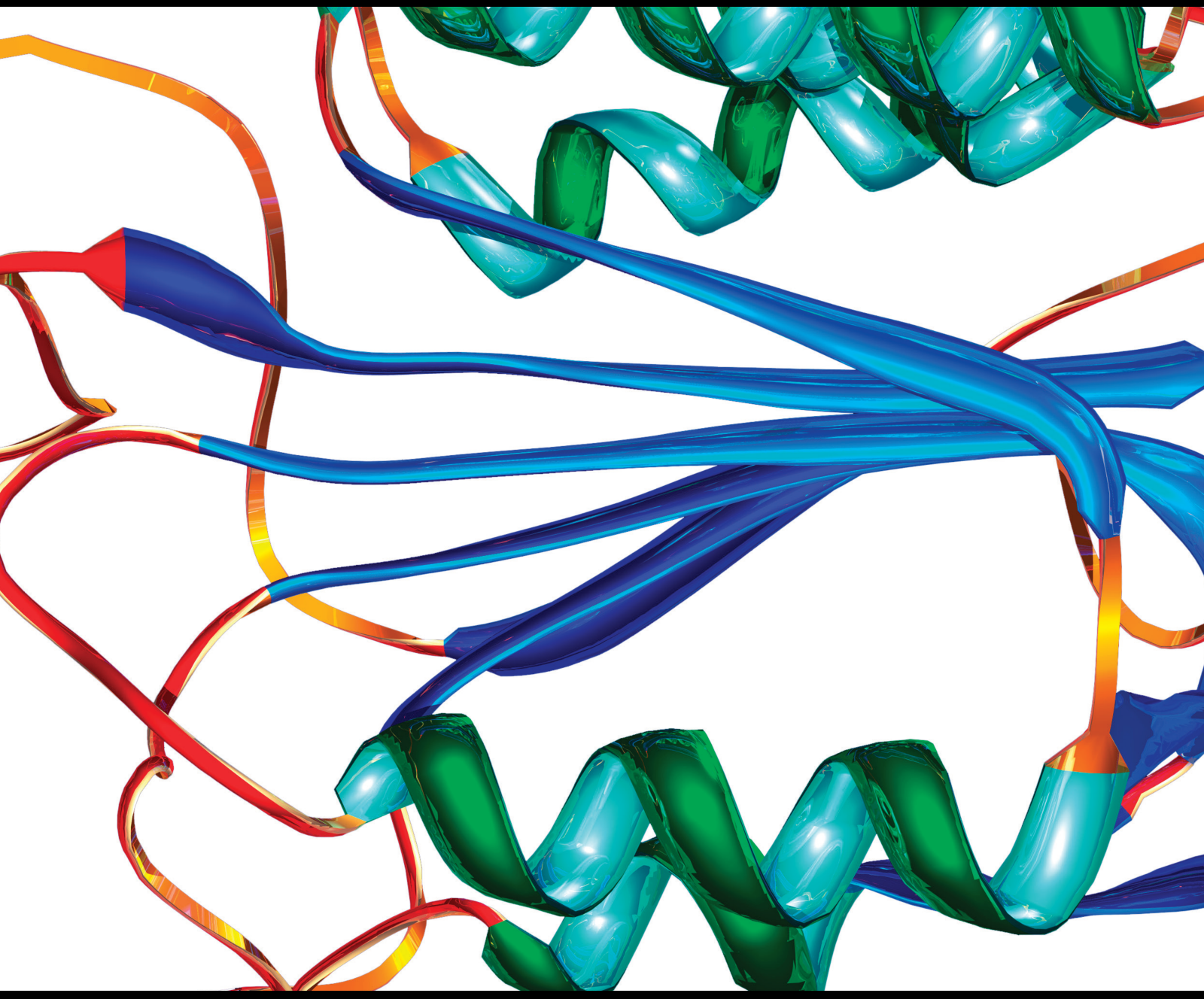

Identification of Novel Biomarkers in the Era of Precision Medicine

Disease Markers

Identification of Novel Biomarkers in the Era of Precision Medicine

Lead Guest Editor: Jian-Xin Shi
Guest Editors: Chang Gu, Jun Yang, Xufeng Pan, Haoran Liu, and Dechen Zhang

Contents

Hindawi
Disease Markers
Volume 2022, Article ID 4882375, 7 pages
https://doi.org/10.1155/2022/4882375

Research Article

miR-877-5p Inhibits Epithelial Mesenchymal Transformation of Breast Cancer Cells by Targeting FGB

Haixia Liu,[1] **Lili Xiang**,[2] **and Yu Mei**[3]

[1]*Department of Pathology, Jinan Maternity and Child Care Hospital, 250001 Jinan, Shandong, China*
[2]*Department of Children's Health Care, Jinan Maternity and Child Care Hospital, 250001 Jinan, Shandong, China*
[3]*Department of Breast Surgery, Jinan Maternity and Child Care Hospital, 250001 Jinan, Shandong, China*

Correspondence should be addressed to Haixia Liu; liuhaixia@fybjy.org.cn

Received 21 July 2022; Revised 12 August 2022; Accepted 16 August 2022; Published 17 November 2022

Academic Editor: Jun Yang

Purpose. This present study is aimed at exploring the FGB expression in breast cancer (BC) and the role of FGB in BC. *Methods*. A total of 150 pairs of BC tissues and adjacent tissues from BC surgery patients were collected. RT-qPCR was utilized to evaluate the mRNA expression of FGB and miR-877-5p. Immunohistochemistry was applied to evaluate the protein expression of FGB. Chi-square test was performed to evaluate the relationship between FGB expression level and clinical characteristics. Cell proliferation was examined using CCK-8 assay. Cell invasion was evaluated by transwell assay. Flow cytometry assay was applied to measure cell apoptosis. The protein expression was evaluated by western blot. BALB/C nude mice were used to establish the xenograft tumor model. *Results*. FGB was more highly expressed in BC tumor, and the expression of FGB was relevant to TNM stage and lymph node metastasis and showed a positive correlation. FGB was proved to be directly regulated via miR-877-5p and enhanced proliferation and invasion of BC cells. FGB downregulation markedly inhibited the tumor growth, including tumor weight and volume. In addition, the Ki-67 expression was observably declined in the sh-FGB group. The protein expression of E-cadherin was markedly raised in the sh-FGB group while the protein expression of N-cadherin and vimentin was markedly declined in the sh-FGB group. *Conclusion*. In conclusion, miR-877-5p inhibits epithelial mesenchymal transformation, cell proliferation, and invasion of BC cells via downregulating FGB.

1. Introduction

BC is a common fatal malignancy, with morbidity and mortality ranking at the forefront of female malignancies. There are about 1.7 million new cases worldwide each year and about 170,000 in China [1]. With the application of various therapies such as surgery, radiotherapy, and endocrine drugs, the prognosis and survival of patients have been improved [2]. Inhibition of tumor cell invasion and metastasis is an urgent scientific problem. Many BC patients have metastases before diagnosis, which will weaken the treatment effect and have a poor prognosis [3]. Hence, it is important to investigate molecular mechanism of BC occurrence, invasion, and metastasis and explore clinical therapeutic targets for early diagnosis and treatment of BC.

MicroRNAs (miRNAs) are a class of endogenous noncoding single-stranded RNA molecules of 18-24 nucleotides in length [4]. The miRNAs suppress the target protein expression or promote mRNA degradation by complementary binding to the 3′UTR of mRNA [5]. Currently, miRNA is found to play a role in various physiological and pathological processes of numerous tumors, containing cell cycle, proliferation, invasion, metastasis, and other biological functions [5]. Multiple specific miRNAs are abnormally expressed in BC tumor tissues, suggesting their involvement in process of BC progression [6, 7]. The mechanisms of miRNA involvement in tumor invasion and metastasis are complex, but epithelial-mesenchymal transition (EMT) has been widely studied in cancer and is believed to be essential in tumor deterioration, which is regulated by a variety of

miRNAs [8]. For example, miR-520c-3p negatively regulated EMT to inhibit cell invasion and migration in BC by targeting IL-8 [7]. miR-130a-3p was poorly expressed in BC cell, and the overexpression of miR-130a-3p impeded BC cell migration and invasion [6]. The involvement of in EMT refers to the process by which tumor cells of epithelial origin lose their epithelial phenotype and acquire a mesenchymal phenotype, thereby gaining the ability to invade and metastasize. EMT is the first and crucial step for tumor cells to undergo invasive metastasis. Fibrinogen beta chain (FGB) was reported to be more obviously highly expressed in the malignant pulmonary nodules by comparison with the benign pulmonary nodules [9]. However, the expression of FGB in BC and whether FGB could regulate the EMT process in BC by miRNAs currently remains unclear.

This present study is aimed at measuring the expression of FGB in BC and the effect of FGB deficiency on progress of BC and EMT.

2. Methods

2.1. Tissue Samples. A total of 150 pairs of BC tissue and adjacent tissue from BC surgery invalids admitted to the hospital from May 2018 to December 2020 were taken. All the patients gave their informed consent. Patients who received radiotherapy or chemotherapy or other anticancer treatment before operation were excluded. After tissue samples was removed, they were stored at -80°C for use. The tumors of the patients were immunostained for ER (SP1 antibody), PR (1E2 antibody), and HER2 (4B5 antibody).

2.2. Cell Culture and Transfection. BC cell MCF-7 was purchased from American Type Culture Collection (ATCC) and maintained in DMEM. 10% fetal bovine serum, 100 U/ml streptomycin, and 100 U/ml penicillin were added to the medium. Cell culture environment was 5% CO_2 and 37°C. MCF-7 cells were transfected using sh-FGB or sh-NC by Lipofectamine 2000 reagent.

2.3. RT-qPCR Assay. Total RNA was extracted by the TRIzol method (Absin, China). cDNA was obtained according to the instructions of reverse transcription kit (Absin, China). The amplification of the target gene was detected by SYBR Premix Ex Taq (Takara, Japan). Table 1 shows the primer sequences.

2.4. Western Blot. MCF-7 cells transfected for 48 h were collected, total protein was extracted, and protein concentration was detected via BCA. After the SDS-PAGE separation, protein was transferred into the PVDF membrane. PVDF membrane was blocked using 5% skim milk powder solution at 4°C overnight. The membrane was incubated using FGB, Ki-67, E-cadherin, vimentin, N-cadherin, or β-actin antibodies for 2 h at 25°C. The membrane was incubated using secondary antibodies for 1 h. Chemiluminescence was developed using a hypersensitive ECL kit (Baiaosi, China).

2.5. CCK-8 Assay. MCF-7 cells transfected using si-FGB and negative control were cultured for one day and digested using 0.25% trypsin. Cell suspension was diluted at 5×10^5 pieces/ml. 10 μL cell suspension was inoculated into 96-well plate. Cells were incubated with 10 μL CCK-8 solution at 37°C for 1 h, and then the absorbance of 450 nm was detected by microplate reader.

Table 1: Primer sequence.

Target	Primer sequence (5′-3′)
miR-877-5p	F: TAGAGGAGATGGCGCAG R: GAACATGTCTGCGTATCTC
U6	F: CTCGCTTCGGCAGCACA R: AACGCTTCACGAATTTGCGT
FGB	F: AGCCTACAGATCACTAGCAAT R: TGTGGTACTGATGCTCTCCACG
β-Actin	F: ACGTCACGAACTACTAGCAAT R: TGTGTGCATGAGTCTCTCCACG

2.6. Transwell Assay. The transwell chamber was placed in a 24-well plate. After evenly mixing the Matrigel matrix gel with DMEM in a 1 : 6 ratio, 50 μL was added to the bottom of the transwell chamber. Complete medium including FBS was added to the down chamber, and 1×10^5 cells in 200 μL medium were added to the upper chamber for 24 h. Cell number attached to the lower surface of the compartment was observed using a microscope.

2.7. Luciferase Reporter Assay. The fragment of miR-877-5p bound to FGB was amplified and inserted into the luciferase reporter plasmid to construct the wild-type FGB plasmid (FGB-WT). The mutant FGB plasmid (FGB-MUT) was constructed after the binding site. Subsequently, 293 T cells were transfected with FGB-WT and FGB-MUT with miR-877-5p mimics, and the fluorescence intensity of each group was measured after 48 h using the Luciferase Reporter Assay Kit.

2.8. Flow Cytometry Assay. Cells were suspended in 500 μL Binding Buffer. The cell suspension was added with 5 μL Annexin V-FITC and stained for 15 min at 25°C. 5 μL PI dye was added and stained for 5 min at 25°C. Flow cytometry was utilized to measure apoptosis.

2.9. Xenograft Tumor Model in BALB/C Nude Mice. BALB/c nude mice were injected with si-NC or si-FGB under the skin of the left flank. Tumor growth was observed on days 9, 14, 19, 24, and 29. On the 29th day, all mice were sacrificed, and tumor tissues were taken out and weighed.

2.10. Statistical Analysis. Analysis was conducted via SPSS 25.0 software. Comparison between two groups was performed by t-test and one-way ANOVA between multiple groups. $P < 0.05$ represented that differences were statistically significant.

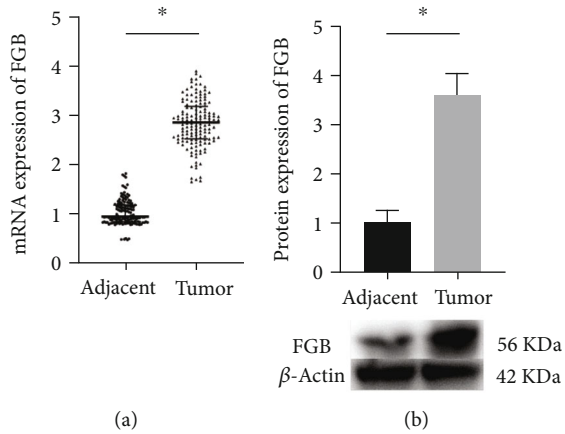

Figure 1: FGB was upregulated in BC tissues. (a) The mRNA expression of FGB was evaluated by qRT-PCR. (b) The expression of FGB was measured in by western blot. $^*P < 0.05$.

Table 2: Relationship between the expression of FGB and clinical features.

Items	N	Low ($n = 76$)	High ($n = 74$)	χ^2	P
Age, year				0.496	0.481
≤50	59	32	27		
>50	91	44	47		
Tumor size, cm				3.311	0.069
≤3	68	40	28		
>3	82	36	46		
ER status				1.102	0.294
Negative	57	32	25		
Positive	93	44	49		
PR status				1.354	0.245
Negative	82	38	44		
Positive	68	38	30		
HER2 status				1.312	0.252
Negative	76	35	41		
Positive	74	41	33		
TNM stage				6.014	0.014
I/II	86	51	35		
III/IV	64	25	39		
Lymph nodes status				5.311	0.021
Negative	91	53	38		
Positive	59	23	36		

3. Results

3.1. FGB Was More Highly Expressed in BC Tissues. The mRNA expression of FGB was obviously raised in BC tumor tissues (Figure 1(a)). By comparison with adjacent tissues, FGB was more highly expressed in BC tumor tissues (Figure 1(b)). The expression of FGB was associated with TNM stage and lymph node metastasis and showed a positive correlation (Table 2). The expression of FGB was not obviously correlated with other indicators.

3.2. Knockdown of FGB Suppressed the Proliferation and Invasion of BC Cells. Western blot was utilized to evaluate the knockdown effect and demonstrate the expression of FGB which was obviously declined in the sh-FGB group (Figure 2(a)). Cell proliferation ability was inhibited by sh-FGB in contrast to the sh-NC group (Figure 2(b)). Knockdown of FGB obviously promoted BC cell apoptosis in contrast to the sh-NC group (Figure 2(c)). Knockdown of FGB markedly decreased BC cell invasion in contrast to the sh-NC group (Figure 2(d)).

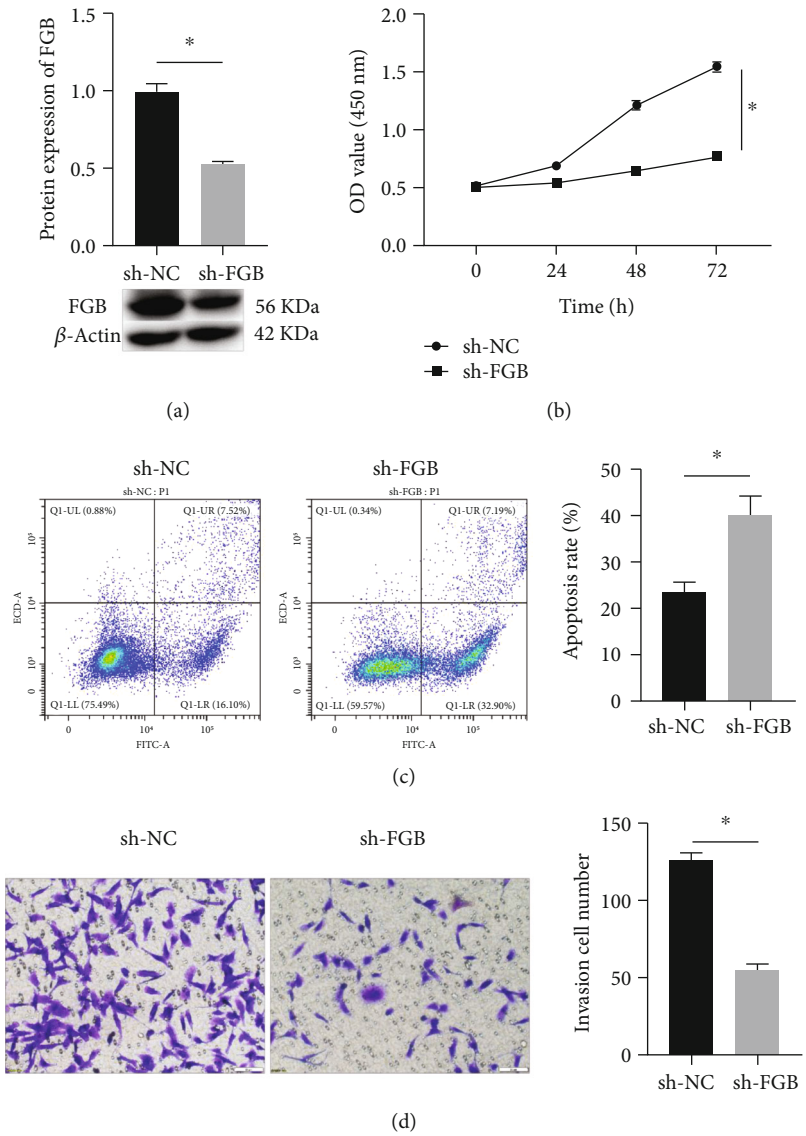

Figure 2: Knockdown of FGB suppressed the proliferation and invasion of BC cells. (a) Western blot was utilized to detect the protein expression of FGB. (b) Hindrance effect of FGB knockdown on MCF-7 cell proliferation. (c) Hindrance effect of FGB knockdown on MCF-7 cell apoptosis. (d) Hindrance effect of FGB knockdown on MCF-7 cell invasion. Magnification ×200.

3.3. Knockdown of FGB Suppressed the Progress of BC In Vivo. The xenograft tumor model was constructed to figure out the influence of FGB knockdown on tumor growth in vivo. As shown in Figure 3(a), knockdown of FGB markedly inhibited the tumor growth. In contrast to the sh-NC group, knockdown of FGB markedly decreased tumor weight (Figure 3(b)) and volume (Figure 3(c)). The Ki-67 expression was observably declined in the sh-FGB group (Figure 3(d)).

3.4. FGB Was Directly Regulated by miR-877-5p. TargetScan online tool was utilized to predict the upstream of FGB and found that FGB might be regulated by miR-877-5p (Figure 4(a)). Luciferase reporter assay confirmed this prediction. miR-877-5p mimic obviously decreased the relative luciferase activity of FGB-WT while the relative luciferase activity of FGB-MUT was not changed (Figure 4(b)). The FGB expression was inhibited in the miR-877-5p mimic group while the FGB expression was raised in the miR-877-5p inhibitor group (Figure 4(c)).

3.5. Knockdown of FGB Suppressed the EMT Progress of BC. The protein expression of E-cadherin was markedly raised in the sh-FGB group while the protein expression of N-cadherin and vimentin was observably decreased in the sh-FGB group (Figure 5(a)). The mRNA expression of E-cadherin was observably raised in the sh-FGB group while the mRNA expression of N-cadherin and vimentin was markedly declined in the sh-FGB group (Figure 5(b)).

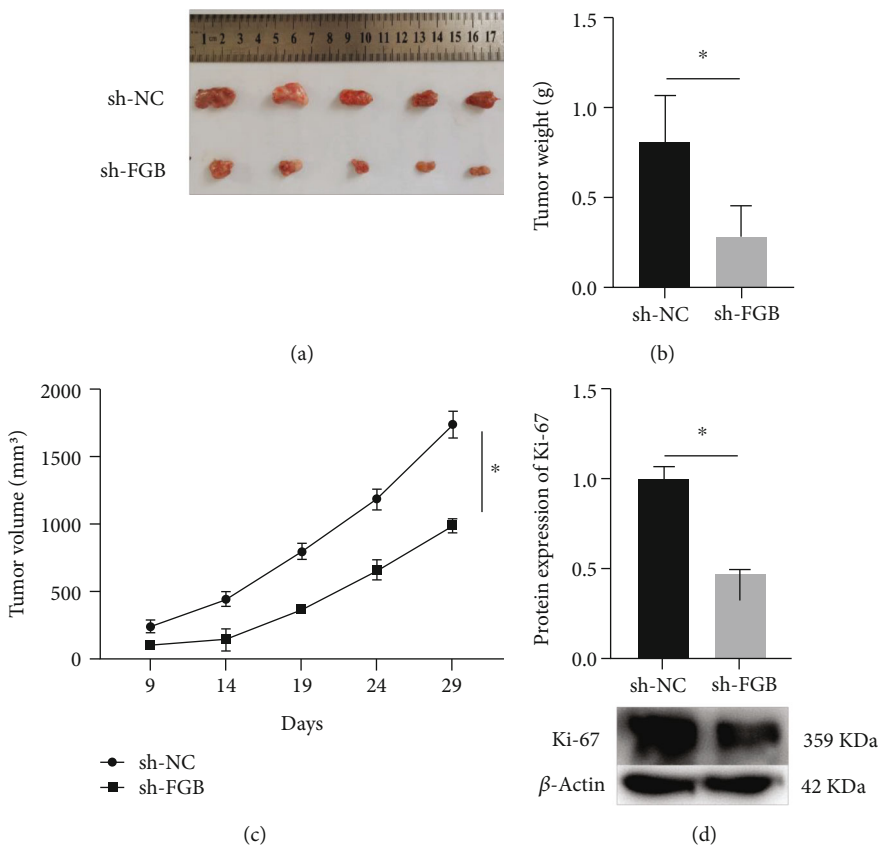

Figure 3: Knockdown of FGB suppressed the progress of BC in vivo. (a) Tumor photos taken by digital camera. (b) Tumor weight was obviously declined in the sh-FGB group. (c) Tumor volume was markedly declined in the sh-FGB group. (d) The Ki-67 protein expression was evaluated by western blot. $^{*}P < 0.05$.

4. Discussion

Local recurrence or distant metastasis may occur after BC surgery. Cancer cells can metastasize because of uncontrolled cell proliferation and migration [10]. Once the free cancer cells spread to the whole body and form cancer metastasis, they will be life-threatening. In recent years, a large number of studies have reported that miRNAs were essential in tumor invasion and metastasis in BC [11]. The present study found that FGB was more highly expressed in BC tumor tissue, and the expression of FGB was relevant to TNM stage and LNM and showed a positive correlation. In addition, FGB was directly regulated by miR-877-5p and enhanced the proliferation and invasion of BC cells. miRNAs were essential in progress of tumor development and EMT, which could regulate the process of tumor EMT mediated by oncogenes or tumor suppressor genes, so as to regulate the process of tumor development [12]. miR-646 inhibited EMT-induced proliferation and metastasis by targeting FOXK1 [13]. miR-1249 inhibited EMT progression, proliferation, and migration in BC cells [14]. In gastric cancer cells, miR-130a-3p inhibited cell migration and invasion via inhibiting the TBL1XR1-mediated EMT process [15]. Inhibition of miR-877-5p promoted migration and invasion of gastric cancer cells via binding to FOXM1 [16]. miR-877-5p inhibited cell proliferation in prostate cancer via binding SSFA2 [17].

In order to figure out the influence of FGB knockdown on tumor growth in vivo, the xenograft tumor model was constructed successfully. Results showed that knockdown of FGB markedly inhibited the tumor growth, including tumor weight and volume. In addition, the Ki-67 expression was observably declined in the sh-FGB group. These results demonstrated that miR-877-5p could inhibit the BC progress by targeting FGB in vivo. It has been proved that EMT can regulate the invasion and migration of tumor cells [18, 19]. EMT is mainly characterized by dissociation of epithelial tight junctions, loss of cellular adhesions, and cytoskeletal rearrangements [20]. The main hallmarks of EMT are a decrease in epithelial cellular markers (E-cadherin) and an increase in mesenchymal cellular markers (N-cadherin, vimentin). E-cadherin, N-cadherin, and vimentin also became the main markers for the evaluation of EMT [20]. The present study demonstrated that the protein expression of E-cadherin was obviously raised in the sh-FGB group while the protein expression of N-cadherin and vimentin was markedly decreased in the sh-FGB group. Therefore, FGB could promote the EMT process to enhance deterioration degree of BC.

In conclusion, miR-877-5p inhibits epithelial mesenchymal transformation, cell proliferation, and invasion of BC cells by targeting FGB.

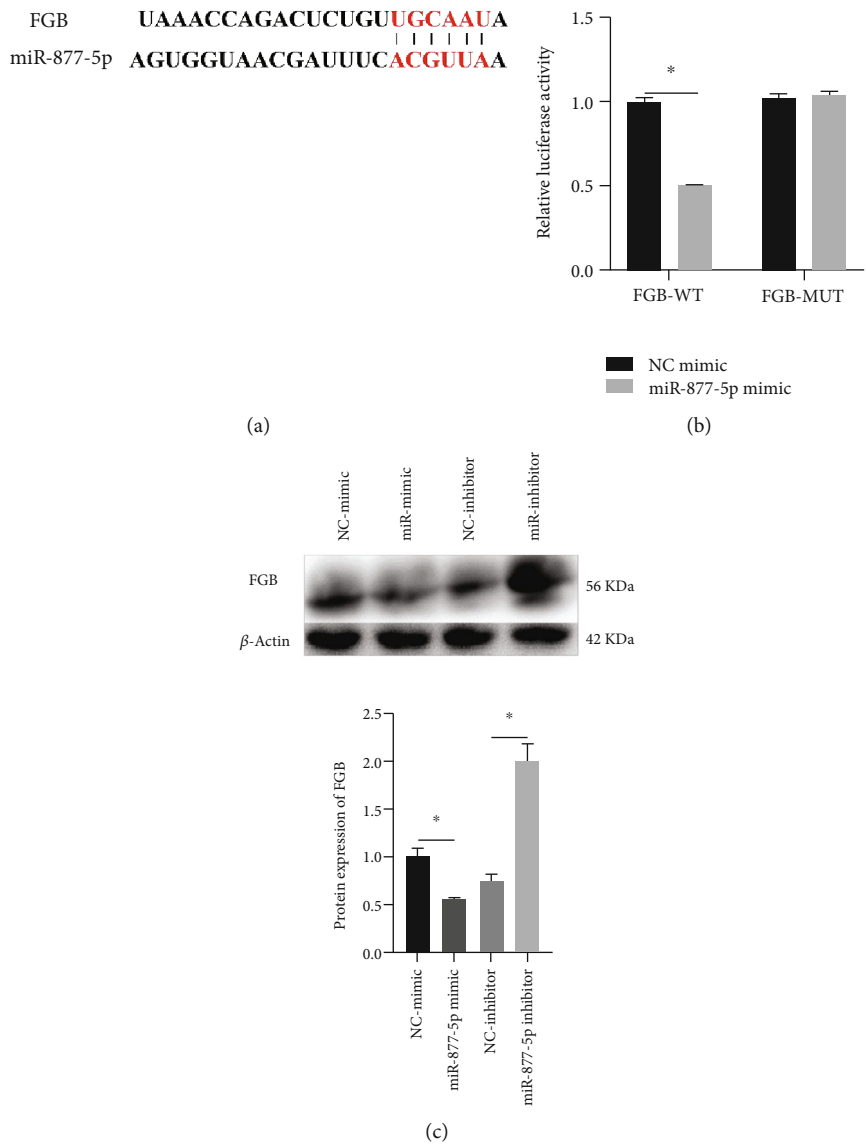

Figure 4: FGB was directly regulated by miR-877-5p. (a) Predicted binding sites. (b) Luciferase reporter assay was conducted. (c) The protein expression of FGB was measured via western blot. $^{*}P < 0.05$.

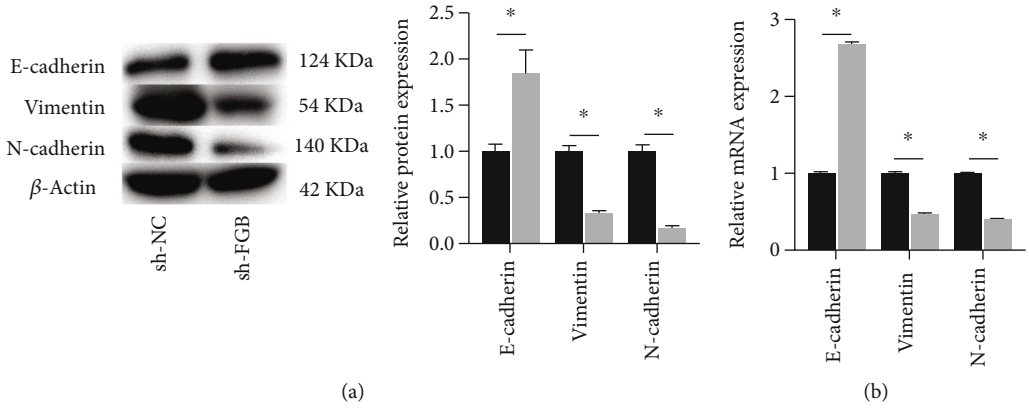

Figure 5: Knockdown of FGB suppressed the EMT progress of BC. (a) Western blot was utilized to measure the protein expression. (b) RT-qPCR was utilized to measure the mRNA expression. $^{*}P < 0.05$.

Data Availability

Data to support the findings of this study is available on reasonable request from the corresponding author.

Conflicts of Interest

The authors have no conflicts of interest to declare.

Acknowledgments

This research was funded by the Shandong Provincial Medical Association Special Fund for Research on Breast Diseases, Grant No. YXH2020ZX072 and Scientific and Technological Project of Jinan Municipal Health Commission, Grant No. 2018-2-32.

References

[1] L. Fan, K. Strasser-Weippl, J. J. Li et al., "Breast cancer in China," *The Lancet Oncology*, vol. 15, no. 7, pp. e279–e289, 2014.

[2] M. Fahad Ullah, "Breast cancer: current perspectives on the disease status," *Advances in Experimental Medicine and Biology*, vol. 1152, pp. 51–64, 2019.

[3] Y. Liang, H. Zhang, X. Song, and Q. Yang, "Metastatic heterogeneity of breast cancer: molecular mechanism and potential therapeutic targets," *Seminars in Cancer Biology*, vol. 60, pp. 14–27, 2020.

[4] S. Wang, Y. Liang, W. Chang, B. Hu, and Y. Zhang, "Triple negative breast cancer depends on sphingosine kinase 1 (SphK1)/sphingosine-1-phosphate (S1P)/sphingosine 1-phosphate receptor 3 (S1PR3)/Notch signaling for metastasis," *Medical Science Monitor*, vol. 24, pp. 1912–1923, 2018.

[5] Y. Shi, Z. Liu, Q. Lin et al., "miRNAs and cancer: key link in diagnosis and therapy," *Genes*, vol. 12, no. 8, p. 1289, 2021.

[6] X. Kong, J. Zhang, J. Li, J. Shao, and L. Fang, "miR-130a-3p inhibits migration and invasion by regulating RAB5B in human breast cancer stem cell-like cells," *Biochemical and Biophysical Research Communications*, vol. 501, no. 2, pp. 486–493, 2018.

[7] C. P. Tang, H. J. Zhou, J. Qin, Y. Luo, and T. Zhang, "MicroRNA-520c-3p negatively regulates EMT by targeting IL-8 to suppress the invasion and migration of breast cancer," *Oncology Reports*, vol. 38, no. 5, pp. 3144–3152, 2017.

[8] Y. Zhang and R. A. Weinberg, "Epithelial-to-mesenchymal transition in cancer: complexity and opportunities," *Frontiers in Medicine*, vol. 12, no. 4, pp. 361–373, 2018.

[9] M. Kuang, Y. Peng, X. Tao et al., "FGB and FGG derived from plasma exosomes as potential biomarkers to distinguish benign from malignant pulmonary nodules," *Clinical and Experimental Medicine*, vol. 19, no. 4, pp. 557–564, 2019.

[10] S. Libson and M. Lippman, "A review of clinical aspects of breast cancer," *International Review of Psychiatry*, vol. 26, no. 1, pp. 4–15, 2014.

[11] B. Mansoori, P. H. G. Duijf, A. Mohammadi et al., "miR-142-3p targets HMGA2 and suppresses breast cancer malignancy," *Life Sciences*, vol. 276, article 119431, 2021.

[12] T. Wang, L. Xu, R. Jia, and J. Wei, "miR-218 suppresses the metastasis and EMT of HCC cells via targeting SERBP1," *Acta Biochimica et Biophysica Sinica*, vol. 49, no. 5, pp. 383–391, 2017.

[13] P. Zhang, W. M. Tang, H. Zhang et al., "miR-646 inhibited cell proliferation and EMT-induced metastasis by targeting FOXK1 in gastric cancer," *British Journal of Cancer*, vol. 117, no. 4, pp. 525–534, 2017.

[14] J. Ding, W. Wu, J. Yang, and M. Wu, "Long non-coding RNA MIF-AS1 promotes breast cancer cell proliferation, migration and EMT process through regulating miR-1249-3p/HOXB8 axis," *Pathology, Research and Practice*, vol. 215, no. 7, article 152376, 2019.

[15] S. Wang, H. Han, Y. Hu et al., "MicroRNA-130a-3p suppresses cell migration and invasion by inhibition of TBL1XR1-mediated EMT in human gastric carcinoma," *Molecular Carcinogenesis*, vol. 57, no. 3, pp. 383–392, 2018.

[16] K. Wu, Z. Yu, Z. Tang et al., "miR-877-5p suppresses gastric cancer cell proliferation through targeting FOXM1," *Oncotargets and Therapy*, vol. Volume 13, pp. 4731–4742, 2020.

[17] W. Wang, J. Yi, D. Dong, W. Mao, X. Wang, and Z. Yan, "miRNA-877-5p inhibits malignant progression of prostate cancer by directly targeting SSFA2," *European Journal of Histochemistry*, vol. 65, no. 3, 2021.

[18] X. Chen, A. M. Bode, Z. Dong, and Y. Cao, "The epithelial–mesenchymal transition (EMT) is regulated by oncoviruses in cancer," *The FASEB Journal*, vol. 30, no. 9, pp. 3001–3010, 2016.

[19] I. Pastushenko and C. Blanpain, "EMT transition states during tumor progression and metastasis," *Trends in Cell Biology*, vol. 29, no. 3, pp. 212–226, 2019.

[20] V. Mittal, "Epithelial mesenchymal transition in tumor metastasis," *Annual Review of Pathology*, vol. 13, no. 1, pp. 395–412, 2018.

Hindawi
Disease Markers
Volume 2022, Article ID 1015593, 9 pages
https://doi.org/10.1155/2022/1015593

Research Article

Identification of Key Genes and miRNAs Affecting Osteosarcoma Based on Bioinformatics

Le Li,[1] **Xin Zhou**,[1] **Wencan Zhang**,[1] **and Ran Zhao**[2]

[1]*Department of Orthopedic Surgery, Qilu Hospital of Shandong University, Jinan, Shandong Province, China*
[2]*Department of Burns and Plastic Surgery, Shandong Provincial Hospital Affiliated to Shandong First Medical University, Jinan, Shandong Province, China*

Correspondence should be addressed to Ran Zhao; zhaoranburn@126.com

Received 6 July 2022; Revised 28 September 2022; Accepted 3 October 2022; Published 16 November 2022

Academic Editor: Jianxin Shi

Object. Osteosarcoma is an intractable malignant disease, and few therapeutic methods can thoroughly eradicate its focuses. This study attempted to investigate the related mechanism of osteosarcoma by bioinformatics methods. *Methods*. GSE70367 and GSE69470 were obtained from the GEO database. The differentially expressed genes (DEGs) and miRNAs were analyzed using the GEO2R tool and then visualized with R software. Moreover, the targets of the miRNAs in the DEGs were screened and then used for enrichment analysis. Besides, the STRING database and Cytoscape were applied to illustrate the protein-protein interaction network. RT-qPCR was performed to measure the expression of key genes and miRNAs. Western blot was applied to detect the signaling pathway. *Results*. 9 upregulated genes and 39 downregulated genes in GSE69470 were identified as the DEGs, and 31 upregulated genes and 56 downregulated genes in GSE70367 were identified as the DEGs. Moreover, 21 common genes were found in the DEGs of GSE70367 and GSE69470. The enrichment analysis showed that the common DEGs of GSE70367 and GSE69470 were related with cell development, covalent chromatin modification, and histone modification and involve in the regulation of MAPK, mTOR, and AMPK pathways. Besides, the miRNAs including miR-543, miR-495-3p, miR-433-3p, miR-381-3p, miR-301a-3p, miR-199b-5p, and miR-125b-5p were identified as the biomarkers of osteosarcoma. In addition, the target genes including HSPA5, PPARG, MAPK14, RAB11A, RAB5A, MAPK8, LEF1, HIF1A, CAV1, GS3KB, FOXO3, IGF1, and NFKBIA were identified as hub nodes. It was found that miR-301a-3p expression was decreased and mRNA expression of RAB5A and NFKBIA was increased in the pathological tissues. The AKT-PI3K-mTOR signaling pathway was activated in pathological tissues. *Conclusion*. In this study, 7 miRNAs and 13 hub genes were identified, which might be candidate markers. miR-301a-3p, RAB5A, and NFKBIA were abnormally expressed in osteosarcoma tissues.

1. Introduction

Osteosarcoma is a frequent malignant bone disease in children and older patients, which is characterized with poor prognosis including physical disability and metastases [1, 2]. Surgery excision, radiotherapy, and chemotherapy have been widely used for osteosarcoma treatment, which can effectively inhibit the development of the tumor progression in the early stage [3]. Nevertheless, considerable patients have been confirmed to be at the advanced stage in their first clinical diagnosis. Moreover, high metastasis rates of osteosarcoma also make the clinical intervention become tricky and then lead to treatment failure [4]. Although the survival times of the patients have been significantly prolonged with the modern medicine techniques, the treatment effect remains unsatisfactory for patients [5, 6]. At present, some reports have focused on revealing the potential mechanism of osteosarcoma, which can provide valuable reference for the progression of medicine strategies [7, 8]. At present, there have been many studies on the molecular mechanism of osteosarcoma, and several osteosarcoma-driving genes have been identified, such as TP53, RB1, and PTEN. There have also been targeted drugs for osteosarcoma, such as pazopanib, appatinib, cabotinib, and ivermex. However, these studies have not clearly explained the pathogenesis and metastasis of osteosarcoma. Therefore, it is urgent to

further study the potential molecular mechanism of osteosarcoma cells, identify reliable molecular markers, and identify new drug targets.

Microarray analysis is a useful method which has been used for screening the key genes in diseases [9]. Recently, the academic and guiding value of bioinformatics methods on improving the clinical practice have been proven by numerous researches [10]. MicroRNA is a class of the short noncoding RNA with 18-20 nucleotides, which plays a great part in the cellular life activity [11]. The abnormal expression of miRNA is a biomarker event in multiple diseases, especially in caner. In osteosarcoma, many studies have indicated that miRNA can regulate the cellular phenotype to influence the progression of the tumor via intervening the expression of key proteins [12]. However, the miRNA-mRNA interaction network of osteosarcoma is still far from complete clarification.

In this project, the purpose was to identify the pivotal biomarkers and related mechanism of the osteosarcoma using bioinformatics methods through obtaining the open-source datasets in the GEO database.

2. Materials and Methods

2.1. Data Source. We searched the datasets comparing mRNA or miRNA expression profiles of osteosarcoma and normal samples using "osteosarcoma" as search terms for the GEO datasets (https://www.ncbi.nlm.nih.gov/geo/). The datasets including GSE70367 and GSE69470 were obtained. GSE69470 contained the expression profile of 15 samples, including 10 osteosarcoma samples and 5 normal samples, which was based on platform GPL20275. For GSE70367 based on GPL16384, 5 samples of tumor cell lines and 1 sample of the hMSC cell line were used for analysis.

2.2. Identification of Differentially Expressed Genes. The DEGs of the datasets were analyzed with the GEO2R tool of the GEO database to obtain the related matrix files. The genes with the $|\log FC| > 2$ and P value < 0.05 were selected as the DEGs.

2.3. KEGG and GO Enrichment Analysis. The targets of the DEGs were predicted with the mirDIP database (http://ophid.utoronto.ca/mirDIP/index.jsp), and the top 5% genes in the results were selected as potential targets of the DEGs in GSE70367 and GSE69470. The KEGG and GO enrichment of DEGs was performed by the DAVID database. In brief, the targets of the DEGS were uploaded into the DAVID database. The pathways and the related functional modules in the results with P value < 0.05 were visualized with the R language.

2.4. Network Analysis. The protein-protein interaction network was performed to identify the hub nodes of the DEGs. Briefly, the targets of the DEGs were uploaded to the STRING database (https://cn.string-db.org/) to analyze and obtain protein interaction information, and then, Cytoscape software was applied to visualize the PPI network.

2.5. Clinical Tissues. The pathological tissues and adjacent healthy tissues were requested from the Qilu Hospital of Shandong University. The experiments were approved by the ethics committee of the hospital. Besides, all tissues were frozen at -70°C.

2.6. qRT-PCR. The RNAs in the tissues were extracted with a TRIzol reagent. The commercial kit (Shanghai Lianmai Biological Engineering Co., Ltd., Shanghai, China) was applied for the reverse transcription of cDNA. Subsequently, the PCR reaction was performed for the quantification of the genes. Moreover, the abundance of the RNAs were measured with the $2^{-\Delta\Delta Ct}$ method.

2.7. Western Blot Analysis. The protein was extracted by the RIPA buffer. Protein was separated by SDS-PAGE and transferred to the nitrocellulose membrane and blocked in 5% skim milk powder solution for 2 h. Then, the membrane was incubated with a primary antibody at 4°C for 12 h. Then, the membrane was incubated by a second antibody at 25°C for 2 h. The protein bands were colored, and the gray value was read under ImageJ software.

2.8. Immunohistochemistry (IHC). IHC was conducted using paraffin-embedded tissue sections. After being deparaffinized and hydrated, the antigen was extracted at 95°C. After treating with 3% H_2O_2, sections were incubated with primary antibody at 4°C overnight and then treated with a second antibody at 37°C for 30 min. Staining was conducted using DAB (Golden Bridge, China).

2.9. Data Analysis. The experiments were repeated for three times, independently. SPSS 19.0 and GraphPad Prism 8.0 was applied for data analysis and visualization, respectively. Moreover, the chi-squared test or ANOVA with Tukey's post hoc test was selected for calculating the difference of data, and $P < 0.05$ represented that the difference was statistically significant.

3. Results

3.1. DEG Identification. To investigate the gene profiles of OS, GSE70367 and GSE69470 were obtained from the GEO database and then analyzed with the GEO2R tool. 9 upregulated DEGs and 37 downregulated DEGs were found in GSE69470, and 31 upregulated DEGs and 55 downregulated DEGs were found in GSE70367 (Figures 1(a) and 1(b)). Moreover, the abundance of the DEGs of GSE70367 and GSE69470 were exhibited in Figure 2. Moreover, 21 downregulated genes were found in GSE70367 and GSE69470 (Figure 1(c)). Those observations suggested that there were significant differences in gene profile of tumor cells and normal cells.

3.2. Identification of Function Model. To investigate the functions of the genes in the progression of osteosarcoma, the targets of the DEGs in GSE70367 and GSE69470 were analyzed with GO enrichment. The results proved that the DEGs in GSE69470 were associated with the regulation of extracellular structure, regulation of protein serine/

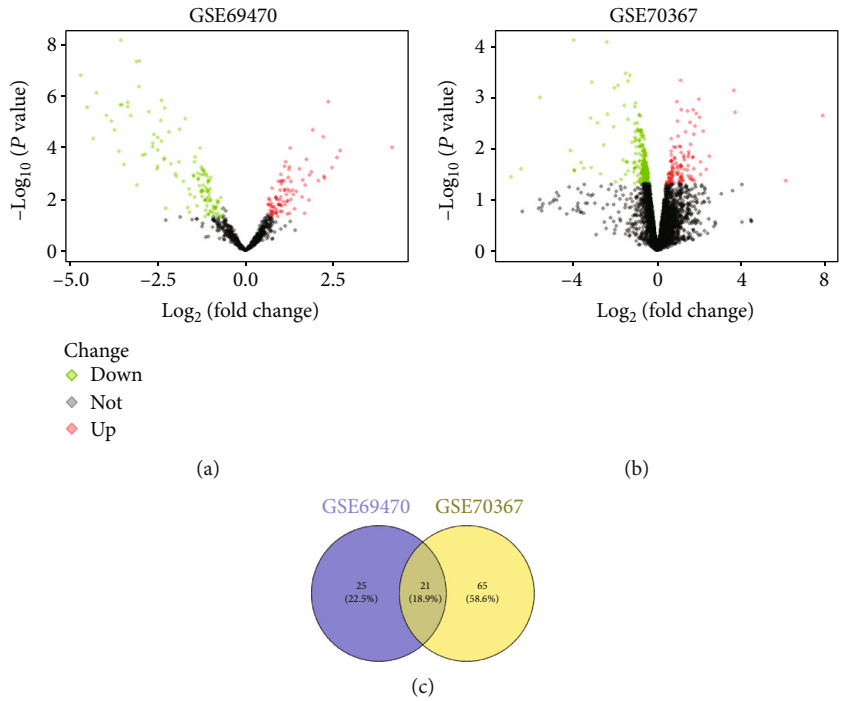

Figure 1: The DEGs in GSE69470 and GSE70367 were visualized with volcano plots. (a) The DEGs in GSE69470. (b) The DEGs in GSE70367. (c) The common genes of GSE69470 and GSE70367 were screened by Venn diagram.

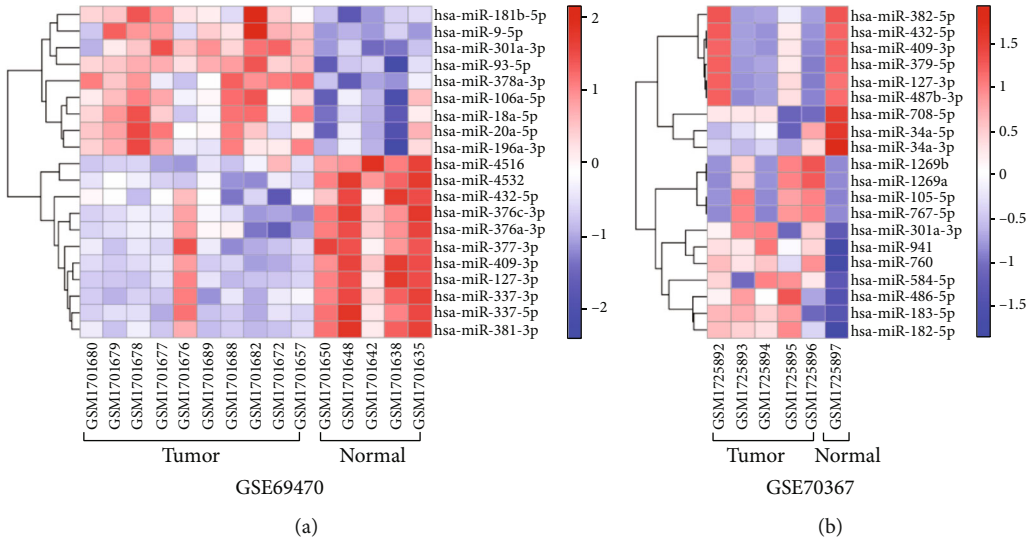

Figure 2: The expressions of DEGs in the samples of GSE69470 and GSE70367 were visualized by heat map: (a) the DEGs in GSE69470; (b) the DEGs in GSE70367.

threonine kinase activity, regulation of GTPase activity, and so on. For GSE70367, the DEGs were related with regulation of cell development, positive regulation of catabolic process, skeletal system development, and so on (Figures 3(a) and 3(b)). Moreover, the common DEGs of GSE70367 and GSE69470 were also related with regulation of cell development, covalent chromatin modification, and histone modification (Figure 3).

3.3. KEGG Enrichment Analysis. For revealing the regulation mechanisms of osteosarcoma, the DEGs of the datasets were analyzed with KEGG enrichment. It was proven that the DEGs in GSE69470 were connected with the extracellular matrix (ECM) receptor interaction, focal adhesion, PI3K/AKT pathways, P53 pathways, TGF-β, Wnt pathway, etc. (Figure 4(a)). The DEGs in GSE70367 were related with the ECM-receptor interaction, PI3K/AKT pathways, TGF-

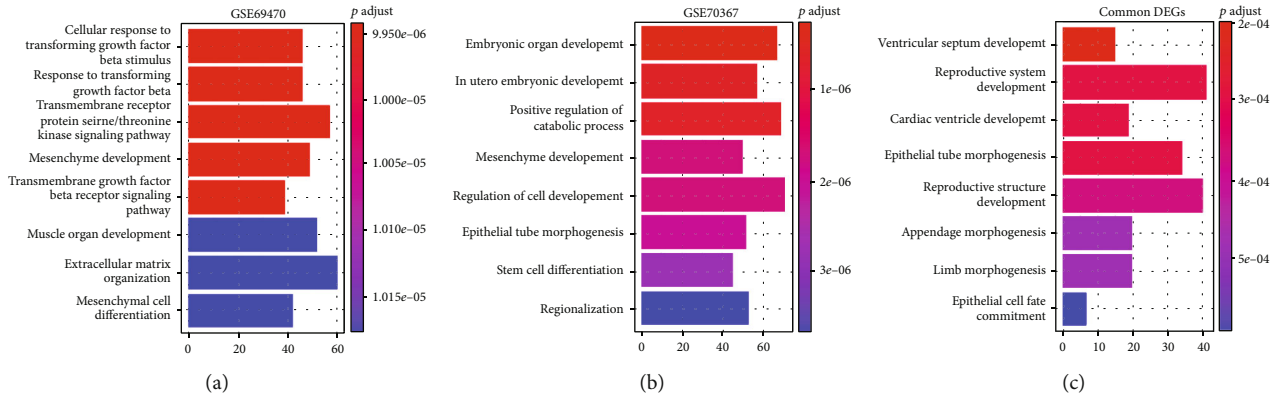

Figure 3: GO enrichment analysis of the DEGs. (a) The GO enrichment analysis of the DEGs in GSE69470. (b) The GO enrichment analysis of the DEGs in GSE70367. (c) The GO enrichment analysis of the common genes in GSE69470 and GSE70367.

β pathway, Hippo pathway, p53 pathway, Wnt pathway, and so on (Figure 4(b)). In addition, the common DEGs of GSE69470 and GSE70367 were related with the MAPK signaling pathway, mTOR signaling pathway, AMPK signaling pathway, Ras signaling pathway, and so on (Figure 4(c)).

3.4. PPI Network. To illustrate the molecular mechanism of osteosarcoma, the protein interactions of DEGs were analyzed to obtain the hub nodes. The results mirrored that for GSE69470, 3 clusters were found in the targets, including cluster 1 with 16 nodes and 234 edges, cluster 2 with 54 nodes and 520 edges, and 84 nodes and 480 edges (Figure 5(a)). For GSE70367, 3 clusters were found in targets, including cluster 1 with 33 nodes and 322 edges, cluster 2 with 43 nodes and 298 edges, and cluster 3 with 71 nodes and 376 edges (Figure 5(b)). Moreover, for the common miRNAs of GSE69470 and GSE70367, there were three clusters including cluster 1 with 22 nodes and 126 edges, cluster 2 with 56 nodes and 308 edges, and cluster 3 with 5 nodes and 20 edges. The results showed that the factors including HSPA5, PPARG, MAPK14, RAB11A, RAB5A, MAPK8, LEF1, GATA3, HIF1A, CAV1, GS3KB, FOXO3, IGF1, and NFKBIA were selected as the hub nodes (Figure 5(c)). In addition, the miRNA-mRNA network was also established (Figure 5(d)). Besides, to verify the relationship of the genes and the progression of osteosarcoma, the screened genes were identified with the published studies or qRT-PCR. It was found that decreased miR-301a-3p and increased RAB5A and NFKBIA were detected in the pathological tissues (Figures 6(a)–6(c)). In addition, IHC results showed that RAB5A and NFKBIA were highly expressed in pathological tissues (Figure 6(d)). The AKT-PI3K-mTOR signaling pathway was activated in pathological tissues (Figure 6(e)).

4. Discussion

Osteosarcoma is one of the dangerous diseases with high incidence, and there are few effective strategies to completely heal this disease [5]. Bioinformatics analysis has been verified as a promising strategy for identifying the biomarkers and researching the molecular mechanism of cancer [13]. In this investigation, the datasets including GSE69470 and GSE70367 were obtained from the GEO database and then used for identifying the hub nodes in osteosarcoma.

Osteosarcoma is characterized with aberrant expression of genes which may involve the some malignant behaviors of the tumor cells. In this project, the expressions of genes in tumor cell lines and normal cell lines were investigated, and 21 downregulated genes were found in GSE69470 and GSE70367. Moreover, downregulation of miR-127-3p, miR-154-5p, miR-323a-3p, miR-409-3p, miR-431-5p, miR-432-5p, miR-433-3p, miR-485-3p, miR-487b-3p, miR-495-3p, and miR-125b-5p was related with cancer development. For instance, miR-127-3p serves as an inhibitor role in the progression of multiple tumors such as glioblastoma and prostate cancer [14, 15]. For osteosarcoma, all of those miRNAs are also involved in the malignant behaviors such as invasion and proliferation.

Cancer development always involves the changes of multiple signaling pathways, such as PI3K/AKT pathways, P53 pathway, and Wnt/β-catenin pathway [16, 17]. For osteosarcoma, the disorder of the cellular signal pathways has also been confirmed as the direct reasons leading to tumor cell proliferation and invasion [18]. The PI3K/AKT pathway is related with cellular proliferation, and the activated PI3K/AKT pathway has been confirmed to involve the progression of multiple cancers. The study of Yang et al. has indicated that the PI3K/AKT pathway was aberrantly activated in the osteosarcoma cells, and inhibiting the PI3K/AKT pathway could effectively impede the proliferation of tumor cells [19]. In this project, it was proven that the DEGs in GSE69470 or GSE70367 were associated with multiple pathways including the PI3K/AKT, TGF-β, Hippo, P53, Wnt, and MAPK pathways. The dysfunctions of signal pathways in tumor cells are closely connected with the miRNA disorder. Increased miR-127-3p, miR-495-3p, and miR-125b-5p have been proven to take part in suppressing the activity of the PI3K/AKT pathway [20–22]. Moreover, the report has proven that miR-409-3p involves regulation of MAPK to block cervical cancer development [23]. Beside, decreased miR-301a-3p was also found in the pathological tissues.

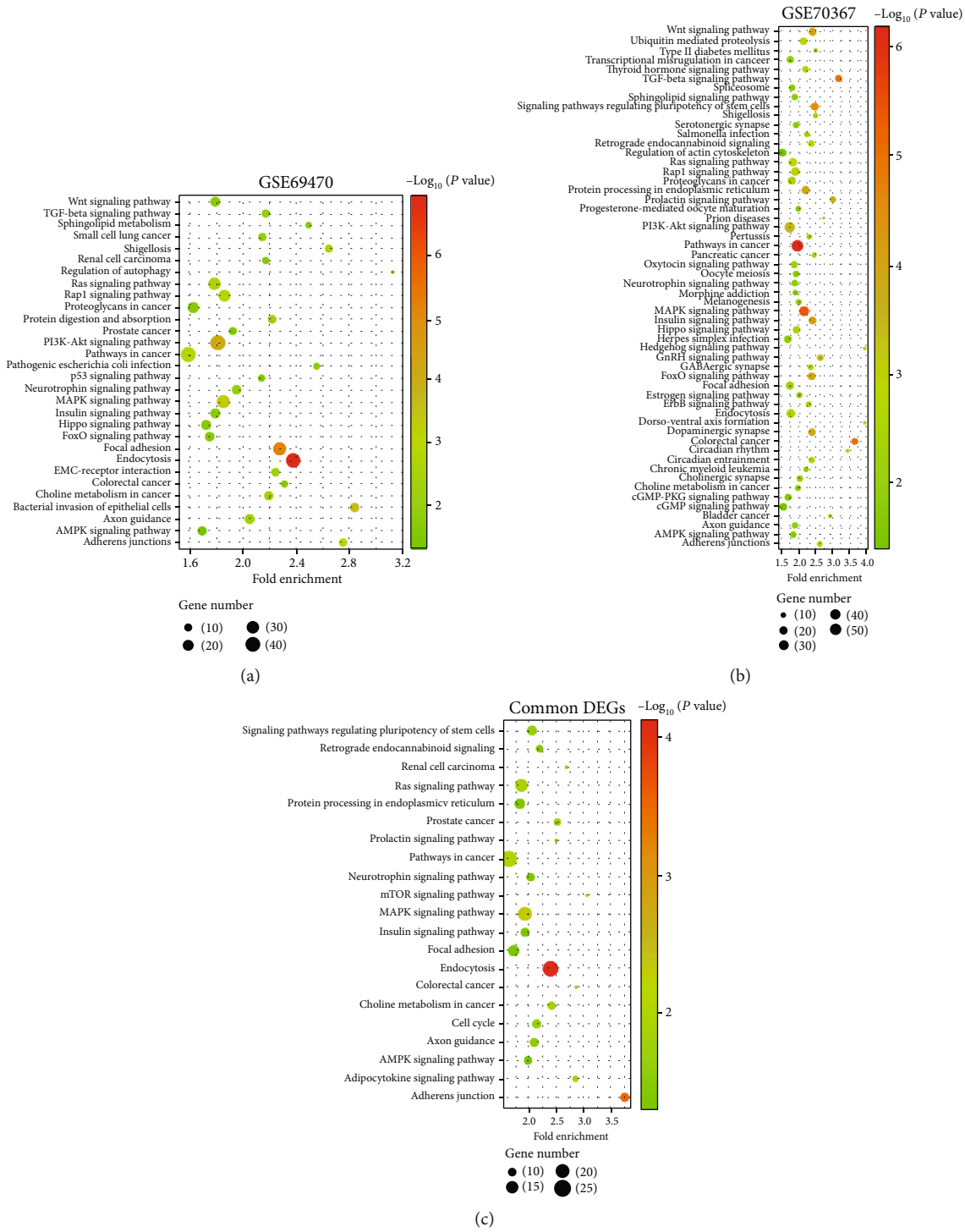

Figure 4: The KEGG enrichment analysis of the DEGs. (a) The KEGG enrichment analysis of the DEGs in GSE69470. (b) The KEGG enrichment analysis of the DEGs in GSE70367. (c) The KEGG enrichment analysis of the common genes in GSE69470 and GSE70367.

miRNA can obstruct the translation progression of proteins via inducing the degradation of the special mRNAs [23]. In this project, the targets of the DEGs in GSE69470 and GSE70367 were predicted and used to reveal the molecular mechanism of osteosarcoma. It was found that the factors including HSPA5, PPARG, MAPK14, RAB11A, RAB5A, MAPK8, LEF1, GATA3, HIF1A, CAV1, GS3KB, FOXO3, IGF1, NFKBIA, and so on were selected as the hub nodes. The study has indicated that HSPA5 inhibition is a promising method for inducing the endoplasmic reticulum stress, autophagy, and apoptosis of tumor cells [24]. MAPK family serves as an important role in the progression

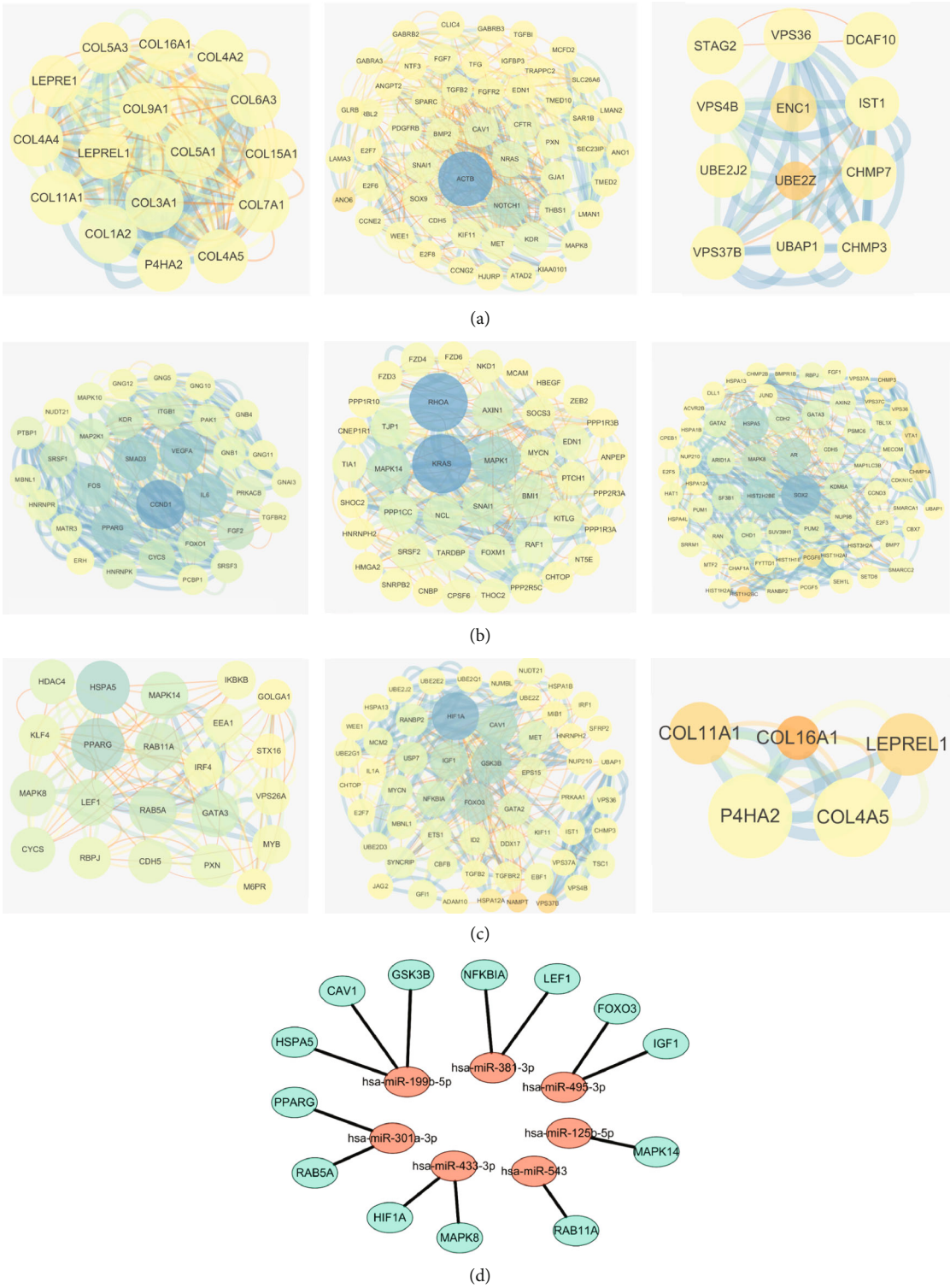

Figure 5: PPI-network analysis and miRNA-mRNA network analysis of DEGs and the related targets. (a) The DEGs in GSE69470 (big and blue sizes were selected as hub nodes). (b) The DEGs in GSE70367 (big and blue sizes were selected as hub nodes). (c) The common genes of GSE69470 and GSE70367. (d) miRNA-mRNA network (red: hsa-miR-433-3p; green: protein).

of multiple tumors. The studies have indicated that increased MAPK8 plays a critical role in the development of colorectal cancer, and MAPK14 downregulation could effectively impede the poor behaviors of the clear cell renal cell carcinoma [25, 26]. Increasing studies have revealed that the disorder of the RAS oncogene family was related with the progression of tumor. In this study, RAB11A and RAB5A were also identified as the hub nodes of

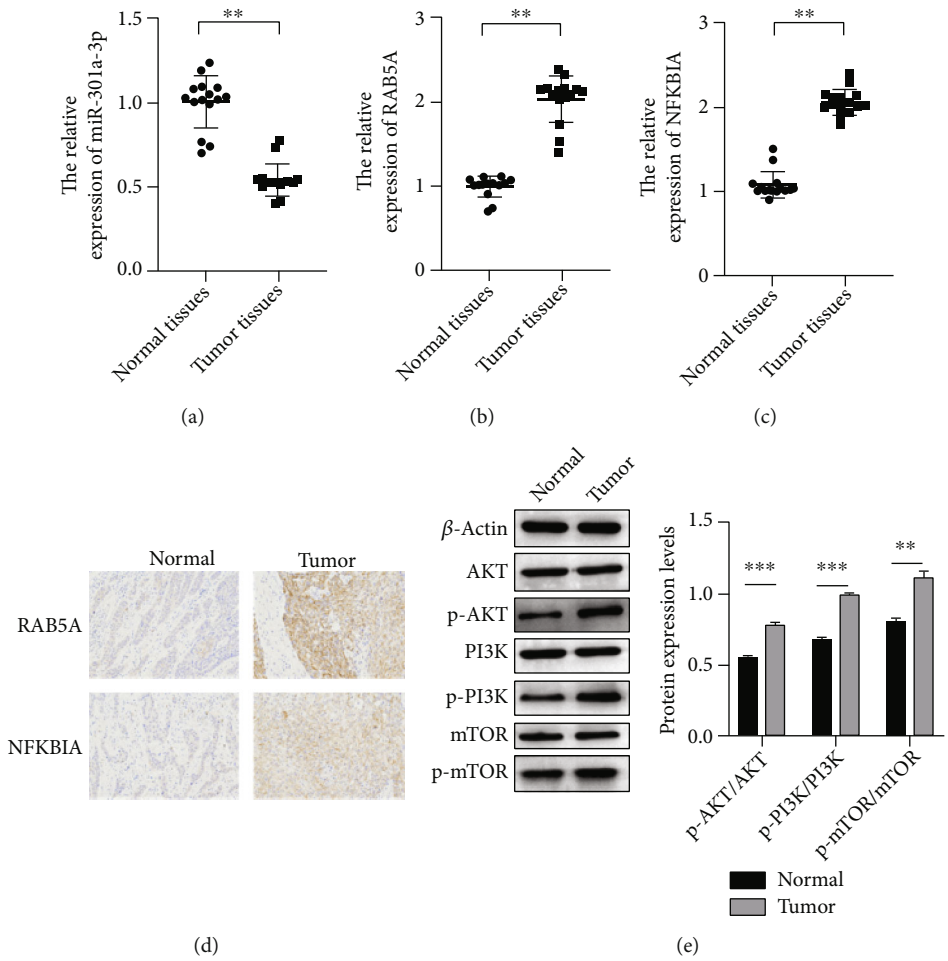

Figure 6: Decreased miR-301a-3p and increased RAB5A and NFKBIA were detected in the pathological tissues. (a–c) The related abundance of miR-301a-3p (a), RAB5A (b), and NFKBIA (c) in the pathological tissues. (d) IHC staining for RAB5A and NFKBIA was performed. (e) Protein expression was measured via western blot.

osteosarcoma. RAB11A involves the regulation of the Wnt/β-catenin pathway to promote the deterioration of prostate cancer, and RAB5A upregulation is related with the proliferation invasion and EMT of ovarian cancer [15, 27]. LEF1 upregulation is related to the resistance of cancer. Fakhr et al. have proven that LEF1 silence could improve the lethal effect of chemotherapy drugs on colorectal cancer cells [28]. HIF1A serves as a key role in regulating the formation of the blood vessel under the hypoxic condition. Some reports have indicated that HIF1A upregulation is related with the invasion and metastasis of tumor cells. In this study, HIF1A was also identified as a hub node. Moreover, CAV1, GS3KB, FOXO3, IGF1, and NFKBIA have also been proven as the biomarkers for prognosis of multiple cancers. Moreover, increased RAB5A and NFKBIA were detected in the pathological tissues.

In conclusion, in this study, 7 miRNAs and 13 hub genes were identified, which might be candidate markers. miR-301a-3p, RAB5A, and NFKBIA were abnormally expressed in osteosarcoma tissues. However, one of the limitations of this study was that no more experiments have been conducted to verify whether miR-301a-3p, RAB5A, and NFKBIA affect tumor progression. In addition, this study lacks more dataset analysis to verify the conclusions of this study.

Data Availability

The data used to support the findings of this study are included within the article.

Conflicts of Interest

The authors declare that they have no competing interest.

Authors' Contributions

Le Li and Ran Zhao were responsible for the conceptualization; Le Li was responsible for the methodology; Ran Zhao was responsible for the software; Le LiRan Zhao and Xin Zhou were responsible for the validation; Wencan Zhang handled the formal analysis; Le Li, Xin Zhou, and Wencan Zhang handled the investigation; Ran Zhao was responsible

for the resources; Le Li handled the data curation; Le Li was responsible for the original draft preparation; Le Li handled the review and editing; Ran Zhao handled the visualization; Ran Zhao supervised the project; Ran Zhao handled project administration; and Ran Zhao was responsible for funding acquisition. All authors have read and agreed to the published version of the manuscript.

Acknowledgments

This research was funded by the Shandong Provincial Natural Science Foundation (grant numbers ZR2022QH143 and ZR2021MH103).

References

[1] Q. Huang, X. Liang, T. Ren et al., "The role of tumor-associated macrophages in osteosarcoma progression-therapeutic implications," *Cellular Oncology (Dordrecht)*, vol. 44, no. 3, pp. 525–539, 2021.

[2] W. Liu, P. Liu, H. Gao, X. Wang, and M. Yan, "Long noncoding RNA PGM5-AS1 promotes epithelial-mesenchymal transition, invasion and metastasis of osteosarcoma cells by impairing miR-140-5p-mediated FBN1 inhibition," *Molecular Oncology*, vol. 14, no. 10, pp. 2660–2677, 2020.

[3] G. M. Shankar, M. J. Clarke, T. Ailon et al., "The role of revision surgery and adjuvant therapy following subtotal resection of osteosarcoma of the spine: a systematic review with meta-analysis," *Journal of Neurosurgery. Spine*, vol. 27, no. 1, pp. 97–104, 2017.

[4] D. Zheng, W. Liu, W. Xie et al., "AHA1 upregulates IDH1 and metabolic activity to promote growth and metastasis and predicts prognosis in osteosarcoma," *Signal Transduction and Targeted Therapy*, vol. 6, no. 1, p. 25, 2021.

[5] K. H. Lu, E. W. Lu, C. W. Lin, J. S. Yang, and S. F. Yang, "New insights into molecular and cellular mechanisms of zoledronate in human osteosarcoma," *Pharmacology & Therapeutics*, vol. 214, article 107611, 2020.

[6] Y. H. Lin, B. E. Jewell, J. Gingold et al., "Osteosarcoma: molecular pathogenesis and iPSC modeling," *Trends in Molecular Medicine*, vol. 23, no. 8, pp. 737–755, 2017.

[7] C. Chen, L. Xie, T. Ren, Y. Huang, J. Xu, and W. Guo, "Immunotherapy for osteosarcoma: fundamental mechanism, rationale, and recent breakthroughs," *Cancer Letters*, vol. 1, no. 500, pp. 1–10, 2021.

[8] X. Zhou, Y. Fan, W. Ye, B. Jia, Y. Yang, and Y. Liu, "Identification of the novel target genes for osteosarcoma therapy based on comprehensive bioinformatic analysis," *DNA and Cell Biology*, vol. 39, no. 7, pp. 1172–1180, 2020.

[9] Y. Sun, L. Wang, C. Li et al., "Construction of an integrated human osteosarcoma database, HOsDb, based on literature mining, microarray analysis, and database retrieval," *BMC Cancer*, vol. 20, no. 1, p. 390, 2020.

[10] S. A. Lozano Calderón, C. Garbutt, J. Kim et al., "Clinical and molecular analysis of pathologic fracture-associated osteosarcoma: microRNA profile is different and correlates with prognosis," *Clinical Orthopaedics and Related Research*, vol. 477, no. 9, pp. 2114–2126, 2019.

[11] R. Chen, G. Wang, Y. Zheng, Y. Hua, and Z. Cai, "Drug resistance-related microRNAs in osteosarcoma: translating basic evidence into therapeutic strategies," *Journal of Cellular and Molecular Medicine*, vol. 23, no. 4, pp. 2280–2292, 2019.

[12] H. Z. Ma, J. Wang, J. Shi, W. Zhang, and D. S. Zhou, "MicroRNA-29c-3p inhibits osteosarcoma cell proliferation through targeting PIK3R3," *European Review for Medical and Pharmacological Sciences*, vol. 24, no. 5, pp. 2239–2247, 2020.

[13] P. Song, Z. Xie, C. Chen et al., "Identification of a novel iron zinc finger protein 36 (ZFP36) for predicting the overall survival of osteosarcoma based on the Gene Expression Omnibus (GEO) database," *Annals of Translational Medicine*, vol. 9, no. 20, p. 1552, 2021.

[14] J. Liu, X. Yu, H. Yu et al., "Knockdown of MAPK14 inhibits the proliferation and migration of clear cell renal cell carcinoma by downregulating the expression of CDC25B," *Cancer Medicine*, vol. 9, no. 3, pp. 1183–1195, 2020.

[15] Y. Zhang and Y. Li, "Long non-coding RNA NORAD contributes to the proliferation, invasion and EMT progression of prostate cancer via the miR-30a-5p/RAB11A/WNT/β-catenin pathway," *Cancer Cell International*, vol. 20, no. 1, p. 571, 2020.

[16] L. Liu, H. Geng, C. Mei, and L. Chen, "Zoledronic acid enhanced the antitumor effect of cisplatin on orthotopic osteosarcoma by ROS-PI3K/AKT signaling and attenuated osteolysis," *Oxidative Medicine and Cellular Longevity*, vol. 2021, Article ID 6661534, 13 pages, 2021.

[17] H. Li, X. Han, S. Yang, Y. Wang, Y. Dong, and T. Tang, "FOXP1 drives osteosarcoma development by repressing P21 and RB transcription downstream of P53," *Oncogene*, vol. 40, no. 15, pp. 2785–2802, 2021.

[18] C. Qiu, W. Su, N. Shen et al., "MNAT1 promotes proliferation and the chemo-resistance of osteosarcoma cell to cisplatin through regulating PI3K/Akt/mTOR pathway," *BMC Cancer*, vol. 20, no. 1, p. 1187, 2020.

[19] C. Yang, Y. Chen, W. Xiong, and K. Xu, "miR-652 inhibits the proliferation, migration, and invasion of osteosarcoma cells by targeting HOXA9 and regulating the PI3K/Akt signaling pathway," *Journal of Oncology*, vol. 202, Article ID 4809312, 10 pages, 2022.

[20] D. Wang, L. Tang, H. Wu, K. Wang, and D. Gu, "miR-127-3p inhibits cell growth and invasiveness by targeting ITGA6 in human osteosarcoma," *IUBMB Life*, vol. 70, no. 5, pp. 411–419, 2018.

[21] D. Yin, G. Wei, F. Yang, and X. Sun, "Circular RNA has circ 0001591 promoted cell proliferation and metastasis of human melanoma via ROCK1/PI3K/AKT by targeting miR-431-5p," *Human & Experimental Toxicology*, vol. 40, no. 2, pp. 310–324, 2021.

[22] S. Liu, Q. Chen, and Y. Wang, "miR-125b-5p suppresses the bladder cancer progression via targeting HK2 and suppressing PI3K/AKT pathway," *Human Cell*, vol. 33, no. 1, pp. 185–194, 2020.

[23] B. Zhou, T. Li, R. Xie et al., "circFAT1 facilitates cervical cancer malignant progression by regulating ERK1/2 and p38 MAPK pathway through miR-409-3p/CDK8 axis," *Drug Development Research*, vol. 82, no. 8, pp. 1131–1143, 2021.

[24] M. Cerezo and S. Rocchi, "New anti-cancer molecules targeting HSPA5/BIP to induce endoplasmic reticulum stress, autophagy and apoptosis," *Autophagy*, vol. 13, no. 1, pp. 216-217, 2017.

[25] X. Liu, L. Li, J. Bai et al., "Long noncoding RNA plasmacytoma variant translocation 1 promotes progression of colorectal

cancer by sponging microRNA-152-3p and regulating E2F3/MAPK8 signaling," *Cancer Science*, vol. 113, no. 1, pp. 109–119, 2022.

[26] B. Chen, M. Wang, R. Huang et al., "Circular RNA circLGMN facilitates glioblastoma progression by targeting miR-127-3p/LGMN axis," *Cancer Letters*, vol. 522, pp. 225–237, 2021.

[27] J. Ji, C. Li, J. Wang et al., "Hsa_circ_0001756 promotes ovarian cancer progression through regulating IGF2BP2-mediated RAB5A expression and the EGFR/MAPK signaling pathway," *Cell Cycle*, vol. 21, no. 7, pp. 685–696, 2022.

[28] E. Fakhr, F. Zare, K. Azadmanesh, and L. Teimoori-Toolabi, "LEF1 silencing sensitizes colorectal cancer cells to oxaliplatin, 5-FU, and irinotecan," *Biomedicine & Pharmacotherapy*, vol. 143, article 112091, 2021.

Hindawi
Disease Markers
Volume 2022, Article ID 1686891, 8 pages
https://doi.org/10.1155/2022/1686891

Research Article

Effect of Standardized Perioperative Management on EEG Indexes and Nerve and Limb Functions of Patients with Acute Cerebral Infarction Undergoing Mechanical Thrombectomy

Yu Gong[1] and Jie Wang[2]

[1]*Department of Interventional, Yantai Mountain Hospital, Yantai, 264003 Shandong, China*
[2]*Department of Neurology, Shandong Provincial Hospital Affiliated to Shandong First Medical University, Jinan, 250021 Shandong, China*

Correspondence should be addressed to Jie Wang; wangjie@sdphospital.cn

Received 26 July 2022; Revised 5 September 2022; Accepted 9 September 2022; Published 26 September 2022

Academic Editor: Jun Yang

Objective. To explore the application value of standardized perioperative management in mechanical thrombectomy for acute cerebral infarction. *Methods*. 98 patients with acute cerebral infarction admitted to our hospital from January 2019 to January 2022 were selected as the study sample in this study, and all patients were given the standardized perioperative management. According to the interventional methods, they were divided into the thrombolytic treatment group (arteriovenous combined thrombolysis, $n = 49$) and mechanical thrombectomy group (mechanical thrombectomy, $n = 49$) to compare the nerve function, limb function, thrombolysis in myocardial infarction (TIMI) flow grade, symptomatic intracranial hemorrhage within 24 hours, acute vascular reocclusion, and the death status within 1 year and incidence of adverse events in 90 days of the two groups after treatment. *Results*. After treatment, the values of brain symmetry index (BSI) and power ratio indices (DTABR) in the two groups were obviously lower than those before treatment ($P < 0.05$), and the values of BSI and DTABR in the mechanical thrombectomy group were lower than those in the thrombolytic treatment group ($P < 0.05$). According to the statistical data of National Institutes of Health Stroke Scale (NIHSS) score in patients, the NIHSS scores of the two groups after treatment were visibly decreased ($P < 0.05$), while the NIHSS score in the mechanical thrombectomy group after treatment was lower than that in the thrombolytic treatment group ($P < 0.05$). The proportion of modified Rankin scale (mRS) score < 3 in the mechanical thrombectomy group was distinctly higher than that in the thrombolytic treatment group ($P < 0.05$). The proportion of TIMI flow grade ≥ 2 in the mechanical thrombectomy group was significantly higher than that in the thrombolytic treatment group ($P < 0.05$). The rate of symptomatic intracranial hemorrhage within 24 hours in the mechanical thrombectomy group was lower than that in the thrombolytic treatment group ($P < 0.05$), with the indistinctive difference between the two groups ($P > 0.05$). The incidence of acute vascular reocclusion in the mechanical thrombectomy group was markedly lower than that in the thrombolytic treatment group ($P < 0.05$). There was no significant difference in 1-year mortality between the two groups ($P > 0.05$). In the mechanical thrombectomy group, there were 1 case of gingiva bleeding, 1 case of hemorrhinia, and 2 cases of recurrent cerebral infarction in 90 days, with a total of 4 cases (8.16%), while in the thrombolytic treatment group, there were 4 cases of gingiva bleeding, 4 cases of hemorrhinia, and 15 cases of recurrent cerebral infarction in 90 days, with a total of 23 cases (46.94%), indicating that the incidence of adverse events in 90 days in the mechanical thrombectomy group was significantly lower than that in the thrombolytic treatment group ($P < 0.05$). *Conclusion*. The standardized perioperative management is effective in patients with acute cerebral infarction who were treated with arteriovenous combined thrombolysis or mechanical thrombectomy, which can improve the neurological function and physical function of patients. However, the mechanical thrombectomy has a better improvement effect on the neurological function and physical function of patients, with the relatively better safety, thrombolytic effect, and long-term prognosis.

1. Introduction

Acute cerebral infarction is a common acute disease in neurological department, and the symptoms of infarction occur due to the abnormal cerebral hemodynamics in patients. After onset of the disease, the reduction of regional blood volume in patients appears, thereby leading to the ischemic necrosis in local tissue, affecting the function of nerve cells and brain tissue, and making the pathological occurrence [1, 2]. The onset of acute cerebral infarction is urgent, which has a greater influence on the normal physiological function of patients, with the features of high mutilation rate and high mortality, and most patients have serious sequelae, which seriously affects the normal life. The epidemiological data show that the mortality in acute stage of cerebral infarction is about 5%-15%, and the disability rate in surviving patients is about 50%. For this disease, the main purpose of clinical treatment is to dredge the occluded blood vessel as soon as possible, thereby promoting the functional recovery of regional blood vessels and nerve cells. The cerebral vascular interventional therapy (arterial thrombolysis, mechanical recanalization, etc.) and intravenous thrombolytic therapy are the main methods of cerebral revascularization. Relatively speaking, the intravenous thrombolysis has a shorter therapeutic time window, but many patients still cannot get the thrombolytic therapy within the time window with the developed medical technology increasingly in today [3, 4]. With the continuous renovation of medical technology and equipment in China, cerebral vascular interventional therapy has developed rapidly. Arteriovenous combined thrombolysis not only reduces the dosage of thrombolytic agents but also extends the therapeutic time window. Related studies have shown that arteriovenous combined thrombolysis is also conducive to reducing the adverse reactions and is considered to be an effective method for rapid recanalization of occluded vessels. Mechanical thrombectomy is a method of reperfusion for acute cerebral infarction, which has the advantages of rapid recanalization in blood vessels and high vascular recanalization rate. However, there are few related clinical studies, and its safety and effectiveness still need to be explored constantly [5, 6]. In addition, complications such as intracranial hemorrhage and vascular injury caused by failure of canalization may occur in the process of interventional therapy, so that the combination of scientific and comprehensive standardized perioperative management can further prevent the occurrence of adverse events. Therefore, this study will deeply explore the application value of standardized perioperative management in mechanical thrombectomy for acute cerebral infarction.

2. Materials and Methods

2.1. Inclusion Criteria in Patients. (1) The onset time of acute cerebral infarction did not exceed 6 h. (2) The imaging manifestations did not show the large intracranial infarction in the early stage by CT examination. (3) The muscle strength of paralytic limbs was 0-3 grade. (4) Patients had the mild consciousness disorders. (5) The blood pressure was 180/100 mmHg. (6) The manifestations of neurological impairment in patients were less than 1 hour. (7) The family members were informed of this study and agreed to consult the patients' medical records.

2.2. Exclusion Criteria in Patients. (1) Patients with the severe liver and kidney dysfunction and cardiac insufficiency; (2) patients with the history of intracranial hemorrhage; (3) patients with active hemorrhage or severe trauma; (4) patients without the therapeutic indications of thrombolysis or mechanical thrombectomy; (5) patients who received the heparin anticoagulant therapy within 48 hours; (6) patients with the low coordination degree or missing visit subsequently; (7) patients with epilepsy at onset of disease; and (8) patients with the myocardial infarction in the near future.

2.3. Screening and Grouping of Patients. By means of the retrospective study, 98 patients with acute cerebral infarction admitted to our hospital from January 2019 to January 2022 were selected as the study sample in this study, and all patients received the standardized perioperative management. According to the interventional methods, they were divided into the thrombolytic treatment group (arteriovenous combined thrombolysis, $n = 49$) and the mechanical thrombectomy group (mechanical thrombectomy, $n = 49$). The study protocol was in line with the ethical and moral principles and approved by the hospital ethics committee.

2.4. Methods

2.4.1. Standardized Perioperative Management. (1) Improvement of emergency operation processes to realize the efficient operation grading management. The notification of emergent surgery in paper version submitted on scene was canceled, and it was submitted online by the electronic medical records system. At the same time, the careful and feasible surgical plans were formulated to ensure the effective reception of electronic surgical application. The relevant information of emergency patients were recorded in detail, including the time of entering the operating room, the consultation hours of staff in operating room, the time of notifying the doctors, the arrival time of doctors, the operative surgery name, and the conditions of acceptance and treatment. The surgical green channel used in rescuing the emergency patients was established to realize the planned treatment of emergency patients in stages [7]. The efficiency of surgery grading management was improved by the information means, and the surgical procedures were recorded and supervised. (2) Real-time intraoperative monitoring. The real-time images of surgery were observed via the central monitor system of operating room. The surgical managers were able to monitor the intraoperative situations and the related data in real-time and immediately dispatch for the emergencies to ensure the perioperative safety. The segments such as entering and leaving the operating room, anesthesia and surgery, and entering and leaving the resuscitation room were displayed timely by controlling the important links and nodes in the perioperative period to provide information and data for ensuring the normal movement of surgery. At the same time, the application of anesthesia

resuscitation room, induction room, and preoperative waiting room should be clarified, so as to ensure the sufficient materials and reasonable storage of goods [8]

2.4.2. Arteriovenous Combined Thrombolysis. 0.9% of sodium chloride injection at a dose of 100 ml added to urokinase (100×10^4 U) was used completely by intravenous drip within 30 min. The thrombolytic steps were as follows. 1% of lidocaine at a dose of 10 ml was used for the local anesthesia of patients, and the right femoral artery was punctured using the modified Sedingger technique, with an inserted 6 F arterial catheter. Heparin (3000 U) was used by a drip chamber putted into the 6 F guiding catheter under the guidance of the guide wire, and the head end was sent to the pathological artery, vertebral artery, or carotid artery. The site of artery stenosis, stenosis degree, and case of collateral compensation were shown by photography [9]. The head of microwire or trensend microtubule was send to the distal thrombus according to the path graph, and the urokinase (10×10^4 U) was given from the microtubule at 10×10^3 U/min via pump. The head of catheter was inserted in thrombus by withdrawing, with the urokinase (10×10^4 U) by injection. The catheter was withdrawn to the proximal thrombus, with the urokinase (10×10^4 U) by injection, and the photography was performed 1time/10 min.

2.4.3. Mechanical Thrombectomy. 1% of lidocaine at a dose of 10 ml was used for the local anesthesia, and the right femoral artery of patients was punctured using the modified Sedingger technique, with an inserted 6 F arterial catheter. Heparin (3000 U) was used by a drip chamber putted into the 6 F guiding catheter under the guidance of the guide wire, and the head end was sent to the pathologic artery, vertebral artery, or carotid artery. The site of artery stenosis, stenosis degree, and case of collateral compensation were shown by photography. Under the roadmap, the Rebar18 microcatheter stent was sent to the delivery system under the guidance of Silver-speed-14 micro-wire or PT wire, and the head of the Rebar catheter was sent to the thrombus. Solitaire AB stent (4-20 mm) was sent from Rebar, with the retracement of Rebar and the release of stent. The stent was withdrawn after photography, and the thrombus that has been extracted was checked, while 30 m1 of blood in the guiding catheter was abstracted. The images were shown using photography after taking the thrombus in order to prevent the fallen thrombus into the cerebral artery again with the blood flow. The arterial catheter was removed, the vascular closure device in Abbott was used for hemostasis, and the puncture point was bandaged.

2.4.4. Detection of Electroencephalogram. The routine electroencephalography (EEG) examination was performed using a digital video-EEG instrument, and the electrodes were placed according to the international 10-20 system to record the single-stage and dual-stage leads. The reference electrode was described when the patients had clear consciousness and full cooperation with the examination, with the detection time of 15-30 minutes. The patients' images and EEG were stored to select the ideal signal segment > 5 min for power spectrum analysis, including the brain symmetry index (BSI) and power ratio indices (DTABR). In addition, 5 ml of fasting venous blood was taken in the morning to centrifuge (1500 r/min and 15 min), and the serum was stored after centrifugation at -20°C for examination.

2.5. Observation Indices. Neurological function. The National Institutes of Health Stroke Scale (NIHSS) was used to evaluate the degree of neurologic impairment in patients, mainly from the 11 aspects of consciousness, eye movement, visual field, situation of facial paralysis, upper limbs motion, lower limbs motion, defective coordination, sensation, language, articulation disorder, and neglect syndrome. The different scores were corresponding to the severity of the disease, with a full score of 42. The higher the score, the more serious the symptoms of neurological deficits.

Physical function. The physical function of patients was evaluated using the modified Rankin scale (mRS) at 3 months after surgery. 0 point was no symptom. 1 point represented that patients had the symptoms but no obvious dysfunction, which could complete all daily work and life. 2 points indicated that patients with the mild disability were unable to complete all normal activities but could take care of their daily affairs without the help of others. 3 points indicated that patients with the moderate disability could walk independently, but they needed to be cared in part of life. 4 points represented that patients had the moderate to severe disability, which were unable to walk independently and needed to be cared in life. 5 points were severe disability, bedridden, urinary and fecal incontinence, and completely dependent on others in daily life.

TIMI flow grade. In the process of coronary angiography, the state of vascular lesions could be judged by the display of the contrast agent in the distal coronary arterial vessels, which was divided into 4 grades. Grade 0 referred to the distal blood vessels without the filling of contrast agent, suggesting that there was no blood perfusion in the distal end and indicating that the blood vessel might have complete occlusive diseases, thereby resulting that blood flow failed to pass completely. Grade 1 meant that the partial visualization of contrast agent was in the vascular stenosis site, but the contrast agent could not reach the distal blood vessel, indicating that the vascular stenosis was a severe lesion that was close to occlusion. Grade 2 represented that the contrast agent could fill the blood vessel with a visualization of blood vessel, but the developing speed was slower than the normal blood vessel, suggesting that there was a certain stenosis or lesion in the coronary artery. Grade 3 showed that the contrast agent could quickly and completely fill the blood vessel and displayed the vascular morphology, indicating that the blood flow was normal.

The symptomatic intracranial hemorrhage rate within 24 h and acute vascular reocclusion rate were counted. The waveform changes of α, β, δ, and θ in the two groups were observed by the EEG indicators, and the BSI and DTABR were compared between the two groups.

The incidence types of adverse events in patients between the two groups in 90 days were counted to calculate the incidence of adverse events.

2.6. Statistical Treatment. The software used for processing the data in this study was SPSS22.0, which mainly calculated the differences in data between the two groups, and GraphPad Prism 7 (GraphPad Software, San Diego, USA) was used for the chart production. The data included in the study were enumeration data and measurement data tested by x^2 and t test, indicated by [n (%)] and ($\bar{x} \pm s$), which were in line with the normal distribution. The statistical results were $P < 0.05$, indicating the statistical differences between the two groups.

3. Results

3.1. General Information. There was no statistical difference in general information such as age, gender, sites of vascular occlusion, and onset time between the two groups ($P > 0.05$). See details in Table 1.

3.2. Detection of EEG. After treatment, the values of BSI and DTABR in the two groups were obviously lower than those before treatment ($P < 0.05$), and the values of BSI and DTABR in the mechanical thrombectomy group were lower than those in the thrombolytic treatment group ($P < 0.05$). See details in Table 2.

3.3. NIHSS Score and mRS Score. According to the statistical data of NIHSS score in Table 3, the NIHSS scores of the two groups after treatment were significantly lower ($P < 0.05$), while the NIHSS score in the mechanical thrombectomy group after treatment was lower than that in the thrombolytic treatment group ($P < 0.05$). According to the statistical results in Table 3, the proportion of mRS score < 3 in the mechanical thrombectomy group was significantly higher than that in the thrombolytic treatment group ($P < 0.05$).

3.4. TIMI Flow Grade. According to the statistical data in Table 4, the proportion of TIMI flow grade ≥ 2 in the mechanical thrombectomy group was significantly higher than that in the thrombolytic treatment group ($P < 0.05$).

3.5. Symptomatic Intracranial Hemorrhage within 24 Hours, and Acute Vascular Reocclusion and Death Status within 1 Year. The rate of symptomatic intracranial hemorrhage within 24 hours in the mechanical thrombectomy group was lower than that in the thrombolytic treatment group ($P < 0.05$), with the indistinctive difference between the two groups ($P > 0.05$). The incidence of acute vascular reocclusion in the mechanical thrombectomy group was markedly lower than that in the thrombolytic treatment group ($P < 0.05$). There was no significant difference in 1-year mortality between the two groups ($P > 0.05$). See details in Figure 1.

3.6. Incidence of Adverse Events in 90 Days. In the mechanical thrombectomy group, there were 1 case of gingiva bleeding, 1 case of hemorrhinia, and 2 cases of recurrent cerebral infarction in 90 days, with a total of 4 cases (8.16%), while in the thrombolytic treatment group, there were 4 cases of gingiva bleeding, 4 cases of hemorrhinia, and 15 cases of recurrent cerebral infarction in 90 days, with a total of 23 cases (46.94%), indicating that the incidence of adverse events in 90 days in the mechanical thrombectomy group was significantly lower than that in the thrombolytic treatment group ($P < 0.05$).

4. Discussion

Acute cerebral infarction is a common cerebrovascular disease with high mutilation rate and mortality, and the therapeutic key is early vascular recanalization. In recent years, with the development of clinical medical technology, the clinical treatment programs of patients with acute cerebral infarction have become more and more perfect, and mechanical thrombectomy is the most advanced interventional treatment for ischemic stroke in clinic, which has a more significant treatment effect especially for large artery occlusion. Clinical studies have shown that intravascular mechanical thrombectomy is an important method for rapid and efficient recanalization of acute aortic occlusive cerebral infarction, which can effectively improve the mRS scores of patients for 90 days [10, 11]. According to the Guidelines for the Diagnosis and Treatment of Acute Ischemic Stroke in China, the intravascular mechanical thrombectomy is recommended for patients with indications [12–14]. Similar to the mechanical thrombolysis, thrombolysis with thrombolytic agents can achieve the cerebral revascularization, reconstruct the cerebral blood flow, and save the ischemic brain tissue, showing that thrombolysis is the most effective and promising method for the treatment of acute cerebral infarction from this perspective. Among them, intravenous thrombolysis is easy to be accepted by patients because of the low requirements of technical equipment and low cost, but intravenous thrombolysis also has the risk of intracranial hemorrhage resulting in low vascular recanalization rate, high mortality, and high probability of early reocclusion after the thrombolysis [15, 16]. However, arterial thrombolysis has more advantages in some aspects compared with the intravenous thrombolysis, for example, the arterial thrombolysis can accurately determine the sites, degree of occlusion, compensation, and the cases of recanalization in occluded vessels by digital subtraction angiography, and the selectivity of local contact medication in thrombus is higher. Related studies have also pointed out that the vascular recanalization rate and safety of arterial thrombolysis are relatively high, but the intracranial hemorrhage transformation is the most serious complication of arterial thrombolysis, with a high mortality [17, 18]. The combination of the two thrombolytic methods has a better therapeutic effect than single method, which can integrate the advantages of the two methods and improve the efficiency and area of drug use, with a better thrombolytic effect. Compared with the arterial-venous thrombolytic treatment, mechanical thrombectomy with a late start can break and remove the thrombus, which greatly reduces the possibility of recurrence. It provides a new method and idea for clinical treatment of acute cerebral infarction and is also a new trend in the future treatment of acute cerebral infarction.

Surgical management is an administrative work with comprehensiveness and multidisciplinary coordination,

Table 1: Comparison of general information in patients between the two groups ($n = 49$).

Observation indices	Thrombolytic treatment group	Mechanical thrombectomy group	X^2/t	P
Age range	55-79	57-78		
Average age (years)	68.55 ± 4.82	68.37 ± 4.71	0.187	0.852
Gender			0.165	0.685
Male	26 (53.06)	28 (57.14)		
Female	23 (46.94)	21 (42.86)		
Sites of vascular occlusion				
M1/M2 segment of middle cerebral artery	12 (24.49)	13 (26.53)	0.054	0.817
Intracranial internal carotid artery	13 (26.53)	12 (24.49)	0.054	0.817
Involvement of middle artery and internal carotid artery	13 (26.53)	11 (22.45)	0.221	0.638
Vetebral-basilar artery	11 (22.45)	13 (26.53)	0.221	0.638
Average onset time (h)	4.05 ± 1.12	4.08 ± 1.01	0.139	0.890

Table 2: Statistics of EEG indexes between the two groups.

Groups	BSI value		DTABR	
	Before treatment	After treatment	Before treatment	After treatment
Thrombolytic treatment group	0.22 ± 0.04*	0.14 ± 0.03	1.09 ± 0.28*	0.82 ± 0.18
Mechanical thrombectomy group	0.23 ± 0.03*	0.09 ± 0.02	1.10 ± 0.25*	0.66 ± 0.15
t	1.400	9.707	0.186	4.780
P	1.165	<0.001	0.853	<0.001

Note. Brain symmetry index (BSI) and power ratio indices (DTABR). * represented a significant difference in the same group before and after treatment ($P < 0.05$).

Table 3: Statistics of NIHSS score and mRS score in patients.

Groups	NIHSS score		mRS score	
	Before treatment	After treatment	<3 points	≥3 points
Thrombolytic treatment group	9.22 ± 3.20*	7.14 ± 1.75	33 (67.35)	16 (32.65)
Mechanical thrombectomy group	9.27 ± 3.19*	4.96 ± 1.11	46 (93.88)	3 (6.12)
t/X^2	0.077	7.364	11.034	
P	0.938	<0.001	4.780	

Notes. The national institutes of health stroke scale (NIHSS) and modified Rankin scale (mRS). * indicated an obvious difference in the same group before and after treatment ($P < 0.05$).

Table 4: Statistics of TIMI flow grade in patients.

Groups	Cases	≥2 grade	>3 grade
Thrombolytic treatment group	49	29 (59.18)	20 (40.82)
Mechanical thrombectomy group	49	47 (95.92)	2 (4.08)
t		18.990	
P		<0.001	

Notes. Thrombolysis in myocardial infarction (TIMI) flow grade.

especially for critically ill patients such as acute cerebral infarction. The scientific and modern perioperative management can be realized only via setting up the reasonable organizational structure and optimizing the management process constantly [19–21]. With the development of medical information technology, information means provide the possibility for the realization of meticulous surgical management. Our hospital actively explored the role of standardized perioperative management in strengthening the attention of surgical efficiency and management efficiency and ensuring the

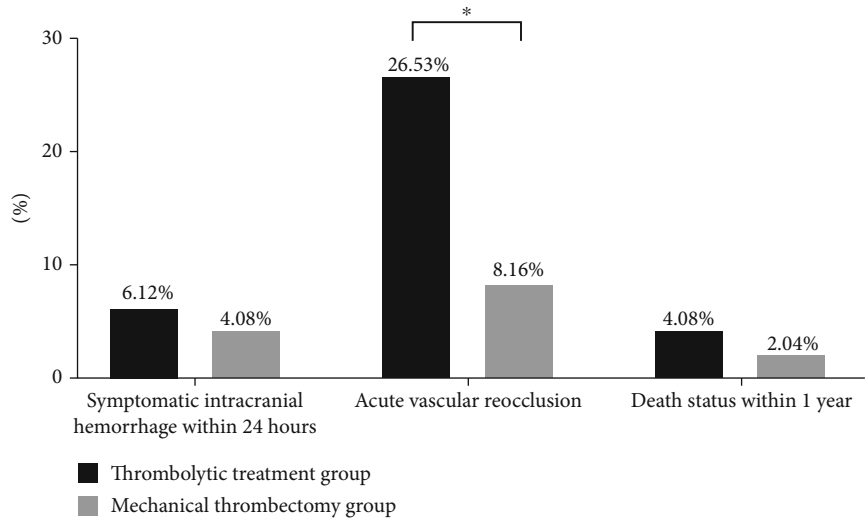

Figure 1: Symptomatic intracranial hemorrhage within 24 hours, acute vascular reocclusion and death status within 1 year. Notes. The horizontal coordinate represented the evaluation dimension, and the vertical coordinate represented the percentage (%). There were 3 cases with symptomatic intracranial hemorrhage within 24 hours, 13 cases with acute vascular reocclusion, and 2 dead cases within 1 year in the thrombolytic treatment group, while there were 2 cases with symptomatic intracranial hemorrhage within 24 hours, 4 cases with acute vascular reocclusion, and 1 dead case within 1 year in the mechanical thrombectomy group. * represented a significant difference in the incidence of acute vascular reocclusion between the two groups ($X^2 = 5.765$, $P = 0.016$).

surgical effect and safety in order to strengthen the attention on perioperative management of patients with acute cerebral infarction [22–24]. Based on this, the following results were further obtained in this study. After treatment, the values of BSI and DTABR in the two groups were obviously lower than those before treatment ($P < 0.05$), and the values of BSI and DTABR in the mechanical thrombectomy group were lower than those in the thrombolytic treatment group ($P < 0.05$). BSI is a monitoring index of cerebral blood flow in common use during carotid endarterectomy, and its application value in diagnosis and prognosis monitoring of brain diseases has gradually become prominent in recent years. The analysis shows that BSI can reflect the difference in activity status of brain cells between the unilateral supply region and contralateral supply region when the patients have changes of cerebral hemodynamics, thereby reflecting the cases of infarction in patients and the change of cerebral blood flow during treatment. DTABR mainly reflects the change on the ratio of $\delta + \theta$ wave and $\alpha + \beta$ wave. When the patients have infarction, the amplitude of the whole brain decreases, α wave disappears, β wave decreases, and the level of $\alpha + \beta$ wave decreases, while the level of $\delta + \theta$ wave increases, resulting in the increase of DTABR value. Therefore, DTABR value has a higher application value for monitoring the curative effect of patients. The results showed that simple mechanical thrombectomy was more effective in improving the intracranial hemodynamics of patients with acute cerebral infarction and was beneficial to the recovery of brain function. According to the NIHSS scores in patients, the NIHSS scores of the two groups after treatment were visibly decreased ($P < 0.05$), while the NIHSS score in the mechanical thrombectomy group after treatment was lower than that in the thrombolytic treatment group ($P < 0.05$), which was consistent with the study of Hoorn et al. [25]. The proportion of mRS score < 3 in the mechanical thrombectomy group was distinctly higher than that in the thrombolytic treatment group ($P < 0.05$), further indicating that mechanical thrombectomy can promote the recovery of neurological function and physical function compared with the thrombolytic therapy. The proportion of TIMI flow grade ≥ 2 in the mechanical thrombectomy group was significantly higher than that in the thrombolytic treatment group ($P < 0.05$), and the rate of symptomatic intracranial hemorrhage within 24 hours in the mechanical thrombectomy group was lower than that in the thrombolytic treatment group, with the indistinctive difference between the two groups ($P > 0.05$), while the incidence of acute vascular reocclusion in the mechanical thrombectomy group was markedly lower than that in the thrombolytic treatment group ($P < 0.05$). The results suggested that mechanical thrombectomy had the best thrombolytic effect on patients with acute cerebral infarction. At the same time, the combination of standardized perioperative management was conducive to ensuring the perioperative safety of patients and was also an important guarantee for the smooth progress of mechanical thrombectomy. There was no significant difference in 1-year mortality between the two groups ($P > 0.05$). At present, the studies on mechanical thrombectomy are mostly in the active exploration period, and the observation results of long-term efficacy are different, which may be related to factors such as thrombectomy device and patient selection. The Solitaire AB stent used in this study is a self-expandable NiTi alloy material with the design of closed mesh, and one side is fully opened. Characterized by a good transport capacity and higher radial support force, the design combines the advantages of closed and open

mesh, without the protrusion and deformation phenomenon, and the thrombus can be removed by pulling the stent after release. Combined with the standardized perioperative management, the short-term curative effect is better, and the long-term mortality is also lower than that in many previous studies.

In summary, the standardized perioperative management is effective in patients with acute cerebral infarction who were treated with arteriovenous combined thrombolysis or mechanical thrombectomy, which can improve the neurological function and physical function of patients. However, mechanical thrombectomy has a better improvement effect on neurological function and physical function of patients, with relatively good safety, thrombolysis effect, and long-term prognosis. It can be affirmed that standardized perioperative management combined with simple mechanical thrombectomy has a greater potential application value for patients with acute cerebral infarction, which can be prioritized in patients that meet the treatment indications. However, each method has certain limitations for the acute thrombolytic therapy of such patients. For the benefit of patients after opening the blood vessels, it is more dependent on the size of the penumbra and the core infarct region, so that the evaluation of early imaging data of patients should be emphasized.

Data Availability

Data to support the findings of this study are available on reasonable request from the corresponding author.

Conflicts of Interest

The authors do not have conflicts of interest to declare.

References

[1] L. Zhu, Z. Huang, X. Sun, M. Wu, Y. Xu, and Z. Sun, "The function of mechanical thrombectomy on improving haemodynamics of patients with acute cerebral infarction," *Basic & clinical pharmacology & toxicology*, vol. 124, no. S1, p. 116, 2019.

[2] C. J. Chen, C. Wang, T. J. Buell et al., "Endovascular mechanical thrombectomy for acute middle cerebral artery M2 segment occlusion: a systematic review," *World neurosurgery*, vol. 107, pp. 684–691, 2017.

[3] J. Uno, K. Kameda, R. Otsuji et al., "Mechanical thrombectomy for acute anterior cerebral artery occlusion," *World Neurosurgery*, vol. 120, pp. e957–e961, 2018.

[4] R. M. Forti, C. G. Favilla, J. M. Cochran et al., "Transcranial optical monitoring of cerebral hemodynamics in acute stroke patients during mechanical thrombectomy," *Journal of stroke and cerebrovascular diseases: The official journal of National Stroke Association*, vol. 28, no. 6, pp. 1483–1494, 2019.

[5] V. L. Ivan, C. Rubbert, J. Caspers et al., "Mechanical thrombectomy in acute middle cerebral artery M2 segment occlusion with regard to vessel involvement," *Neurological Sciences*, vol. 41, no. 11, pp. 3165–3173, 2020.

[6] B. Lapergue, J. Labreuche, R. Blanc et al., "First-line use of contact aspiration for thrombectomy versus a stent retriever for recanalization in acute cerebral infarction: the randomized ASTER study protocol," *International journal of stroke: official journal of the International Stroke Society*, vol. 13, no. 1, pp. 87–95, 2018.

[7] K. Aydin, M. Barburoglu, O. O. Cakmak, N. Yesilot, E. N. Vanli, and S. Akpek, "Crossing Y-solitaire thrombectomy as a rescue treatment for refractory acute occlusions of the middle cerebral artery," *Journal of neurointerventional surgery*, vol. 11, no. 3, pp. 246–250, 2019.

[8] S. Male, T. Mehta, H. Tore et al., "Gadolinium to the rescue for mechanical thrombectomy in acute ischemic stroke," *Interventional Neuroradiology*, vol. 25, no. 3, pp. 301–304, 2019.

[9] O. O. Zaidat, A. C. Castonguay, R. G. Nogueira et al., "TREVO stent-retriever mechanical thrombectomy for acute ischemic stroke secondary to large vessel occlusion registry," *Journal of neurointerventional surgery*, vol. 10, no. 6, pp. 516–524, 2018.

[10] H. Yang, N. Ma, L. Liu, F. Gao, D. Mo, and Z. Miao, "The basilar artery on computed tomography angiography score for acute basilar artery occlusion treated with mechanical thrombectomy," *Journal of stroke and cerebrovascular diseases: The official journal of National Stroke Association*, vol. 27, no. 6, pp. 1570–1574, 2018.

[11] T. Mehta, S. Male, C. Quinn et al., "Institutional and provider variations for mechanical thrombectomy in the treatment of acute ischemic stroke: a survey analysis," *Journal of neurointerventional surgery*, vol. 11, no. 9, pp. 884–890, 2019.

[12] L. Meyer, M. Alexandrou, H. Leischner et al., "Mechanical thrombectomy in nonagenarians with acute ischemic stroke," *Journal of neurointerventional surgery*, vol. 11, no. 11, pp. 1091–1094, 2019.

[13] X. Huang, Q. Yang, X. Shi et al., "Predictors of malignant brain edema after mechanical thrombectomy for acute ischemic stroke," *Journal of neurointerventional surgery*, vol. 11, no. 10, pp. 994–998, 2019.

[14] N. Goyal, G. Tsivgoulis, D. Frei et al., "Comparative safety and efficacy of modified TICI 2b and TICI 3 reperfusion in acute ischemic strokes treated with mechanical thrombectomy," *Neurosurgery*, vol. 84, no. 3, pp. 680–686, 2019.

[15] B. J. Cord, S. Kodali, S. Strander et al., "Direct carotid puncture for mechanical thrombectomy in acute ischemic stroke patients with prohibitive vascular access," *Journal of Neurosurgery*, vol. 135, no. 1, pp. 53–63, 2020.

[16] C. J. Chen, T. Y. Chuang, L. Hansen et al., "Predictors of 30-day mortality after endovascular mechanical thrombectomy for acute ischemic stroke," *Journal of clinical neuroscience: official journal of the Neurosurgical Society of Australasia*, vol. 57, pp. 38–42, 2018.

[17] A. N. Isaacs, K. L. Knight, and S. A. Nisly, "Analysis of a standardized perioperative pain management order set in highly opioid-tolerant patients," *Journal of Patient Safety*, vol. 15, no. 2, pp. 105–110, 2019.

[18] D. J. Lum, P. A. Ross, M. A. Bishop, M. L. Caetano, R. Malpani, and M. B. Streiff, "Evaluation of a standardized perioperative management protocol in the adult hematology anticoagulation management service," *The Annals of Pharmacotherapy*, vol. 51, no. 12, pp. 1077–1083, 2017.

[19] A. Travieso-Gonzalez, I. J. Nunez-Gil, H. Riha, J. A. Donaire, and H. Ramakrishna, "Management of arterial hypertension: 2018 ACC/AHA versus ESC guidelines and perioperative implications," *Journal of Cardiothoracic and Vascular Anesthesia*, vol. 33, no. 12, pp. 3496–3503, 2019.

[20] S. Matsuda, F. Ikawa, O. H. Hideo et al., "Questionnaire survey regarding prevention of surgical site infection after neurosurgery in Japan: focus on perioperative management and administration of surgical antibiotic prophylaxis," *Neurologia Medico-Chirurgica*, vol. 59, no. 6, pp. 197–203, 2019.

[21] M. Thomaschewski, F. Beyer, M. Thomaschewski et al., "Application-based management of perioperative anticoagulant therapy: description of POPACTApp," *Langenbeck's Archives of Surgery*, vol. 404, no. 5, pp. 633–645, 2019.

[22] B. A. Guenthart, W. Trope, W. Keeyapaj et al., "Intracardiac paragangliomas: surgical approach and perioperative management," *General Thoracic and Cardiovascular Surgery*, vol. 69, no. 3, pp. 555–559, 2021.

[23] L. A. Nascimento, A. K. Garcia, M. F. Conchon et al., "Advances in the management of perioperative patients' thirst," *AORN Journal*, vol. 111, no. 2, pp. 165–179, 2020.

[24] T. S. Kinlaw and D. Whiteside, "Surgical specimen management in the preanalytic phase: perioperative nursing implications," *AORN Journal*, vol. 110, no. 3, pp. 237–250, 2019.

[25] C. E. van Hoorn, S. A. Costerus, J. Lau et al., "Perioperative management of esophageal atresia/tracheo-esophageal fistula: an analysis of data of 101 consecutive patients," *Paediatric Anaesthesia*, vol. 29, no. 10, pp. 1024–1032, 2019.

Hindawi
Disease Markers
Volume 2022, Article ID 6113807, 12 pages
https://doi.org/10.1155/2022/6113807

Research Article

Identification of the Hub Genes and Potential Regulation Network in Chronic Hepatitis B via Bioinformatics Analysis

Jingjing Fan,[1] Yong Chen,[1] Wei Zhang,[2] Xiaoying Zhou,[1] Xue Bai,[1] Caifang Chang,[1] Yongping Han,[1] and Jinlu Liu[2]

[1]*Department of Infectious Diseases, The First Affiliated Hospital of Hebei North University, Zhangjiakou, 075000 Hebei, China*
[2]*Department of Microbiology, The First Affiliated Hospital of Hebei North University, Zhangjiakou, 075000 Hebei, China*

Correspondence should be addressed to Jingjing Fan; fanjingjing@hbbfyfy.com.cn

Received 30 June 2022; Revised 19 August 2022; Accepted 29 August 2022; Published 23 September 2022

Academic Editor: Jun Yang

Background. Chronic hepatitis B (CHB) is a serious infectious disease which is induced by hepatitis B virus (HBV) infection. This project was conducted to reveal the potential mechanism in CHB development via analyzing the public clinical data. *Methods*. GSE33857 and GSE110217, obtained from the GEO database, were used for bioinformatics excavation. Briefly, the raw data of GSE33857 and GSE110217 were analyzed with the GEO2R, and then the expressed matrix files were generated. The matrix files was visualized as heat map with *R* software. The targets of the miRNAs were analyzed with the miRDIP database. The functional annotation and pathway enrichment were performed using "clusterProfiler" package in *R* software. The STRING database was utilized to analyze the interaction of the DEGs, and the PPI and miRNA-mRNA network were established according to the related results. *Results*. 93 downregulated genes and 17 upregulated genes in GES33857, and 111 downregulated and 40 upregulated genes in GSE110217 were identified as the hub nodes. The targets of the DEGs in the datasets were enriched in PI3K/AKT and MAPK pathways and associated with transcriptional regulation. Moreover, PPI and miRNA-mRNA networks were also established with the DEGs and related targets in the datasets. miR-122-5p, miR-125b-5p, miR-136-5p, miR-194-5p, miR-139-5p, miR-140-5p, miR-181a-5p, and miR-29b-3p were identified as the potential biomarkers in CHB. *Conclusion*. Eight miRNAs, including miR-122-5p, miR-125b-5p, miR-136-5p, miR-194-5p, miR-139-5p, miR-140-5p, miR-181a-5p, and miR-29b-3p, were identified as the potential biomarkers in CHB, and the PPI and miRNA-mRNA networks were also established.

1. Introduction

Chronic hepatitis B (CHB) is an intractable malignant infectious disease which has high incidence in the whole world [1, 2]. At present, there are few ways to completely heal this disease. The infection of chronic hepatitis B virus is the direct factor inducing the formation and development of major patients with CHB, while some virus carriers also exhibit normal clinical indexes as well as healthy people [3]. Over the decade, increasing patients have been diagnosed with CHB year by year. HBV infections has been generally recognized as the critical reason inducing the liver-related diseases [4]. Statistically, since 1998, almost 250 million people have been confirmed to infect the CHB virus [5]. The patients with CHB may develop to various poor outcomes. At present, some antiviral drugs can impede the progression of CHB virus-induced complications, while they could not remove the persistent damage of the virus on patients in a long term [6].

Abundant research has reported that the patients with CHB generally exhibited remarkably difference in gene profile compared with healthy persons [7, 8]. miRNAs serve as critical roles in cellular activities, and the disorder of miRNA profile is also direct reason leading the formation and deterioration of the diseases [9]. For CHB, considerable reports have indicated the pathological tissues of the

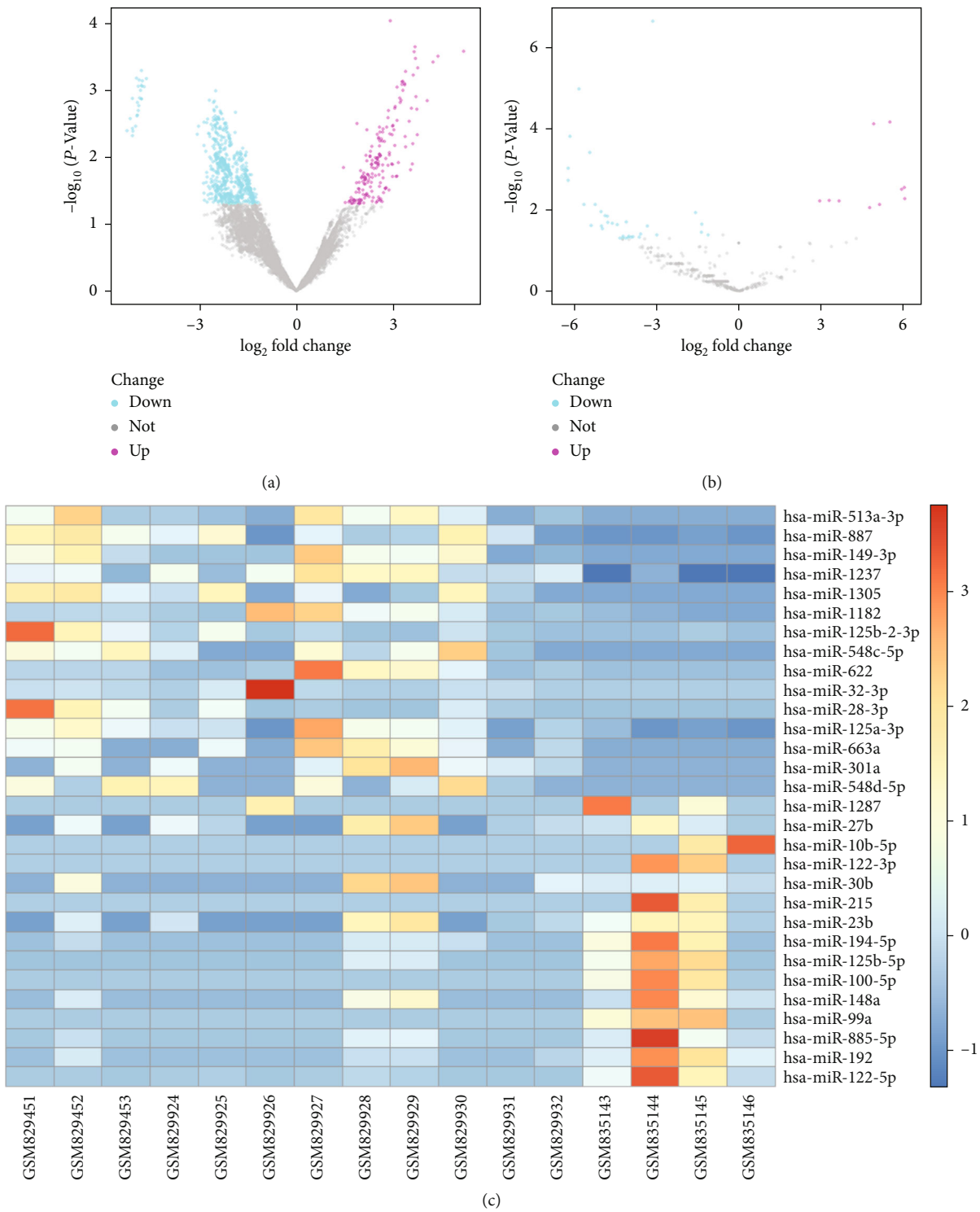

Figure 1: Continued.

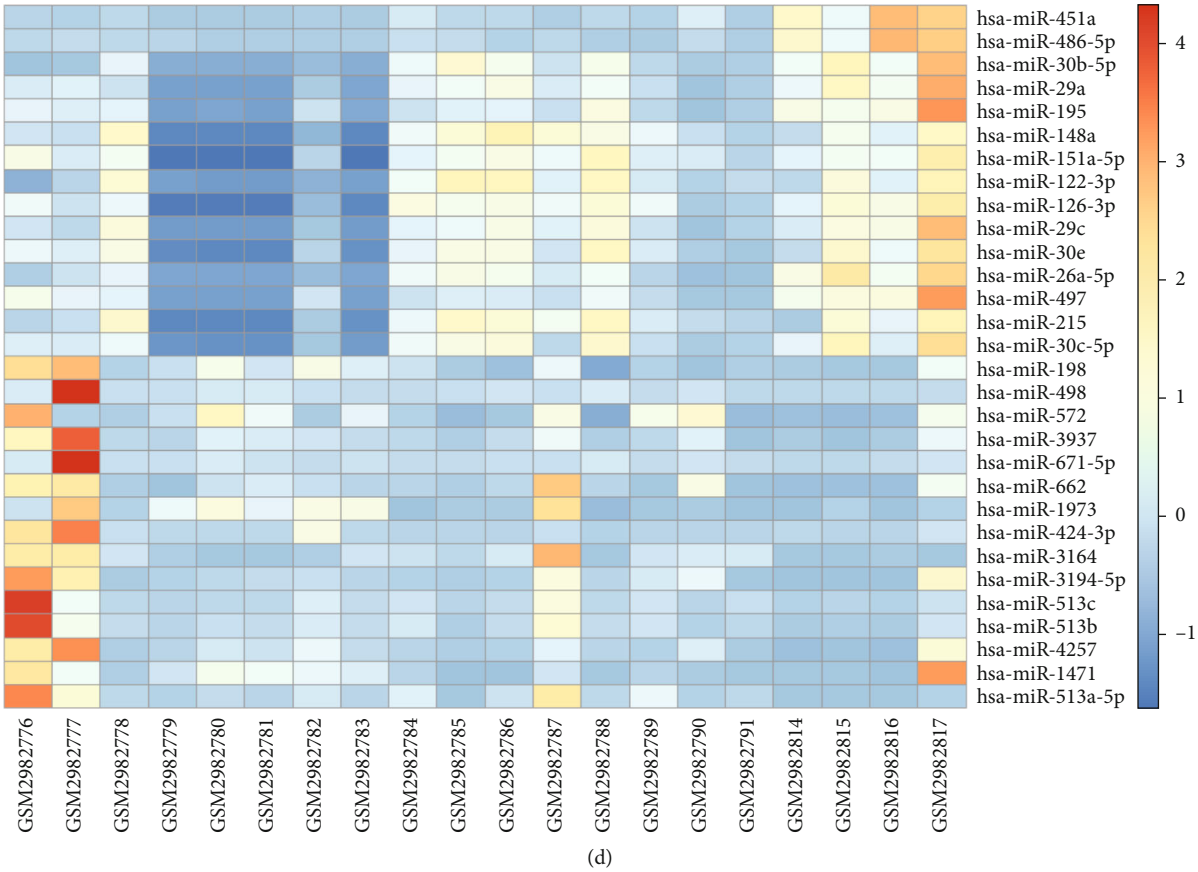

(d)

Figure 1: The DEGs identified from GSE33857 and GSE110217. (a, b) The hot diagrams of GSE33857 and GSE110217. (c, d) The heat maps of GSE33857 and GSE110217.

patients generally exhibit obvious difference in miRNA profiles [10]. With the application of HTS analysis methods, accumulating miRNAs have been investigated and successfully applied for clinical diagnosis and treatment [11]. The excavation of public data may be a promising way to reveal the potential mechanism in CHB development. Increasing researches try to illustrate the profile change in CHB development [12]. Some genes may have great potential for clinical application.

This research was conducted to analyze the potential mechanism of CHB progression via bioinformatics analysis and construct the miRNA-mRNA network to provide some reference for CHB treatment.

2. Materials and Methods

2.1. Data Source. The datasets including GSE33857 (GPL10656) and GSE110217 (GPL15018) were originated from the GEO database, and the related matrix files of the datasets were obtained via GEO2R analysis. For GSE33857, 12 normal liver tissues and 4 CHB tissues were selected as the subjects. For GSE110217, 4 normal liver tissues and 16 non-HCC CHB tissues were selected as the subjects.

2.2. Identification of DEGs. The matrix files of GES and GES were obtained to screen the DEGs. In brief, the genes with $|\log FC| \geq 2$ and p value <0.05 were selected as the DEGs for next analysis. The volcano map and heat map of the DEGs were figured with *R* language.

2.3. Enrichment Analysis. To obtain the related functional annotation and enrichment results of the DEGs, the DEGs or the related targets (for miRNAs) were analyzed using "clusterProfiler" package in *R* software [13, 14]. The related GO annotation of the DEGs was obtained for GO enrichment, and the related results of the genes in cellular component (CC), biological process (BP), and molecular function (MF) were obtained. The enrichment results were visualized with *R* language.

2.4. Networks Establishment and Modular Analysis. The DEGs or the related targets (for miRNAs) were analyzed with the STRING database to establish the interactions of the DEGs. Moreover, the combined score more than 0.4 was considered as statistical meaning. For modular analysis, the results obtained from STRING were analyzed with the plug-in unit of Cytoscape (MCODE). The mirDIP was utilized to predict target mRNA of miRNAs. For miRNA-mRNA network establishment, the miRNAs and the target mRNAs in GES were constructed with the Cytoscape.

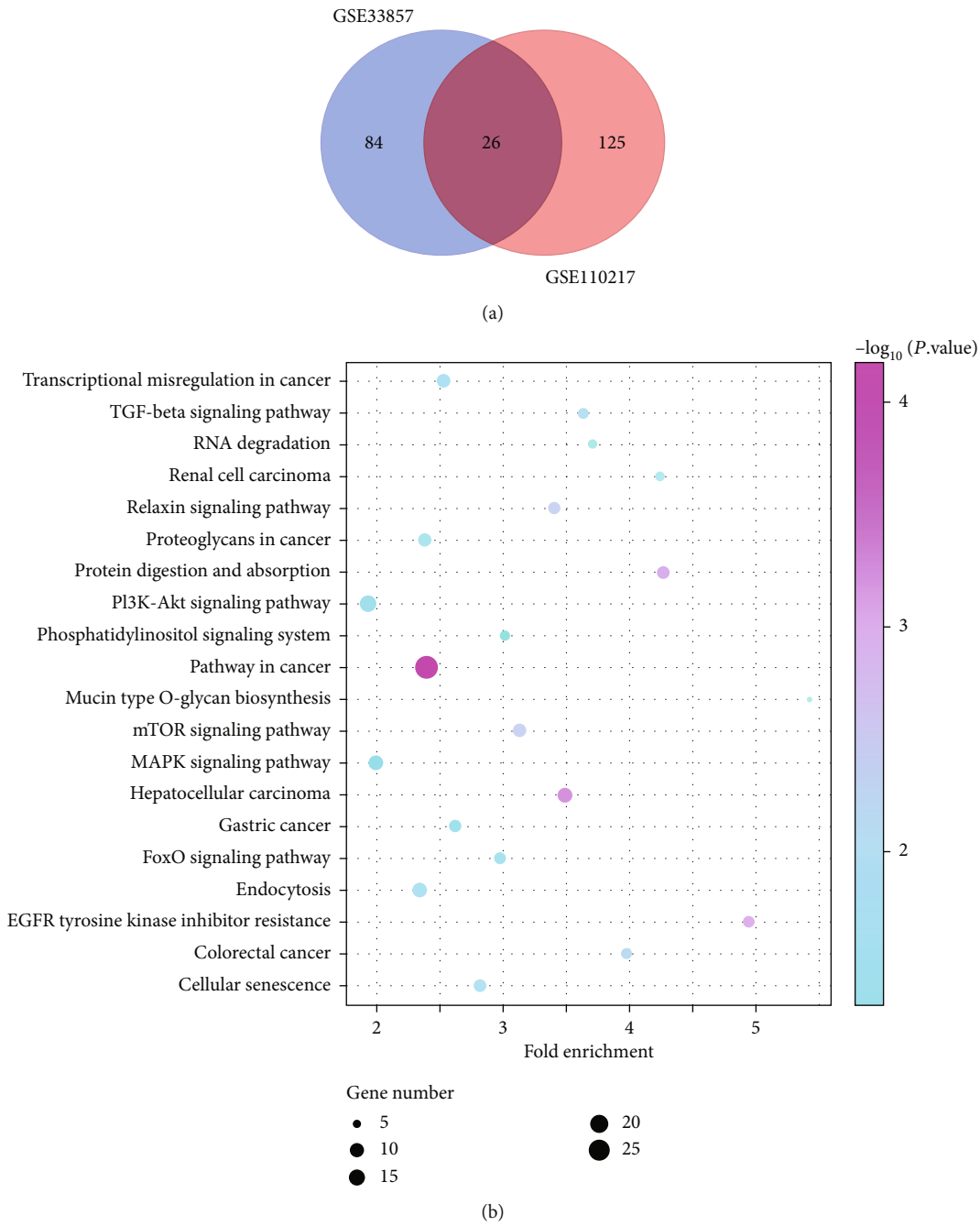

Figure 2: Continued.

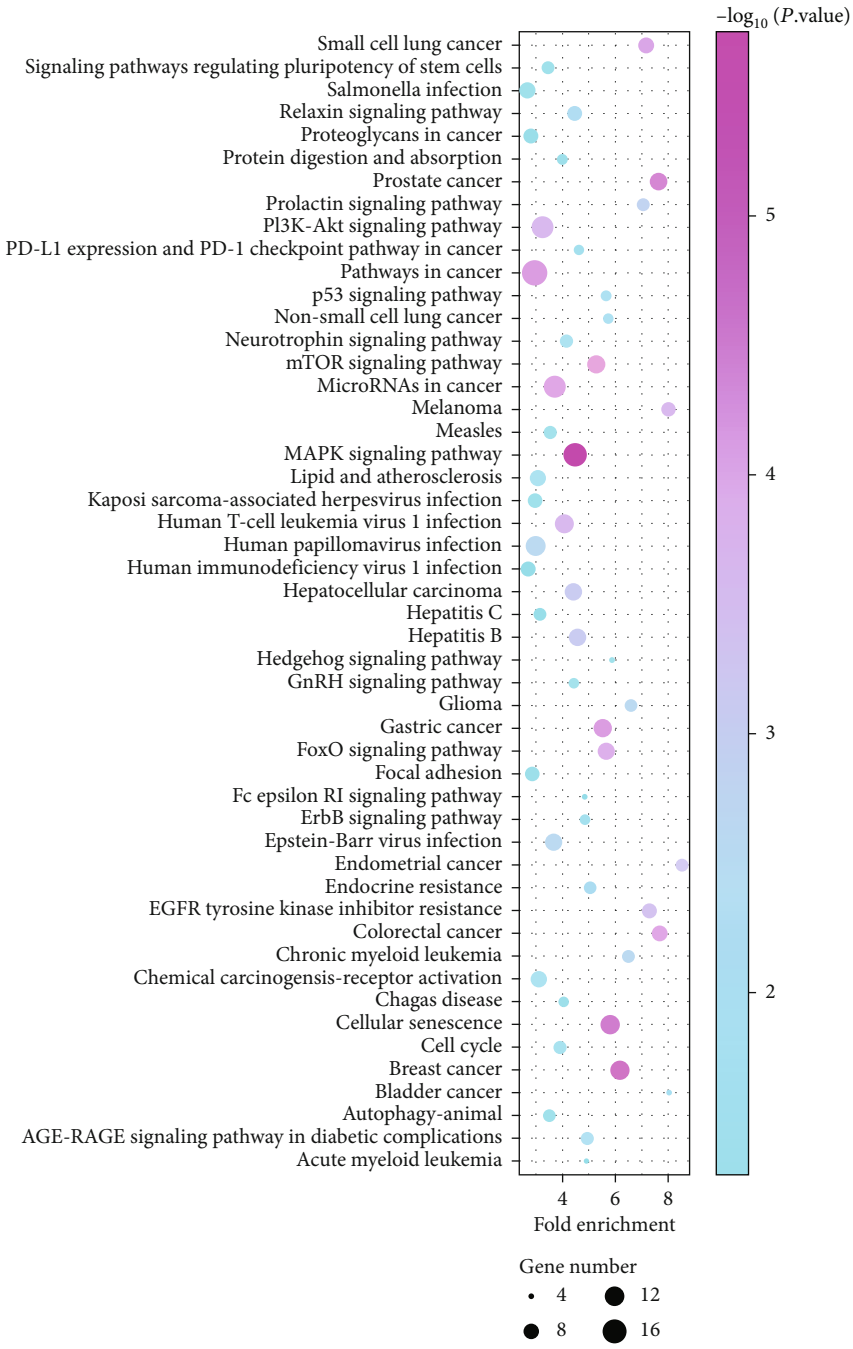

(c)

Figure 2: Continued.

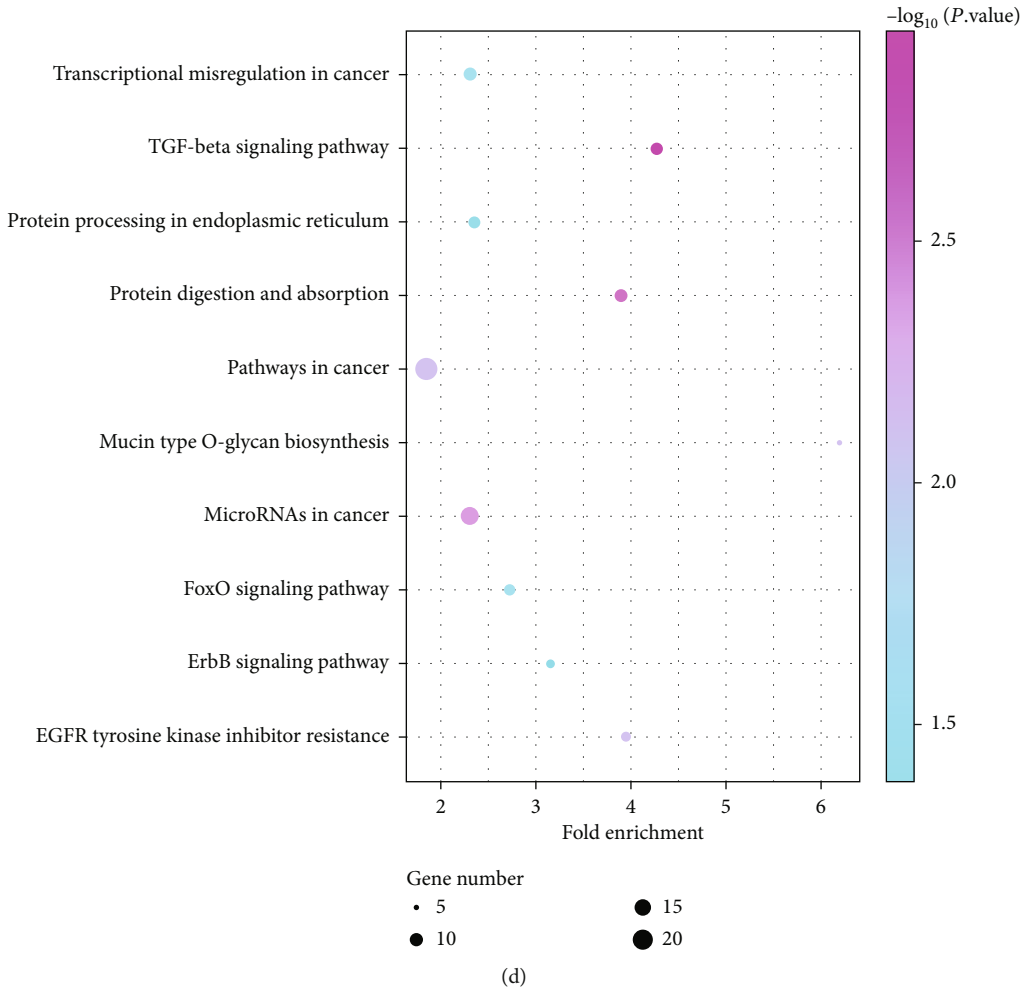

Figure 2: The KEGG enrichment of the DEGs in GSE33857 and GSE110217. (a) The common DEGs in GSE33857 and GSE110217. (b) The KEGG enrichment of the DEGs in GSE33857. (c) The KEGG enrichment of the DEGs in GSE110217. (d) The KEGG enrichment of common genes in GSE33857 and GSE110217.

3. Results

3.1. Identification of the DEGs. The GSE33857 and GSE110217 were analyzed with the GEO2R to identify the DEGs in the progression of CHB. In the results, 93 downregulated genes and 17 upregulated genes were found in the GES33857, and 111 downregulated and 40 upregulated genes were found in the GSE110217 (Figures 1(a) and 1(b)). The top 10 upregulated and top 10 downregulated DEGs were visualized with heat maps (Figures 1(c) and 1(d)).

3.2. KEGG Enrichment Analysis. To reveal the potential pathological mechanism of CHB, the targets of the DEGs were analyzed with the DAVID database. The results showed that 26 common genes were found in GSE33857 and GSE110217 (Figure 2(a)). The targets of the DEGs in GSE33857 were mainly enriched in PI3K/AKT and MAPK pathways, and the genes including SMAD2, FZD3, SMARCD2, PTEN, GAB1, TGFA, ARID1A, ARID2, MET, SOS2, TGFBR2, and NFE2L2 were related with the hepatocellular carcinoma related pathway (Figure 2(b)). For GSE110217, the targets of the DEGs were also enriched in PI3K/AKT and MAPK pathways, and the genes including NRAS, CCND1, AKT3, PTEN, E2F1, AXIN2, SOS2, TGFBR1, and LRP6 were enriched in hepatocellular carcinoma related pathway (Figure 2(c)). Moreover, the common targets of the DEGs in GSE33857 and GSE110217 were majorly associated with the cancer development pathways including pathways in cancer, microRNA in cancer, and transcriptional in cancer (Figure 2(d)).

3.3. Functional Analysis. To reveal the molecular functions of the DEGs in CHB development, the targets of the DEGs in GSE33857 and GSE110217 were used for GO enrichment analysis. The results showed that the targets of the DEGs in GSE33857 and GSE110217 were located in nucleus, cytosol, nucleoplasm, and so on and were associated with the regulation of RNA transcription. Moreover, the molecular functions of these genes were related with the binding of protein, metal ion, the promoter DNA sequence, and so on (Figure 3).

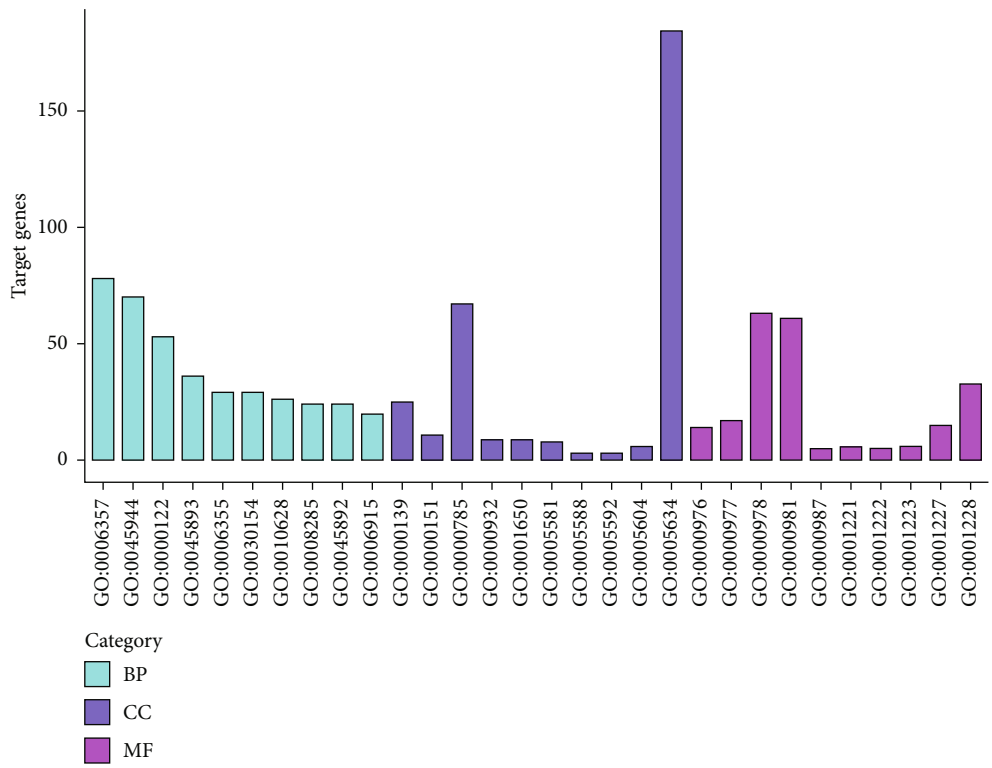

(a)

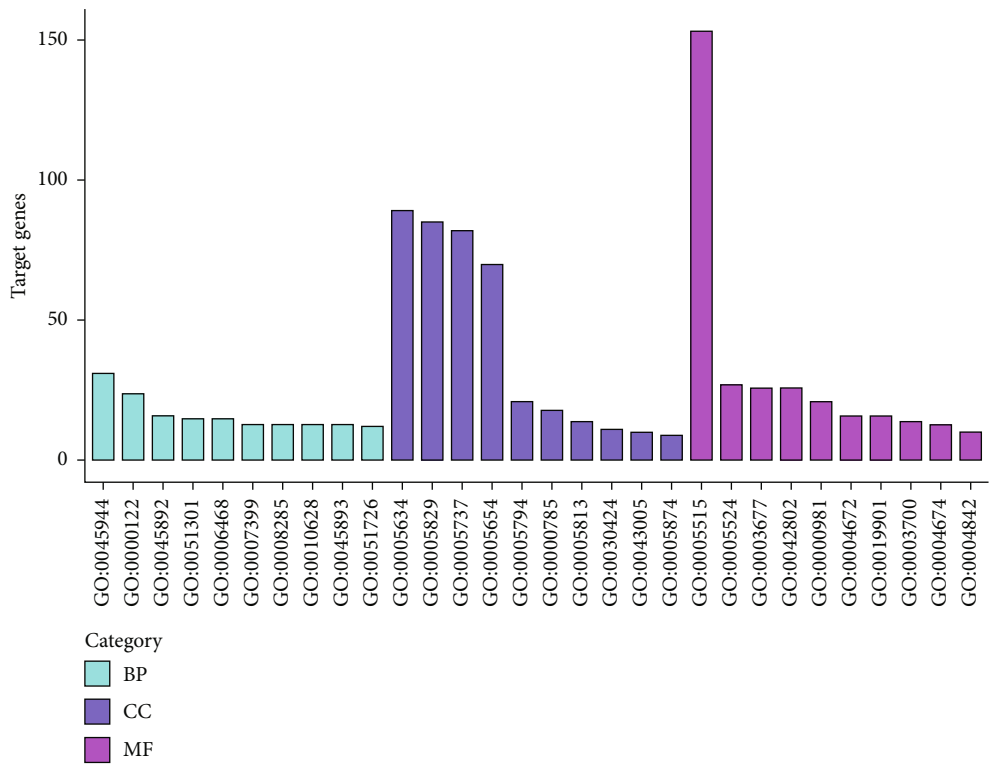

(b)

Figure 3: Continued.

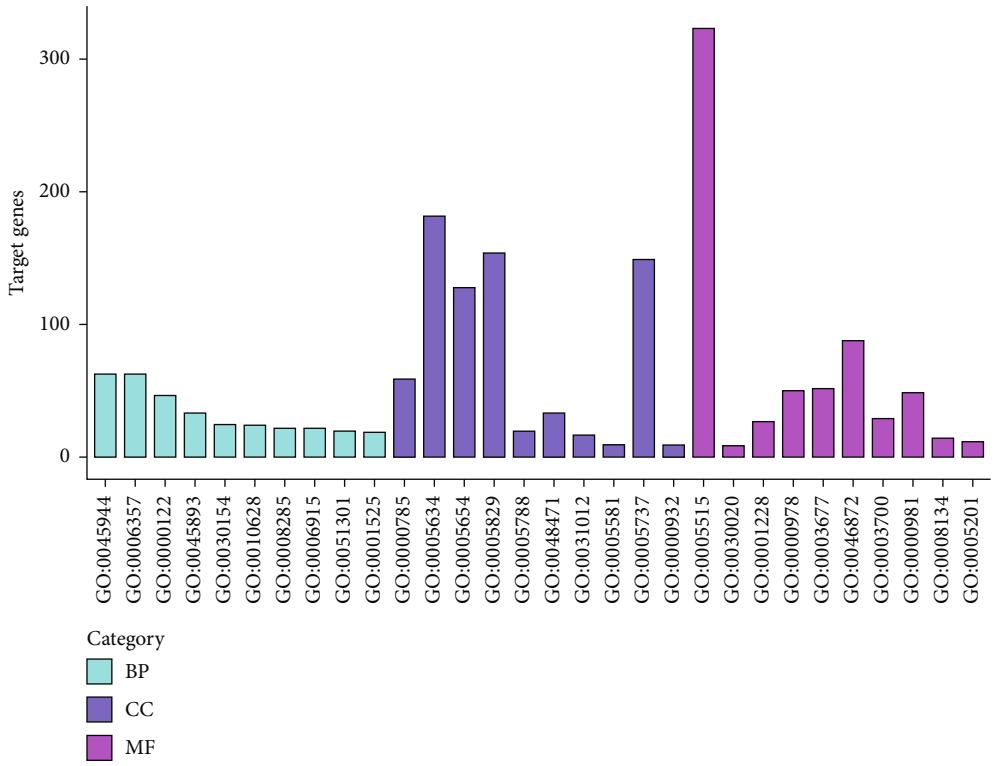

(c)

Figure 3: The GO enrichment of the DEGs. (a) GSE33857. (b) GSE110217. (c) The common DEGs in GSE33857 and GSE110217.

3.4. Network Establishment. To reveal the potential molecular interaction relationship, the targets of the DEGs in GSE33857 and GSE110217 were analyzed with the STRING database. Moreover, the top 500 genes were used to establish the PPI network and miRNA-mRNA network.

The results showed that 3 clusters were screened in both GSE33857 and GSE110217 via MCODE plug-in unit. For GSE33857, the targets of DEGs including PTEN, HIF1, VEGFA, SMAD2, PPARG, and ESR1 were identified as the hub nodes (Figures 4(a)–4(c)). ESR1, FBXW7, NRAS, PTEN, CCND1, and BTRC were identified as the hub nodes in GSE110217 (Figures 4(d)–4(f)). For common targets VEGFA, ESR1, DNMT1, KMT2A, and KAT2B were identified as hub nodes (Figures 4(g)–4(i)). Moreover, the miRNA-mRNA network was also established based on the targets of common DEGs in GSE33857 and GSE110217, and the results showed that 15 miRNA nodes and 351 mRNA nodes were included in the network (Figure 5).

4. Discussion

Chronic hepatitis B (CHB) is still a malignant infectious disease which seriously threatens the health of human and provides great challenge for the modern medical system [15]. In this research, the bioinformatics analysis was applied to investigate the potential regulation mechanism in the progression of CHB, and the GSE33857 and GSE110217 were used to investigate the potential biomarkers.

miRNAs have been confirmed as critical roles in regulating the normal progression of cells, and miRNA dysfunction has been proved as a direct reason leading the malignant progression of multiple diseases [16]. This investigation also discovered that the miRNA profile in the patient's tissues exhibited significant difference compared with that in the normal subjects [17]. 15 miRNAs were selected as the hub nodes in CHB. The research has confirmed that reduced miR-122-5p is closely related with the progression of HBV-induced liver fibrosis, and miR-122-5p can effectively impeded the deterioration of the symptom via targeting IL7R [18]. Increased miR-125b-5p has been identified as a serum biomarker for HBV infection by several reporters [19]. Deng et al. has also confirmed that miR-125b-5p can interact with LIN28B to induce the posttranscriptional regulation of HBV [20]. He et al. have indicated that decreased miR-136-5p can aggravate the liver cancer development induced by HBV [21]. miR-194-5p is also upregulated in the HBV host cells [22]. Moreover, miR-139-5p has been found to block the malignant behaviors of hepatocellular carcinoma cells [23]. miR-140-5p has also been confirmed to impede the EMT process via targeting TGFBR1 [24]. miR-181a-5p inhibited the cellular malignant proliferation via repressing EGR1 in hepatocellular carcinoma [25]. Zhou et al. have indicated that miR-29b-3p can impede the metastasis of hepatocellular carcinoma via blocking DNMT3A [26].

miRNA is characterized with repressing the translation via binding with the $3'$-UTR of the proteins. In this research,

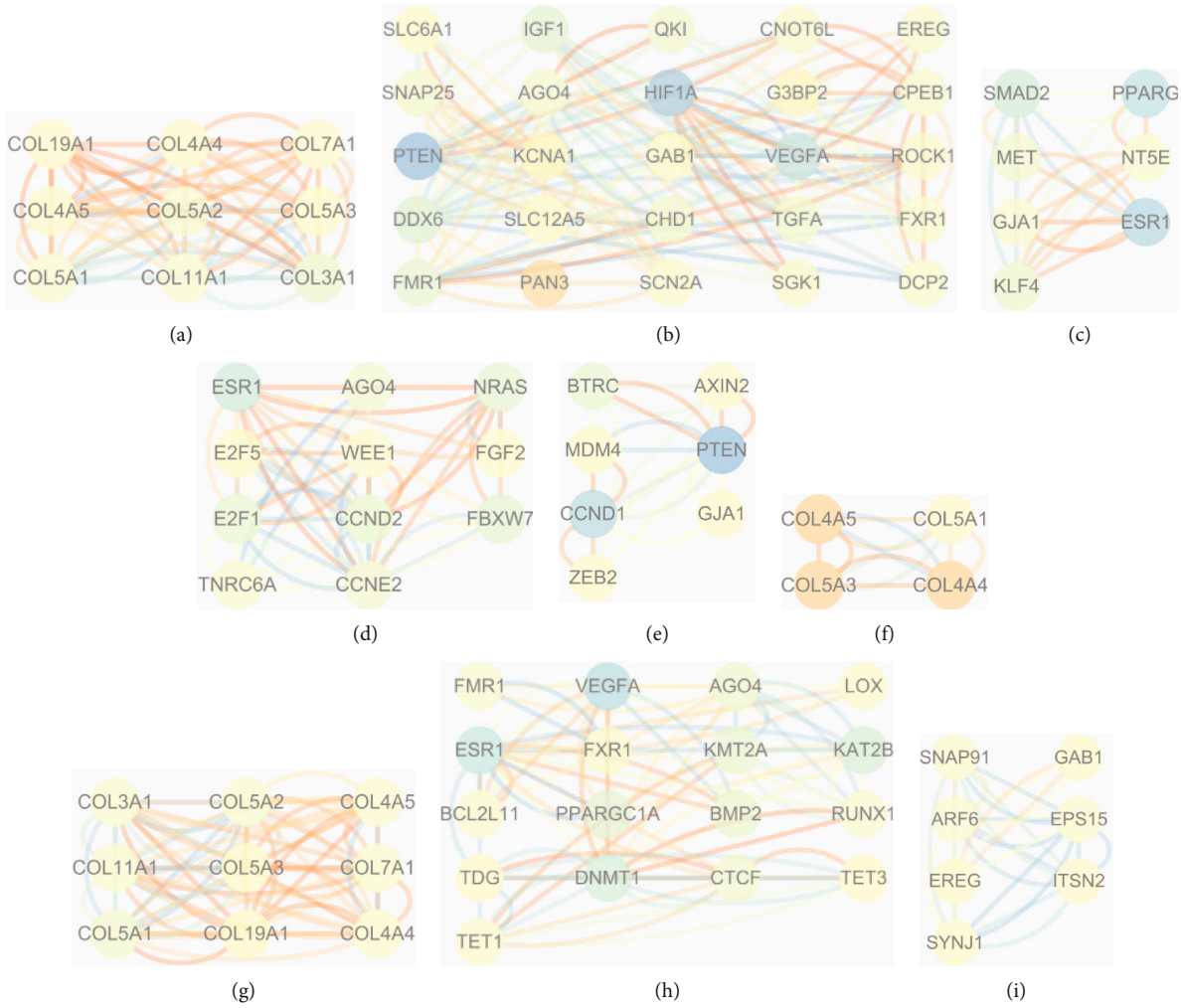

Figure 4: The PPI network analysis of DEGs in GSE33857 and GSE110217. (a)–(c) PPI network of the DEGs in GSE33857. (d)–(f) PPI network of the DEGs in GSE110217. (g)–(i) PPI network of the DEGs in common genes.

the targets of the miRNAs have been screened by miRDIP targets. PTEN, HIF1, VEGFA, SMAD2, PPARG, and ESR1 were identified as the hub nodes in GSE3857. ESR1, FBXW7, NRAS, PTEN, CCND1, and BTRC were identified as the hub nodes in GSE110217. VEGFA, ESR1, DNMT1, KMT2A, and KAT2B were identified as hub nodes in common targets of GSE3857 and GSE110217. DNMT1 has been identified as a serum biomarker event in cancer development, and DNMT1 has been also confirmed to be associated with HBV-related liver cancer [27]. In this research, DNMT1 was identified as the target of miR-148a-3p. FBXW7 plays a tumor supporter role in multiple tumors, and increased FBXW7 has been confirmed to be closely related with resistance of liver cancer cells on sorafenib [28]. This research found that FBXW7 served as a target of miR-27b-3p, and miR-27b-3p was dramatically reduced in HBV-infected tissues. Neovascularization is a biomarker event in the progression of some tumors. For gaining more nutrient, the tumor focuses generally exhibit aberrant angiopoiesis. VEGFA serves as critical role in driving the process of angiopoiesis in local low oxygen environment, which has been also identified as the biomarker in cancer development. Increased VEGFA is associated with liver cancer development, and several reports have indicated that VEGFA inhibition can extremely block the malignant behaviors of the cancer cells [29]. Moreover, increased VEGFA has been observed in HBV-related liver cancer.

Abundant reports have confirmed that HBV infection can induce the aberrant activities of the pathways in liver cells. This research has indicated that the DEGs in GSE33857 and GSE110217 were enriched in PI3K/AKT and MAPK pathways. PI3K/Akt signaling pathway is an important signal transduction pathway in cells, which plays an important role in inhibiting apoptosis and promoting cell survival and proliferation. Akt is an important downstream target kinase in PI3K signal transduction pathway, which has silk threonine kinase activity. When cells are stimulated by extracellular signals, PI3K activation generates PIP3 to translocate Akt to the cell membrane and localize near PDK1 and PDK2. The conformation of Akt changes,

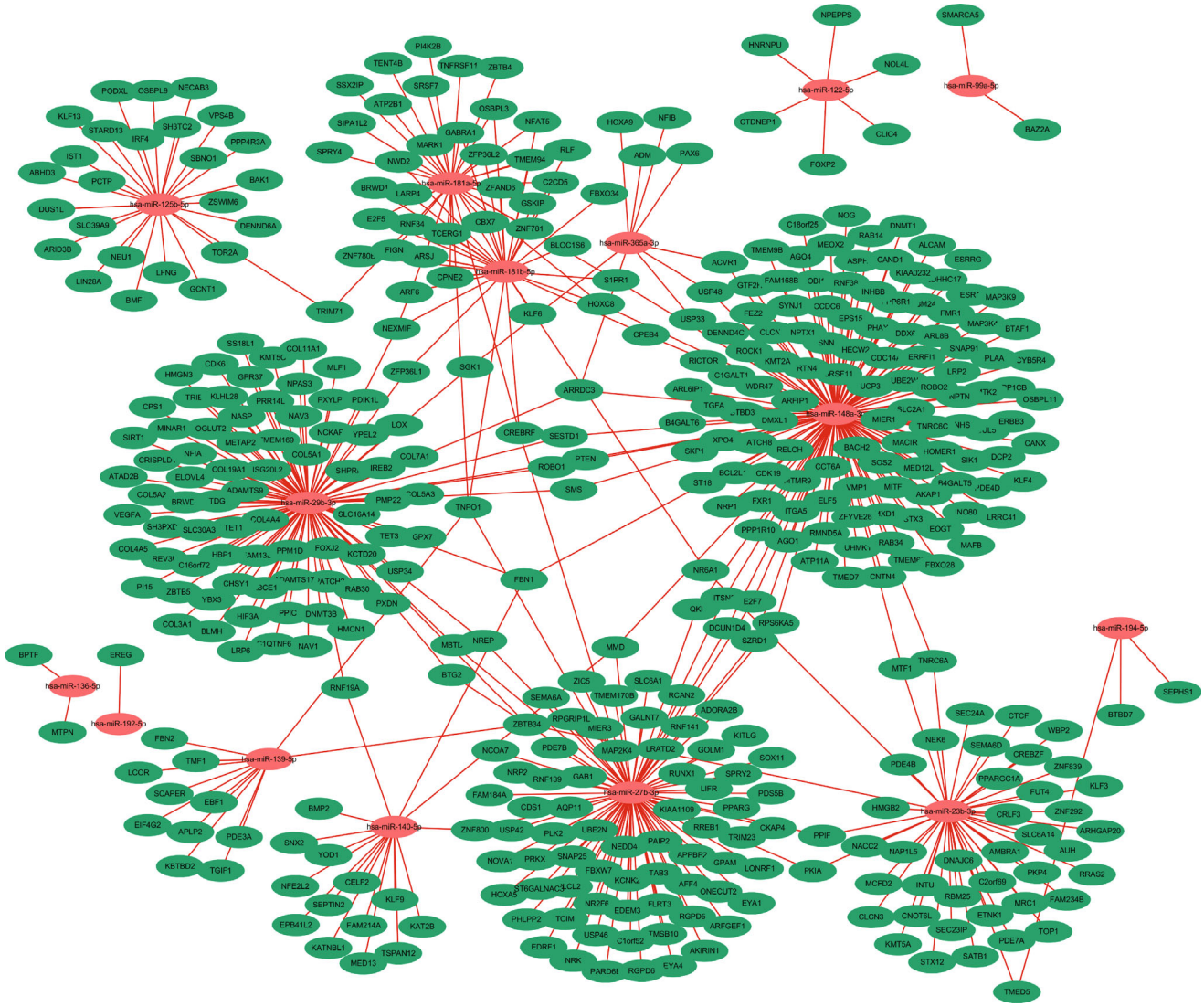

Figure 5: The miRNA-mRNA network of the common genes in GSE33857 and GSE110217.

exposing its phosphorylation site. Subsequently, Akt activation further acts on its downstream molecules, thus participating in cell growth, development, differentiation, and proliferation. The abnormal activation of PI3K/AKT pathways is related with the aberrant proliferation and enhanced invasive ability of tumor cells. HBV has been confirmed to induce the antiapoptosis ability of liver cancer cells via activating the PI3K/AKT pathway [29]. Moreover, MAPK pathway dysfunction could drive the deterioration of HBV-mediated liver cancer via promoting the transcription of surface protein hPIAS1 of HBV [30].

In conclusion, eight miRNAs, including miR-122-5p, miR-125b-5p, miR-136-5p, miR-194-5p, miR-139-5p, miR-140-5p, miR-181a-5p, and miR-29b-3p, were identified as the potential biomarkers in CHB, and the PPI and miRNA-mRNA networks were also established. The limitations of this study lie in the use of too few data sets and the lack of experimental validation. The next study should further verify the effect of these candidate biomarkers on CHB in vivo and in vitro.

Data Availability

Data to support the findings of this study is available on reasonable request from the corresponding author.

Conflicts of Interest

The authors do not have conflicts of interest to declare.

Acknowledgments

This research was funded by the 2018 Hebei Medical Science Research Key Project Plan (analysis of HBV genome sequence and molecular characteristics in patients with chronic hepatitis B in Zhangjiakou, Hebei Province), grant number 20180827.

References

[1] K. S. Liem, S. Fung, D. K. Wong et al., "Limited sustained response after stopping nucleos(t)ide analogues in patients

with chronic hepatitis B: results from a randomised controlled trial (Toronto STOP study)," *Gut*, vol. 68, no. 12, pp. 2206–2213, 2019.

[2] T. C. Tseng, C. Y. Peng, Y. C. Hsu et al., "Baseline mac-2 binding protein glycosylation isomer level stratifies risks of hepatocellular carcinoma in chronic hepatitis B patients with oral antiviral therapy," *Liver Cancer*, vol. 9, no. 2, pp. 207–220, 2020.

[3] D. Qiao, Y. Chen, and L. Liu, "Engineered therapeutic nanovaccine against chronic hepatitis B virus infection," *Biomaterials*, vol. 269, p. 120674, 2021.

[4] J. Ahn, J. K. Lim, H. M. Lee et al., "Lower observed hepatocellular carcinoma incidence in chronic hepatitis B patients treated with entecavir: results of the ENUMERATE study," *The American Journal of Gastroenterology*, vol. 111, no. 9, pp. 1297–1304, 2016.

[5] S. Tran, D. Jeong, L. Henry, R. C. Cheung, and M. H. Nguyen, "Initial evaluation, long-term monitoring, and hepatocellular carcinoma surveillance of chronic hepatitis B in routine practice: a nationwide US study," *The American Journal of Gastroenterology*, vol. 116, no. 9, pp. 1885–1895, 2021.

[6] Y. E. Chon, J. Y. Park, S. M. Myoung et al., "Improvement of liver fibrosis after long-term antiviral therapy assessed by Fibroscan in chronic hepatitis B patients with advanced fibrosis," *The American Journal of Gastroenterology*, vol. 112, no. 6, pp. 882–891, 2017.

[7] H. Wakasugi, H. Takahashi, T. Niinuma et al., "Dysregulation of miRNA in chronic hepatitis B is associated with hepatocellular carcinoma risk after nucleos(t)ide analogue treatment," *Cancer Letters*, vol. 434, pp. 91–100, 2018.

[8] Y. Ouyang, Y. Tang, L. Fu et al., "Exosomes secreted by chronic hepatitis B patients with PNALT and liver inflammation grade ≥ A2 promoted the progression of liver cancer by transferring miR-25-3p to inhibit the co-expression of TCF21 and HHIP," *Cell Proliferation*, vol. 53, no. 7, article e12833, 2020.

[9] W. Gan, X. Chen, Z. Wu et al., "The relationship between serum exosome HBV-miR-3 and current virological markers and its dynamics in chronic hepatitis B patients on antiviral treatment," *Annals of Translational Medicine*, vol. 10, no. 10, p. 536, 2022.

[10] Y. Mao, X. Wang, W. Hu et al., "Long-term and efficient inhibition of hepatitis B virus replication by AAV8-delivered artificial microRNAs," *Antiviral Research*, vol. 204, p. 105366, 2022.

[11] V. V. Loukachov, K. A. van Dort, I. Maurer et al., "Identification of liver and plasma microRNAs in chronic hepatitis B virus infection," *Frontiers in Cellular and Infection Microbiology*, vol. 12, p. 790964, 2022.

[12] G. Ning, L. M. Zhen, W. X. Xu et al., "Suppression of complement component 2 expression by hepatitis B virus contributes to the viral persistence in chronic hepatitis B patients," *Journal of Viral Hepatitis*, vol. 27, no. 10, pp. 1071–1081, 2020.

[13] T. Wu, E. Hu, S. Xu et al., "clusterProfiler 4.0: a universal enrichment tool for interpreting omics data," *Innovation*, vol. 2, no. 3, article 100141, 2021.

[14] C. Gu, J. Chen, X. Dang et al., "Hippo pathway core genes based prognostic signature and immune infiltration patterns in lung squamous cell carcinoma," *Frontiers in Oncology*, vol. 11, p. 680918, 2021.

[15] B. Chen, W. Wang, W. Xu, L. Ying, C. Zhou, and M. Zheng, "Serum free light chain is associated with histological activity and cirrhosis in patients with chronic hepatitis B," *International Immunopharmacology*, vol. 99, p. 107881, 2021.

[16] Q. Chu, J. Li, J. Chen, and Z. Yuan, "HBV induced the discharge of intrinsic antiviral miRNAs in HBV-replicating hepatocytes via extracellular vesicles to facilitate its replication," *Journal of General Virology*, vol. 103, no. 5, 2022.

[17] J. Zhao, X. C. Zhu, X. S. Wu et al., "Identification of miR-4644 as a suitable endogenous normalizer for circulating miRNA quantification in hepatocellular carcinoma," *Journal of Cancer*, vol. 11, no. 23, pp. 7032–7044, 2020.

[18] B. Li, Y. Li, S. Li, H. Li, L. Liu, and H. Yu, "Circ_MTM1 knockdown inhibits the progression of HBV-related liver fibrosis via regulating IL7R expression through targeting miR-122-5p," *American Journal of Translational Research*, vol. 14, no. 4, pp. 2199–2211, 2022.

[19] M. Ninomiya, Y. Kondo, O. Kimura et al., "The expression of miR-125b-5p is increased in the serum of patients with chronic hepatitis B infection and inhibits the detection of hepatitis B virus surface antigen," *Journal of Viral Hepatitis*, vol. 23, no. 5, pp. 330–339, 2016.

[20] W. Deng, X. Zhang, Z. Ma, Y. Lin, and M. Lu, "MicroRNA-125b-5p mediates post-transcriptional regulation of hepatitis B virus replication via the LIN28B/let-7 axis," *RNA Biology*, vol. 14, no. 10, pp. 1389–1398, 2017.

[21] W. He, X. Zhu, X. Tang, X. Xiang, J. Yu, and H. Sun, "Circ_0027089 regulates NACC1 by targeting miR-136-5p to aggravate the development of hepatitis B virus-related hepatocellular carcinoma," *Anti-Cancer Drugs*, vol. 33, no. 1, pp. e336–e348, 2022.

[22] K. O. Nielsen, K. S. Jacobsen, A. H. Mirza et al., "Hepatitis B virus upregulates host microRNAs that target apoptosis-regulatory genes in an *in vitro* cell model," *Experimental Cell Research*, vol. 371, no. 1, pp. 92–103, 2018.

[23] S. Hua, L. Lei, L. Deng et al., "miR-139-5p inhibits aerobic glycolysis, cell proliferation, migration, and invasion in hepatocellular carcinoma via a reciprocal regulatory interaction with ETS1," *Oncogene*, vol. 37, no. 12, pp. 1624–1636, 2018.

[24] Y. H. Tang, G. L. He, S. Z. Huang et al., "The long noncoding RNA AK002107 negatively modulates miR-140-5p and targets TGFBR1 to induce epithelial-mesenchymal transition in hepatocellular carcinoma," *Molecular Oncology*, vol. 13, no. 5, pp. 1296–1310, 2019.

[25] J. G. Bi, J. F. Zheng, Q. Li et al., "MicroRNA-181a-5p suppresses cell proliferation by targeting Egr1 and inhibiting Egr1/TGF-β/Smad pathway in hepatocellular carcinoma," *The International Journal of Biochemistry & Cell Biology*, vol. 106, pp. 107–116, 2019.

[26] Y. Zhou, K. Li, T. Dai et al., "Long non-coding RNA HCP5 functions as a sponge of miR-29b-3p and promotes cell growth and metastasis in hepatocellular carcinoma through upregulating DNMT3A," *Aging (Albany NY)*, vol. 13, no. 12, pp. 16267–16286, 2021.

[27] Y. Deng, J. Wang, M. Huang, G. Xu, W. Wei, and H. Qin, "Inhibition of miR-148a-3p resists hepatocellular carcinoma progress of hepatitis C virus infection through suppressing c-Jun and MAPK pathway," *Journal of Cellular and Molecular Medicine*, vol. 23, no. 2, pp. 1415–1426, 2019.

[28] X. Feng, B. Zou, T. Nan et al., "MiR-25 enhances autophagy and promotes sorafenib resistance of hepatocellular carcinoma via targeting FBXW7," *International Journal of Medical Sciences*, vol. 19, no. 2, pp. 257–266, 2022.

[29] Y. Chen, X. Bai, Q. Zhang et al., "The hepatitis B virus X protein promotes pancreatic cancer through modulation of the PI3K/AKT signaling pathway," *Cancer Letters*, vol. 380, no. 1, pp. 98–105, 2016.

[30] H. Wang, D. Wu, X. Wang et al., "Hepatitis B virus surface protein-induced hPIAS1 transcription requires TAL1, E47, MYOG, NFI, and MAPK signal pathways," *Biological Chemistry*, vol. 397, no. 11, pp. 1173–1185, 2016.

Hindawi
Disease Markers
Volume 2022, Article ID 7177192, 14 pages
https://doi.org/10.1155/2022/7177192

Research Article

HSPA5 Could Be a Prognostic Biomarker Correlated with Immune Infiltration in Breast Cancer

Chao Zhang,[1] **Qing Liu**,[2] **Yubo Zhou**,[2] **Jianfen Hua**,[2] **Ruijun Su**,[2] **and Jun Ai**[2]

[1]*Qujing First People's Hospital, No. 1, Yuanlin Road, Qujing 655000, China*
[2]*Department of Thyroid and Breast Surgery, Qujing First People's Hospital, No. 1, Yuanlin Road, Qujing 655000, China*

Correspondence should be addressed to Chao Zhang; chesanjin@163.com and Jun Ai; aijunmvp2022@163.com

Received 23 June 2022; Accepted 17 August 2022; Published 20 September 2022

Academic Editor: Chang Gu

Background. Breast cancer (BC) is a frequent disease in females. The heat shock 70 kDa protein 5 (HSPA5) has recently been discovered to have an important function in tumor growth. However, the biological significance of HSPA5 in BC is unknown. *Material and Method*. Firstly, The Cancer Genome Atlas (TCGA) database was applied to analyze the expressions of HSPA5 in different cancer types, especially in BC. Then, the LinkedOmics database was used to screen genes coexpressed with HSPA5 in BC, presented by protein-protein interaction (PPI) and analyzed by functional enrichment analyses. Next, the Kaplan-Meier plotter was adopted to study the prognostic significance of HSPA5 and the relation between HSPA5 expression and different clinical factors in BC. Finally, the Tumor Immune Estimation Resource (TIMER) method was adopted to explore the relation between immune infiltration and HSPA5 in BC. *Result*. HSPA5 was highly expressed in most cancers, including BC. Genes coexpressed with HSPA5 were mainly related to endoplasmic reticulum unfolded protein response, melanosome, thyroid hormone synthesis, N-glycan biosynthesis, and so on. In the survival analysis, high HSPA5 expression indicated a poor prognosis in BC, and the expression of HSPA5 in BC was elevated after the incidence of BC, changing with different clinical factors. In the immune infiltration, HSPA5 was positively correlated with most immune cells. *Conclusion*. HSPA5 is an oncogene in BC progression, and it is connected with the prognosis and the immune infiltration in BC. Our findings suggest that HSPA5 could be an immunotherapy target and a prognostic biomarker in BC.

1. Background

Breast cancer (BC) is a frequent disease in females [1], with a certain genetic risk [2]. According to the latest global cancer statistics, the number of new BC cases reaches 2.26 million, making it the world's biggest cancer, accounting for 11.7% of all new cancer patients, and its mortality rate is about 6.6% [3]. In the early stages, 80% of patients often have breast lumps, nipple discharge, abnormal nipples, and areolas. In the middle and advanced stages, symptoms like loss of appetite, weight loss, fatigue, and anemia may appear, and some patients may also develop tumor metastases in the lung, pleura, liver, and brain [4, 5]. Due to the fact that symptoms of early BC are not obvious, most patients are already in the advanced stage at the time of diagnosis. Although more and more adjuvant treatment methods can improve the therapeutic effect of BC [6], the recurrence and metastasis of BC are still high [7]. Thus, it is urgent to find new specific BC markers to increase the clinical diagnosis rate and improve the prognosis of BC patients.

HSPA5, a member of the heat shock protein 70 (HSP70) family [8], is the master regulator of ER homeostasis [9] and participates in antiapoptosis and negative regulation of caspase [10]. Correspondingly, multiple research investigations have shown this gene is also related to the progression of some cancers. For example, Kim et al. reported that HSPA5 was related to tumor progression and could promote the survival of head and neck cancer (HNC) by maintaining lysosomal activity [11]. Teng et al. analyzed by two-dimensional gel electrophoresis and other methods that PKM2 and HSPA5 were highly expressed in high-risk endometrial cancer (EC), which could be used as potential biomarkers of EC [12]. Moreover, this gene is also actively expressed in liver cancer, glioblastoma, osteosarcoma [13],

and other cancers. However, the role of HSPA5 and its carcinogenic mechanism in BC are still poorly understood, and further exploration is still needed.

In recent years, bioinformatics [14] has become an important technology for exploring molecular markers related to tumor diseases, which promotes the research progress of genomic and proteomic data. This time, we first analyze the expression and function of HSPA5 in BC through comprehensive databases, including The Cancer Genome Atlas (TCGA), LinkedOmics database, and Tumor Immune Estimation Resource (TIMER). The above analysis will provide strong evidence for exploring the mechanism of HSPA5 in the development of BC.

2. Material and Methods

2.1. TCGA Database. TCGA database contains clinical sample information of more than 20,000 patients and 33 cancers, as well as sequencing data of various omics, such as genome, transcriptome, and epigenetics, which can effectively help 1 better understand the molecular mechanism of cancer. This time, we explored the expressions of HSPA5 in different cancer types based on TCGA database.

2.2. The HSPA5 Coexpressed Genes in BC by LinkedOmics. LinkedOmics is an online analysis tool of TCGA database, including 3 analysis modules: LinkFinder, LinkInterpreter, and LinkCompare. Among them, LinkFinder is convenient for users to search and query information. LinkInterpreter is used to perform rich analysis of Gene Ontology (GO), biological path, network module, and other functional categories. LinkCompare uses visualization functions to compare the correlation results, and supports multigroup analysis of cancer types. Based on the above three modules, we first analyzed the genes related to HSPA5 in BC, the top 50 upregulated and downregulated genes, and the top 200 genes with significance that were displayed by heat maps and protein-protein network (PPI), respectively. Then, GO term and Kyoto Encyclopedia of Genes and Genomes (KEGG) analyses were conducted on these genes.

2.3. The Prognostic Analysis on HSPA5 in BC. To verify the relation between HSPA5 and the prognosis of BC patients, we analyzed the effects of different levels of HSPA5 on the probability of relapsed-free survival (RFS) and postprogression survival (PPS) by the Kaplan-Meier plotter. After that, the relation between HSPA5 and pathological parameters (pathologic stage, age, HER2 status, T stage, N stage, and M stage) in BC samples was compared in the UALCAN database to explore the therapeutic value of the gene for patients.

2.4. Timer Database. TIMER is an online tumor immune cell assessment tool based on TCGA, which provides researchers with the infiltration status of 6 immune cells, CD4+ T cells, B cells, CD8+ T cells, macrophages, neutrophils, and dendritic cells. Herein, based on this tool, we conducted a correlation study between 6 immune infiltrating cells and the HSPA5 gene in BC. When $P < 0.05$, the results obtained were meaningful.

3. Results

3.1. The Expression of HSPA5 in the Pan-Cancers. Based on TCGA database, we verified the expressions of the HSPA5 in different cancers. According to the results of Figures 1(a) and 1(b), the expression of the HSPA5 gene was higher in most tumors than normal groups, and in BC, it also had a higher expression in BC tumors.

3.2. HSPA5 Coexpressed Genes and the Functional Enrichment Analysis. Through the LinkedOmics database, we identified the positive and negative coexpressed genes associated with HSPA5 (Figure 2(a)), displayed by heat maps (Figures 2(b) and 2(c)). In the STRING database, we uploaded the coexpressed gene information related to HSPA5 and obtained a PPI network of the top 200 significant genes with 58 nodes and 411 edges (Figure 3). Then, the functional enrichment results showed that the enrichment items of these genes in biological process (BP) were response to topologically incorrect protein, response to unfolded protein, cellular response to unfolded protein (Figure 4(a)), in cell component (CC) were endoplasmic reticulum lumen, pigment granule, melanosome, oligosaccharyltransferase complex, and endoplasmic reticulum chaperone complex (Figure 4(b)), and in molecular function (MF) were disulfide oxidoreductase activity, intramolecular oxidoreductase activity, peptide disulfide oxidoreductase activity, and oligosaccharyltransferase activity (Figure 4(c)). Furthermore, the first 5 pathways for these genes enriched in KEGG were thyroid hormone synthesis, N-Glycan biosynthesis, protein export, and so on (Figure 4(d)).

3.3. The Prognostic Value Analysis of HSPA5 in BC. To evaluate the clinical value of HSPA5 in BC patients, we used the Kaplan-Meier mapping tool to plot the relationship between differently expressed HSPA5, RPS, and PPS in BC patients. The results demonstrated high expression of HSPA5 that indicated poor RFS (hazard ratio, HR = 1.23, log-rank $P = 5.8e-05$, Figure 5(a)); on the contrary, low expression of HSPA5 promotes the probability of PPF ($HR = 1.34$, log-rank $P = 0.013$, Figure 5(b)). In addition, we made a comparative analysis between the expression of HSPA5 and clinicopathological parameters in BC. From the results in Figures 6(a)–6(f), it was found that the expression of HSPA5 in BC was all significantly higher after BC occurrence and changed with pathologic stage, age, HER2 status, T stage, N stage, and M stage. These results showed that HSPA5 could be a prognostic biomarker in BC progression.

3.4. Correlation Analysis between HSPA5 Gene and Tumor Immune Infiltrating Cells in BC. Based on TIMER, we analyzed the relation between the expression of HSPA5 and 6 immune infiltrating cells in BC tissues. The results in Figure 7 showed that the expression of HSPA5 was positively related to B cell (correlation = 0.159, $P = 5.50e-07$), CD8+ T cell (correlation = 0.209, $P = 4.57e-11$), macrophage (correlation = 0.077, $P = 1.55e-02$), neutrophil (correlation = 0.212, $P = 4.41e-11$), and dendritic cell (correlation = 0.158, $P = 9.67e-07$). Besides, the level of

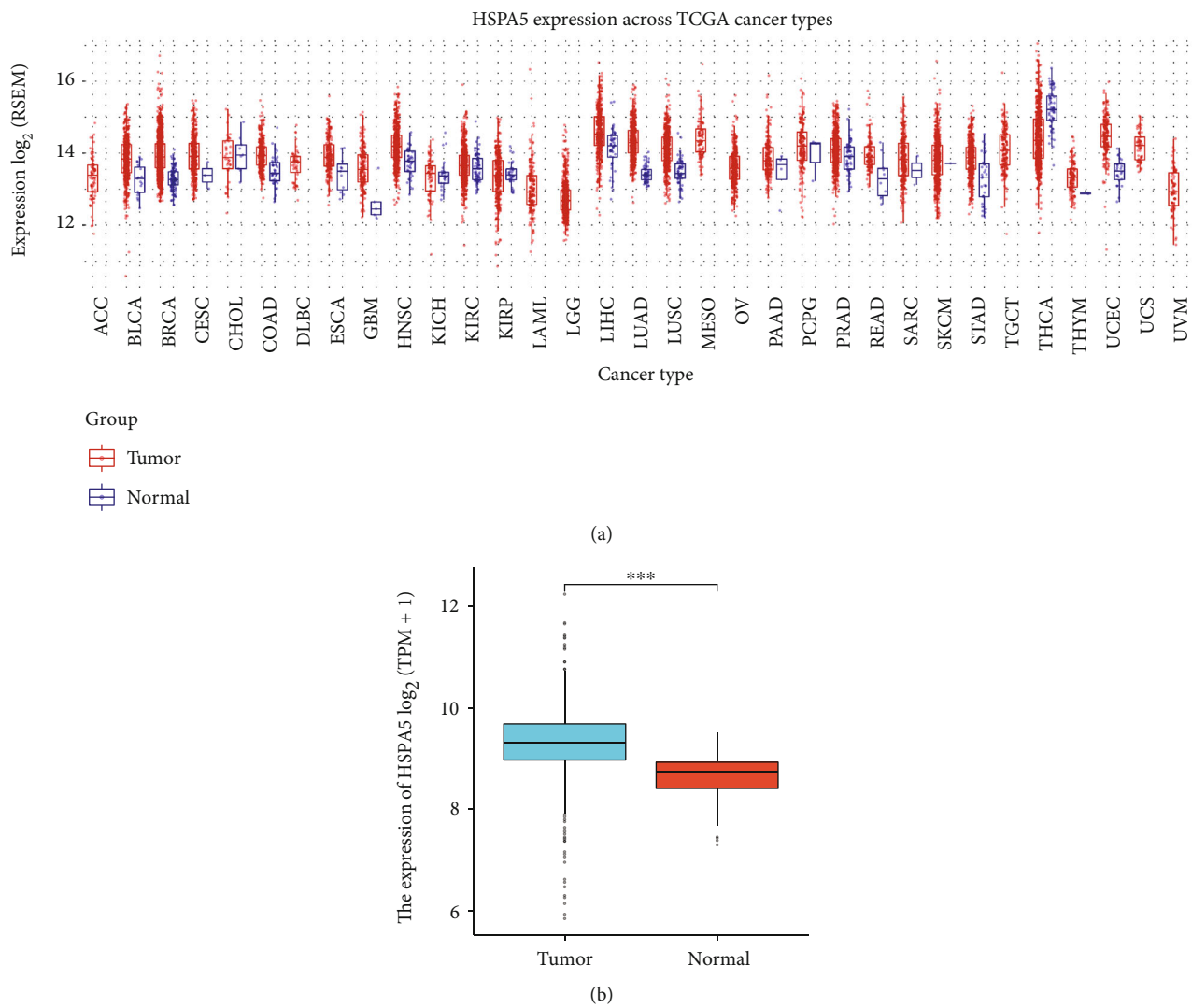

Figure 1: The expressions of HSPA5 in the pan-cancers. (a) The expressions of HSPA5 in pan-cancers. (b) The expression of HSPA5 in BC tissues and normal tissues. $^{***}P < 0.001$.

HSPA5 was negatively correlated with CD4+ T cell (correlation = −0.011, $P = 7.36e - 01$). The finding indicates that HSPA5 might be an immunotherapeutic target in BC.

3.5. Network Analysis of Relation between HSPA5 and BC Clinical Factors. The Search Tool for the Retrieval of Interacting Genes (STRING) database (http://string-db.org) can critically assess and integrate protein–protein interactions (PPI), including both direct (physical) and indirect (functional) associations. To detect potential relationships among our initial candidate genes, we mapped all the genes to the STRING network and visualized the network using Cytoscape [15].

4. Discussion

The prevalence of BC is a significant global public health concern. Early detection of BC is the most effective way to diagnose and treat BC in time [16]. Currently, breast ultrasound is an important and reliable method for the diagnosis of BC [17]. Although blood testing is convenient for screening in asymptomatic people, there are few effective biomarkers for detecting early disease [18, 19]. Therefore, it is necessary to develop more reliable biomarkers for early diagnosis and new treatment for BC patients.

Numerous cellular activities require iron, and improper iron metabolism can potentially result in cell death [20]. A group of iron-dependent proteins, which are broken down into stages of iron absorption, use, storage, and efflux, tightly regulates the metabolism of iron. Iron metabolism genes are tightly controlled and have a coordinated feedback control over unstable iron [21]. Ferroptosis is a regulatory cell death caused by oxidative damage, but the specific molecular regulatory mechanism remains unclear [22]. Previously, HSPA5 is found to negatively regulate the ferroptosis in human pancreatic ductal adenocarcinoma, and the HSPA5-GPX4 pathway could regulate ferroptosis resistance and inhibit the anticancer activity of gemcitabine [23]. Besides, Torti and others have discussed in their article that there is a large amount of laboratory

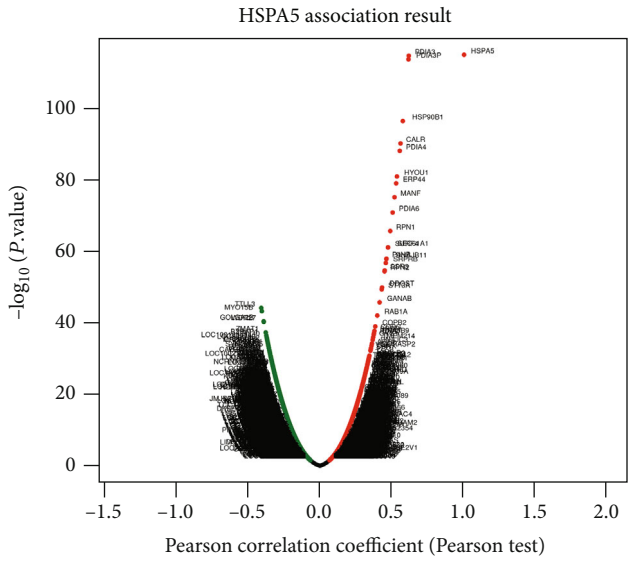

(a)

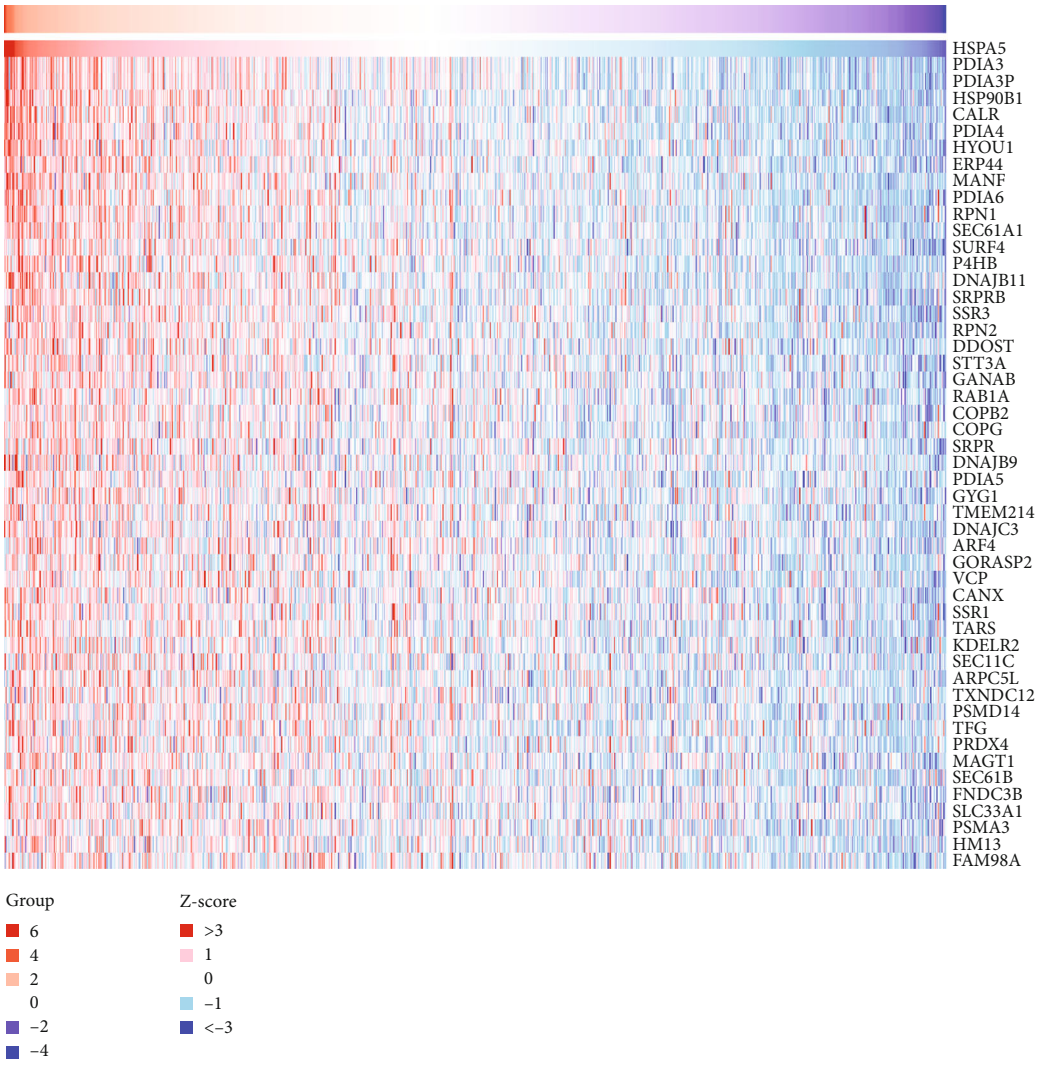

(b)

Figure 2: Continued.

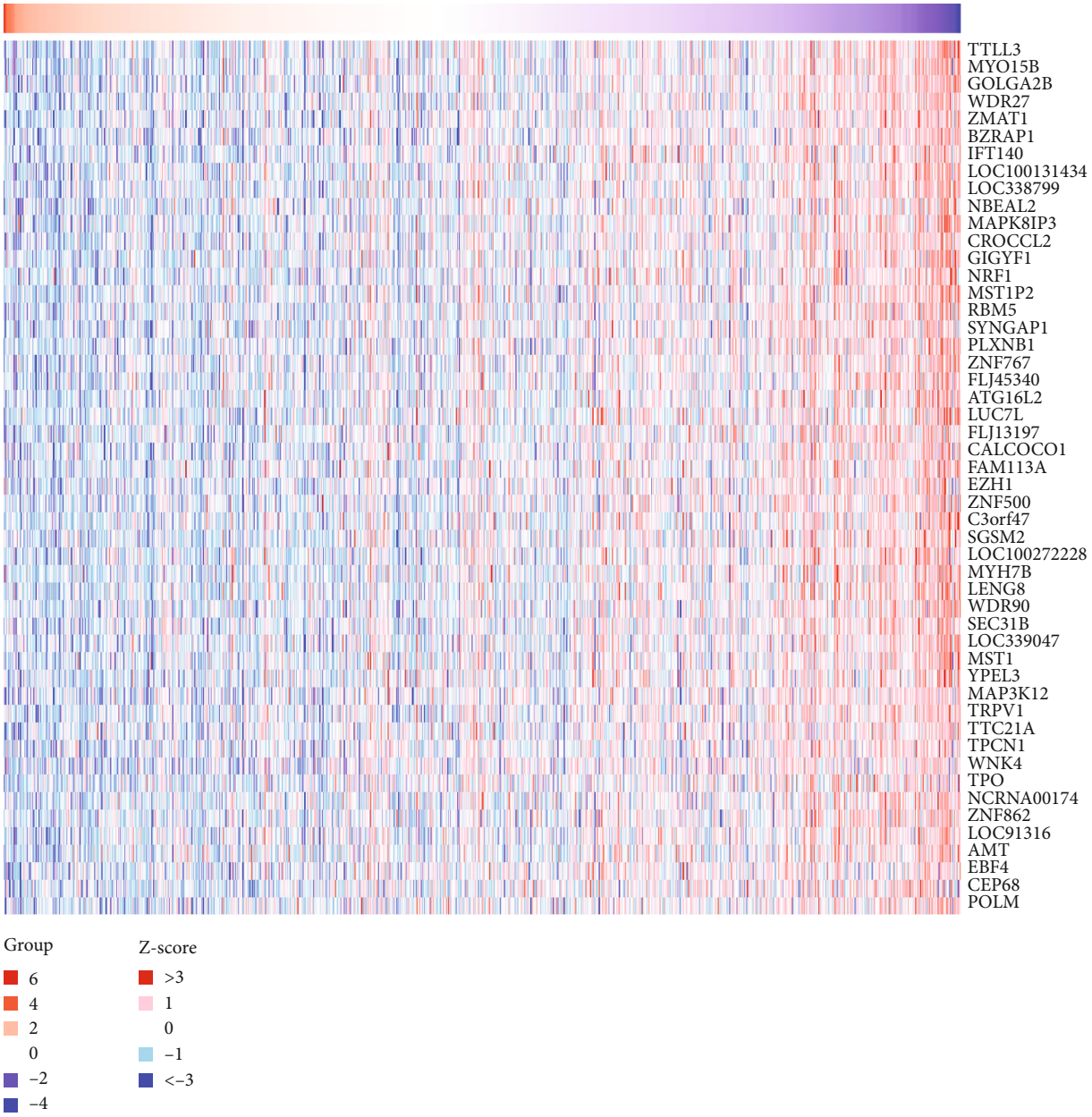

(c)

Figure 2: HSPA5 coexpressed genes and the functional enrichment analysis. (a) The HSPA5 coexpressed genes in BC. (b) The top 50 positive genes. (c) The top 50 negative genes.

and clinical evidence that iron is closely connected with the growth and metastasis of BC [24]. BC cells increase their intracellular iron levels through various ways, such as increasing uptake and reducing outflow. In addition, breast tumor growth may potentially be aided by changes in iron metabolism in macrophages and other cells in the tumor microenvironment [25]. Therefore, we aim to explore the expression and function in BC progression.

Herein, we firstly found that the expression of HSPA5 was upregulated in most cancers, including BC. Then, we screened the HSPA5 coexpressed genes, mainly enriched in response to unfolded protein, melanosome, thyroid hormone synthesis, and N-Glycan biosynthesis. Unfolded or improperly folded proteins that accumulate in the endoplasmic reticulum's lumen trigger the unfolded protein response (UPR), a stress reaction (ER). Numerous human illnesses, including cancer, neurological and inflammatory disorders, and metabolism, are mechanistically caused by this unchecked activation. In breast tumors, some evidence suggests that chronic activation of UPR is related to treatment resistance and disease recurrence. It was reported that the role of abnormal UPR activation and overexpression of UPR components were resistant to apoptosis and drug therapy in BC [26]. Ruffolo et al. experimentally determined that

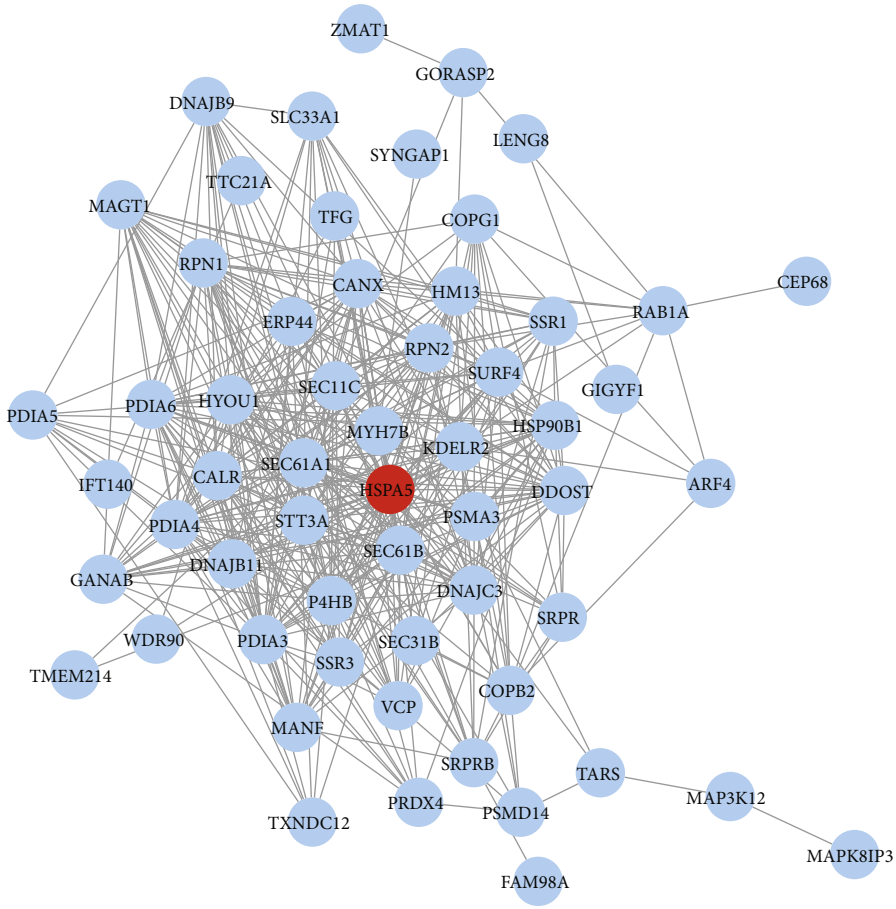

Figure 3: PPI network of the top 200 genes with statistical significance. 58 nodes and 411 edges.

breast tumors originated from melanin synthesized by breast epithelium and tumor cells. They suggested that this breast tumor should be diagnosed as a melanocyte-differentiated cancer, and melanocytes might be the basis for the formation of primary breast melanoma [27]. Recent epidemiology describes a close relationship between thyroid function and BC, which indicates that the thyroid hormone is a vital part in the development of BC. There is also clinical evidence that hypothyroidism is beneficial to the recovery of BC. Hercbergs et al. proved that L-thyroxine, T4, was an *in vitro* proliferation factor of BC cells, and in the absence of estrogen, thyroid hormone could greatly help promote the proliferation of nuclear estrogen receptor-α- (ERα-) dependent BC cells [28]. At present, people have observed changes in serum protein glycosylation in several cancers including BC [29], which indicates that serum glycans may be potential biomarkers of BC.

In the survival analysis of HSPA5 in BC, we found the high level of HSPA5 in BC patients led to poor RFS and PPS by the Kaplan-Meier plotter. To investigate whether HSPA5 could be a prognostic biomarker in BC progression, we investigated the relationship between HSPA5 and clinicopathological parameters in TCGA database. It was found the expressions of HSPA5 were differentially expressed in patients with different pathologic stage, age, HER2 status, T stage, N stage, and M stage. From these results, we can conclude that HSPA5 is highly expressed in BC tumor tissues, and the highly expressed HSPA5 has a shorter survival time than the lowly expressed HSPA5. Therefore, HSPA5 has the potential to be a new diagnostic and prognostic biomarker in BC patients.

Tumor does not simply contain tumor cells, but it consists of various cells, stromal cells, and immune cells, which constitutes the tumor microenvironment [30]. Different immune cells play different roles in tumorigenesis with their own characteristics. Currently, the promising immunotherapy refers to a therapeutic method targeting the immune function of the body for the purpose of treating diseases [31]. In this study, we observed the relation between HSPA5 and 6 immune infiltration cells. The data showed that HSPA5 was positively related with most cells, which indicated HSAP5 might be a new immunotherapeutic target in BC. In recent years, researchers found that high expression of HSPA5 is associated with antitumor cell activity, because factors such as insufficient blood supply and nutritional conditions may lead to the existence of stressful microenvironments such as hypoxia, hypoglycemia, and acidosis in tumor entities, which may lead to the overexpression of HSPA5 in tumors, which may be a defense mechanism of tumor cells under unfavorable survival conditions. As a

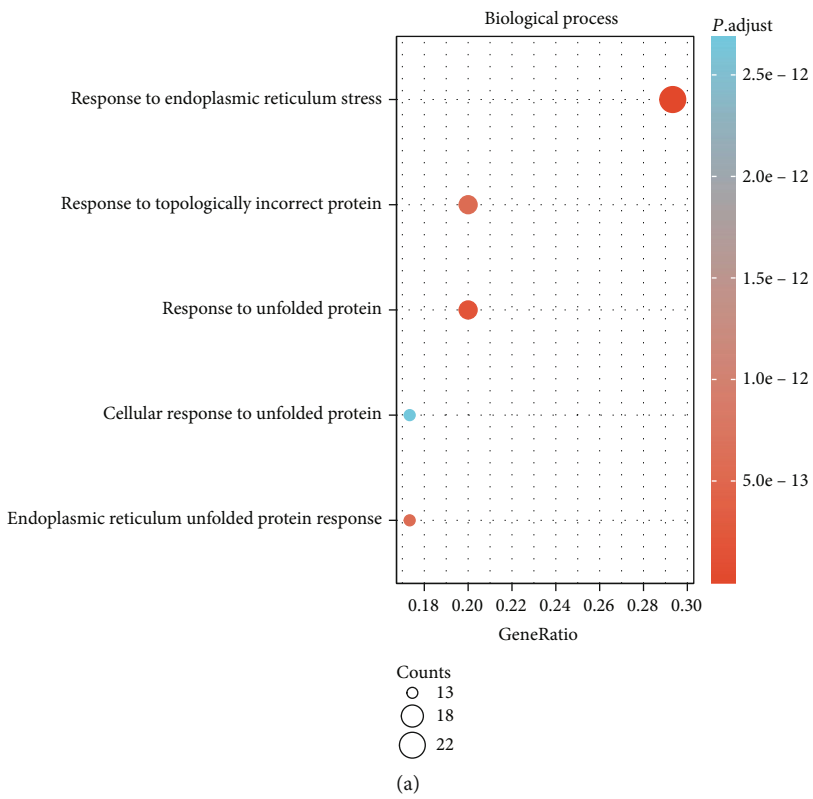

(a)

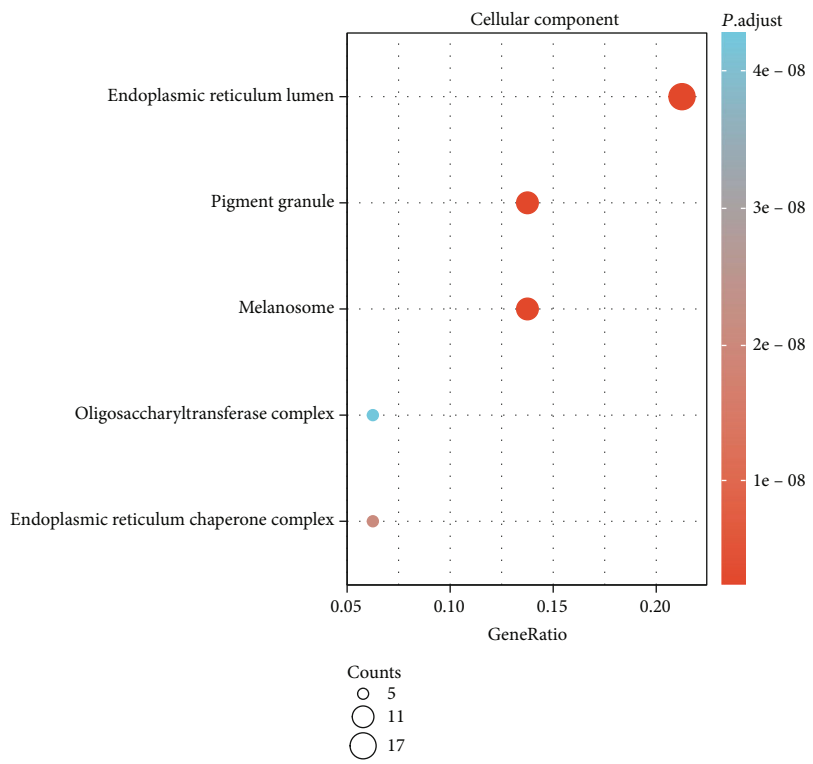

(b)

Figure 4: Continued.

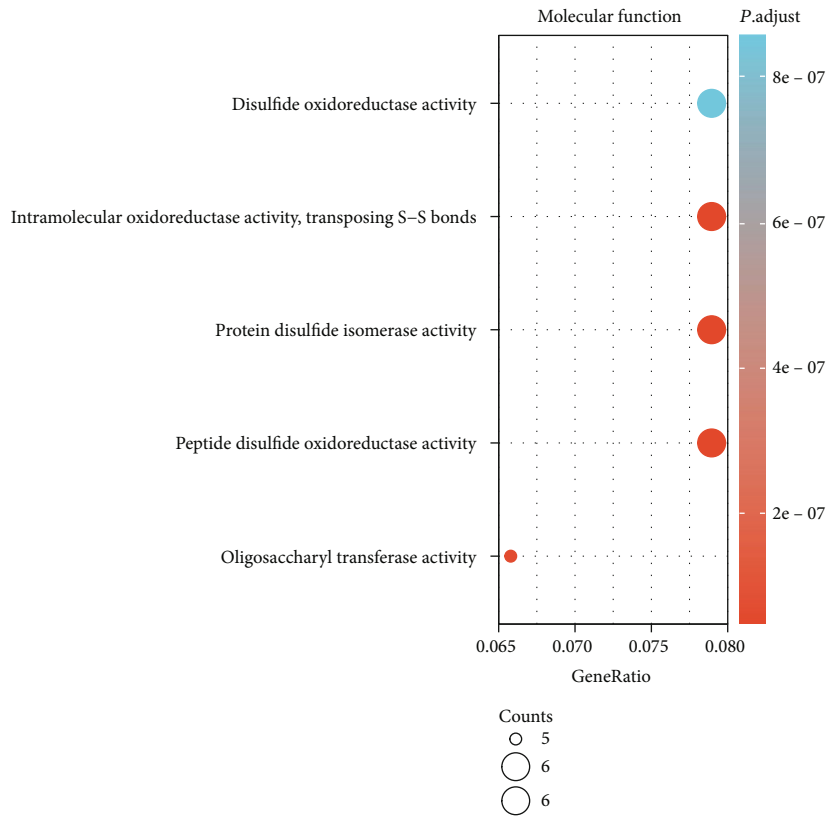

(c)

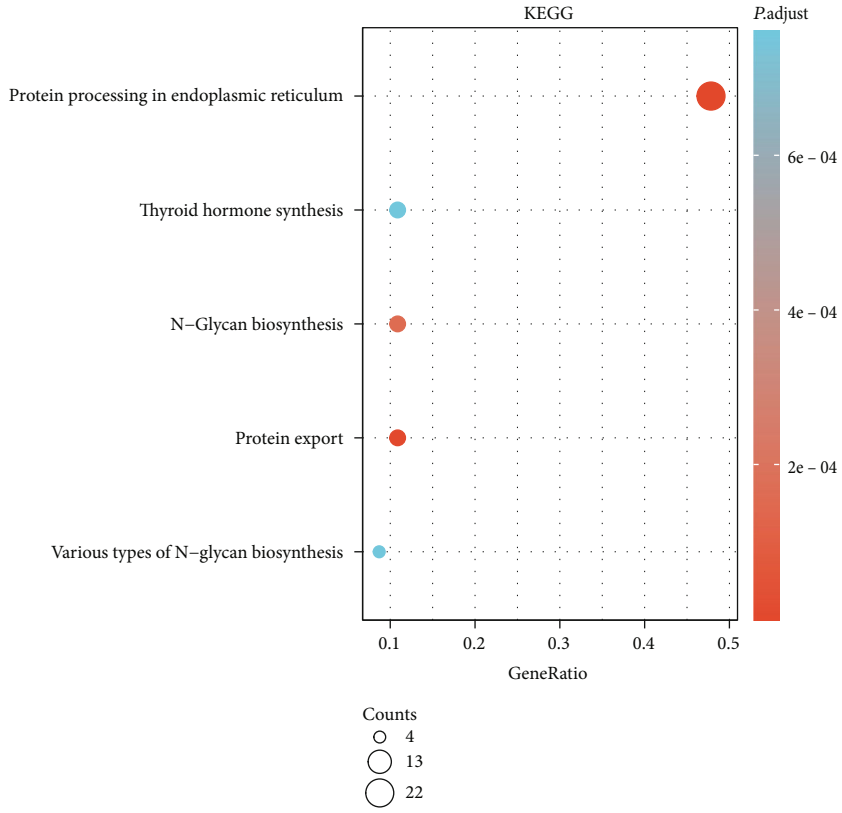

(d)

Figure 4: The functional enrichment analyses on the HSPA5 coexpressed genes. (a) BP. (b) CC. (c) MF. (d) KEGG pathway. The size of the dot represents the amount of gene enrichment, and different colors indicate different *P* values.

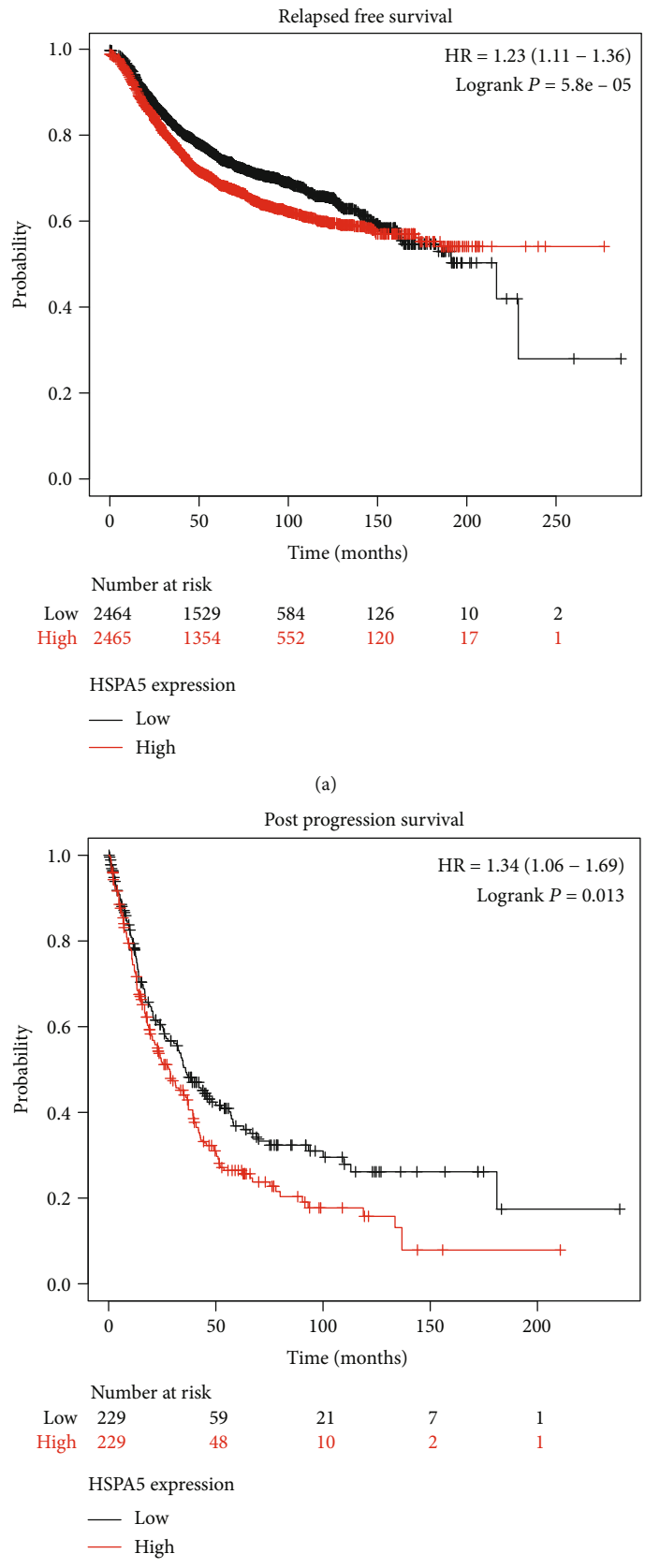

Figure 5: The survival curve of HSPA5 in BC. The effect of HSPA5 expression on the (a) RFS and (b) PPS, the vertical axis represents the probability, and the horizontal axis represents time.

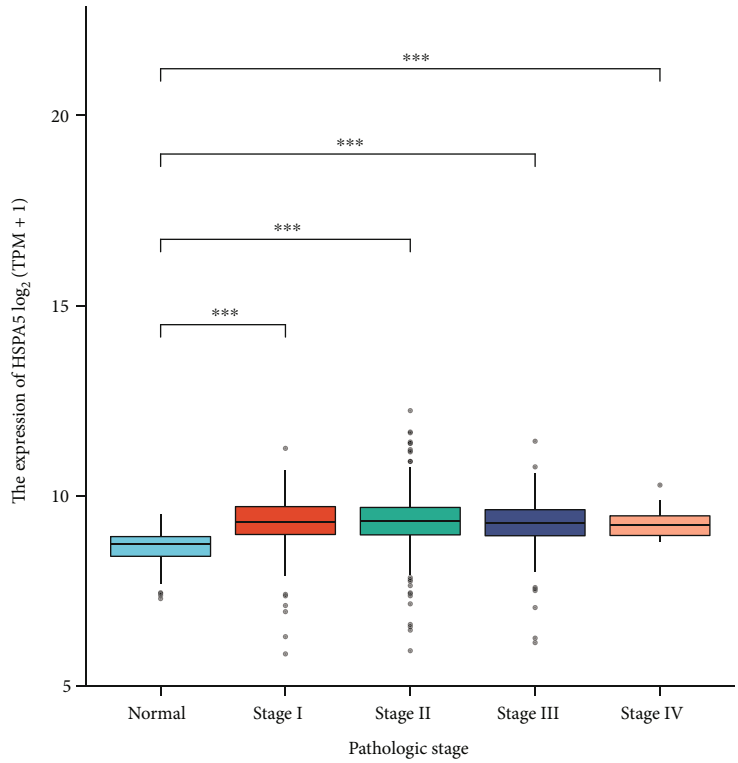

(a)

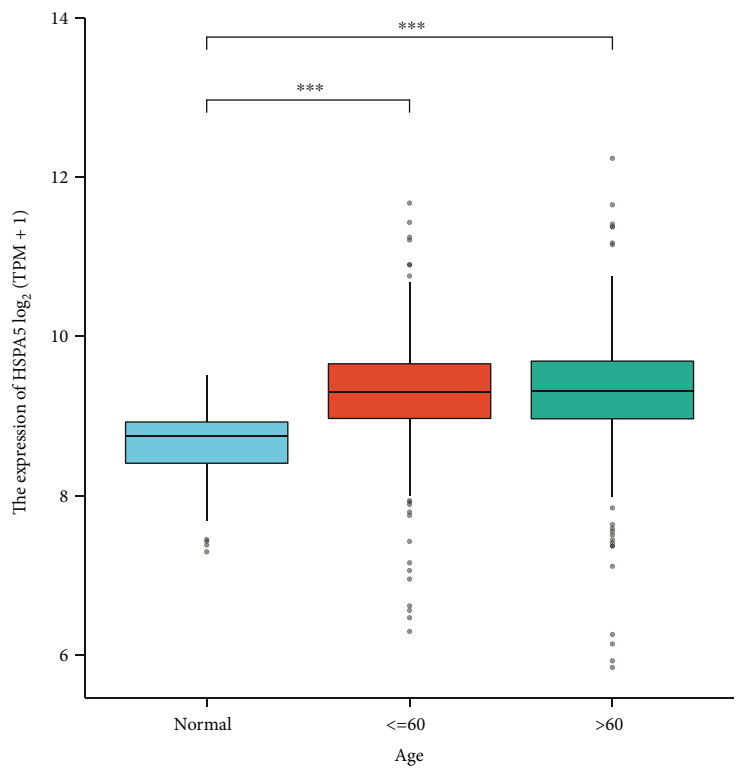

(b)

Figure 6: Continued.

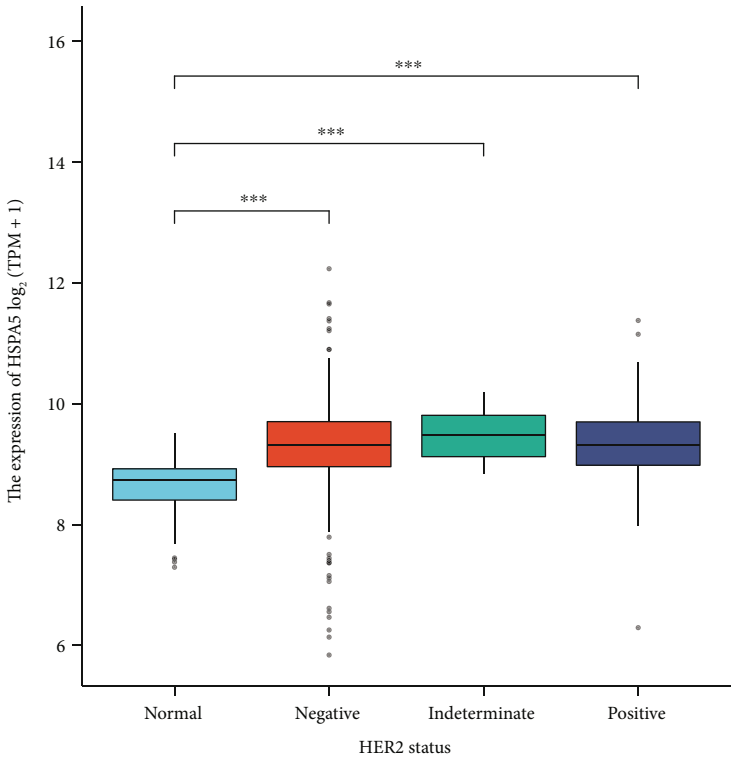

(c)

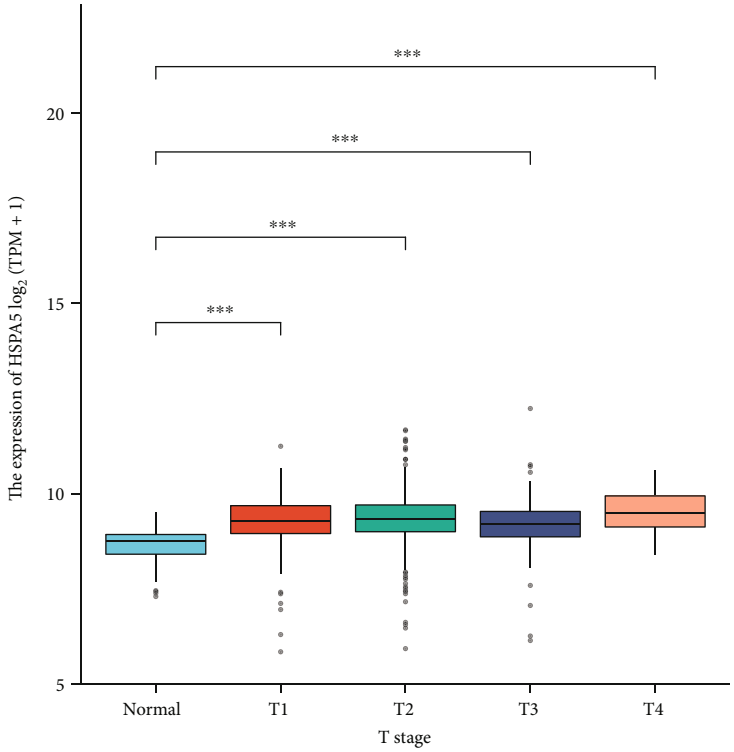

(d)

Figure 6: Continued.

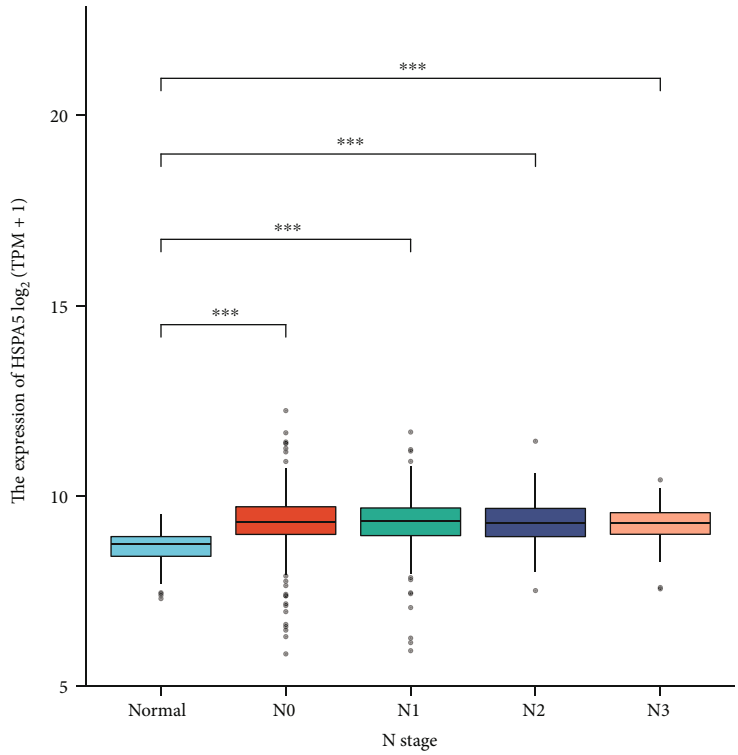

(e)

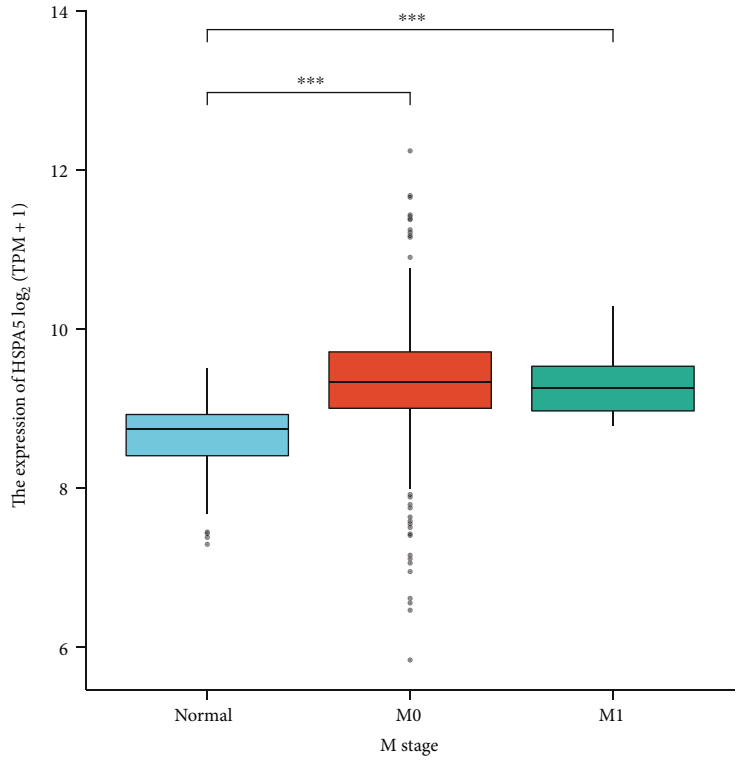

(f)

Figure 6: The relation between HSPA5 and BC clinical factors. (a) Pathologic stage. (b) Age. (c) HER2 status. (d) T stage. (e) N stage. (f) M stage. $^{***}P < 0.001$.

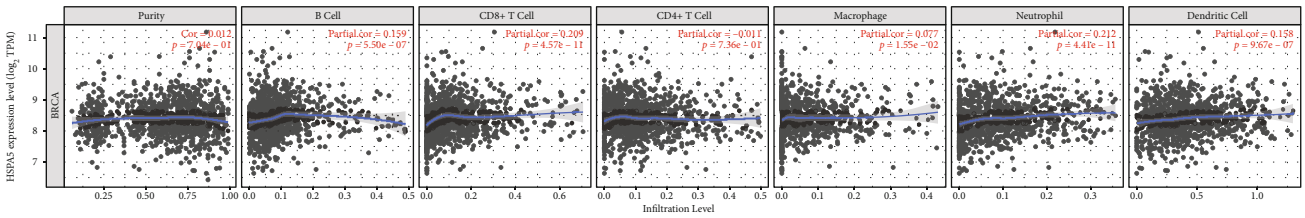

Figure 7: The relationship between HSPA5 gene and 6 immune infiltrating cells in BC.

calcium-binding protein in the endoplasmic reticulum, HSPA5 directly inhibits the activation of proapoptotic tissue components under stressful conditions and diverts folded proteins that accumulate in the endoplasmic reticulum to maintain cellular protein synthesis, thereby maintaining calcium homeostasis and the stability of the endoplasmic reticulum of tumor cells. Therefore, the high expression of HSPA5 in tumor cells has a certain protective effect on the growth of tumor cells. This has a close relationship with the biological behavior of tumor cells and can have a direct impact on the efficacy of tumor treatment. The positive expression rate of HSPA5 protein in breast cancer tissues was significantly higher than that in the group with lymph node metastasis, suggesting that those with high expression of HSPA5 protein in breast cancer tissues have a poorer prognosis. It is also suggested that HSPA5, as a new marker for breast cancer, may be a new target for breast cancer treatment, which may provide new ideas for further research on breast cancer. Our research revealed the role of HSPA5 in breast cancer through public databases and comprehensive bioinformatics analysis. However, further experiments are needed for verification.

In conclusion, the level of HSPA5 in BC tumor tissues was significantly higher, and its high expression was related to poor PFS and PPS in BC patients. In addition, HSPA5 is positively correlated with most immune infiltration cells. Based on these results, HSPA5 can be used as a potential biomarker for the diagnosis and prognosis and a new target in the immunotherapy of BC.

Data Availability

Data will be shared on request.

Conflicts of Interest

There is no conflict of interest.

References

[1] C. E. DeSantis, F. Bray, J. Ferlay, J. Lortet-Tieulent, B. O. Anderson, and A. Jemal, "International variation in female breast cancer incidence and mortality rates," *Cancer Epidemiology, Biomarkers & Prevention*, vol. 24, no. 10, pp. 1495–1506, 2015.

[2] J. Lilyquist, K. J. Ruddy, C. M. Vachon, and F. J. Couch, "Common genetic variation and breast cancer risk—past, present, and future," *Cancer Epidemiology, Biomarkers & Prevention*, vol. 27, no. 4, pp. 380–394, 2018.

[3] Z. Rezanejad Gatabi, M. Mirhoseini, N. Khajeali, I. Rezanezhad Gatabi, M. Dabbaghianamiri, and S. Dorri, "The accuracy of electrical impedance tomography for breast cancer detection: a systematic review and meta-analysis," *The Breast Journal*, vol. 2022, pp. 1–9, 2022.

[4] P. Boyle, "Breast cancer control: signs of progress, but more work required," *The Breast*, vol. 14, no. 6, pp. 429–438, 2005.

[5] M. Fahad Ullah, "Breast cancer: current perspectives on the disease status," *Breast Cancer Metastasis and Drug Resistance*, pp. 51–64, 2019.

[6] J. A. Sparano, R. J. Gray, P. M. Ravdin et al., "Clinical and genomic risk to guide the use of adjuvant therapy for breast cancer," *New England Journal of Medicine*, vol. 380, no. 25, pp. 2395–2405, 2019.

[7] A. I. Riggio, K. E. Varley, and A. L. Welm, "The lingering mysteries of metastatic recurrence in breast cancer," *British Journal of Cancer*, vol. 124, no. 1, pp. 13–26, 2021.

[8] A. Bolhassani and E. Agi, "Heat shock proteins in infection," *Clinica Chimica Acta*, vol. 498, pp. 90–100, 2019.

[9] J. Wang, J. Lee, D. Liem, and P. Ping, "HSPA5 gene encoding Hsp70 chaperone BiP in the endoplasmic reticulum," *Gene*, vol. 618, pp. 14–23, 2017.

[10] C.-C. Cheng, B. L. Yang, W. C. Chen et al., "STAT3 mediated miR-30a-5p inhibition enhances proliferation and inhibits apoptosis in colorectal cancer cells," *International Journal of Molecular Sciences*, vol. 21, no. 19, p. 7315, 2020.

[11] S.-Y. Kim, H. J. Kim, H. J. Kim et al., "HSPA5 negatively regulates lysosomal activity through ubiquitination of MUL1 in head and neck cancer," *Autophagy*, vol. 14, no. 3, pp. 385–403, 2018.

[12] Y. Teng, Z. Ai, Y. Wang, J. Wang, and L. Luo, "Proteomic identification of PKM2 and HSPA5 as potential biomarkers for predicting high-risk endometrial carcinoma," *Journal of Obstetrics and Gynaecology Research*, vol. 39, no. 1, pp. 317–325, 2013.

[13] X. Tang, L. Luo, Y. Li et al., "Therapeutic potential of targeting HSPA5 through dual regulation of two candidate prognostic biomarkers ANXA1 and PSAT1 in osteosarcoma," *Aging (Albany NY)*, vol. 13, no. 1, pp. 1212–1235, 2021.

[14] A. Lesk, *Introduction to bioinformatics*, Oxford university press, 2019.

[15] X. Shi, T. Huang, J. Wang et al., "Next-generation sequencing identifies novel genes with rare variants in total anomalous pulmonary venous connection," *eBioMedicine*, vol. 38, pp. 217–227, 2018.

[16] K. L. Britt, J. Cuzick, and K.-A. Phillips, "Key steps for effective breast cancer prevention," *Nature Reviews Cancer*, vol. 20, no. 8, pp. 417–436, 2020.

[17] R. F. Brem, M. J. Lenihan, J. Lieberman, and J. Torrente, "Screening breast ultrasound: past, present, and future,"

American Journal of Roentgenology, vol. 204, no. 2, pp. 234–240, 2015.

[18] O. Ginsburg, C. H. Yip, A. Brooks et al., "Breast cancer early detection: a phased approach to implementation," *Cancer*, vol. 126, no. S10, pp. 2379–2393, 2020.

[19] G. Khakpour, A. Pooladi, P. Izadi, M. Noruzinia, and J. Tavakkoly Bazzaz, "DNA methylation as a promising landscape: a simple blood test for breast cancer prediction," *Tumor Biology*, vol. 36, no. 7, pp. 4905–4912, 2015.

[20] G. Papanikolaou and K. Pantopoulos, "Iron metabolism and toxicity," *Toxicology and Applied Pharmacology*, vol. 202, no. 2, pp. 199–211, 2005.

[21] X. Chen, C. Yu, R. Kang, and D. Tang, "Iron metabolism in ferroptosis," *Frontiers in Cell and Development Biology*, vol. 8, article 590226, 2020.

[22] X. Jiang, B. R. Stockwell, and M. Conrad, "Ferroptosis: mechanisms, biology and role in disease," *Nature Reviews Molecular Cell Biology*, vol. 22, no. 4, pp. 266–282, 2021.

[23] D. Tang, X. Chen, P. B. Comish, and R. Kang, "The dual role of ferroptosis in pancreatic cancer: a narrative review," *Journal of Pancreatology*, vol. 4, no. 2, pp. 76–81, 2021.

[24] S. V. Torti, D. H. Manz, B. T. Paul, N. Blanchette-Farra, and F. M. Torti, "Iron and cancer," *Annual Review of Nutrition*, vol. 38, no. 1, pp. 97–125, 2018.

[25] Y. Wang, L. Yu, J. Ding, and Y. Chen, "Iron metabolism in cancer," *International Journal of Molecular Sciences*, vol. 20, no. 1, p. 95, 2019.

[26] E. P. McGrath, S. Logue, K. Mnich et al., "The unfolded protein response in breast cancer," *Cancers*, vol. 10, no. 10, p. 344, 2018.

[27] E. F. Ruffolo, F. C. Koerner, and H. M. Maluf, "Metaplastic carcinoma of the breast with melanocytic differentiation," *Modern pathology: an official journal of the United States and Canadian Academy of Pathology, Inc*, vol. 10, no. 6, pp. 592–596, 1997.

[28] Y.-F. Chen, Y. N. Yang, H. R. Chu et al., "Role of integrin $\alpha v\beta 3$ in doxycycline-induced anti-proliferation in breast cancer cells," *Frontiers in Cell and Development Biology*, vol. 10, 2022.

[29] K. Mariño, R. Saldova, B. Adamczyk, and P. M. Rudd, "Chapter 3. Changes in serum N-glycosylation profiles: functional significance and potential for diagnostics," *Carbohydrate chemistry*, vol. 37, pp. 57–93, 2011.

[30] B. Arneth, "Tumor microenvironment," *Medicina*, vol. 56, no. 1, p. 15, 2020.

[31] H. Tang, J. Qiao, and Y.-X. Fu, "Immunotherapy and tumor microenvironment," *Cancer Letters*, vol. 370, no. 1, pp. 85–90, 2016.

Hindawi
Disease Markers
Volume 2022, Article ID 4870981, 11 pages
https://doi.org/10.1155/2022/4870981

Research Article

Comprehensive Analysis of Novel Genes and Pathways Associated with Osteogenic Differentiation of Adipose Stem Cells

Qiuni Gao,[1] Xiaorong Ma,[2] and Zuoliang Qi[3]

[1]*Department of Plastic and Cosmetic Surgery, Tongji Hospital, School of Medicine, Tongji University, Shanghai 200065, China*
[2]*Department of Plastic and Reconstructive Surgery, Xinhua Hospital, Kongjiang Road 1665, Shanghai 200092, China*
[3]*Department of Plastic and Reconstructive Surgery, Plastic Surgery Hospital, Chinese Academy of Medical Sciences and Peking Union Medical College, No. 33 Badachu Road, Shijingshan District, Beijing 100144, China*

Correspondence should be addressed to Xiaorong Ma; maxiaorong@xinhuamed.com.cn and Zuoliang Qi; public_qi@163.com

Received 31 May 2022; Accepted 20 July 2022; Published 12 September 2022

Academic Editor: Jianxin Shi

Background. Adipose-derived stem cells (ADSCs) are an important alternative source of mesenchymal stem cells (MSCs) and show great promise in tissue engineering and regenerative medicine applications. However, identifying the novel genes and pathways and finding the underlying mechanisms regulating ADSCs osteogenic differentiation remain urgent. *Methods*. We downloaded the gene expression profiles of GSE63754 and GSE37329 from the Gene Expression Omnibus (GEO) Database. We derived differentially expressed genes (DEGs) before and after ADSC osteogenic differentiation, followed by Gene Ontology (GO) functional and KEGG pathway analysis and protein-protein interaction (PPI) network analysis. 211 differentially expressed genes (142 upregulated genes and 69 downregulated genes) were aberrantly expressed. GO analysis revealed that these DEGs were associated with extracellular matrix organization, protein extracellular matrix, and semaphorin receptor binding. *Conclusions*. Our study provides novel genes and pathways that play important roles in regulating ADSC osteogenic differentiation, which may have potential therapeutic targets for clinic.

1. Introduction

Millions of patients around the world suffer from bone defects caused by tumors, infections, and trauma, and their repair and treatment are a major problem [1]. Over 10 million bone transplants are performed worldwide each year, and the number is still growing at a rate of 10% annually [2]. Presently, autologous bone transplantation and allogeneic bone transplantation are the two main surgical options for treating bone defects and nonunion [3, 4]. Autologous bone transplants are a common treatment for bone defects, but their use is limited due to their limited source, poor plasticity, and damaging to the donor site [5]. Allogeneic bone transplantation results in a significantly higher rate of postoperative complications, which has exceeded 30%, and includes fractures, insufficiency, and infections [6, 7].

By creating replacements for natural bone grafts, bone tissue engineering aims to address the shortcomings [8]. As well as having the ability to form on demand, it should also easy to be prepared. Several advances have been made recently, including the development of human ADSCs that can perform paracrine functions as well as multilineage differentiation [9–11]. As a result of their properties, ADSCSs are especially useful in bone tissue engineering. Transplanting human ADSCs as a prospective treatment has recently received some attention [12, 13]. The treatment of bone trauma with autologous cells is therefore relatively promising. Transcriptional, posttranscriptional, and epigenetic factors regulate osteogenic differentiation of ADSCs [14]. A high-efficiency osteoinductive factor is also required as part of repairing bone tissue [15]. Wnt, PI3K/Akt, and MAPK signaling pathways were associated with osteogenic differentiation of ADSCs [16]. So, we have focused on developing osteoinductive factors that are effective. To uncover the molecular mechanisms of osteogenesis, further research is required.

ADSCs have become a hot spot in bone tissue engineering research because of their abundant sources and easy access to materials. However, the molecular biological

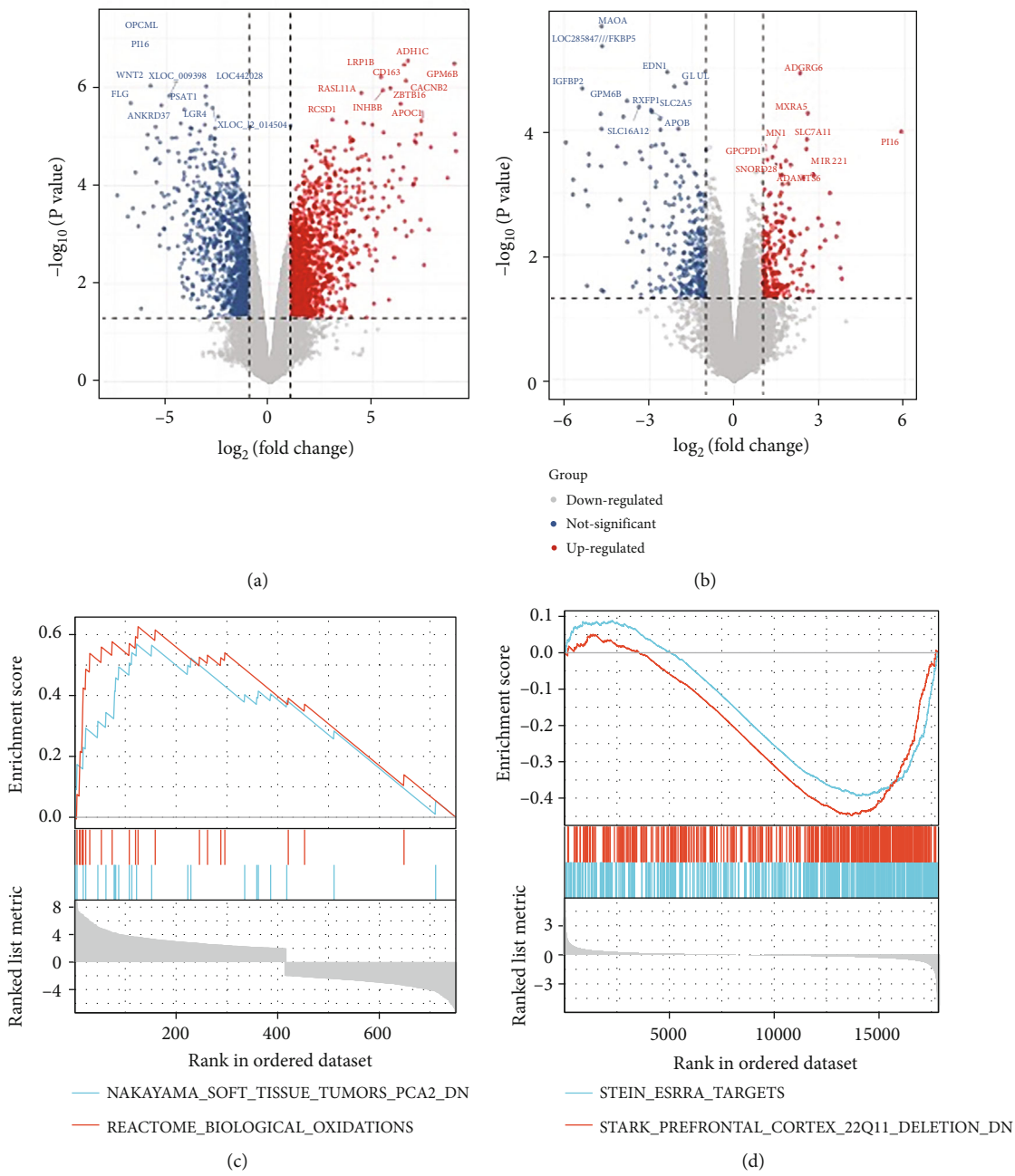

Figure 1: Continued.

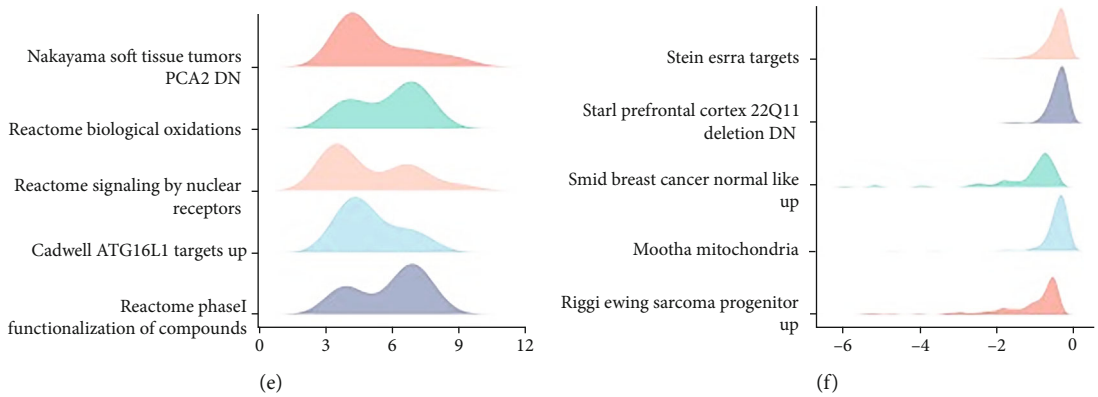

Figure 1: DEGs of GSE63754 and GSE37329. (a–d) Volcano plot: the volcano plot was constructed using the fold change values and *P* -adjust. Red dots indicate upregulated genes; blue dots indicate downregulated genes. (c–f) Gene set enrichment analysis (GSEA) of two significantly enriched classes of genes: ADSCs and noninduced ADSC datasets.

mechanism of osteogenic differentiation of ADSCs has not been fully elucidated [17]. With the rapid development of big data and bioinformatics, as well as the application of ADSCs in the field of clinical medicine, some scholars have carried out RNA microarray and sequencing studies on the osteogenic differentiation of ADSCs to further explore the role of these RNAs in the osteogenesis of ADSCs [18, 19]. Molecular biological mechanisms during differentiation remains elusive. Molecular biology and functional genomics utilize microarray profiling to discover genes that are upregulated or downregulated, respectively [20, 21]. Therefore, in this study, bioinformatics methods were used to screen the differentially expressed genes and their involved signaling pathways during the osteogenic differentiation of ADSCs, in order to explore the molecular biological mechanism of potential key genes during the osteogenic differentiation of ADSCs. We first identified the differentially expressed genes (DEGs) from two microarray datasets selected from Gene Expression Omnibus (GEO) database. A bioinformatics approach was used to analyze the signaling pathway involving novel genes and to construct a protein–protein interaction (PPI) network. To sum up, this study found the potential key genes and the pathways involved in the osteogenic differentiation of ADSCs by mining the data related to the osteogenic differentiation of ADSCs in GEO database. These results may provide new ideas and a basis for further experimental studies to explore the genesis, development, and molecular biological mechanism of osteogenic differentiation of ADSCs in the future.

2. Methods

2.1. Data Collection. Transcript profile data on osteogenic differentiation between ADSCSs and noninduced ADSCs were derived from NCBI GEO databases (http://www.ncbi.nlm.nih.gov/geo/).

GSE63754 (3 undifferentiated ADSCs and 3 osteogenic differentiated ADSCs) and GSE37329 (3 ADSCs and 2 ADSC-derived osteocytes) are the accession numbers for the collections. All of these ADSCSDs were collected from human tissues and underwent osteogenic induction.

2.2. Identification of Differentially Expressed Gene. R software and Bioconductor packages were applied to data mining and statistical analyses. The Limma package was subsequently used for identifying DEGs.

$P < 0.05$ and log2 fold change (log 2FC) > 1 or < −1 were considered as the cutoff values for DEGs to be considered statistically significant. R software was used to produce heat maps of common significant differentially expressed genes between GSE63754 and GSE37329.

2.3. GO and KEGG Enrichment Analysis. GSEA was performed using GSEA 3.0 (http://www.broadinstitute.org/gsea/). Geneset with a *P* value less than 0.05 was considered to be significantly enriched. GO enrichment analysis was performed using the Gene Ontology Consortium Enrichment analysis tool (http://www.geneontology.org). To analyze the enriched biological processes (BPs), cellular components (CCs), molecular functions (MFs), and pathways of DEGs, GO analysis and KEGG pathway enrichment analysis were performed with the online tools DAVID (https://david.ncifcrf.gov/) and MetADSCsape (http://metADSCsape.org).

2.4. PPI Network Construction. STRING database (http://string-db.org) and Cytoscape software (Version 3.4.0) were used to identify 142 upregulated DEGs and 69 downregulated DEGs. The network was visualized using Cytoscape, a widely-used tool for exploring interactions among biomolecules, including proteins and genes.

2.5. Statistical Methods. These statistics were generated using the R software and were two-sided. *P* values less than 0.05 were considered statistically significant.

3. Results

3.1. DEGs of GSE63754 and GSE37329. Differential gene expression analyses were visualized by volcano plots. To explore the biological classification of the DEGs overlapping in the dataset, all genes were identified in the two datasets using DAVID and MetADSCsape software. The genes are commonly regulated ($P < 0.05$ and log2 fold change (log 2FC) > 1 or < −1) in GSE63754. Then, we compared the gene expression

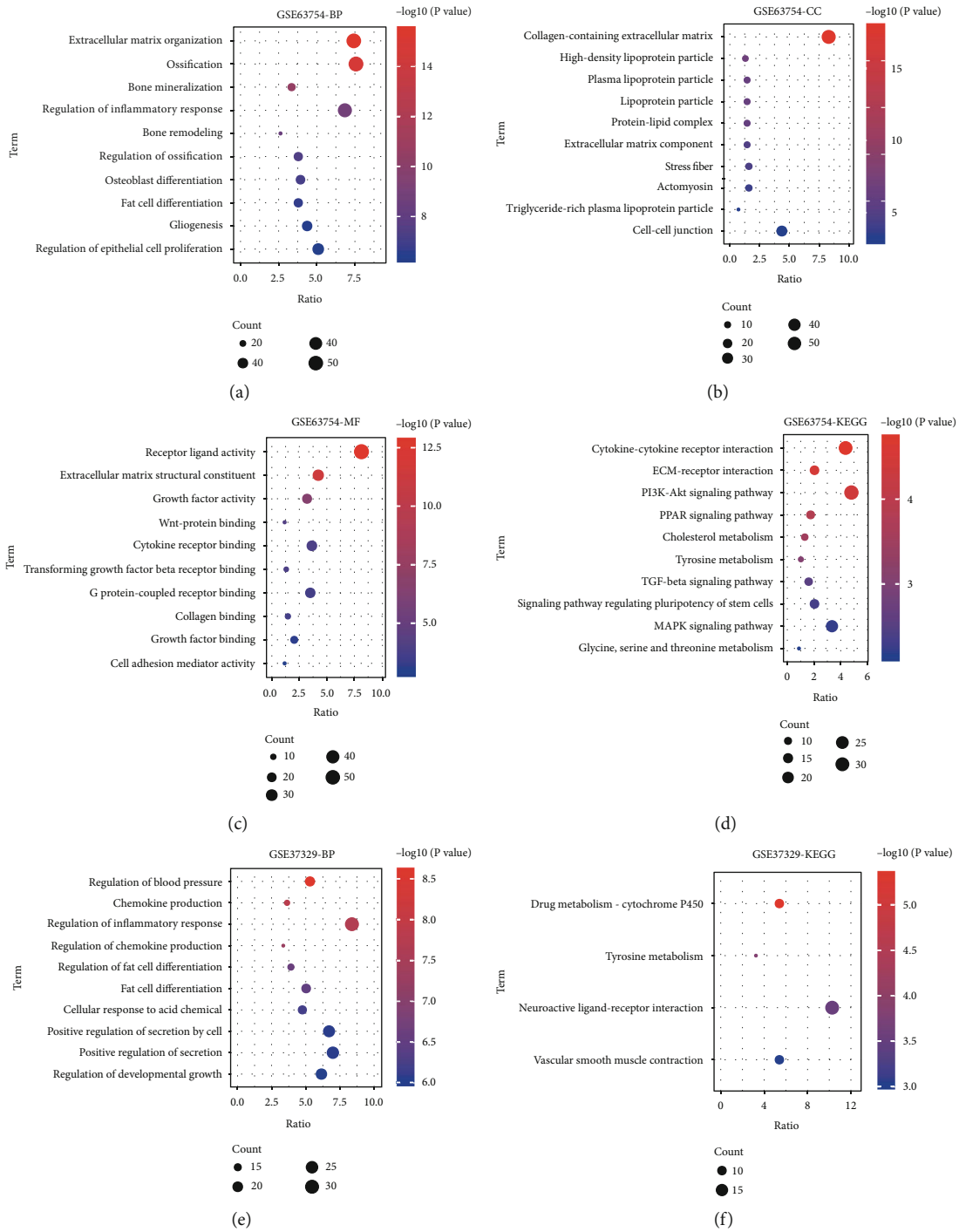

Figure 2: Continued.

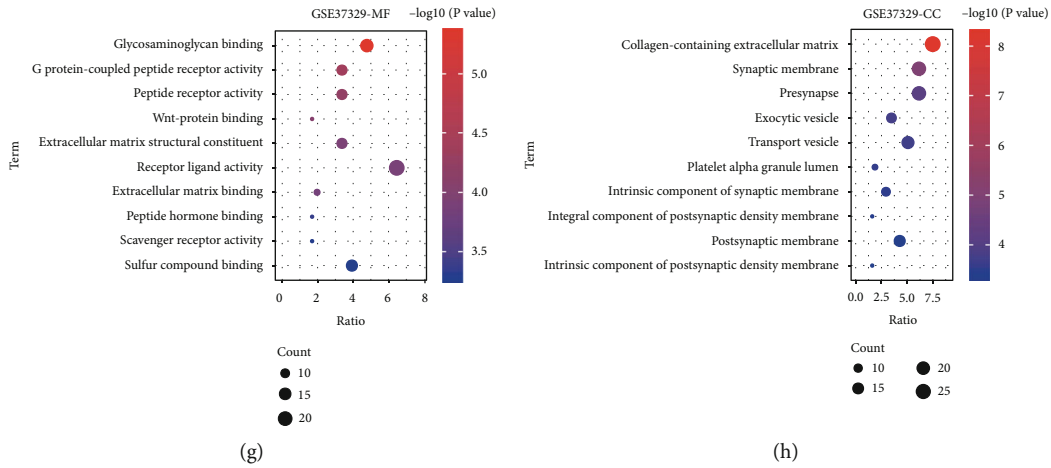

Figure 2: GO and KEGG pathway enrichment analysis. (a–h) Gene Ontology (GO) analysis and enriched KEGG signaling pathways were selected to demonstrate the primary biological actions of major potential genes. Colors represent the significance of differential enrichment, the size of the circles represents the number of genes, the larger the circle, the greater the number of genes. In the enrichment result, $P < 0.05$ or FDR < 0.05 is considered to be a meaningful pathway (enrichment score with −log10 (P) of more than 1.3). BP: biological process; CC: cellular component; MF: molecular function.

Table 1: Gene Ontology analyses of upregulated DEGs.

Ontology	ID	Description	GeneRatio	BgRatio	*P* value	*P*.adjust	*Q* value
BP	GO: 1903532	Positive regulation of secretion by cell	13/130	399/18670	4.36e-06	0.009	0.008
BP	GO: 0051047	Positive regulation of secretion	13/130	428/18670	9.27e-06	0.009	0.008
BP	GO: 0002532	Production of molecular mediator involved in inflammatory response	6/130	72/18670	1.09e-05	0.009	0.008
BP	GO: 0070542	Response to fatty acid	6/130	86/18670	3.03e-05	0.014	0.012
BP	GO: 0050727	Regulation of inflammatory response	13/130	485/18670	3.44e-05	0.014	0.012
CC	GO: 0034358	Plasma lipoprotein particle	4/134	37/19717	1.13e-04	0.012	0.011
CC	GO: 1990777	Lipoprotein particle	4/134	37/19717	1.13e-04	0.012	0.011
CC	GO: 0032994	Protein-lipid complex	4/134	39/19717	1.39e-04	0.012	0.011
CC	GO: 0099061	Integral component of postsynaptic density membrane	4/134	50/19717	3.69e-04	0.017	0.015
CC	GO: 0099146	Intrinsic component of postsynaptic density membrane	4/134	53/19717	4.61e-04	0.017	0.015
MF	GO: 0016709	Oxidoreductase activity	4/130	39/17697	1.87e-04	0.065	0.058
MF	GO: 0004745	Retinol dehydrogenase activity	3/130	20/17697	4.03e-04	0.070	0.063
MF	GO: 0004497	Monooxygenase activity	5/130	99/17697	8.16e-04	0.094	0.084
KEGG	hsa00982	Drug metabolism-cytochrome P450	8/66	71/8076	9.12e-08	1.48e-05	1.40e-05
KEGG	hsa00350	Tyrosine metabolism	5/66	36/8076	9.69e-06	7.85e-04	7.45e-04
KEGG	hsa00071	Fatty acid degradation	4/66	44/8076	4.32e-04	0.023	0.022
KEGG	hsa04979	Cholesterol metabolism	4/66	50/8076	7.07e-04	0.029	0.027
KEGG	hsa00830	Retinol metabolism	4/66	68/8076	0.002	0.073	0.069

profiles between ADSCSs before and after osteogenic induction by using GSEA. Figures 1(a)–1(c) show DEGs in GSE63754. Figures 1(d)–1(f) show DEGs in GSE37329.

3.2. GO and KEGG Pathway Enrichment Analysis. Through GO and KEGG analysis, we found that DEGs of GSE63754, extracellular matrix organization, ossification, bone mineralization, regulation of inflammatory response, and bone remodeling were mainly showed enrichment in the biological process (BP) categories. As for cellular component (CC) categories, collagen-containing extracellular matrix, high-density lipoprotein particle, plasma lipoprotein particle, plasma lipoprotein particle, and protein-lipid complex were detected; and in molecular function (MF), receptor ligand activity, extracellular matrix structural constituent, growth factor activity, Wnt-protein binding, and cytokine receptor binding. With regard to KEGG pathway, cytokine-cytokine receptor interaction, ECM-receptor interaction, PI3K-Akt signaling pathway, PPAR

Table 2: Gene Ontology analyses of downregulated DEGs.

Ontology	ID	Description	GeneRatio	BgRatio	*P* value	*P*.adjust	*Q* value
BP	GO: 0010721	Negative regulation of cell development	12/66	344/18670	2.55e-09	5.10e-06	3.85e-06
BP	GO: 0060537	Muscle tissue development	12/66	408/18670	1.71e-08	1.71e-05	1.29e-05
BP	GO: 0014706	Striated muscle tissue development	11/66	390/18670	1.10e-07	7.34e-05	5.54e-05
BP	GO: 0050768	Negative regulation of neurogenesis	9/66	295/18670	9.14e-07	4.57e-04	3.45e-04
BP	GO: 0051961	Negative regulation of nervous system development	9/66	315/18670	1.57e-06	6.29e-04	4.75e-04
CC	GO: 0005913	Cell-cell adherens junction	4/66	117/19717	6.39e-04	0.026	0.024
CC	GO: 0045121	Membrane raft	6/66	315/19717	6.44e-04	0.026	0.024
CC	GO: 0098857	Membrane microdomain	6/66	316/19717	6.55e-04	0.026	0.024
CC	GO: 0098589	Membrane region	6/66	328/19717	7.95e-04	0.026	0.024
CC	GO: 0016342	Catenin complex	2/66	29/19717	0.004	0.092	0.084
MF	GO: 0045499	Chemorepellent activity	4/63	27/17697	2.41e-06	5.22e-04	4.61e-04
MF	GO: 0001158	Enhancer sequence-specific DNA binding	5/63	119/17697	6.50e-05	0.005	0.005
MF	GO: 0030215	Semaphorin receptor binding	3/63	23/17697	7.24e-05	0.005	0.005
MF	GO: 0035326	Enhancer binding	5/63	133/17697	1.10e-04	0.006	0.005
MF	GO: 0005539	Glycosaminoglycan binding	6/63	229/17697	1.61e-04	0.007	0.006
KEGG	hsa04550	Signaling pathways regulating pluripotency of stem cells	5/40	143/8076	6.48e-04	0.064	0.061
KEGG	hsa04350	TGF-beta signaling pathway	4/40	94/8076	0.001	0.064	0.061

signaling pathway, and cholesterol metabolism were the top pathways involved in the osteogenic differentiation of ADSCs (Figures 2(a)–2(d)). Gene Ontology analyses of upregulated and downregulated DEGs are listed in Tables 1 and 2.

In GSE37329 dataset, regulation of blood pressure, chemokine production, regulation of inflammatory response, regulation of chemokine production, and regulation of fat cell differentiation were detected in BP. In CC categories, we found collagen-containing extracellular matrix, synaptic membrane, presynapse, exocytic vesicle, and transport vesicle were mainly shown. As for MF, glycosaminoglycan binding, G protein-coupled peptide receptor activity, peptide receptor activity, Wnt-protein binding, and extracellular matrix structural constituent were figured out. The results of KEGG pathway demonstrated that drug metabolism-cytochrome P450, tyrosine metabolism, neuroactive ligand-receptor interaction, and vascular smooth muscle contraction were important in the osteogenic differentiation of ADSCs (Figures 2(e)–2(h)).

3.3. Overlapping DEGs of Datasets. The commonly and differentially expressed genes in GSE63754 and GSE37329 during osteogenic differentiation of ADSCs were identified ($P < 0.05$ and log2 fold change $(\log 2\mathrm{FC}) > 1$ or < -1). To investigate the biological classification of the 142-overlapping upregulated DEGs and 69-overlapping downregulated DEGs, DAVID and MetADSCsape software packages were used to identify genes in the two datasets. In 142 upregulated overlapping DEGs, we found that positive regulation of secretion and positive regulation and fatty acid degradation were in the center of GO network. In 69-overlapping downregulated DEGs, striated muscle tissue development and muscle tissue development were significantly different (Figures 3(a)–3(d)).

3.4. Key Candidate Gene Identification with DEG PPI Network. Based on the STRING online database and Cytoscape software, DEG protein–protein interaction (PPI) network complex was constructed. We collected 142-overlapping upregulated DEGs and 69-overlapping downregulated DEGs to create the PPI network. The central node genes might potentially play an important role in regulating ADSC osteogenic differentiation (Figure 4).

4. Discussion

In the field of tissue engineering, the use of biocompatible scaffolds has increased in recent years [22]. The ability to self-renew, the proliferation potential, and the multipotency of ADSCs make them attractive for regenerative medicine applications [23, 24]. Since ADSCs are readily available and easy to obtain in large quantities, they have become promising seed cells for bone tissue engineering [25]. In order for ADSC-based therapies to be successful in vivo, they must be paired with a substance that facilitates their osteogenic differentiation in vivo [26]. Thus, it is critical that we understand the molecular mechanisms that underlie osteogenic differentiation in ADSCSs.

We firstly analyses GSE63754 (3 undifferentiated ADSCs and 3 osteogenic differentiated ADSCs) and GSE37329 (3 ADSCs and 2 ADSC-derived osteocytes). Because of this study, we found 211 significant DEGs common to both microarrays (142 upregulated and 69 downregulated). The most enrichment is extracellular matrix organization in the BP category. The extracellular matrix is an active factor in cellular differentiation, and modifying its composition can greatly influence osteogenic differentiation of mesenchymal stem cells (Hwang et al., 2015). Other BP, such as ossification, bone mineralization, regulation of inflammatory response, and bone

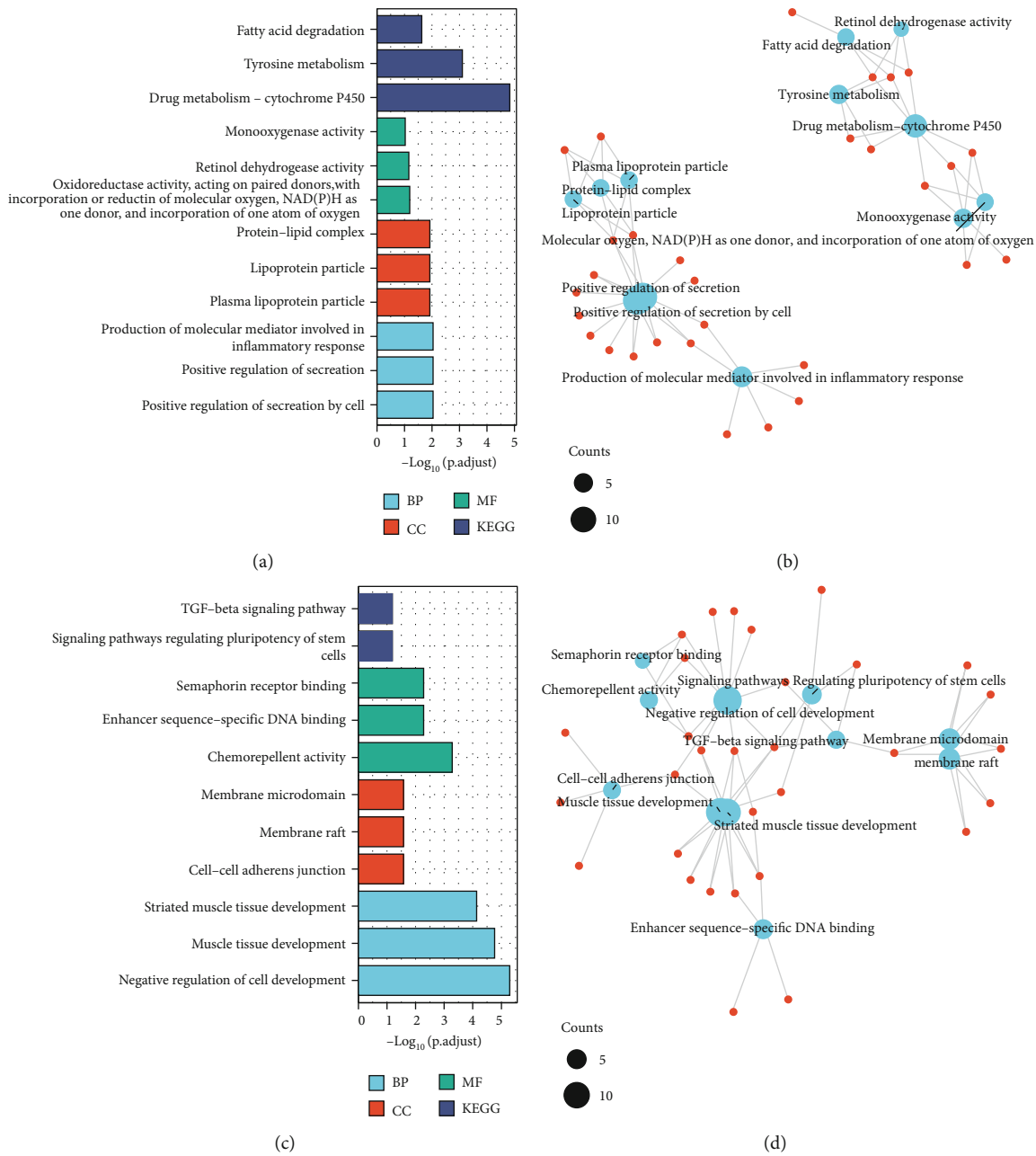

Figure 3: Overlapping DEGs of datasets. (a–d) Gene Ontology (GO) analysis and enriched KEGG signaling pathways were selected to demonstrate the primary biological actions of major potential genes. Colors represent the significance of differential enrichment, the size of the circles represents the number of genes, the larger the circle, the greater the number of genes. In the enrichment result, $P < 0.05$ or FDR < 0.05 is considered to be a meaningful pathway (enrichment score with –log10 (P) of more than 1.3). BP: biological process; CC: cellular component; MF: molecular function.

remodeling, were also showed enrichment. ADSCSs undergo osteogenic differentiation, thus, a regulation of genes negatively related to cell proliferation is observed.

In CC categories, collagen-containing extracellular matrix, high-density lipoprotein particle, plasma lipoprotein particle, plasma lipoprotein particle, and protein-lipid complex showed the highest enrichment score. It is interesting to note that two of the top eight CCs that are highly associated with ADSCS osteogenic differentiation are either located in the extracellular space or are located in the cell membrane, indicating that cell-to-cell signaling plays a crucial role in osteogenic differentiation. In MF categories, except chemorepellent activity, enhancer sequence-specific DNA binding, and semaphorin receptor binding, Wnt-protein binding and Wnt-activated receptor activity are most important factors. ADSCs differentiate into osteoblasts through Wnt proteins, and bone formation occurs via these proteins. It is possible that disrupting Wnt signaling pathway might significantly affect bone regeneration and remodeling [27–29]. ADSCs differ in their osteogenic differentiation in response

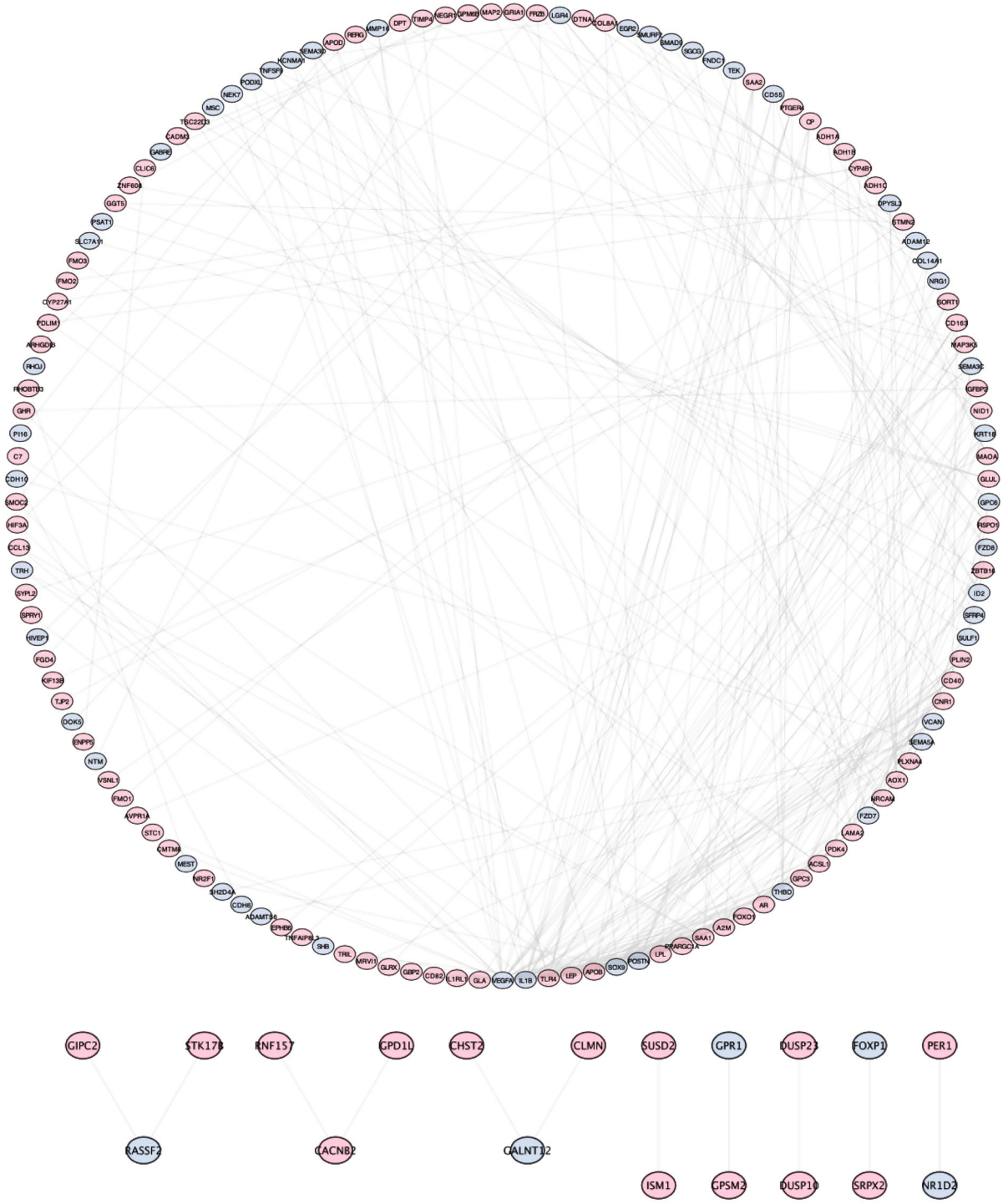

Figure 4: Key candidate gene identification with DEG PPI network. PPI network of the common significant differentially expressed genes was constructed. A total of 142-overlapping upregulated DEGs and 69-overlapping downregulated DEGs were identified by Cytoscape. PPI: protein–protein interaction.

to a variety of signaling pathways, including ERK1/2, Wnt, PI3K/Akt, and BMP-Smad. These proteins enable ADSCs to differentiate into osteoblasts and lead to bone formation. In KEGG pathway, the top significantly changed pathways of upregulated genes are related to drug metabolism-cytochrome P450, tyrosine metabolism, fatty acid degradation, cholesterol metabolism, retinol metabolism, and PPAR signaling pathway. ADSCSs that differentiate into osteoblasts have downregulated genes influenced by the adipogenesis pathway.

ADSCs were targeted by several pathways which affected osteogenic differentiation and, as a result, affected bone formation. In our study, we constructed a PPI network which is composed of the associated genes. PODXL is a negatively charged sialic acid glycoprotein, belonging to the type I transmembrane glycoprotein, which has been reported to be associated with poor prognosis in oral squamous cell carcinoma, colon cancer, glioblastoma, and breast cancer and has an impact on cell adhesion and migration. It has a promoting effect, and PODXL is an important condition for maintaining the stability of the pod cytoskeleton [30]. SEMA3D is a member of the class III semaphorin family and is a marker of osteoarthritis. Class III semaphorins are involved in normal bone homeostasis and bone pathology and have a complex relationship between osteoblasts and osteoclasts which has the potential to treat bone disease [31]. The ADGRG6 single nucleotide polymorphism is associated with human height, and its deletion in osteoblasts may delay osteoblast differentiation and bone formation, resulting in shortened body length and reduced bone mass in mice [32–34]. CADM3 is an immunoglobulin adhesion molecule belonging to the Nectin molecule-like family of proteins [35]. The constitutive expression level of RERG in calvaria was 1000-fold higher than in femoral osteoblasts; during osteogenic induction, RERG expression was downregulated in calvarial osteoblasts and upregulated in femoral osteoblasts [20]. The osteocytes of the skull are fundamentally different from those of the femur and respond differently to a range of stimuli. These site-specific differences may have important implications in developing strategies to address metabolic bone disease [36]. APCDD1 is an inhibitor of Wnt signaling pathway, which can promote the adipogenic differentiation and lipid anabolism of bone marrow stromal cells [37]. NRCAM may modulate geometric parameters of the femoral neck and contribute to an improved understanding of osteoporosis and pathophysiological mechanisms [38, 39]. The target genes supported by these literatures are related to bone homeostasis, osteogenic differentiation, bone diseases, and metabolism, which supports the feasibility of this study to explore the underlying molecular mechanisms during the osteogenic differentiation of adipose-derived stem cells [40].

The drawback of our study is the lack of functional cellular and animal experiments for validation to explore the occurrence, development, and molecular biology of osteogenic differentiation of ADSCs. In conclusion, based on two transcript profile data on osteogenic differentiation between ADSCs and noninduced ADSC datasets and comprehensive analysis, we have identified several genes and pathways that could be crucial to osteogenic differentiation of ADSCs. Understanding of how ADSCs differentiate into osteoblasts could be improved significantly by our new findings. Moreover, manipulation of these genes and pathways may lead to bone regeneration and tissue engineering.

Data Availability

All the data in this manuscript can be acquired by request.

Conflicts of Interest

The authors declare that they there is no conflicts of interest.

References

[1] J. H. Cheng, C. C. Hsu, S. L. Hsu et al., "Adipose-derived mesenchymal stem cells-conditioned medium modulates the expression of inflammation induced bone morphogenetic protein-2, -5 and -6 as well as compared with shockwave therapy on rat knee osteoarthritis," *Biomedicine*, vol. 9, no. 10, 2021.

[2] X. Liu, G. Zhao, X. Huo et al., "Adipose-derived stem cells facilitate ovarian tumor growth and metastasis by promoting epithelial to mesenchymal transition through activating the TGF-β pathway," *Frontiers in Oncology*, vol. 11, article 756011, 2021.

[3] A. Soltani, M. Moradi, A. R. Nejad et al., "Adipose-derived stem cells: potentials, availability and market size in regenerative medicine," *Current Stem Cell Research & Therapy*, vol. 17, 2022.

[4] M. Maj, Ł. Kaźmierski, K. Balik et al., "Bladder cancer cells exert pleiotropic effects on human adipose-derived stem cells," *Life (Basel)*, vol. 12, no. 4, 2022.

[5] Q. Liu, L. Cen, S. Yin et al., "A comparative study of proliferation and osteogenic differentiation of adipose-derived stem cells on akermanite and β-TCP ceramics," *Biomaterials*, vol. 29, no. 36, pp. 4792–4799, 2008.

[6] Y. Ye, Y. Du, F. Guo, C. Gong, K. Yang, and L. Qin, "Comparative study of the osteogenic differentiation capacity of human bone marrow- and human adipose-derived stem cells under cyclic tensile stretch using quantitative analysis," *International Journal of Molecular Medicine*, vol. 30, no. 6, pp. 1327–1334, 2012.

[7] K. R. Hixon, D. B. Katz, J. A. McKenzie, A. N. Miller, F. Guilak, and M. J. Silva, "Cryogel scaffold-mediated delivery of adipose-derived stem cells promotes healing in murine model of atrophic non-union," *Frontiers in Bioengineering and Biotechnology*, vol. 10, article 851904, 2022.

[8] W. Oliva-Olivera, A. L. Gea, S. Lhamyani et al., "Differences in the osteogenic differentiation capacity of omental adipose-derived stem cells in obese patients with and without metabolic syndrome," *Endocrinology*, vol. 156, no. 12, pp. 4492–4501, 2015.

[9] J. Fan, J. Dai, F. Lu, and Y. Zhang, "Editorial: regulation mechanism of adipose-derived stem cells in differentiation and translation," *Frontiers in Physiology*, vol. 13, article 852275, 2022.

[10] K. Kornicka, K. Marycz, K. A. Tomaszewski, M. Maredziak, and A. Smieszek, "The effect of age on osteogenic and adipogenic differentiation potential of human adipose derived stromal stem cells (hASCs) and the impact of stress factors in the course of the differentiation process," *Oxidative Medicine and Cellular Longevity*, vol. 2015, Article ID 309169, 2015.

[11] W. K. Ko, D. N. Heo, H. J. Moon et al., "The effect of gold nanoparticle size on osteogenic differentiation of adipose-derived stem cells," *Journal of Colloid and Interface Science*, vol. 438, pp. 68–76, 2015.

[12] S. E. Kim, Y. P. Yun, K. S. Shim, K. Park, S. W. Choi, and D. H. Suh, "Effect of lactoferrin-impregnated porous poly(lactide-co-glycolide) (PLGA) microspheres on osteogenic differentiation of rabbit adipose-derived stem cells (rADSCs)," *Colloids and Surfaces. B, Biointerfaces*, vol. 122, pp. 457–464, 2014.

[13] L. Xia, K. Lin, X. Jiang et al., "Effect of nano-structured bioceramic surface on osteogenic differentiation of adipose derived stem cells," *Biomaterials*, vol. 35, no. 30, pp. 8514–8527, 2014.

[14] M. Nii, J. H. Lai, M. Keeney et al., "The effects of interactive mechanical and biochemical niche signaling on osteogenic differentiation of adipose-derived stem cells using combinatorial hydrogels," *Acta Biomaterialia*, vol. 9, no. 3, pp. 5475–5483, 2013.

[15] J. Li, Z. Li, S. Wang, J. Bi, and R. Huo, "Exosomes from human adipose-derived mesenchymal stem cells inhibit production of extracellular matrix in keloid fibroblasts via downregulating transforming growth factor-β2 and Notch-1 expression," *Bioengineered*, vol. 13, no. 4, pp. 8515–8525, 2022.

[16] Y. K. Jeon, M. J. Bae, J. I. Kim et al., "Expression of glucagon-like peptide 1 receptor during osteogenic differentiation of adipose-derived stem cells," *Endocrinol Metab (Seoul)*, vol. 29, no. 4, pp. 567–573, 2014.

[17] X. Shi, X. Shao, B. Liu et al., "Genome-wide screening of functional long noncoding RNAs in the epicardial adipose tissues of atrial fibrillation," *Biochimica et Biophysica Acta - Molecular Basis of Disease*, vol. 1866, no. 7, article 165757, 2020.

[18] S. Y. Choi, M. S. Song, P. D. Ryu, A. T. Lam, S. W. Joo, and S. Y. Lee, "Gold nanoparticles promote osteogenic differentiation in human adipose-derived mesenchymal stem cells through the Wnt/β-catenin signaling pathway," *International Journal of Nanomedicine*, vol. 10, pp. 4383–4392, 2015.

[19] X. Hu, X. Zhang, L. Dai et al., "Histone deacetylase inhibitor trichostatin A promotes the osteogenic differentiation of rat adipose-derived stem cells by altering the epigenetic modifications on Runx2 promoter in a BMP signaling-dependent manner," *Stem Cells and Development*, vol. 22, no. 2, pp. 248–255, 2013.

[20] L. De Girolamo, M. F. Sartori, E. Arrigoni et al., "Human adipose-derived stem cells as future tools in tissue regeneration: osteogenic differentiation and cell-scaffold interaction," *The International Journal of Artificial Organs*, vol. 31, no. 6, pp. 467–479, 2008.

[21] A. C. de Paula, A. A. C. Zonari, T. M. . M. Martins et al., "Human serum is a suitable supplement for the osteogenic differentiation of human adipose-derived stem cells seeded on poly-3-hydroxibutyrate-co-3-hydroxyvalerate scaffolds," *Tissue Engineering. Part A*, vol. 19, no. 1-2, pp. 277–289, 2013.

[22] M. Brisset, R. Ben Yaou, R. Y. Carlier et al., "X-linked Emery-Dreifuss muscular dystrophy manifesting with adult onset axial weakness, camptocormia, and minimal joint contractures," *Neuromuscular Disorders*, vol. 29, no. 9, pp. 678–683, 2019.

[23] W. Jiang, J. Zhang, X. Zhang, C. Fan, and J. Huang, "VAP-PLGA microspheres (VAP-PLGA) promote adipose-derived stem cells (ADSCs)-induced wound healing in chronic skin ulcers in mice via PI3K/Akt/HIF-1α pathway," *Bioengineered*, vol. 12, no. 2, pp. 10264–10284, 2021.

[24] X. Liu, Q. Feng, A. Bachhuka, and K. Vasilev, "Surface modification by allylamine plasma polymerization promotes osteogenic differentiation of human adipose-derived stem cells," *ACS Applied Materials & Interfaces*, vol. 6, no. 12, pp. 9733–9741, 2014.

[25] R. Vij, K. A. Stebbings, H. Kim, H. Park, and D. Chang, "Safety and efficacy of autologous, adipose-derived mesenchymal stem cells in patients with rheumatoid arthritis: a phase I/IIa, open-label, non-randomized pilot trial," *Stem Cell Research & Therapy*, vol. 13, no. 1, p. 88, 2022.

[26] H. Gu, Z. Huang, X. Yin et al., "Role of c-Jun N-terminal kinase in the osteogenic and adipogenic differentiation of human adipose-derived mesenchymal stem cells," *Experimental Cell Research*, vol. 339, no. 1, pp. 112–121, 2015.

[27] B. Krief, S. W. Algor, I. Nakdimon et al., "Retinal lineage therapeutic specific effect of human orbital and abdominal adipose-derived mesenchymal stem cells," *Stem Cells International*, vol. 2021, Article ID 7022247, 15 pages, 2021.

[28] S. Yang, S. Guo, S. Tong, and X. Sun, "Promoting osteogenic differentiation of human adipose-derived stem cells by altering the expression of exosomal miRNA," *Stem Cells International*, vol. 2019, Article ID 1351860, 15 pages, 2019.

[29] M. Sattary, M. Rafienia, M. Kazemi, H. Salehi, and M. Mahmoudzadeh, "Promoting effect of nano hydroxyapatite and vitamin D3 on the osteogenic differentiation of human adipose-derived stem cells in polycaprolactone/gelatin scaffold for bone tissue engineering," *Materials Science & Engineering. C, Materials for Biological Applications*, vol. 97, pp. 141–155, 2019.

[30] L. Feng, J. Zhou, B. Xia, and B. F. Tian, "The positive effect of TET2 on the osteogenic differentiation of human adipose-derived mesenchymal stem cells," *Cellular Reprogramming*, vol. 22, no. 1, pp. 3–13, 2020.

[31] S. H. Hong, J. Nam, H. J. Kim, and J. J. Yoo, "Platelet-rich plasma pretreatment on grit-blasted titanium alloy for enhanced osteogenic differentiation of human adipose-derived stem cells," *Clinics in Orthopedic Surgery*, vol. 11, no. 3, pp. 361–368, 2019.

[32] G. Ramazzotti, R. Fiume, F. Chiarini et al., "Phospholipase C-β1 interacts with cyclin E in adipose- derived stem cells osteogenic differentiation," *Advances in biological regulation*, vol. 71, pp. 1–9, 2019.

[33] G. F. Petersen, B. J. Hilbert, G. D. Trope, W. H. Kalle, and P. M. Strappe, "A paper-based scaffold for enhanced osteogenic differentiation of equine adipose-derived stem cells," *Biotechnology Letters*, vol. 37, no. 11, pp. 2321–2331, 2015.

[34] S. M. Mihaila, A. K. Gaharwar, R. L. Reis, A. Khademhosseini, A. P. Marques, and M. E. Gomes, "The osteogenic differentiation of SSEA-4 sub-population of human adipose derived stem cells using silicate nanoplatelets," *Biomaterials*, vol. 35, no. 33, pp. 9087–9099, 2014.

[35] Y. Luo, R. Ge, H. Wu et al., "The osteogenic differentiation of human adipose-derived stem cells is regulated through the let-7i-3p/LEF1/β-catenin axis under cyclic strain," *Stem Cell Research & Therapy*, vol. 10, no. 1, p. 339, 2019.

[36] B. Yan, S. Lv, P. Tong et al., "Intra-articular injection of adipose-derived stem cells ameliorates pain and cartilage anabolism/catabolism in osteoarthritis: preclinical and clinical evidences," *Frontiers in Pharmacology*, vol. 13, article 854025, 2022.

[37] M. Nahrendorf and F. K. Swirski, "Lifestyle effects on hematopoiesis and atherosclerosis," *Circulation Research*, vol. 116, no. 5, pp. 884–894, 2015.

[38] L. Labusca, D. D. Herea, A. Emanuela Minuti et al., "Magnetic nanoparticles and magnetic field exposure enhances chondrogenesis of human adipose derived mesenchymal stem cells but not of Wharton jelly mesenchymal stem cells," *Frontiers in Bioengineering and Biotechnology*, vol. 9, article 737132, 2021.

[39] L. Lv, Y. Liu, P. Zhang et al., "The nanoscale geometry of TiO_2 nanotubes influences the osteogenic differentiation of human adipose-derived stem cells by modulating H3K4 trimethylation," *Biomaterials*, vol. 39, pp. 193–205, 2015.

[40] M. S. Carvalho, L. Alves, I. Bogalho, J. M. S. Cabral, and C. L. da Silva, "Impact of donor age on the osteogenic supportive capacity of mesenchymal stromal cell-derived extracellular matrix," *Frontiers in Cell and Development Biology*, vol. 9, article 747521, 2021.

Hindawi
Disease Markers
Volume 2022, Article ID 5160624, 10 pages
https://doi.org/10.1155/2022/5160624

Research Article

Protein Tyrosine Phosphatase Receptor Type R (PTPRR) Reduces AChR Clustering by Dephosphorylating MuSK

Yanxun Chen,[1] **Maohao Guan**,[2] **Fengqiang Yu**,[2] **Zhongshan Yang**,[2] **Weiqiang Yi**,[2] **Xuan Huang**,[2] **Ruiqin Qiu**,[2] **and Fancai Lai**[2]

[1]*Department of Thoracic Surgery, Quangang General Hospital, The First Affiliated Hospital of Fujian Medical University, Quanzhou, Fujian Province, China*
[2]*Department of Thoracic Surgery, The First Affiliated Hospital of Fujian Medical University, Fuzhou, Fujian Province, China*

Correspondence should be addressed to Fancai Lai; laifancai@fjmu.edu.cn

Received 12 June 2022; Revised 7 August 2022; Accepted 10 August 2022; Published 5 September 2022

Academic Editor: Jun Yang

Neuromuscular junction (NMJ) formation and maintenance depend on the proper localization and concentration of various molecules at synaptic contact sites. Acetylcholine receptor (AChR) clustering on the postsynaptic membrane is a cardinal event in NMJ formation. Muscle-specific tyrosine kinase (MuSK), which functions depending on its phosphorylation, plays an essential role in AChR clustering. In the present study, we used plasmid-based biochemical screening and determined that protein tyrosine phosphatase receptor type R (PTPRR) is responsible for dephosphorylating MuSK on tyrosine residue 754. Furthermore, we showed that PTPRR significantly reduced MuSK-dependent AChR clustering in C2C12 myotubes. Collectively, these data illustrate a negative regulation function of PTPRR in AChR clustering.

1. Introduction

The neuromuscular junction (NMJ) is a chemical synapse between motoneurons and muscle fibers and consists of neuronal presynaptic membranes, a synaptic cleft and muscle postsynaptic membranes [1, 2]. The fast and accurate neuromuscular transmissions between presynaptic and postsynaptic membranes rely on highly concentrated acetylcholine receptors (AChRs) at the postsynaptic membranes [3, 4]. In vertebrates, high-density clusters of AChRs are orchestrated by various effector molecules and an intricate network of signaling pathways.

Muscle-specific tyrosine kinase (MuSK), a transmembrane and tyrosine phosphorylated protein, plays a vital role in the clustering of AChRs and is indispensable in both the formation and maintenance of NMJs [5]. MuSK is activated by motoneuron-released agrin, which is prone to aggregation at synaptic basal lamina and binds with low-density lipoprotein receptor-related protein 4 (LRP4) to form the tetrameric agrin-LRP4 complex at postsynaptic membranes [6]. This supercomplex induces the dimerization and autophosphorylation of MuSK. Phosphorylated MuSK recruits intracellular downstream of kinase 7 (Dok-7), which stabilizes and phosphorylates MuSK [7–9]. Tyrosine phosphorylation of MuSK ultimately leads to AChR clustering at postsynaptic membranes.

MuSK exerts physiological functions depending on its phosphorylation. Impairments of MuSK phosphorylation have been associated with several disorders, such as myasthenia gravis (MG) and congenital myasthenia (CMS) [10, 11]. The process of a kinase phosphorylation and dephosphorylation is coordinated in the regulation of signaling responses [12]. As previously noted, the auto- and trans-phosphorylation of MuSK depends on its dimerization activated by LRP4 and Dok-7. However, which phosphatases dephosphorylate MuSK and mediate the formation of AChR clustering is still unclear.

In the present study, we determined via a plasmid-based biochemical screening that protein tyrosine phosphatase receptor type R (PTPRR) dephosphorylates MuSK on

tyrosine residue 754. Furthermore, we showed that PTPRR significantly reduced MuSK-dependent AChR clustering in C2C12 myotubes. Collectively, these data illustrate a negative regulatory function of PTPRR in AChR clustering.

2. Results

2.1. C2C12 Myotubes Represent an Excellent Experimental Model System for Studying Agrin-Induced AChR Clustering. Prior research has shown that C2C12 myotubes provide an excellent experimental model to examine whether certain synaptic proteins are associated with AChR clustering in muscles. We examined the distribution of AChRs in C2C12 myotubes exposed to increasing concentrations of agrin for 24 h. The agrin concentration gradient (0, 0.3, 0.6, 2.5, 5, 10, and 20ng/ml) was set to determine the optimal concentration. AChRs were visualized and measured via labeling with Alexa Fluor 555 α-bungarotoxin (α-BTX) for 1 h.

As indicated in Figure 1, C2C12 myotubes expressed infrequent AChR clusters ($\geq 5\,\mu$m in length) in the absence of agrin. The addition of 0.3 ng/ml to 10 ng/ml agrin induced AChR clustering in a dose-dependent manner. However, C2C12 myotubes treated with 10 ng/ml and 20 ng/ml agrin did not demonstrate a significant difference. Treatment with 20 ng/ml agrin for 24 h increased the AChR cluster length almost 14.7-fold, and the number of AChR clusters (within a 1 mm tube) increased almost 11-fold compared with untreated myotubes (Figures 1(a) and 1(b)). These results indicated that we successfully constructed a C2C12 myotube experimental model system for studying agrin-induced AChR clustering. Furthermore, the optimal agrin concentration was defined as 10 ng/ml, and this concentration was used in the following experiments.

2.2. MuSK Is Essential in the Mediation of AChR Clustering. To verify the role of MuSK in agrin-induced AChR clustering, *MuSK* knockout (*MuSK*$^{-}$) single clone C2C12 was constructed using the CRISPR/Cas9 system. The efficiency of *MuSK*$^{-}$ was validated by western blot (Figure 2(a)), which showed notable decreased expression in *MuSK*$^{-}$ compared with that in wild-type C2C12. *MuSK*$^{-}$ single clone C2C12 generated by CRISPR sgRNA2 was chosen for this study. After treatment with 10 ng/ml agrin for 24 h, *MuSK*$^{-}$ C2C12 completely abolished the agrin-induced AChR clusters compared with wild-type C2C12 myotubes (Figures 2(b) and 2(c)). These findings suggested that MuSK is essential in the mediation of AChR clustering.

2.3. PTPRR Was Identified as the Tyrosine Phosphatases Responsible for Dephosphorylation of MuSK. MuSK serves as a tyrosine phosphorylated protein and is inactivated by phosphatases. Therefore, we speculated that there might be several phosphatases responsible for MuSK dephosphorylation and that participate in the regulation of agrin-induced AChR clustering at postsynaptic membranes.

To verify the hypothesis, we performed a protein tyrosine phosphatases screening upon coexpression of 10 classical tyrosine phosphatases with Flag-MuSK in HEK293T cells. An empty vector plasmid (pcDNA3.1) was used as a control. After cotransfection with tyrosine phosphatase for 24 h, the phosphorylation of MuSK cotransfected with PTPRR was significantly decreased compared with that of the empty vector. In contrast, MuSK cotransfected with other phosphatases had relatively high levels of phosphorylation compared with that of the empty vector (Figure 3(a)). The various tyrosine phosphatases were probed and showed in Supplementary Figure S1.

In addition, we generated an Asp to Ala mutation for C-terminal residue 554 of PTPRR. The PTPRR-D554A mutant was a substrate-trapping mutant resulting in PTPRR lacking phosphatase activity. Wild-type PTPRR (PTPRR-WT) and PTPRR-D554A were transiently transfected with MuSK into HEK293T cells. MuSK was purified from cell lysates by immunoprecipitation with Flag-Beads, probed with 4G10 to reveal pY-MuSK, and probed with PTPRR to reveal the interaction between MuSK and PTPRR. Ectopic expression of PTPRR-WT, but not PTPRR-D554A, decreased the phosphorylation level of MuSK (Figure 3(b)). These results suggest that PTPRR may be the tyrosine phosphatase responsible for MuSK dephosphorylation.

2.4. PTPRR-Dephosphorylated MuSK-Tyr754. To determine the phosphorylated sites of MuSK, Flag-MuSK was overexpressed in HEK293T cells and purified from cell lysates by immunoprecipitation with Flag-Beads. Purified Flag-MuSK was detected by mass spectrometry. We identified Tyr-553, Tyr-750, Tyr-754, and Tyr-755 as the primary sites of MuSK phosphorylation (Figure 4(a)).

We generated Tyr to Phe triple mutations for C-terminal residues 750/754/755, 553/754/755, 553/750/755, and 553/750/754 of MuSK, which were cotransfected into HEK293T cells with PTPRR for 24 h. No phosphorylation was detected by pTyr (4G10) blotting for MuSK Y750/754/755F, Y553/754/755F, or Y553/750/754F (data not shown). MuSK Y553/750/755F, for which phosphorylation depends on Tyr754, showed attenuated phosphorylation compared with MuSK-WT. Additionally, we found that phospho-Tyr754 was dephosphorylated by PTPRR (Figure 4(b)). Unexpectedly, PTPRR profoundly diminished the phosphorylation of MuSK Y754F (Figure 4(c)). These results demonstrated that PTPRR could dephosphorylate MuSK-Tyr754.

2.5. PTPRR Significantly Reduced MuSK-Dependent AChR Clustering in C2C12 Myotubes. PTPRR expression in C2C12 myotubes was highest after one day of differentiation (Supplementary Figure S2). To verify the hypothesis that PTPRR inhibits agrin-induced AChR clustering, monoclonal C2C12 cell lines overexpressing PTPRR-WT, PTPRR-D554A, or empty vector (LW009) were constructed. The efficiency of overexpression PTPRR was verified by western blot (Figure 5(a)). Compared with AChR clusters of WT or PTPRR-D554A C2C12, PTPRR-WT C2C12 was markedly reduced in both the number and length (Figures 5(b) and 5(c)). These results indicate that PTPRR significantly reduced MuSK-dependent AChR clustering in C2C12 myotubes.

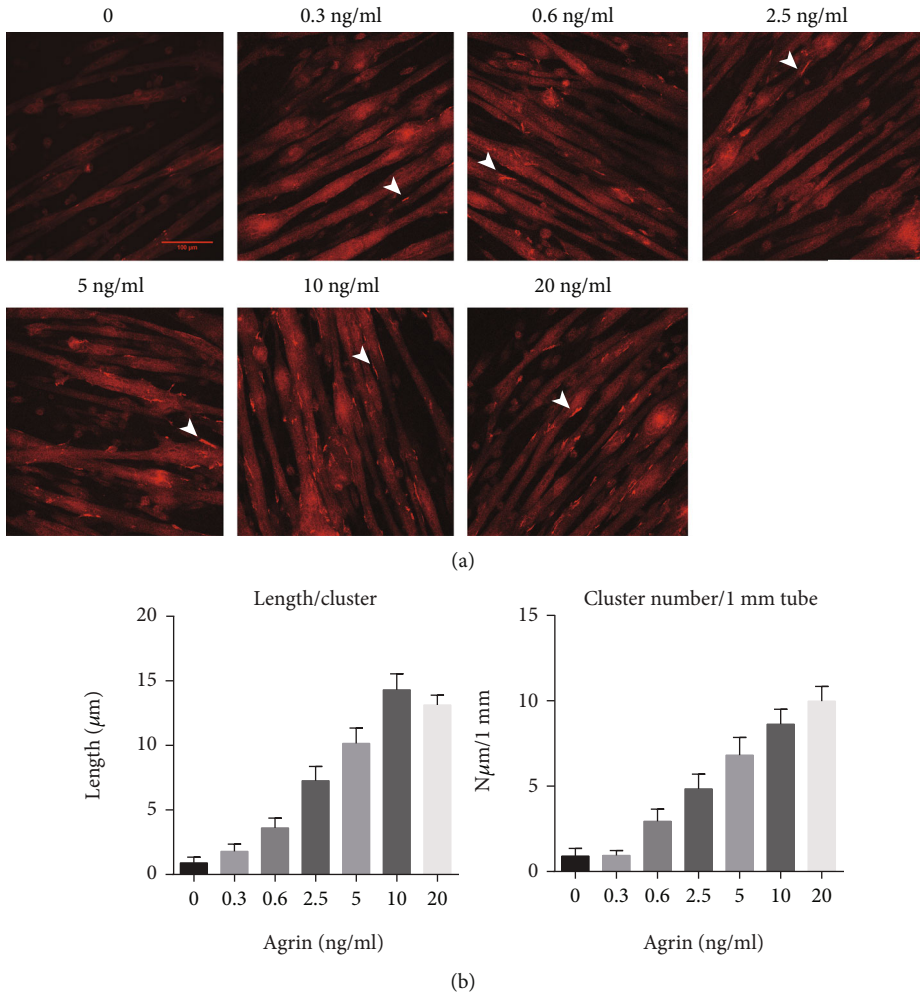

Figure 1: C2C12 myotubes provide an excellent experimental model system for studying agrin-induced acetylcholine receptor (AChR) clustering. (a) Wild-type C2C12 myotubes were incubated with increasing concentrations of agrin (0 to 20 ng/ml) for 24 h, and AChRs were labeled with Alexa Fluor 555 α-bungarotoxin. AChR clustering increased with increasing agrin concentrations (0 to 10 ng/ml). C2C12 myotubes treated with 10 ng/ml and 20 ng/ml agrin did not demonstrate a significant difference. White arrowheads indicate AChR clusters. (b) Quantification of AChR clusters $\geq 5\,\mu$m in length from Figure 1. The average length of each AChR cluster and the average number of AChR clusters within a 1 mm tube were quantified. The data were obtained from at least three experiments. Data were shown as mean ± S.D.

3. Discussion

The formation and maintenance of NMJs ensures the efficient transmission of synaptic signals. Many neuromuscular diseases that present as neurological disorders, including MG and CMS, are due to deficits in NMJ formation or maintenance. The first key event in NMJ formation and maintenance is a high concentration of AChRs in the postsynaptic membrane. The redistribution of AChRs in muscle is modulated by a series of molecules including agrin, LRP4, MuSK, Src, tyrosine kinases, and phosphatases [13].

In NMJ formation, muscle fibers form primitive AChR clusters prior to the arrival of motor nerve terminals in process called muscle prepatterning [14]. New clusters are induced, and those in nonsynaptic areas disperse as the nerve terminals innervate muscle fibers. Tyrosine phosphorylation, which accumulates in muscle prepatterning, has been demonstrated to play an important role in the generative stages of AChR clusters [15–17]. AChR clustering can be inhibited by tyrosine kinase inhibitors such as RG50864. Labeled phosphotyrosine disappears before AChR clusters disassembly at the sites where AChR clusters disperse [13]. This suggests that tyrosine phosphatases function in restricting the spread of the activated kinase signal and thereby disperse AChR clusters. Zhao et al. [18] showed that tyrosine phosphatase Shp-2 regulates agrin-induced AChR clustering in vitro. Other studies have reported that NSC-87877, a Shp-2-specific inhibitor, increases MuSK phosphorylation and protects AChRs from the effects of MG MuSK antibody [19]. Nevertheless, NMJ formation and maintenance appeared normal in mice with Shp-2 conditional knockout in skeletal muscle [20]. These findings suggest that there are other tyrosine phosphatases that regulate NMJ formation and maintenance in muscle.

MuSK is essential for NMJ formation during embryogenesis and maintenance in adults [5]. Impairment of MuSK

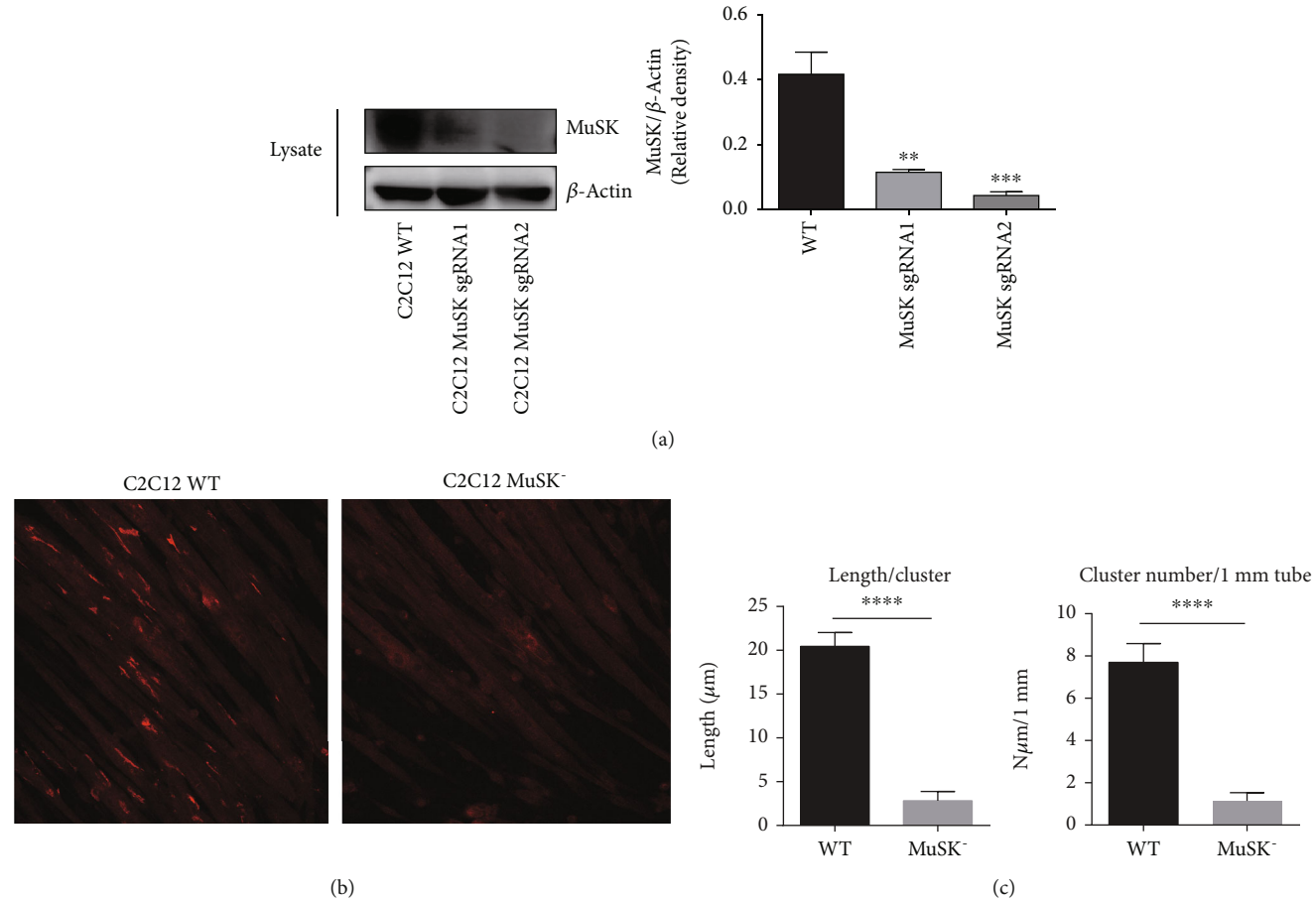

Figure 2: MuSK is an essential molecule that mediates AChR clustering. (a) The efficiency of *MuSK* knockout (*MuSK*$^{-}$) was validated by western blot. MuSK^{-} single clone C2C12 generated by CRISPR sgRNA2 was chosen for the following experiments. (b) Almost no clusters of AChRs were formed in *MuSK*$^{-}$ C2C12 myotubes compared with wild-type myotubes. White arrowheads indicate AChR clusters. (c) Quantification of AChR clusters $\geq 5\,\mu$m in length from (b). The data were obtained from at least three experiments. Data were shown as mean ± S.D. $^{**}P < 0.01$, $^{***}P < 0.001$, and $^{****}P < 0.0001$.

expression in adult mice leads to disassembly and destabilization of new synapses [21, 22]. Previous studies have shown that a MuSK mutation that impairs its kinase activity causes CMS [10]. Coincidentally, autoantibodies to MuSK are responsible for MuSK-dependent MG [11]. We found that conditional knockout of MuSK in C2C12 myotubes completely abolished the agrin-induced AChR clustering compared with wild-type myotubes. The intracellular region of MuSK contains four major tyrosine phosphorylation sites, three in the activation loop and one in the juxta-membrane region [23–26]. Here, we verified that MuSK tyrosine-553, tyrosine-750, tyrosine-754, and tyrosine-755 are the major tyrosine phosphorylation sites.

In this study, by combining the PTP substrate-trapping strategy with immunoprecipitation, we identified PTPRR as the tyrosine phosphatases responsible for dephosphorylating MuSK. PTPRR is a subfamily of classical PTPs and is considered as a tumor suppressor regulating proliferation or differentiation of cancer cells including oral squamous cell carcinoma, cervical cancer, breast tumor, and colorectal carcinomas [27–30]. We identified Tyr754 as the possible site of MuSK dephosphorylation by PTPRR through generating Tyr to Phe triple mutations for the C-terminal residues 553/750/755 of MuSK. Additionally, there are other candidate Tyr sites, considering that the Y754F mutation can still be dephosphorylated by PTPRR. However, these other candidate Tyr sites were hard to confirm by immunoblot because the triple mutations Y750/754/755F, Y553/754/755F, and Y553/750/754F did not show enough phosphorylation to detect. To confirm the candidate Tyr sites in future studies, we would perform MS analysis from C2C12 myotubes stably expressing PTPRR (active and inactive) to demonstrate MuSK dephosphorylation.

PTPRR-knockout mice display defects in motor coordination and balancing skills but display normal cerebellar morphological characteristics [31]. Using monoclonal C2C12 cell lines overexpressing PTPRR-WT or D554A, we found that PTPRR significantly reduced MuSK-dependent AChR clustering *in vitro*. The phenotype suggests that PTPRR-knockout mice may fail to form or maintain NMJs. However, it is a limitation for our study considering overexpressing PTPRR may cause artefacts or unphysiological response. Furthermore, Wang et al. [32] showed that PTPRR dephosphorylated and inactivated β-catenin as a tumor

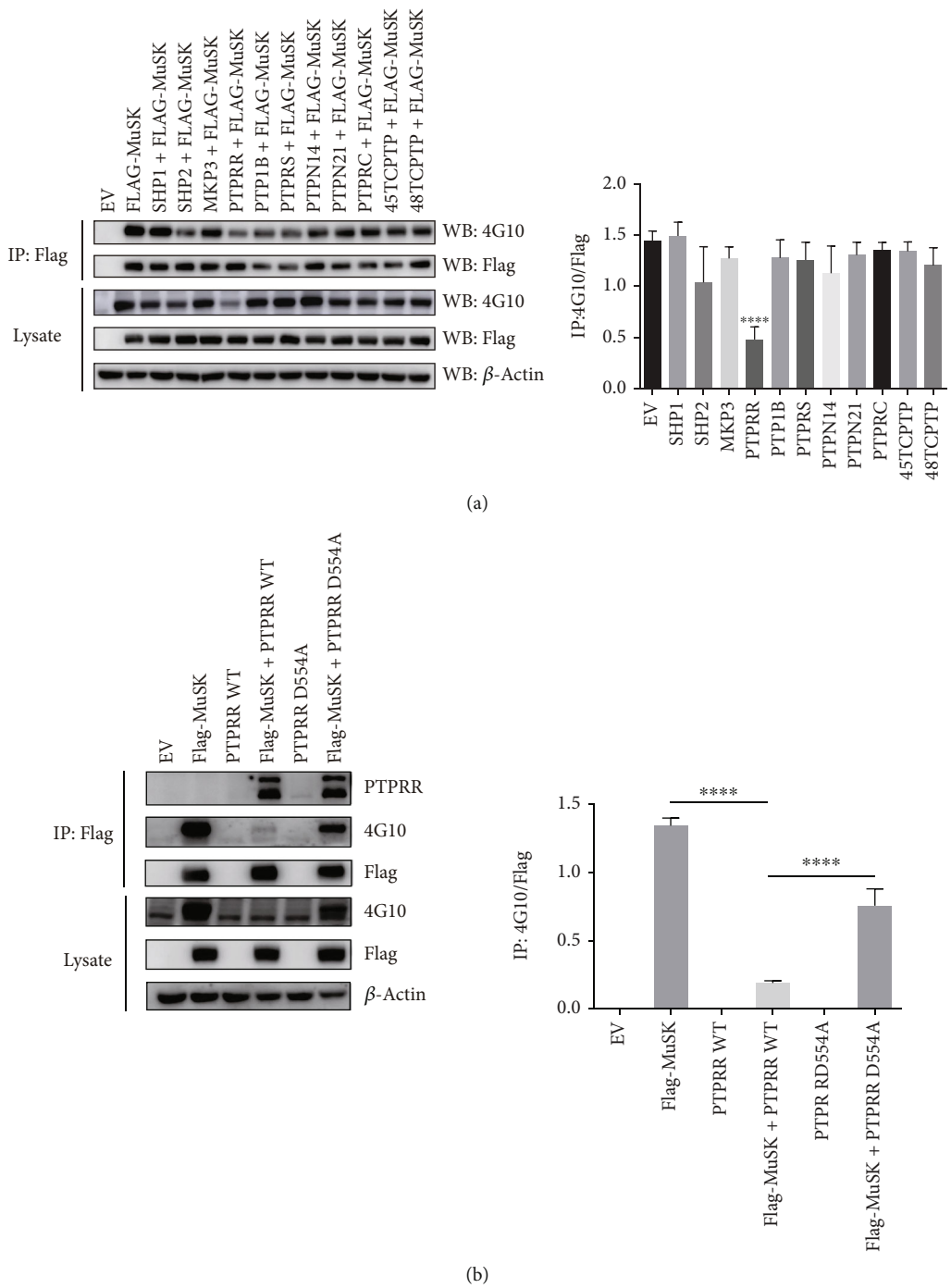

Figure 3: PTPRR was identified as the tyrosine phosphatases responsible for dephosphorylating MuSK via a protein tyrosine phosphatases screening. (a) HEK293T cells were cotransfected with flag-MuSK and 10 various tyrosine phosphatases as indicated. Tyrosine phosphorylation of MuSK and actin were probed. (b) HEK293T cells were transiently transfected with MuSK, PTPRR-WT, or PTPRR-DA mutant. MuSK was isolated by immunoprecipitation with anti-Flag antibody, probed with 4G10 to reveal pY-MuSK, and probed with PTPRR to reveal the interaction between MuSK and PTPRR. Lysates were probed with antibodies against MuSK, PTPRR, and β-actin. The data were obtained from at least three experiments. Data were shown as mean ± S.D. $^{****}P < 0.0001$.

suppressor in ovarian cancer. Another study reported that β-catenin played a negative role in AChR clustering at NMJs [33]. That study suggests that PTPRR may also regulate AChR clustering by dephosphorylating β-catenin. To solve this problem, the construction of mouse model of skeletal muscle-specific PTPRR-knockout and related-MS analysis would be performed for further study. The formation and maintenance of NMJs would also be studied.

In summary, during NMJ formation and maintenance, tyrosine phosphatases function in restricting the spread of activated MuSK and thereby regulate AChR clustering. We determined that PTPRR is responsible for dephosphorylating

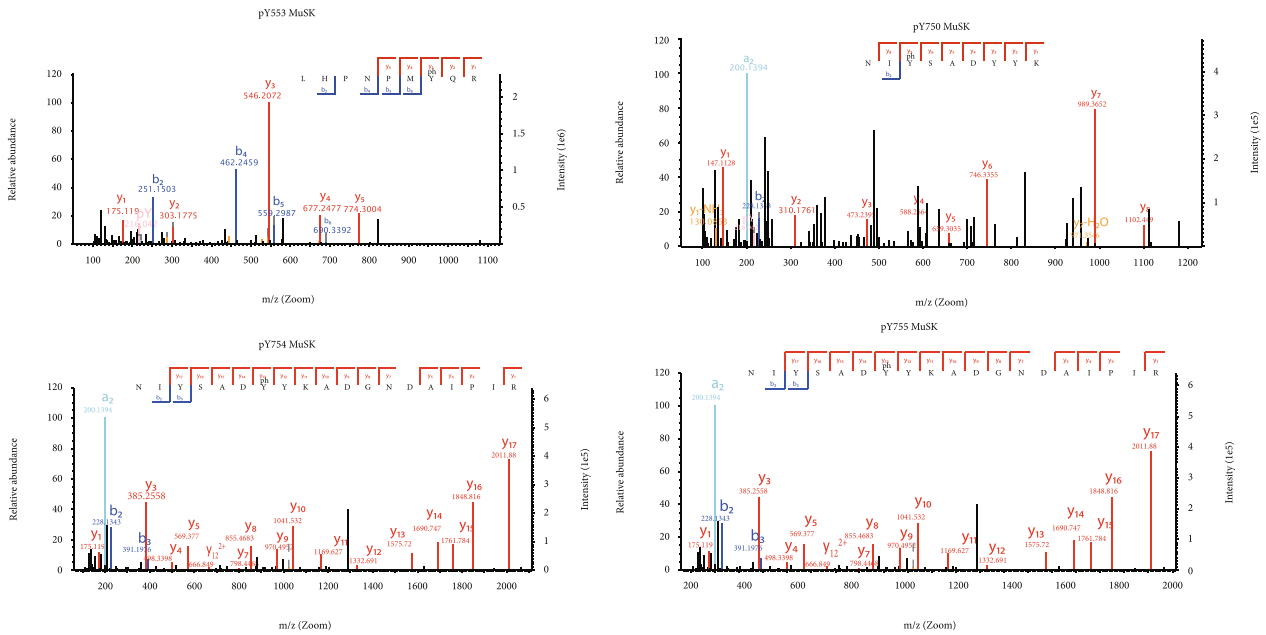

(a)

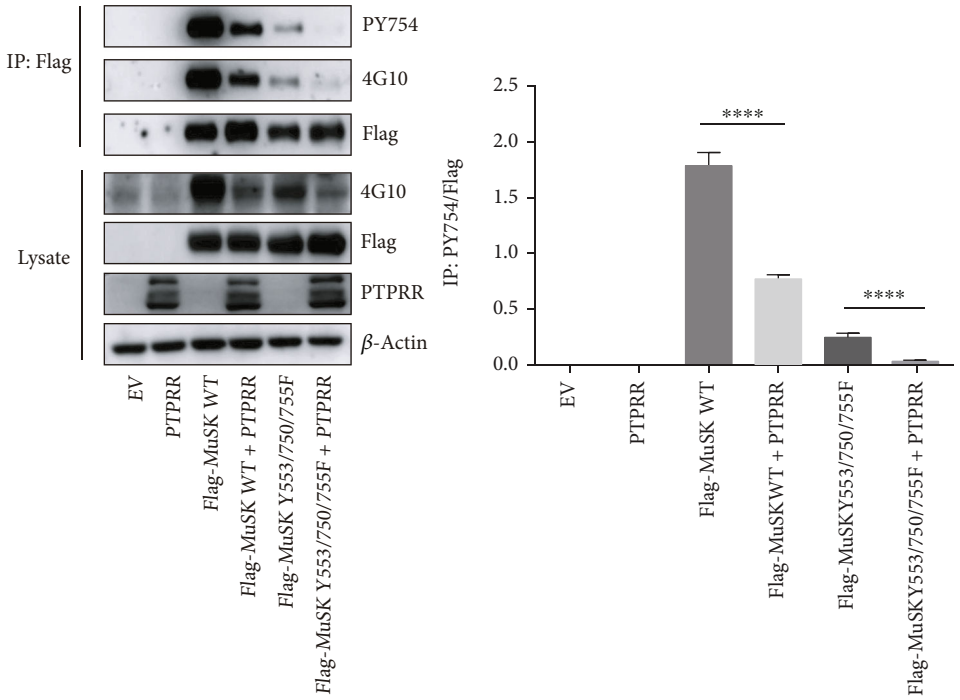

(b)

Figure 4: Continued.

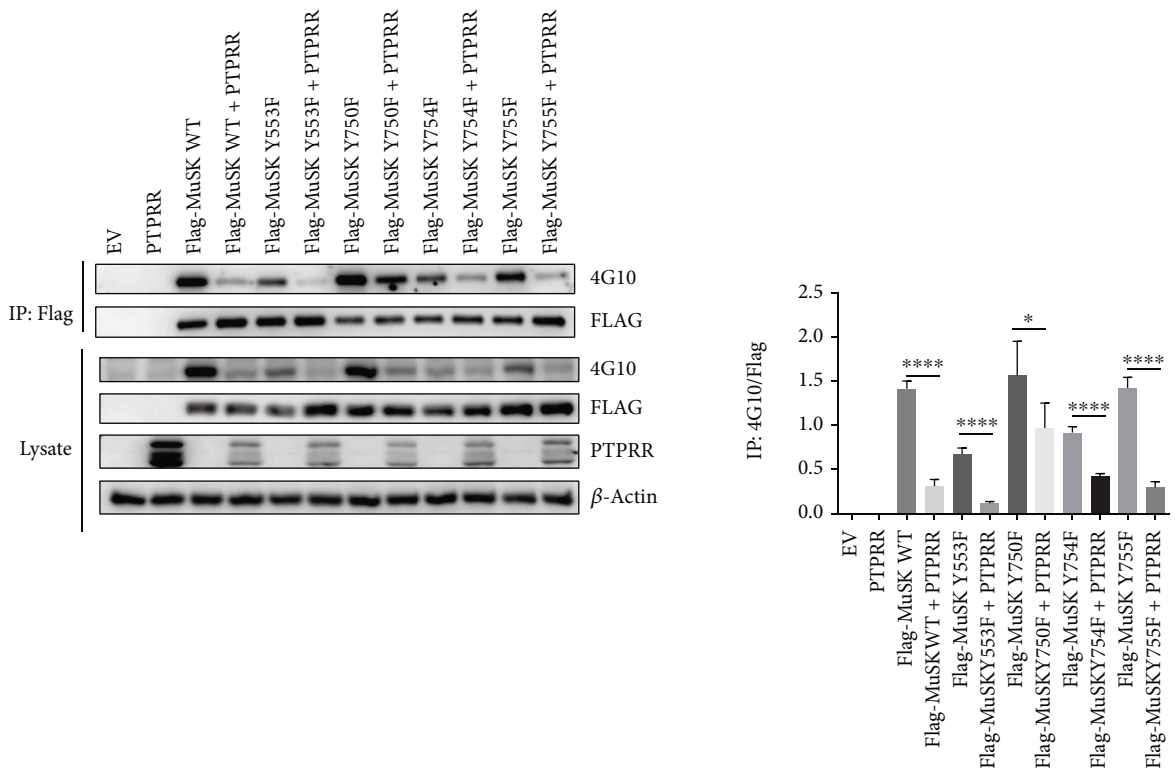

(c)

Figure 4: PTPRR dephosphorylated MuSK-Tyr754. (a) HEK293T cells were transiently transfected with Flag-MuSK or empty vector plasmids. Proteins were separated by SDS-PAGE and stained with Coomassie Blue. Bands corresponding to MuSK were excised, digested with trypsin, and analyzed by LC-MS. The LC peaks corresponding to the peptide fragments containing Tyr-553, Tyr-750, Tyr-754, and Tyr-755 in MuSK fractions were further analyzed by MS/MS. (b) HEK293T cells were transiently transfected with PTPRR, MuSK, or MuSK Y553/750/754F. MuSK was isolated by immunoprecipitation with anti-Flag antibody, probed with PY754 antibody to reveal pY-MuSK Y754, and probed with 4G10 to reveal total pY-MuSK. Lysates were probed with antibodies against MuSK, pY-MuSK, and β-actin. (c) HEK293T cells were transiently transfected with PTPRR, MuSK, MuSK Y553F, MuSK Y750F, MuSK Y754F, or MuSK Y755F. MuSK was isolated by immunoprecipitation with anti-Flag antibody and probed with 4G10 to reveal pY-MuSK. Lysates were probed with antibodies against MuSK, PTPRR, pY-MuSK, and β-actin. The data were obtained from at least three experiments. Data were shown as mean ± S.D. NS: no significant difference. $^{*}P < 0.05$ and $^{****}P < 0.0001$.

MuSK-Tyr754. Moreover, we have shown that PTPRR significantly reduced MuSK-dependent AChR clustering in vitro. Consequently, inhibition of PTPRR may improve MuSK activity and offer an improved strategy for therapeutic intervention in MG and CMS.

4. Method and Materials

4.1. Reagents and Antibodies. PrimeSTAR® GXL DNA Polymerase, Premix Taq™ DNA Polymerase, and PrimeScript™ RT Master Mix were from TaKaRa. TransIT®-2020 Transfection Reagent was from Mirusbio. Fetal bovine serum was from Cellgro. Horse serum was from Gibco. Anti-phosphotyrosine antibody (4G10) was from Merck/Millipore. Anti-Flag-monoclonal antibody was from GNI. Anti-PTPRR antibody was from Thermo Fisher. Anti-MuSK phosphotyrosine (phospho Y754) antibody was from Abcam. Anti-MuSK antibody and agrin were from R&D. Alexa Fluor 555-conjugated α-BTX was from Promokine.

4.2. Plasmids and Transfection. Site-directed mutagenesis of MuSK and PTPRR was executed following the Agilent protocol. Generated mammalian expression plasmids were MuSK Y553F, Y750F, Y754F, Y755F, Y750/754/755F, Y553/754/755F, Y553/750/755F, Y553/750/754F (pFlag-cmv-MuSK), and PTPRR D554A (pcDNA3.1). Transient transfection followed the Mirus manufacturer protocol (Transit-2020, Mirus). Cells were harvested 24 h after transfection for further experiments.

4.3. Infection and FACS Sorting. The PTPRR-WT and D554A cDNA were subcloned into the LWT009-GFP vector using BamHI/NOTI restriction sites. Construction of PTPRR-overexpression or sgRNA knockout cell lines was via lentiviral infection. Specifically, lentivirus expressing PTPRR-WT (LWT009-GFP), D554A (LWT009-GFP), or CAS9-BFP was generated in 293T cells by cotransfecting the corresponding vector, PAX2, and VSVG at a ratio of 2 : 1 : 1. Forty-eight hours after transfection, viral medium was harvested and then incubated with C2C12. After reaching 30% confluence, GFP^{+} or BFP^{+} cells were subsequently

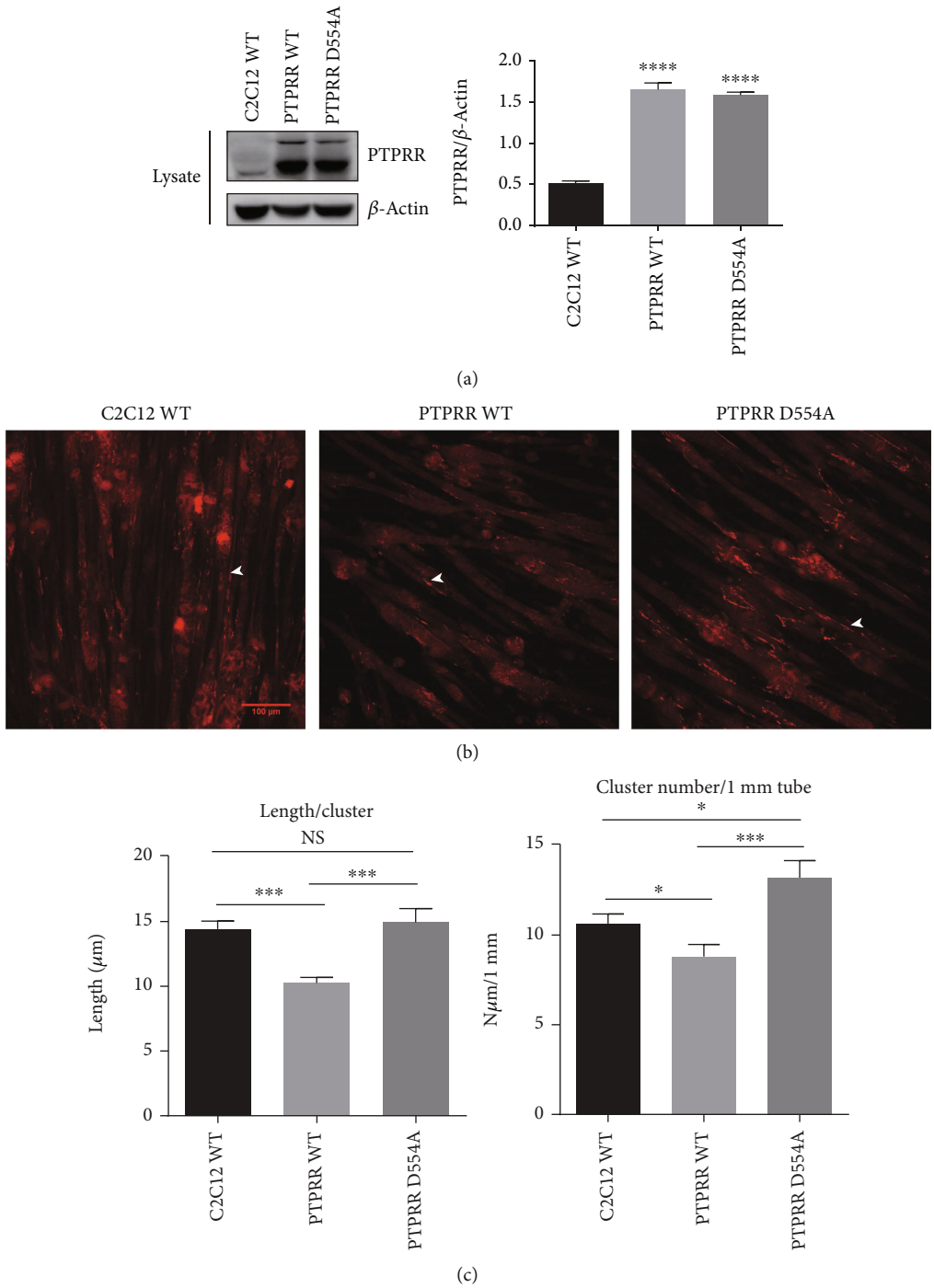

Figure 5: PTPRR significantly reduced MuSK-dependent AChR clustering in C2C12 myotubes. (a) C2C12 myoblasts were stably transfected with PTPRR, DA mutant, or empty vector plasmids. The efficiency of overexpression PTPRR was verified by western. (b) Compared with the C2C12 transfected with DA mutant or empty vector, C2C12 transfected with PTPRR had markedly reduced AChR clusters. White arrowheads indicate AChR clusters. (c) Quantification of AChR clusters ≥5 μm in length from (b). The data were obtained from at least three experiments. Data were shown as mean ± S.D. NS: no significant difference. $^{*}P < 0.05$, $^{***}P < 0.001$, and $^{****}P < 0.0001$.

purified by FACS sorting via the BD FACS Aria III flow cytometer. The sorted single clone C2C12 cell was cultured to expand the cell population. The overexpression of PTPRR-WT and D554A was confirmed by immunoblotting with anti-PTPRR antibody.

MuSK^{-} single clone C2C12 was generated by the CRISPR/Cas9 system. We used the online software (CRISPR gRNA Design tool: https://www.atum.bio/eCommerce/cas9) to design the sgRNA for targeting MuSK genes. The sequences were as follows: sgRNA1, 5′-AAGTTTCTCAG

TCCCGCTG-3′, and sgRNA2, 5′-AGCATTGTCCCCCTTG ATCC-3′. The complementary oligos of the sgRNAs were synthesized, phosphorylated, and incubated at 37°C for 1 h. The pairs of complementary oligos were mixed and PCR was performed: 95°C for 5 min, −10°/cycle, 0.1°/second, back to step one X7, 25°C 20 min, and 4°C hold. The MP783-GFP plasmid was digested with AarI and then ligated with the PCR product. The resulting MP783-GFP-sgRNA plasmid for targeting MuSK was confirmed by sequencing. CAS9-BFP C2C12 was infected with viral packaging MP783-GFP-sgRNA plasmid as previously mentioned. The CAS9-BFP/MP783-GFP-sgRNA double positive stable C2C12 was sorted by flow cytometry. The sorted single clone cells were expanded in culture, and the efficiency of MuSK knockout was validated by immunoblotting.

4.4. Immunoblotting and Immunoprecipitation. Cells were lysed with lysis buffer (20 mM Hepes pH 7.5, 150 mM NaCl, 1% NP40, 50 mM NaF, 1 mM Na_3VO_4, 10% glycerol, protease inhibitor cocktail from Roche) at 4°C for 30 min. After the concentration was determined, proteins were separated by SDS-PAGE and transferred to nitrocellulose membranes. Membranes were blocked and then incubated for 2 h at room temperature with primary antibody. Proteins were detected with horseradish peroxidase-conjugated secondary antibodies (Genscript) and ECL (Pierce).

For immunoprecipitation, precleared cell extracts were incubated with the indicated antibody for 4 h in a cold room with rotation followed by 1 h of pulldown by 1 : 1 Protein A/G-agarose beads. Immunoprecipitate was washed three times with lysis buffer on a rotating wheel at 4°C for 5 min before SDS-PAGE and immunoblotting.

4.5. Mass Spectrometry. Flag-MuSK was overexpressed in HEK293T cells and purified from cell lysates by immunoprecipitation with Flag-Beads. Purified Flag-MuSK proteins were then analyzed by mass spectrometry on a Thermo Fisher Scientific LTQ XL ion trap mass spectrometer.

4.6. C2C12 Myotube Culture and AChR Cluster Analysis. C2C12 myoblasts were propagated in Dulbecco's modified Eagle medium (DMEM) containing 4.5 g/l D-glucose and pyruvate, supplemented with 20% fetal bovine serum and 1% penicillin/streptomycin (growth medium). After reaching 90% confluence, differentiation was then induced by switching the growth medium to differentiation medium containing DMEM, 2% horse serum, and 1% penicillin/streptomycin. The differentiation medium was refreshed daily. Contracting myotubes were usually observed after 3 days and then used for further experiments. Cells were maintained at 37°C in an atmosphere of 5% CO_2.

AChR clusters of C2C12 myotubes were induced by application of agrin for 24 h. To visualize AChR clusters, C2C12 myotubes were fixed in 4% paraformaldehyde for 15 min, stained with Alexa Fluor 555-conjugated α-BTX, rinsed with phosphate buffered saline, and viewed under a confocal microscope (Zeiss LSM 710 NLO). AChR clusters were analyzed for number and length ($\geq 5\ \mu$m) using ImageJ software.

4.7. Statistical Analysis. Statistical tests were performed with GraphPad Prism 6 as indicated in the figure legends. Error bars represent the standard error of the mean unless otherwise stated. Unpaired Student's t-test was used to compare data between two groups. Differences were considered significant at $P < 0.05$.

Data Availability

The data used to support the findings of this study are included in the article/Supplementary Material. Further inquiries can be directed to the corresponding authors.

Conflicts of Interest

The authors declare that they have no competing interests.

Authors' Contributions

FC Lai designed the study. YX Chen and MH Guan performed the experiments. ZS Yang, WQ Yi, X Huang, and RQ Qiu analyzed the data. YX Chen drafted the manuscript. FC Lai and FQ Yu contributed to the critical revision of the manuscript for important intellectual content. FC Lai approved the final version of the manuscript. All authors have read and approved the manuscript. Yanxun Chen and Maohao Guan contributed equally to this work.

Acknowledgments

This study was supported by grants from the Fujian Provincial Health Technology Project (Grant No. 2018-ZQN-47) and Fujian Provincial Finance Project (Grant No. BPB-2020LFC). We thank Prof. Gaofeng Fan (ShanghaiTech University) for the reagent support for protein tyrosine phosphatase research in this study.

Supplementary Materials

Supplementary Figure S1: HEK293 T cells were cotransfected with flag-musk and various 10 tyrosine phosphatases as indicated. Tyrosine phosphorylation of MuSK, actin, and various PTPS was probed. Supplementary Figure S2: C2C12 cells were induced to differentiate for various lengths of time without and with agrin-stimulative for one day (as indicated). PTPRR expression was highest after one day of differentiation. *(Supplementary Materials)*

References

[1] Y. Badawi and H. Nishimune, "Impairment mechanisms and intervention approaches for aged human neuromuscular junctions," *Frontiers in Molecular Neuroscience*, vol. 13, article 568426, 2020.

[2] J. R. Sanes and J. W. Lichtman, "Induction, assembly, maturation and maintenance of a postsynaptic apparatus," *Nature Reviews. Neuroscience*, vol. 2, no. 11, pp. 791–805, 2001.

[3] Y. Chen, F. C. Ip, L. Shi et al., "Coronin 6 regulates acetylcholine receptor clustering through modulating receptor

anchorage to actin cytoskeleton," *The Journal of Neuroscience*, vol. 34, no. 7, pp. 2413–2421, 2014.

[4] Z. Dai, X. Luo, H. Xie, and H. B. Peng, "The actin-driven movement and formation of acetylcholine receptor clusters," *The Journal of Cell Biology*, vol. 150, no. 6, pp. 1321–1334, 2000.

[5] T. M. DeChiara, D. C. Bowen, D. M. Valenzuela et al., "The receptor tyrosine kinase MuSK is required for neuromuscular junction formation in vivo," *Cell*, vol. 85, no. 4, pp. 501–512, 1996.

[6] B. Zhang, S. Luo, Q. Wang, T. Suzuki, W. C. Xiong, and L. Mei, "LRP4 serves as a coreceptor of agrin," *Neuron*, vol. 60, no. 2, pp. 285–297, 2008.

[7] E. Bergamin, P. T. Hallock, S. J. Burden, and S. R. Hubbard, "The cytoplasmic adaptor protein Dok7 activates the receptor tyrosine kinase MuSK via dimerization," *Molecular Cell*, vol. 39, no. 1, pp. 100–109, 2010.

[8] K. Okada, A. Inoue, M. Okada et al., "The muscle protein Dok-7 is essential for neuromuscular synaptogenesis," *Science*, vol. 312, no. 5781, pp. 1802–1805, 2006.

[9] L. Shi, A. K. Fu, and N. Y. Ip, "Molecular mechanisms underlying maturation and maintenance of the vertebrate neuromuscular junction," *Trends in Neurosciences*, vol. 35, no. 7, pp. 441–453, 2012.

[10] A. G. Engel, X. M. Shen, D. Selcen, and S. M. Sine, "Further observations in congenital myasthenic syndromes," *Annals of the New York Academy of Sciences*, vol. 1132, no. 1, pp. 104–113, 2008.

[11] W. Hoch, J. McConville, S. Helms, J. Newsom-Davis, A. Melms, and A. Vincent, "Auto-antibodies to the receptor tyrosine kinase MuSK in patients with myasthenia gravis without acetylcholine receptor antibodies," *Nature Medicine*, vol. 7, no. 3, pp. 365–368, 2001.

[12] N. K. Tonks, "Protein tyrosine phosphatases: from genes, to function, to disease," *Nature Reviews. Molecular Cell Biology*, vol. 7, no. 11, pp. 833–846, 2006.

[13] R. Madhavan, X. T. Zhao, M. A. Ruegg, and H. B. Peng, "Tyrosine phosphatase regulation of MuSK-dependent acetylcholine receptor clustering," *Molecular and Cellular Neurosciences*, vol. 28, no. 3, pp. 403–416, 2005.

[14] T. T. Kummer, T. Misgeld, and J. R. Sanes, "Assembly of the postsynaptic membrane at the neuromuscular junction: paradigm lost," *Current Opinion in Neurobiology*, vol. 16, no. 1, pp. 74–82, 2006.

[15] L. P. Baker and H. B. Peng, "Tyrosine phosphorylation and acetylcholine receptor cluster formation in cultured Xenopus muscle cells," *The Journal of Cell Biology*, vol. 120, no. 1, pp. 185–195, 1993.

[16] H. B. Peng, L. P. Baker, and Z. Dai, "A role of tyrosine phosphorylation in the formation of acetylcholine receptor clusters induced by electric fields in cultured Xenopus muscle cells," *The Journal of Cell Biology*, vol. 120, no. 1, pp. 197–204, 1993.

[17] B. G. Wallace, "Regulation of the interaction of nicotinic acetylcholine receptors with the cytoskeleton by agrin-activated protein tyrosine kinase," *The Journal of Cell Biology*, vol. 128, no. 6, pp. 1121–1129, 1995.

[18] X. T. Zhao, Y. K. Qian, A. W. Chan, R. Madhavan, and H. B. Peng, "Regulation of ACh receptor clustering by the tyrosine phosphatase Shp2," *Developmental Neurobiology*, vol. 67, no. 13, pp. 1789–1801, 2007.

[19] S. Huda, M. Cao, A. De Rosa et al., "SHP2 inhibitor protects AChRs from effects of myasthenia gravis MuSK antibody," *Neurology Neuroimmunology & Neuroinflammation*, vol. 7, no. 1, p. e645, 2020.

[20] X. P. Dong, X. M. Li, T. M. Gao et al., "Shp2 is dispensable in the formation and maintenance of the neuromuscular junction," *Neurosignals*, vol. 15, no. 2, pp. 53–63, 2006.

[21] B. A. Hesser, O. Henschel, and V. Witzemann, "Synapse disassembly and formation of new synapses in postnatal muscle upon conditional inactivation of MuSK," *Molecular and Cellular Neurosciences*, vol. 31, no. 3, pp. 470–480, 2006.

[22] X. C. Kong, P. Barzaghi, and M. A. Ruegg, "Inhibition of synapse assembly in mammalian muscle in vivo by RNA interference," *EMBO Reports*, vol. 5, no. 2, pp. 183–188, 2004.

[23] A. L. Stiegler, S. J. Burden, and S. R. Hubbard, "Crystal structure of the frizzled-like cysteine-rich domain of the receptor tyrosine kinase MuSK," *Journal of Molecular Biology*, vol. 393, no. 1, pp. 1–9, 2009.

[24] J. H. Till, M. Becerra, A. Watty et al., "Crystal structure of the MuSK tyrosine kinase: insights into receptor autoregulation," *Structure*, vol. 10, no. 9, pp. 1187–1196, 2002.

[25] A. Watty, G. Neubauer, M. Dreger, M. Zimmer, M. Wilm, and S. J. Burden, "The in vitro and in vivo phosphotyrosine map of activated MuSK," *Proceedings of the National Academy of Sciences of the United States of America*, vol. 97, no. 9, pp. 4585–4590, 2000.

[26] Y. Zong, B. Zhang, S. Gu et al., "Structural basis of agrin-LRP4-MuSK signaling," *Genes & Development*, vol. 26, no. 3, 2012.

[27] K. Duś-Szachniewicz, M. Woźniak, K. Nelke, E. Gamian, H. Gerber, and P. Ziółkowski, "Protein tyrosine phosphatase receptor R and Z1 expression as independent prognostic indicators in oral squamous cell carcinoma," *Head & Neck*, vol. 37, no. 12, pp. 1816–1822, 2015.

[28] G. Fan, S. Aleem, M. Yang, W. T. Miller, and N. K. Tonks, "Protein-tyrosine phosphatase and kinase specificity in regulation of SRC and breast tumor kinase," *The Journal of Biological Chemistry*, vol. 290, no. 26, pp. 15934–15947, 2015.

[29] P. H. Su, Y. W. Lin, R. L. Huang et al., "Epigenetic silencing of PTPRR activates MAPK signaling, promotes metastasis and serves as a biomarker of invasive cervical cancer," *Oncogene*, vol. 32, no. 1, pp. 15–26, 2013.

[30] J. L. Wang, Y. Wang, and G. P. Ren, "Identification of PTPRR and JAG1 as key genes in castration-resistant prostate cancer by integrated bioinformatics methods()," *Journal of Zhejiang University. Science. B*, vol. 21, no. 3, pp. 246–255, 2020.

[31] M. Menigatti, E. Cattaneo, J. Sabates-Bellver et al., "The protein tyrosine phosphatase receptor type R gene is an early and frequent target of silencing in human colorectal tumorigenesis," *Molecular Cancer*, vol. 8, no. 1, 2009.

[32] Y. Wang, J. Cao, W. Liu et al., "Protein tyrosine phosphatase receptor type R (PTPRR) antagonizes the Wnt signaling pathway in ovarian cancer by dephosphorylating and inactivating β-catenin," *The Journal of Biological Chemistry*, vol. 294, no. 48, pp. 18306–18323, 2019.

[33] J. Wang, N. J. Ruan, L. Qian, W. L. Lei, F. Chen, and Z. G. Luo, "Wnt/beta-catenin signaling suppresses Rapsyn expression and inhibits acetylcholine receptor clustering at the neuromuscular junction," *The Journal of Biological Chemistry*, vol. 283, no. 31, pp. 21668–21675, 2008.

Hindawi
Disease Markers
Volume 2022, Article ID 5834218, 7 pages
https://doi.org/10.1155/2022/5834218

Research Article

Effect of Dapagliflozin on Indicators of Myocardial Fibrosis and Levels of Inflammatory Factors in Heart Failure Patients

Chuanqiang Wang,[1] Yiteng Qin,[2] Xiaojun Zhang,[1] Yang Yang,[1] Xuan Wu,[1] Jing Liu,[1] Shuhui Qin,[3] Ke Chen,[4] and Wenliang Xiao[1]

[1]*Department of Cardiology, The Third Hospital of Hebei Medical University, 050051 Shijiazhuang City, Hebei Province, China*
[2]*Basic Medicine College, Hebei Medical University, 050017 Shijiazhuang City, Hebei Province, China*
[3]*Hebei Orthopedic Research Institution, 050051 Shijiazhuang City, Hebei Province, China*
[4]*Catheter Room, Third Hospital of Hebei Medical University, 050051 Shijiazhuang City, Hebei Province, China*

Correspondence should be addressed to Wenliang Xiao; xiaowenliang@cthhmu.org.cn

Received 29 June 2022; Accepted 24 August 2022; Published 5 September 2022

Academic Editor: Jun Yang

Objective. To explore the effect of dapagliflozin on the myocardial fibrosis and the levels of inflammatory factors in heart failure patients. *Methods*. 60 patients with T2DM who were diagnosed as acute left heart failure or acute exacerbation of chronic left heart failure in the Department of Cardiology of our hospital from November 1, 2020, to December 31, 2021, during hospitalization were the study subjects. According to the treatment regimen, they were divided into the experimental group (EG) which received dapagliflozin and conventional drugs and the control group (CG) which received conventional drugs, with 30 cases in each group to compare and analyze the clinical indicators such as myocardial fibrosis and inflammatory factors. *Results*. The levels of TNF-α, IL-1β, IL-6, and hs-CRP in the two groups were decreased gradually after treatment, and the levels of TNF-α, IL-1β, IL-6, and hs-CRP in the EG were visibly lower compared with those in the CG at week 4 of treatment ($P < 0.05$). The cardiac function evaluation of patients showed that the levels of LVEF and LVEDD in both groups were gradually improved after treatment, with a significant difference from the fourth week. In other words, compared with the CG, the LVEF level in the EG was obviously higher ($P < 0.05$), the LVEDD level was distinctly lower ($P < 0.05$), and the levels of ST2, BNP, and MCP-1 in the EG were clearly lower at week 4 of treatment ($P < 0.05$) with a statistical significance in difference. *Conclusion*. Dapagliflozin has a definite curative effect in heart failure patients with type 2 diabetes mellitus, which can effectively reduce the inflammatory response of patients and inhibit the myocardial fibrosis, and has a potential value in improving cardiac function and promoting prognosis.

1. Introduction

In recent years, diabetes mellitus has become a serious public health problem globally, which can cause vascular endothelial injury and lead to the changes of heart construction and function, and is a high risk factor for heart failure and poor prognosis [1, 2]. Therefore, the development of hypoglycemic programs for patients with diabetes mellitus should not only consider the blood glucose control effect but also prevent the heart failure. Dapagliflozin, as a new hypoglycemic agent and also a sodium-glucose cotransporter2 (SGLT2) inhibitor, can reduce reabsorption of filtered glucose and the renal threshold value of glucose by inhibiting SGLT2, thereby increasing the urine glucose excretion [3, 4]. At present, clinical studies have confirmed that SGLT2 inhibitor can inhibit or reduce renal and hepatic fibrosis, and related animal experiments have also confirmed that SGLT2 inhibitor has a good inhibitory effect on myocardial fibrosis in rats [5, 6]. In addition, in multiple large-scale clinical studies, dapagliflozin has shown a better curative effect in reducing the mortality and rehospitalization rate of heart failure [7, 8]. However, the inflammatory response is an important mechanism of myocardial fibrosis, and a variety of inflammatory factors are involved in the process of

myocardial fibrosis, but it is unclear whether SGLT2 inhibitor affects the inflammatory response and whether it inhibits the process of myocardial fibrosis through the procedure of inflammatory response. Based on the current clinical study progress, this study further explores the effect of dapagliflozin on the myocardial fibrosis and the levels of inflammatory factors in heart failure patients in order to provide more directions for the treatment of heart failure. The report is discussed in the succeeding sections.

2. Materials and Methods

2.1. Inclusion Criteria. The criteria were as follows. (1) All patients met the diagnostic criteria of type 2 diabetes mellitus (T2DM) in the Guideline for the Prevention and Treatment of Type 2 Diabetes Mellitus in China (2017 edition) [9] and the diagnostic criteria of heart failure in the Chinese Guidelines for the Diagnosis and Treatment of Heart Failure in 2018 [10]. (2) The age of patients exceeded 18 years old. (3) The cardiac function was graded as II-IV by the New York Heart Association (NYHA) (the clinical features in grade II showed the slight limitation of physical activity and palpitation, short breath, fatigue, and dyspnea caused by common activities; the clinical features in grade III showed the obvious limitation of physical activity and breathlessness and palpitation caused by slight activity with the sign of mild congestion in organs; and the clinical features in grade IV showed the severe limitation of activities and the occurrence of breathlessness and palpitation at rest with the sign of severe-degree congestion in organs). (4) Patients had complete clinical data and high treatment coordination degree. (5) All patients signed the informed consent. (6) Patients could receive the long-term follow-up visit.

2.2. Exclusion Criteria. The criteria were as follows: (1) patients with the diseases such as severe sepsis and acute cerebrovascular disease that could cause cardiac dysfunction; (2) female patients in pregnancy or lactation period; (3) patients with other heart diseases like severe congenital heart disease, myocarditis, and valvular heart disease; (4) patients with malignant tumor, thyroid hyperfunction, or multiple organ failure; (5) patients with acute complication of diabetes mellitus; and (6) patients with psychic cognitive impairment or language communication disorder.

2.3. Screening and Grouping of Patients. 60 patients with T2DM who were diagnosed as acute left heart failure or acute exacerbation of chronic left heart failure in the Department of Cardiology of our hospital from November 1, 2020, to December 31, 2021, during hospitalization were the study subjects, and they were divided into the experimental group (EG) and the control group (CG) according to the treatment regimen, with 30 cases in each group. This study was in line with the criteria of ethics and morality and was adopted after discussion by the ethics committee of our hospital.

2.4. Methods

2.4.1. Medication Regimen. Patients in the CG were treated with conventional drug treatment, that is to say, giving them antidiabetic drugs such as metformin and insulin according to the individualized situation of patients. At the same time, beta-adrenergic blockade, calcium channel blockers, diuretics, and digitalis glycosides were used for antiheart failure treatment, and the diet guidance with low glucose and low sodium was given.

Patients in the EG were treated with dapagliflozin (specification: 10 mg∗30 s; manufacturer: AstraZeneca Pharmaceuticals Co., Ltd.; NMPA approval no. J20170040) on the basis of conventional medication regimen at a dose of 5 mg in the morning once a day.

2.4.2. Sample Collection. 10-15 ml of venous blood was collected before entering the group with the spontaneous coagulation at room temperature for 10-20 minutes and was centrifuged for about 20 minutes (2000-3000 r/min) to carefully collect the clear supernatant and then was sent to experiment center of our hospital for inspection. The specimens were repeatedly collected at week 1 and week 4 of treatment.

2.5. Observation Indices

(1) The general information includes age, gender, systolic pressure, heart rate, duration of diabetes mellitus, course of heart failure, NYHA grade, previous medication history, and complications

(2) The blood was collected at admission time and at week 1 and week 4 of treatment for centrifugation to collect the clear supernatant, and the tumor necrosis factor-α (TNF-α), interleukin-1β (IL-1β), interleukin-6 (IL-6), high-sensitivity c-reactive protein (hs-CRP), soluble suppression of tumorigenicity 2 (ST2), and b-type natriuretic peptide (BNP) were detected in the department of laboratory. The level of monocyte chemoattractant protein-1 (MCP-1) in serum was detected using enzyme-linked immunosorbent assay (ELISA method)

(3) The ultrasound cardiography (UCG) examination was performed at admission time and week 1 and week 4 of treatment to analyze statistically the left ventricle ejection fraction (LVEF) and left ventricular end diastolic dimension (LVEDD)

2.6. Statistical Treatment. The software SPSS 23.0 was used for the data processing in this study to calculate the differences in data between the two groups, and GraphPad Prism 7 (GraphPad Software, San Diego, USA) was used for chart production. The study data including enumeration and measurement were tested by x^2 and t-test, indicated by [n (%)] and ($\bar{x} \pm s$), which were in line with the normal distribution. When statistical results were $P < 0.05$, the differences were considered to be statistically significant.

3. Results

3.1. General Information. The age, gender, systolic pressure, heart rate, duration of diabetes mellitus, course of heart failure, NYHA grade, previous medication history, complications, and other general information in both groups were

Table 1: Comparison of general information in patients between the two groups ($n = 30$).

Observation indices	CG	EG	x^2/t	P
Age (years)	67.50 ± 6.90	67.43 ± 6.70	0.040	0.968
Gender (male/female)	17/13	18/12	0.069	0.793
Systolic pressure (mmHg)	125.63 ± 8.67	127.00 ± 9.18	0.594	0.555
Heart rate (times/min)	68.53 ± 4.07	68.87 ± 4.20	0.318	0.751
Duration of diabetes mellitus (years)	9.41 ± 3.16	9.24 ± 3.24	0.206	0.834
Course of heart failure (months)	8.17 ± 2.73	8.73 ± 2.58	0.817	0.418
NYHA grade				
Grade II	10 (33.33)	7 (23.33)	0.739	0.390
Grade III	18 (60.00)	20 (66.67)	0.287	0.592
Grade IV	2 (6.67)	3 (10.00)	0.218	0.640
Previous medication history				
Dipeptidyl peptidase-4 inhibitor	22 (73.33)	23 (76.67)	0.089	0.766
Sulfonylurea	9 (30.00)	8 (26.67)	0.082	0.774
Alpha glucosidase inhibitor	7 (23.33)	8 (26.67)	0.089	0.766
Nitrotyrosine	10 (33.33)	12 (40.00)	0.287	0.592
Biguanides	15 (50.00)	13 (43.33)	0.268	0.605
ACEI/ARB	24 (80.00)	25 (83.33)	0.111	0.739
Calcium channel blockers	8 (26.67)	10 (33.33)	0.318	0.573
Beta-adrenergic blockade	15 (50.00)	14 (46.67)	0.067	0.796
Atorvastatin	22 (73.33)	19 (63.33)	0.693	0.405
Complications				
Hypertension	9 (30.00)	10 (33.33)	0.077	0.781
COPD	4 (13.33)	5 (16.67)	0.131	0.718
Hyperlipidemia	7 (23.33)	5 (16.67)	0.417	0.519

Table 2: Levels of inflammatory factors in patients.

Inflammatory factors		CG	EG	t	P
	At admission time	49.26 ± 7.66	48.82 ± 7.35	0.227	0.821
TNF-α (ng/l)	At week 1 of treatment	43.11 ± 7.15	40.72 ± 7.03	1.306	0.197
	At week 4 of treatment	35.33 ± 8.17	28.10 ± 6.30	3.838	<0.001
	At admission time	745.2 ± 84.1	743.8 ± 84.8	0.064	0.949
IL-1β (ng/ml)	At week 1 of treatment	572.7 ± 72.8	531.9 ± 78.5	1.883	0.065
	At week 4 of treatment	497.5 ± 74.3	356.4 ± 60.2	8.082	<0.001
	At admission time	150.9 ± 15.4	151.3 ± 15.7	0.100	0.921
IL-6 (ng/l)	At week 1 of treatment	138.9 ± 12.3	132.4 ± 13.8	1.926	0.059
	At week 4 of treatment	120.5 ± 11.2	107.8 ± 9.5	4.736	<0.001
	At admission time	9.88 ± 2.28	9.64 ± 2.51	1.908	0.061
hs-CRP (mg/L)	At week 1 of treatment	9.10 ± 2.13	8.86 ± 2.01	0.449	0.655
	At week 4 of treatment	7.59 ± 1.01	6.87 ± 1.05	2.707	0.009

counted, with no statistical significance between the two groups ($P > 0.05$). See details in Table 1.

3.2. Inflammatory Factors. According to the statistical data of inflammatory factors in Table 2, the levels of TNF-α, IL-1β, IL-6, and hs-CRP in the two groups were decreased gradually after treatment, and there were slight differences in the levels of inflammatory factors between the two groups at week 1 of treatment, with no significant difference ($P < 0.05$), while the levels of TNF-α, IL-1β, IL-6, and hs-CRP in the EG were significantly lower compared with the CG at week 4 of treatment ($P < 0.05$).

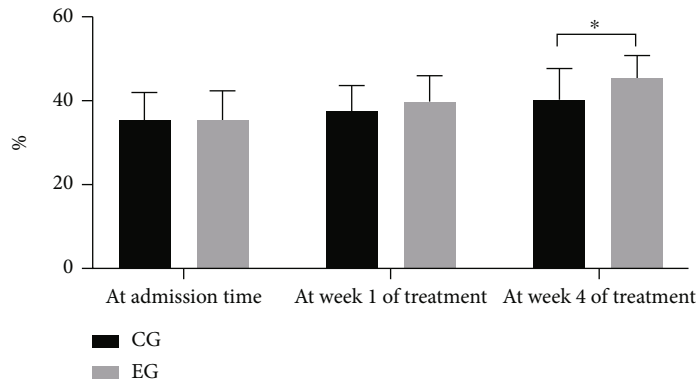

Figure 1: LVEF level of patients. Notes: the horizontal coordinate represented time points, and the horizontal coordinate represented LVEF level (%). The levels of LVEF at admission time and at week 1 and week 4 of treatment in the CG were 35.49 ± 6.55, 37.60 ± 5.91, and 40.25 ± 7.43, respectively. The levels of LVEF at admission time and at week 1 and week 4 of treatment in the EG were 35.57 ± 6.78, 39.85 ± 6.04, and 45.36 ± 5.46, respectively. *An apparent difference in the levels of LVEF between the two groups at week 4 of treatment ($t = 3.035$, $P = 0.004$).

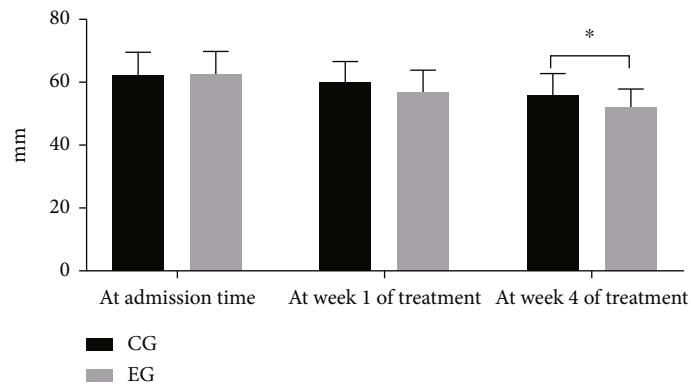

Figure 2: LVEDD level of patients. Notes: the horizontal coordinate represented time points, and the horizontal coordinate represented LVEDD level (mm). The levels of LVEDD at admission time and at week 1 and week 4 of treatment in the CG were 62.40 ± 7.15, 60.11 ± 6.54, and 55.88 ± 7.01, respectively. The levels of LVEDD in the EG at admission time and at week 1 and week 4 of treatment were 62.55 ± 7.24, 56.84 ± 7.07, and 52.10 ± 5.73, respectively. *An apparent difference in the levels of LVEDD between the two groups at week 4 of treatment ($t = 2.287$, $P = 0.026$).

Table 3: Indicators of myocardial fibrosis in patients.

Inflammatory factors		CG	EG	t	P
ST2 (μg/l)	At admission time	52.25 ± 4.62	51.82 ± 4.53	0.821	0.415
	At week 1 of treatment	49.21 ± 4.68	47.10 ± 4.17	1.844	0.070
	At week 4 of treatment	45.82 ± 3.15	39.15 ± 3.02	8.372	<0.001
BNP (pmol/l)	At admission time	75.59 ± 9.52	74.90 ± 9.83	0.276	0.783
	At week 1 of treatment	70.87 ± 9.14	66.29 ± 9.20	1.934	0.058
	At week 4 of treatment	59.12 ± 8.56	49.53 ± 8.25	4.418	<0.001
MCP-1 (ng/l)	At admission time	18.03 ± 4.04	17.95 ± 4.10	0.076	0.940
	At week 1 of treatment	16.55 ± 3.43	15.08 ± 3.30	1.692	0.096
	At week 4 of treatment	13.41 ± 3.21	10.28 ± 1.43	4.878	<0.001

3.3. Cardiac Function. The cardiac function evaluation of patients showed that the levels of LVEF and LVEDD in both groups were gradually improved after treatment with a significant difference from the fourth week. In other words, compared with the CG, the LVEF level in the EG was obviously higher ($P < 0.05$), and the LVEDD level was distinctly lower ($P < 0.05$). See details in Figures 1 and 2.

3.4. Myocardial Fibrosis. At week 4 of treatment, the levels of ST2, BNP, and MCP-1 in the EG were obviously lower than

those in the CG ($P < 0.05$) with a statistical significance in difference. See details in Table 3.

4. Discussion

Heart failure is a serious and terminal stage of various heart diseases, which is one of the most important cardiovascular diseases today with high morbidity and mortality despite the continuous development of medical technology. The two key processes in the progression of heart failure caused by the reconstruction of myocardial pathology are one of the main pathogenesis mechanism of heart failure, that is, the occurrence of myocardial death (necrosis, apoptosis, and autophagy), such as acute myocardial infarction and severe myocarditis on the one hand, and, on the other hand, system response caused by excessive activation of neuroendocrine system, in which myocardial fibrosis is an important pathological change in the process of heart failure [11, 12]. Therefore, cutting off or delaying the two key processes is an important means to effectively prevent and treat heart failure. SGLT2 inhibitor is a new type of hypoglycemic agent, and various SGLT2 inhibitors can significantly reduce the left ventricle ejection fraction of patients in several large-scale recently finished and underway clinical studies, which is expected to reduce the mortality of heart failure patients. More importantly, these benefits can be observed in patients with or without diabetes mellitus, suggesting that the benefits are independent of the effects on reducing blood glucose [13, 14]. The tablet of oral dapagliflozin (a SGLT2 inhibitor) has been approved by the Food and Drug Administration (FDA) used for the treatment of heart failure on May 5, 2020 (CAS registration no. 461432-26-8), mainly for the heart failure patients with reduced ejection fraction, which is aimed at reducing the risk of cardiovascular mortality and admission due to heart failure of patients. At present, dapagliflozin has been marketed in China, but it is only approved for the treatment of adults with type 2 diabetes mellitus, and there are few related study reports in China. However, our province, as an area with high incidence of cardiovascular disease, has many heart failure patients, and it is worth further exploring the inhibitory effect of dapagliflozin on myocardial fibrosis in heart failure patients, so as to provide more scientific and accurate guidance for the treatment and prognosis of heart failure.

More and more studies have shown that immune inflammatory response exerts a vital role in the process of myocardial fibrosis so that it may be a new way to improve the myocardial fibrosis by regulating the abnormal immune inflammatory response [15]. Inflammation is an important factor inducing the myocardial fibrosis, and inflammatory response and myocardial fibrosis often coexist in the same lesion sites in a variety of cardiovascular diseases. When the damage occurs in the heart, the immune system activation releases a variety of inflammatory factors and activates cardiac fibroblasts leading to the abnormal collagen metabolism and myocardial necrosis and degeneration, thus causing the pathological changes such as myocardial fibrosis. Therefore, the short-term therapeutic target of heart failure alleviates the condition by improving the clinical symptoms of patients, while the long-term therapeutic target improves the survival prognosis of patients with heart failure by reversing the target organ damage such as myocardial fibrosis caused by multiple adverse factors like immune inflammatory response [16, 17]. In this study, the levels of TNF-α, IL-1β, IL-6, and hs-CRP in the two groups were decreased gradually after treatment, and the levels of TNF-α, IL-1β, IL-6, and hs-CRP in the EG were obviously lower than those in the CG at week 4 of treatment ($P < 0.05$). The inflammatory cascade reaction mediated by neutrophil granulocyte and mononuclear macrophages is one of the common mechanisms leading to the myocardial fibrosis, which can secrete a variety of proinflammatory cytokines such as TNF-α, IL-1β, and IL-6, leading to the myocardial fibrosis. The results of this study showed that dapagliflozin can effectively inhibit the inflammatory response in heart failure patients in the short term and reduce the levels of inflammatory factors, thus alleviating myocardial fibrosis. The clinical studies have found that the clinical pharmacological mechanism of dapagliflozin in the treatment of heart failure includes the following points. (1) Dapagliflozin can effectively reduce ventricular hypertrophy and restore dilation function. (2) The apoptosis of cardiomyocytes was inhibited, thus delaying the progress of diastolic dysfunction, and the activation of mitochondrial autophagy is an important mechanism for mediating the protective mechanism produced by dapagliflozin. (3) Dapagliflozin also reduces the oxidative stress reaction through Nrf2/ARE and other pathways, so as to hinder myocardial fibrosis and ventricular hypertrophy, improve myocardial dilation function, and promote the myocardial remodeling and improvement effect of myocardial microcirculation. The cardiac function evaluation of patients showed that the levels of LVEF and LVEDD in the two groups were gradually improved after treatment, with a significant difference from the fourth week. In other words, compared with the CG, the LVEF level in the EG was obviously higher ($P < 0.05$), and the LVEDD level was distinctly lower ($P < 0.05$), which was consistent with the results of previous studies [18, 19], confirming that dapagliflozin is helpful to improve the cardiac function of heart failure patients. Dapagliflozin can promote the excretion of sugar and sodium in patients, with an effect on osmotic diuresis, thereby reducing the cardiac preload, while it also reduces the cardiac afterload by reducing the blood pressure and arterial stiffness and improving the vascular endothelial function, thereby improving the cardiac diastolic function.

In this study, the levels of ST2, BNP, and MCP-1 in the EG were overtly lower than those in the CG ($P < 0.05$) at week 4 of treatment, indicating that dapagliflozin has an obvious inhibitory effect on myocardial fibrosis in heart failure patients with type 2 diabetes mellitus. Besides reducing the blood glucose, dapagliflozin also has multiple cardiovascular protective effects and alleviates the heart failure symptoms mainly by early hemodynamic changes. The possible mechanisms are as follows. (1) The cardiovascular risk factors were improved, including reducing the BMI, blood lipid, systolic pressure, and blood uric acid level, postponing the kidney disease, and reducing the excretion of urine protein [20–22]. (2) The vasodilation function in patients was

improved to increase the amount of blood pump. Previous studies have shown that dapagliflozin can reduce the myocardial oxidative stress and inhibit the expression of inflammatory factors like TNF-α, IL-1β, IL-6, and MCP-1 in myocardium by the reduction of malonaldehyde and the increase of superoxide dismutase, thus inhibiting the myocardial hypertrophy and myocardial fibrosis [23–25]. (3) Dapagliflozin enables to improve the hemodynamics through osmotic diuresis and improving the arteriosclerosis, thus reducing the cardiac preload and afterload.

The shortcomings of this study were as follows. (1) Dapagliflozin may benefit heart failure patients through multiple mechanisms, but SGLT2 is not expressed in human cardiomyocytes, mainly distributed in the kidney, and it is not clear whether dapagliflozin directly affects the cardiomyocytes, which needs to be supported by a large number of experimental results. (2) In this study, the sample size is small and the long-term efficacy of patients is not tracked, and large sample studies are still needed to further clarify its clinical value. (3) At the same time, limited by the research conditions, this study lacked the study on the adverse reactions of patients after medication, so this problem should be paid attention to in the follow-up studies.

In summary, dapagliflozin has a definite curative effect on heart failure patients with type 2 diabetes mellitus, which effectively reduces the levels of inflammatory factors in patients and improves the cardiac function, and further studies will help to establish a better solution for such patients.

Data Availability

The data to support the findings of this study is available on reasonable request from the corresponding author.

Conflicts of Interest

The authors have no conflicts of interest to declare.

Authors' Contributions

Chuanqiang Wang and Yiteng Qin contributed equally to this work.

Acknowledgments

This research was funded by the 2021 Medical Science Research Project of Hebei Provincial Health Committee, grant number 20211597.

References

[1] F. Xianu, "Efficacy and safety evaluation of dagglitazone in the treatment of type 2 diabetes with chronic heart failure," *Drug evaluation*, vol. 18, no. 15, pp. 936–938, 2021.

[2] H. Liangweihua, "Effects of dagglitazone on insulin resistance, blood lipid, and Hcy in patients with type 2 diabetes mellitus," *Shenzhen Journal of integrated traditional Chinese and Western medicine*, vol. 31, no. 17, pp. 47–49, 2021.

[3] M. Gupte, H. Lal, F. Ahmad, D. B. Sawyer, and M. F. Hill, "Chronic neuregulin-1β treatment mitigates the progression of postmyocardial infarction heart failure in the setting of type 1 diabetes mellitus by suppressing myocardial apoptosis, fibrosis, and key oxidant-producing enzymes," *Journal of Cardiac Failure*, vol. 23, no. 12, pp. 887–899, 2017.

[4] W. J. Paulus and M. R. Zile, "From systemic inflammation to myocardial fibrosis the heart failure with preserved ejection fraction paradigm revisited," *Circulation research: a journal of the American Heart Association*, vol. 128, no. 10, pp. 1451–1467, 2021.

[5] A. Gulati, A. G. Japp, S. Raza et al., "Absence of myocardial fibrosis predicts favorable long-term survival in new-onset heart failure," *Circulation. Cardiovascular imaging.*, vol. 11, no. 9, article e007722, 2018.

[6] A. Gonzalez, E. B. Schelbert, J. Diez, and J. Butler, "Myocardial interstitial fibrosis in heart failure: biological and translational perspectives," *Journal of the American College of Cardiology*, vol. 71, no. 15, pp. 1696–1706, 2018.

[7] D. W. Ma, T. Xu, and G. Cai, "Effects of ivabradine hydrochloride combined with trimetazidine on myocardial fibrosis in rats with chronic heart failure," *Experimental and Therapeutic Medicine*, vol. 18, no. 3, pp. 1639–1644, 2019.

[8] A. Gonzalez, B. Lopez, S. Ravassa, G. San José, and J. Díez, "The complex dynamics of myocardial interstitial fibrosis in heart failure. Focus on collagen cross-linking," *Molecular Cell Research*, vol. 1866, no. 9, pp. 1421–1432, 2019.

[9] M. B. Elming, S. Hammer-Hansen, I. Voges et al., "Myocardial fibrosis and the effect of primary prophylactic defibrillator implantation in patients with nonischemic systolic heart failure-DANISH-MRI," *Autonomic Neuroscience: Basic & Clinical*, vol. 221, pp. 165–176, 2019.

[10] C. Yang, J. Liu, K. Liu et al., "Ghrelin suppresses cardiac fibrosis of postmyocardial infarction heart failure rats by adjusting the activin A-follistatin imbalance," *International Journal*, vol. 99, pp. 27–35, 2018.

[11] J. Wang, Y. Zhang, L. Zhang et al., "Assessment of myocardial fibrosis using two-dimensional and three-dimensional speckle tracking echocardiography in dilated cardiomyopathy with advanced heart failure," *Journal of Cardiac Failure*, vol. 27, no. 6, pp. 651–661, 2021.

[12] M. L. Lindsey, K. Y. Deleon-Pennell, A. D. Bradshaw et al., "Focusing heart failure research on myocardial fibrosis to prioritize translation," *Journal of Cardiac Failure*, vol. 26, no. 10, pp. 876–884, 2020.

[13] Y. Liu, Y. Fan, J. Li et al., "Combination of LCZ696 and ACEI further improves heart failure and myocardial fibrosis after acute myocardial infarction in mice," *Biomedicine & Pharmacotherapy*, vol. 133, article 110824, 2021.

[14] M. E. Nassif, S. L. Windsor, B. A. Borlaug et al., "The SGLT2 inhibitor dapagliflozin in heart failure with preserved ejection fraction: a multicenter randomized trial," *Nature Medicine*, vol. 27, no. 11, pp. 1954–1960, 2021.

[15] B. Feng, N. Zhang, and B. Shi, "A SGLT2 inhibitor dapagliflozin prevents heart failure with preserved ejection fraction through activating mitophagy in ZDF diabetic rats," *Diabetologia: Clinical and Experimental Diabetes and Metabolism Organ of the European Association for the Study of Diabetes (EASD)*, vol. 62, no. 1, p. S101, 2019.

[16] S. C. Shao, K. C. Chang, S. J. Lin et al., "Differences in outcomes of hospitalizations for heart failure after SGLT2 inhibitor treatment: effect modification by atherosclerotic

cardiovascular disease," *Cardiovascular Diabetology*, vol. 20, no. 1, 2021.

[17] K. D. Faulkenberg, J. B. Williams, D. M. Isaacs, and L. M. West, "Practical considerations and opportunities for SGLT2 inhibitor prescription in heart failure," *Current Treatment Options in Cardiovascular Medicine*, vol. 22, no. 10, pp. 1–15, 2020.

[18] V. Woo, K. Connelly, P. Lin, and P. McFarlane, "The role of sodium glucose cotransporter-2 (SGLT-2) inhibitors in heart failure and chronic kidney disease in type 2 diabetes," *Current Medical Research and Opinion*, vol. 35, no. 7, pp. 1283–1295, 2019.

[19] K. M. Hallow, G. Helmlinger, P. J. Greasley, J. J. McMurray, and D. W. Boulton, "Why do SGLT2 inhibitors reduce heart failure hospitalization? A differential volume regulation hypothesis," *Diabetes, Obesity & Metabolism*, vol. 20, no. 3, pp. 479–487, 2018.

[20] P. Martens, C. Mathieu, and F. H. Verbrugge, "Promise of SGLT2 inhibitors in heart failure: diabetes and beyond," *Current Treatment Options In Cardiovascular Medicine.*, vol. 19, no. 3, pp. 1–14, 2017.

[21] C. Chim and S. Newaz, "SGLT2 inhibitors and heart failure outcomes," *U. S. pharmacist*, vol. 45, no. 2, pp. 18–22, 2020.

[22] S. S. Joshi, T. Singh, D. E. Newby, and J. Singh, "Sodium-glucose cotransporter 2 inhibitor therapy: mechanisms of action in heart failure," *Heart*, vol. 107, no. 13, pp. 1032–1038, 2021.

[23] K. Katsurada, S. S. Nandi, N. M. Sharma, and K. P. Patel, "Enhanced expression and function of renal SGLT2 (sodium-glucose cotransporter 2) in heart failure: role of renal nerves," *Circulation. Heart Failure.*, vol. 14, no. 12, article e008365, 2021.

[24] J. Mcmurray, "A trial to evaluate the effect of the sodium–glucose cotransporter 2 inhibitor dapagliflozin on morbidity and mortality in patients with heart failure and reduced left ventricular ejection fraction (DAPA-HF)," *European journal of heart failure: journal of the Working Group on Heart Failure of the European Society of Cardiology*, vol. 21, no. 5, pp. 665–675, 2019.

[25] G. M. Gager, D. von Lewinski, H. Sourij et al., "Effects of SGLT2 inhibitors on ion homeostasis and oxidative stress associated mechanisms in heart failure," *Biomedicine & Pharmacotherapy*, vol. 143, article 112169, 2021.

Hindawi
Disease Markers
Volume 2022, Article ID 9996946, 32 pages
https://doi.org/10.1155/2022/9996946

Research Article

The Prognostic Role of Cuproptosis in Head and Neck Squamous Cell Carcinoma Patients: A Comprehensive Analysis

Qin Ding,[1,2] Xiaochuan Chen,[1,2] Wenquan Hong,[1,2] Lihua Wang,[1,2] Wei Liu,[1,2] Sunqin Cai,[1,2] Xin Chen,[2,3] Jun Lu,[2,3] and Sufang Qiu[2,3]

[1]*Clinical Oncology School of Fujian Medical University, Fujian Cancer Hospital, Fuzhou, China*
[2]*Fujian Provincial Key Laboratory of Translational Cancer Medicine, Fuzhou, China*
[3]*Department of Radiation Oncology, Clinical Oncology School of Fujian Medical University, Fujian Cancer Hospital, Fuzhou, China*

Correspondence should be addressed to Jun Lu; lujvip@126.com and Sufang Qiu; sufangqiu@fjmu.edu.cn

Received 14 June 2022; Revised 12 August 2022; Accepted 16 August 2022; Published 2 September 2022

Academic Editor: Jun Yang

Purpose. Head and neck squamous cell carcinoma (HNSCC) exhibits a high mortality and morbidity rate, and its treatment is facing clinical challenges. Cuproptosis, a copper-dependent cell death process, can help derive new forms of cancer therapies. However, the potential of cuproptosis-related genes (CRGs) as novel biomarkers for risk prediction, screening, and prognosis remains to be further explained in HNSCC. *Methods.* We built a prognostic multigene signature with CRGs, which is associated with the tumor immune microenvironment (TME) by gene set enrichment analysis (GSEA), in the TCGA cohort. Furthermore, we systematically correlated risk signature with immunological characteristics in TME including tumor-infiltrating immune cells (TIICs), immune checkpoints, T cell inflamed score, and cancer immunity cycles. We also thoroughly investigated the biological functions of cuproptosis-associated lncRNAs and its immunological characteristics. *Results.* CRGs-related prognostic model showed good prediction performance. A higher risk score was associated with a poorer overall survival (OS) than those with low-risk scores, according to the results of the survival analysis ($p < 0.0001$). The risk score was significantly related to the variable clinicopathological factors. Samples with high-risk scores had lower levels of CD8+ T cells infiltration. Immune therapy might be effective for the low-risk subtype of HNSCC patients ($p < 0.05$). Moreover, 11 differentially expressed lncRNAs as the independent prognostic factor could also predict TME in an accurate manner. *Conclusion.* Our study identified and validated novel cuproptosis-related biomarkers for HNSCC prognosis and screening, which offer better insights into developing accurate, reliable, and novel cancer therapies in the era of precision medicine.

1. Introduction

Head and neck squamous cell carcinoma (HNSCC) is recorded to be the 8th most commonly occurring form of cancer in the world, with a high mortality and morbidity rate [1, 2]. Approximately 600,000 new HNSCC cases and 350,000 HNSCC-related deaths take place every year across the globe [3–5]. Though many new techniques have been developed for diagnosing the patients during their early stages, more than half of the HNSSC patients are diagnosed only in their advanced stages [6]. In the past few years, many significant breakthroughs have been achieved in the HNSCC treatment, including chemotherapy, radiotherapy, and surgery. Despite these breakthroughs, the 5-year survival rate of HNSCC patients is still poor [7, 8]. Hence, it is essential to consider alternative probable causes of cell death to overcome the chemotherapy resistance and identify novel biomarkers that can be used as therapeutic agents for improving the prognosis of patients with HNSCC.

Many researchers are investigating the role of cuproptosis in cancer. Protein lipoylation is mainly responsible for copper-induced cell death (i.e., cuproptosis). In their study, Tsvetkov et al. identified a new type of copper-induced cell death mechanism, where the Cu ions disrupted some particular mitochondrial metabolic enzymes, which was more toxic in the actively respiring cells [9, 10]. An increase in the number of respiratory cells increases the level of the lipoylated enzymes, which, in turn, leads to the formation

of more protein aggregates [10, 11]. It is concluded that copper ions can sabotage the cell and cause the death of cells if the metabolic pathway in the cells was disrupted [12, 13]. Hence, we believe that an investigation into the copper toxicity-based pathology can help determine and uncover the genetic diseases related to genetic copper overload and derive new forms of cancer therapies.

Very few researchers have investigated the role played by the cuproptosis-related molecular signatures in predicting the overall survival (OS) rate of HNSCC patients. In this study, we have evaluated the expression profile of cuproptosis-related genes (CRGs), initially described by Tsvetkov et al. [10], and developed a prognostic multigene signature that was based on the CRGs. Additionally, we also studied the role of the CRGs, immune tumor microenvironment, lncRNAs, and immune responses in HNSCC.

2. Materials and Methods

2.1. Data Collection. In this study, we downloaded the dataset that included the mRNA expression and the related clinical data for 502 tumor tissues along with 44 adjacent normal tissues of HNSCC, from The Cancer Genome Atlas (TCGA; https://portal.gdc.cancer.gov/) (Table 1).

Thereafter, we retrieved 10 CRGs (Table 2) from the published studies [10]. We used the Clinical Proteomic Tumor Analysis Consortium (CPTAC, https://proteomics.cancer.gov/programs/cptac), developed by the National Cancer Institute, and a cBioPortal (http://www.cbioportal.org/) for the purpose of comparing the methylation sequences, RNAseq, and proteomics data between the tumor and nontumor tissues. The correlation between the CRGs and lncRNAs was determined with the help of the Pearson correlation analysis. Based on the values of the correlation coefficient, $|R^2| > 0.1$, and $p < 0.05$, the cuproptosis-associated lncRNAs were regarded as statistically significant lncRNAs. Furthermore, we conducted the functional analysis with the help of the Kyoto Encyclopedia of Genes and Genomes (KEGG) and Gene Ontology (GO) databases, by implementing the R language ggplot2 package for assessing the roles of all identified CRGs.

2.2. Designing the Cuproptosis-Associated Prognostic Gene Signature. We used the Lasso-penalized Cox regression technique for developing the cuproptosis-associated prognostic gene and lncRNA signatures. We used the formula described below for predicting the risk score of every HNSCC patient:

$$\text{risk score} = \sum_{i=1}^{n} (\exp \times \text{coef}), \quad (1)$$

where exp denotes the gene and the lncRNA expression value, while *coef* refers to the coefficient of a gene and lncRNA in LASSO analysis. We also downloaded and studied the related clinical data of HNSSC patients. We classified this data as low-risk (with a value lesser than the median number) or high-risk (with a value higher than the median number) groups. We used the Kaplan-Meier survival analysis for assessing the survival rate. Then, we tested these two signatures with the help of the univariate and multivariate Cox regression models for determining if they were independent prognostic factors or not. Finally, we used the receiver-operator characteristics (ROC) and the respective areas under the curve (AUC) for analyzing the performance of the prediction models.

Table 1: Baseline information of TCGA.

TCGA ($N = 501$)		
Age (%)	19-39	18 (3.6)
	40-49	58 (11.6)
	50-59	145 (28.9)
	60-90	280 (55.9)
Gender (%)	Female	134 (26.7)
	Male	367 (73.3)
Stage (%)	Stage I-II	113 (22.6)
	Stage III-IV	374 (74.7)
	NA	14 (3.7)

Table 2: 10 cuproptosis-related genes.

FDX1 LIAS LIPT1 DLD DLAT PDHA1 PDHB MTF1 GLS CDKN2A

Table 3: 18 inflammatory genes in T cell-inflamed gene expression profile (GEP).

CCL5 CD27 CD274 CD276 CD8A CMKLR1 CXCL9 CXCR6 HLA-DQA1 HLA-DRB1 HLA-E IDO1 LAG3 NKG7 PDCD1LG2 PSMB10 STAT1 TIGIT

2.3. Assessing the Immunological Characteristics of TME. We estimated the stromal, immune, and ESTIMATE scores using the R package "ESTIMATE." Immunological features of the TME include the inhibitory immune checkpoints, immunomodulators, and tumor-infiltrating immune cells (TIICs). We acquired the data regarding the 92 immunomodulators such as receptors, chemokines, and MHC from an earlier study [14]. We used the MCP-counter, Cibersort, Cibersort-ABS, quanTIseq, xCell, TIMER, and EPIC algorithms for assessing the TIIC infiltration level in TME [15–19]. We also derived the effector genes of the TIICs from multiple earlier studies [20].

From an earlier study, we retrieved a group of 10 inhibitory immune checkpoints that displayed therapeutic efficacy [21]. A gene set that showed a T cell-inflamed gene expression profile (GEP) and included 18 inflammatory genes was downloaded from an earlier study (Table 3) [22]. We also derived the Shannon Entropy data of the T cell receptor (TCR) and B cell receptor (BCR) from an earlier report [23].

We acquired the Microsatellite Instability (MSI) for somatic mutation analysis from an earlier report [24]. We assessed the tumor mutation burden (TMB) and the mutant-allele tumor heterogeneity (MATH) data, which

Table 4: The seven steps of cancer immunity cycle.

The seven steps of cancer immunity cycle	
Step 1	Release of cancer cell antigens
Step 2	Cancer antigen presentation
Step 3	Priming and activation
Step 4	Trafficking of immune cells to tumors
Step 5	Infiltration of immune cells into tumors
Step 6	Recognition of cancer cells by T cells
Step 7	Killing of cancer cells

comprised the wound healing, silent and non-silent mutation rate, lymphocyte infiltration signature score, fraction altered, and macrophage regulation from the somatic mutation data for 465 tumor samples, with the help of the "maftools" R package [24, 25].

The anticarcinoma immune response was reflected in the cancer immunity cycle using 7 steps (Table 4). The fate of tumor cells was determined throughout the procedure. Thereafter, we used a single-sample gene set enrichment analysis (ssGSEA) technique for assessing the gene expression of single samples [19].

2.4. Prediction of the Response of Comprehensive Therapy. By constructing the ridge regression model based on Genomics of Drug Sensitivity in Cancer (GDSC) (http://www.cancerrxgene.org/) cell line expression spectrum and TCGA gene expression profiles, the "pRRophetic" package in R could be applied to predict the half-maximal inhibitory concentration (IC50) of chemotherapy in the high- and low-risk groups of HNSCC patients and to infer the sensitivity of the different patients [26].

2.5. Statistical Analysis. All statistical analyses were done on R version 3.6.0. Continuous variables were compared between the two groups using Wilcoxon rank sum test. Categorical variables were compared between the groups using the chi-square test. The prognostic value of categorical variables was assessed using the log-rank test. For all analyses, two-paired p value ≤ 0.05 indicated statistically significant differences. $*$, $**$, $***$, and $****$ indicate p value ≤ 0.05, <0.01, <0.001, and<0.0001, respectively.

3. Results

3.1. Identification of CRGs and Expression Profile in HNSCC. The results showed that a majority of CRGs (8/10, 80%) were expressed differentially in the tumor and adjacent nontumor tissues (Figures 1(a) and 1(b)), which was validated (9/10, 90%) with the help of the CPTAP RNAseq (Figure 1(c)) and CPTAC Proteomics data (Figure 1(d)). Moreover, differential CDKN2A and LIAS methylation levels were noted in the tumor and adjacent nontumor tissues (Figure 1(e)). Next, we studied the genetic mutations in the CRGs and identified CDKN2A as the gene that underwent the most frequent mutations (Figure 1(f)).

3.2. Development of a Prognostic Cuproptosis-Related Gene Model. We implemented the LASSO Cox regression analysis for developing a prognostic model that was based on the expression profile of the 10 abovementioned genes. They identified a 7-gene signature based on the optimal λ value (Figure 2(a)). Table 2 presents a list of the coefficients of every gene.

We carried out the survival analyses using the values of the risk score and observed that a higher risk score was associated with a poor prognosis ($p < 0.05$, Figures 2(b), S1(a), and S1(b)), which was further validated using the CPTAC clinical data (Figure 2(c)). It has been reported the expression of CRGs may be correlated with disease grade in clear renal cell carcinoma, hepatocellular carcinoma, and melanoma [27–29]. In our study, the high-risk group was significantly related to a higher clinical T stage (Figure 2(d)), HPV^-(Figure 2(e)), PD/SD (Figure 2(f)), higher pathologic T stage (Figure S1(c)), a higher number of positive lymph nodes (Figure S1(d)), and higher grade and shorter PFS (Figure S1(e)) in the TCGA cohort. We determined the risk factors for establishing a 7-CRG-based prognostic model. Our results confirmed that the age, risk score, and radiation therapy could be considered independent prognostic factors for OS (Figures 2(g) and 2(h)). We used the molecular signature for predicting the AUC values of the 1-, 3-, and 5-year survival rates of the patients to be 0.605, 0.662, and 0.621, respectively (Figure 2(i)). Thereafter, we combined the prognostic and clinical pathology models for constructing a nomogram (Figure 2(j)). This combination improved the predictive value of OS over 1, 3, and 5 years and can be effectively used for informing the clinical management about the ideal predictive performance (Figures 2(k) and 2(l)) and clinical advantages (Figure 2(m)). Furthermore, we used a heat map library for determining the risk scores. While assessing the predictive ability of the risk scores, we classified the patients into the low-risk and high-risk groups. We presented the gene heat maps and population follow-up time in order of the ranking (Figure S1(f)). It was noted that the survival rate of the patients decreased with an increase in the risk score.

3.3. Functional Analyses in the TCGA Cohort. After the above steps, we carried out the functional annotation using GSEA and identified 5 enriched KEGG pathways. We noted that the intestinal immune network for T cell receptor signaling pathway, Fc epsilon RI signaling pathway, IgA production, B cell receptor signaling pathway, and the primary immunodeficiency pathways were subjected to enrichment in the low-risk group (Figure 3(a)). Additionally, the Gene Ontology (GO) terms such as immune response regulating cell surface receptor signaling pathway, cell recognition, B cell-mediated immunity, Fc epsilon receptor signaling pathway, Fc receptor signaling pathway, Fc receptor-mediated stimulatory signaling pathway, and the humoral immune response were enriched in the HNSC samples and exhibited a low-risk score (Figure 3(b)). Figure 3(c) presents the 5 CRGs that were enriched in the cancer-related pathway, such as the NF-κB pathway. For determining the relationship between the risk scores and immune status, we determined the enrichment scores of various immune cell sub-

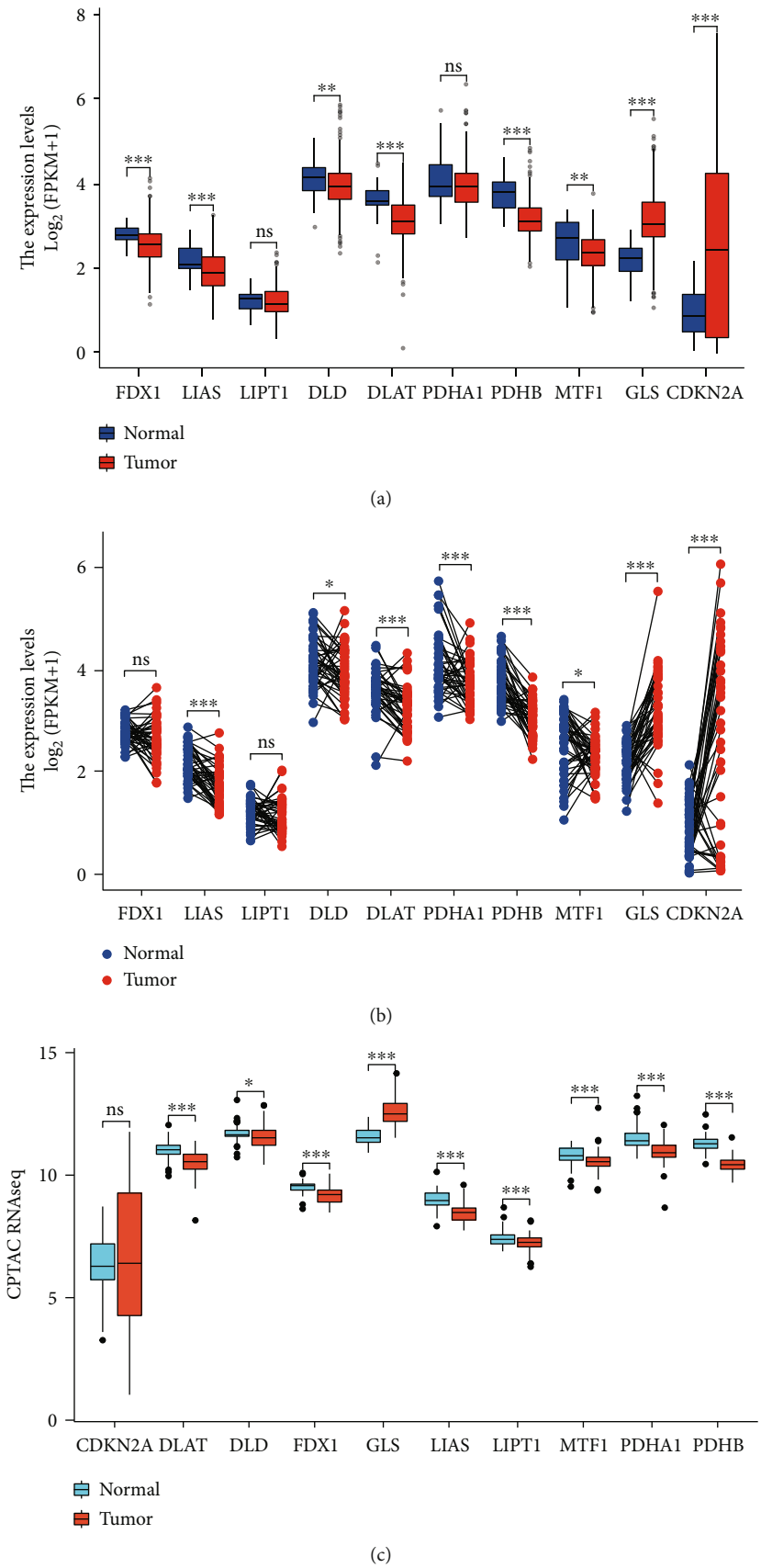

Figure 1: Continued.

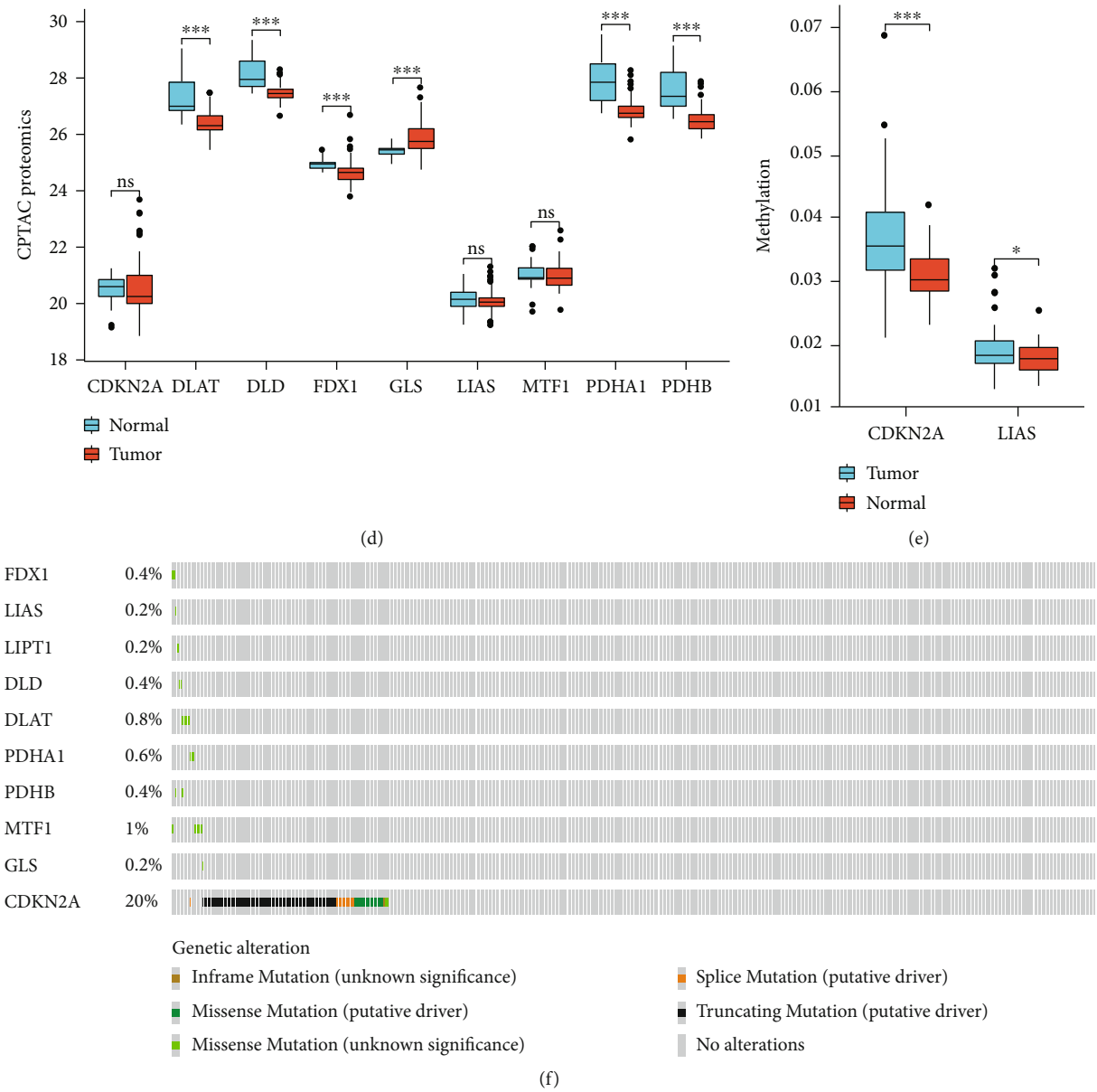

Figure 1: Expression profile of cuproptosis-related genes. (a), (b) Box plots present the differentially expressed cuproptosis-related genes between HNSCC and normal sample. (c), (d) Box plots validated the expression profile from CPTAC RNAseq and proteomics data. (e) The methylation degree of CDKN2A and LIAS. (f) Mutation status.

populations using ssGSEA. We assessed the immune landscape of 22 immune cell types in the HNSCC patients with the help of the ssGSEA technique (Figure 3(d)). Comparing the data in the TCGA cohort highlighted the varying number of activated CD4 T cells, activated B cells, activated CD8 T cells, follicular helper CD8 T cells, effector memory CD8 T cells, and natural killer cells in the two risk groups ($p < 0.05$, Figure 3(e)). This study showed that the ESTIMATE and immune scores were inversely linked to the risk scores (Figure 3(f)). For avoiding any errors in the calculations, we estimated the infiltration level of the TIICs using 7 algorithms, i.e., MCP-counter, Cibersort, Cibersort-ABS, TIMER, xCell, quanTIseq, and EPIC (Figure 3(g)).

3.4. Prediction of the Tumor Immune Microenvironment Using the Risk Model. Here, we noted that the risk signature was inversely related to the B cell and CD8+ T cells effector genes (Figures 4(a) and 4(b)). This risk signature was negatively related to a majority of the immune checkpoint inhibitors, like TIGIT, LAIR, PDCD1, LAG3, KIR3DL1, HAVCR2, IDO1, and CTLA-4 (Figure 4(c)). Additionally, the risk signature exhibited a strong correlation with the T cell-inflamed GEP in the HNSCC, which further showed an increase in the low-risk score group (Figure 4(d)). The anticancer immune response is reflected in the cancer immunity cycle consisting of seven phases [14]. A majority of the components in the immune cycle, like the priming

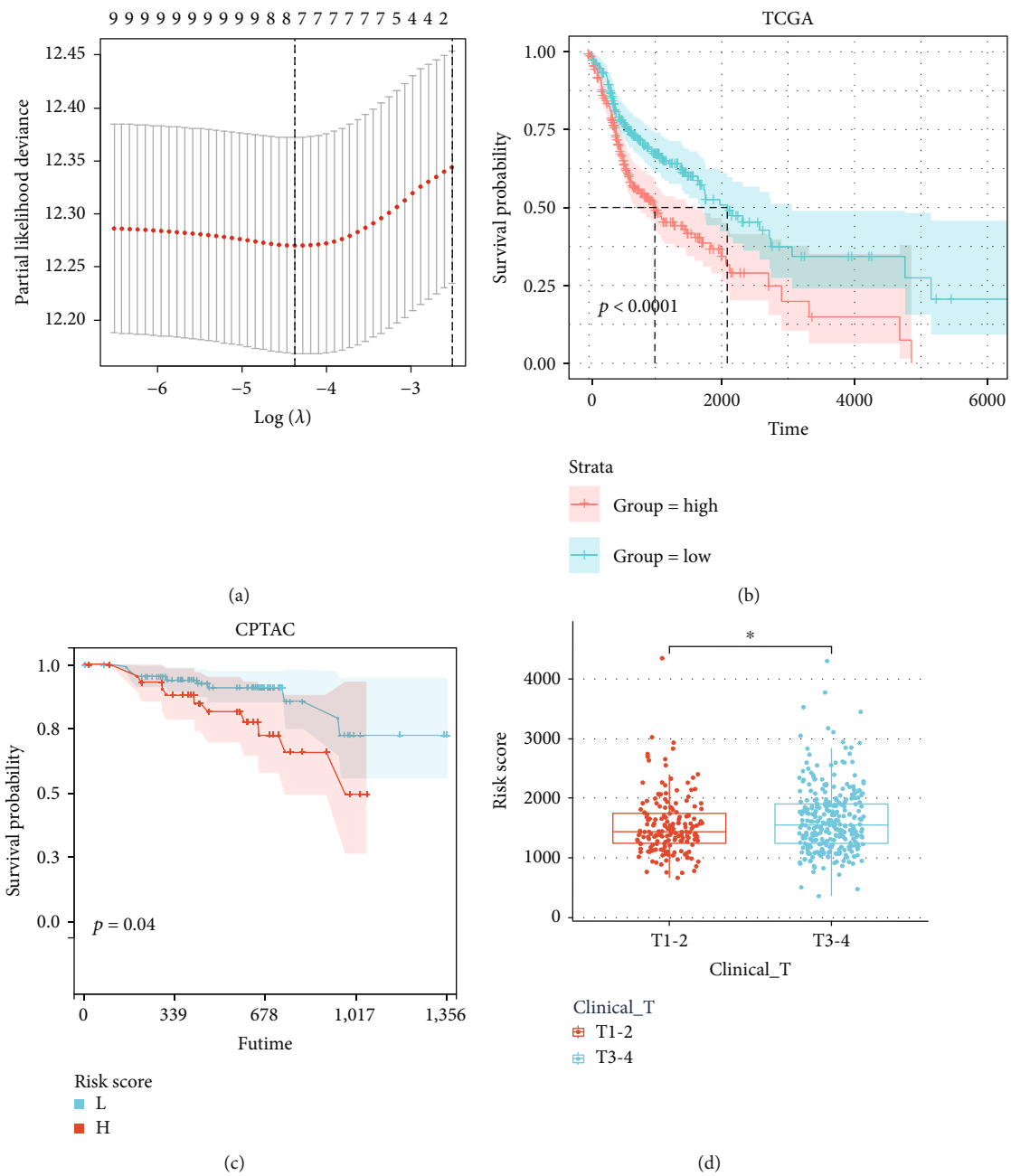

Figure 2: Continued.

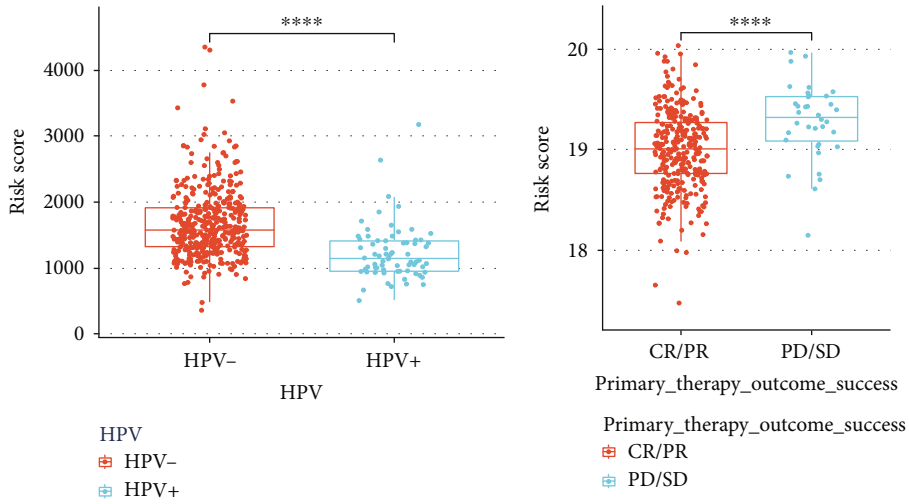

(e) (f)

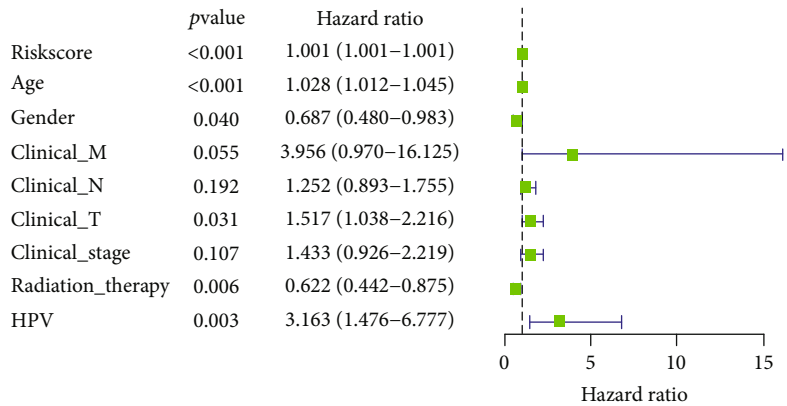

(g)

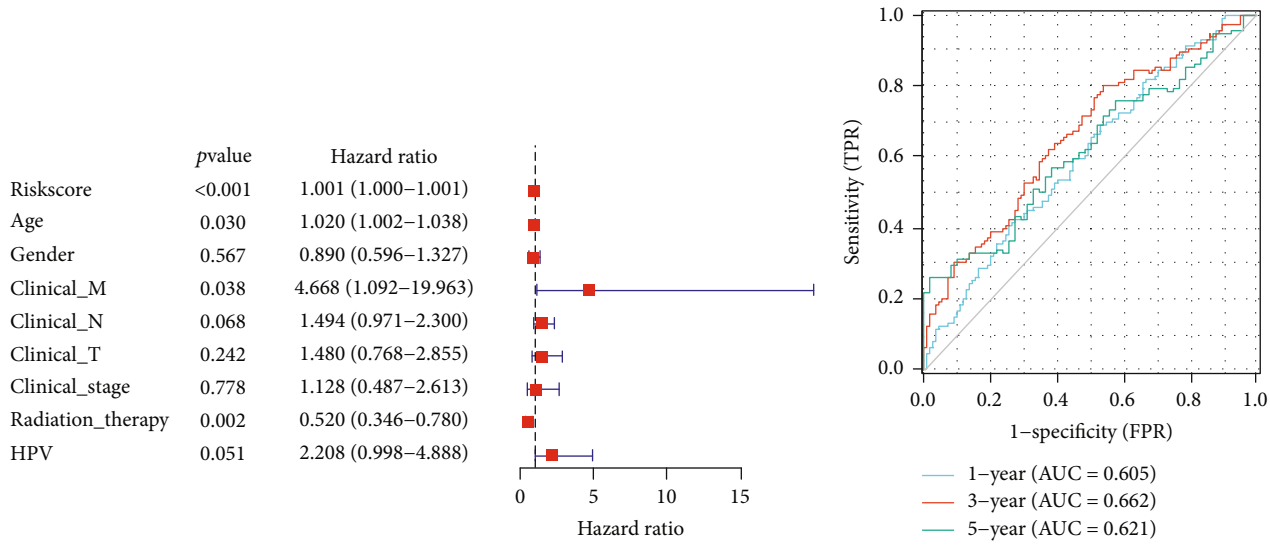

(h) (i)

Figure 2: Continued.

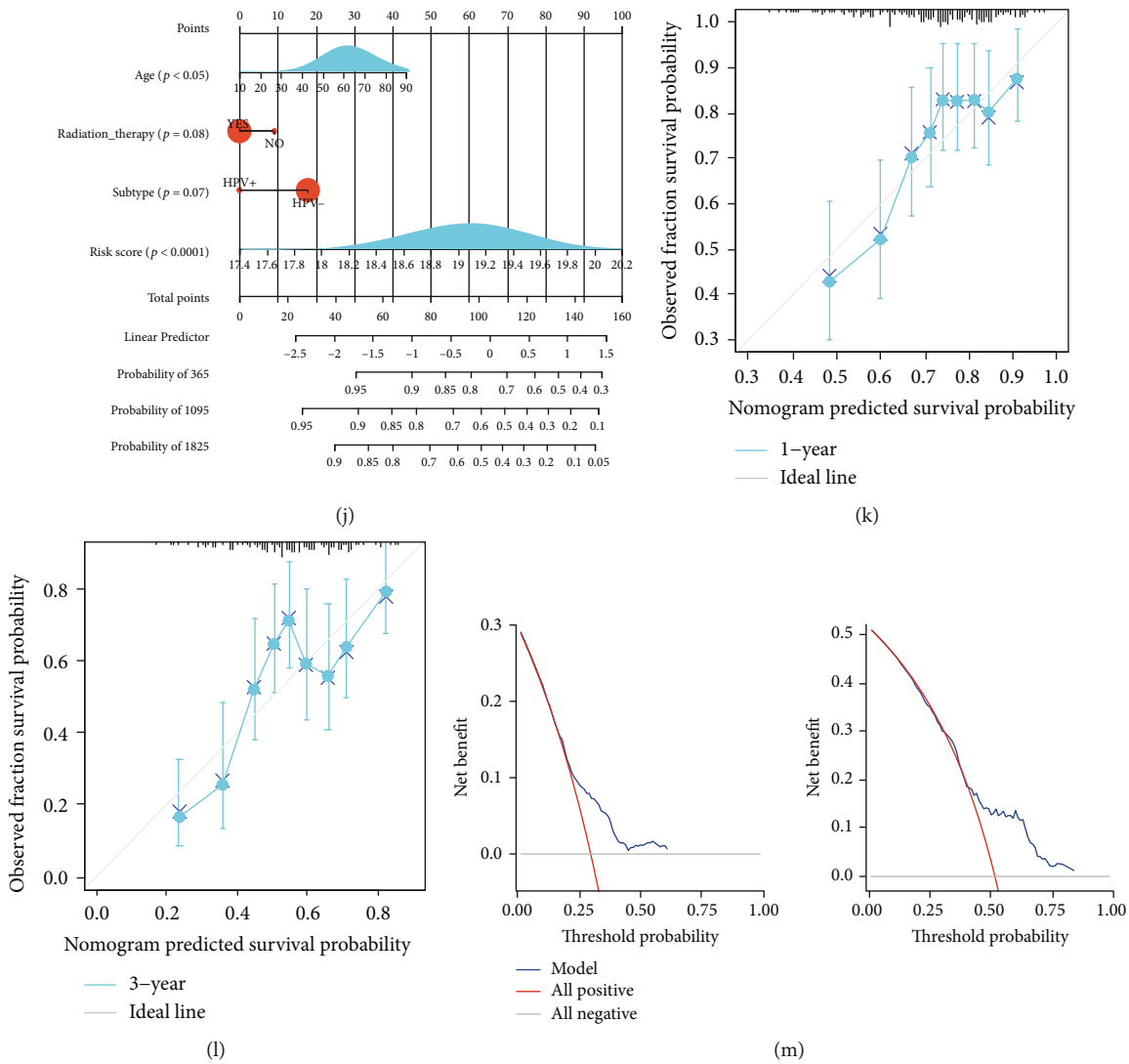

Figure 2: Construction of CRGs prognostic model and survival analysis. (a) The 7 CRGs used for construction of the gene risk model. (b), (c) In TCGA and CPTAC cohorts, low-risk group patients had favorable OS rates compared with those in the high-risk group. (d–f) Correlation analysis of risk score and clinical characteristics. (g), (h) Cox analyses, univariate and multivariate, showing the independent prognostic significance of the risk signature in predicting the OS of HNSCC patients in the TCGA cohort. (i) The ROC curve for 1-, 3-, and 5-year OS of HNSCC patients in the TCGA cohorts. (j) The predicted the 1-year, 3-year, and 5-year OS of HNSCC patients based on the constructed nomogram. (k), (l) Calibration curve of the OS predicted by the nomogram model. The dashed diagonal line represents the ideal nomogram. (m) DCA curve for 1- and 3-year prognosis.

and activation (Step 3), as well as immune cell transportation to the tumors (Step 4) (recruiting monocytes, CD4 T cells, Th2 cells, Th17 cells, and Tregs), were found to be higher in the low-risk score group (Figure 4(e)).

The abilities of the TCR and BCR from the TCGA high-grade serous ovarian cancer (HGSOC) cohort were then examined. The mean TCR and BCR diversity values were variable based on the risk signature, wherein the low-risk score group showed the maximal diversity (Figure 5(a)). Then, we investigated MATH, TMB, and MSI data and observed that the patients in the high-risk score group showed a higher MATH score (which included the silent mutation rate, non-silent mutation rate, wound healing, macrophage regulation, fraction altered, and the lymphocyte infiltration signature score), TMB score, and MSI score (Figures 5(b)–5(d)). We used the TIDE algorithm for predicting the immune checkpoint blockade (ICB) responses to help identify patients who might benefit from immunotherapy. Compared to the patients in the high-risk score group, patients belonging to the low-risk group showed a significantly better response to immunotherapy (Figures 5(e)–5(f)). Furthermore, we estimated the IC50 for every subtype using the predictive model of gemcitabine, cisplatin, doxorubicin, and docetaxel, similar to the technique proposed by Wang [26]. The results of these experiments indicated that the patients with a high-risk score were more susceptible to chemotherapy than the low-risk patients

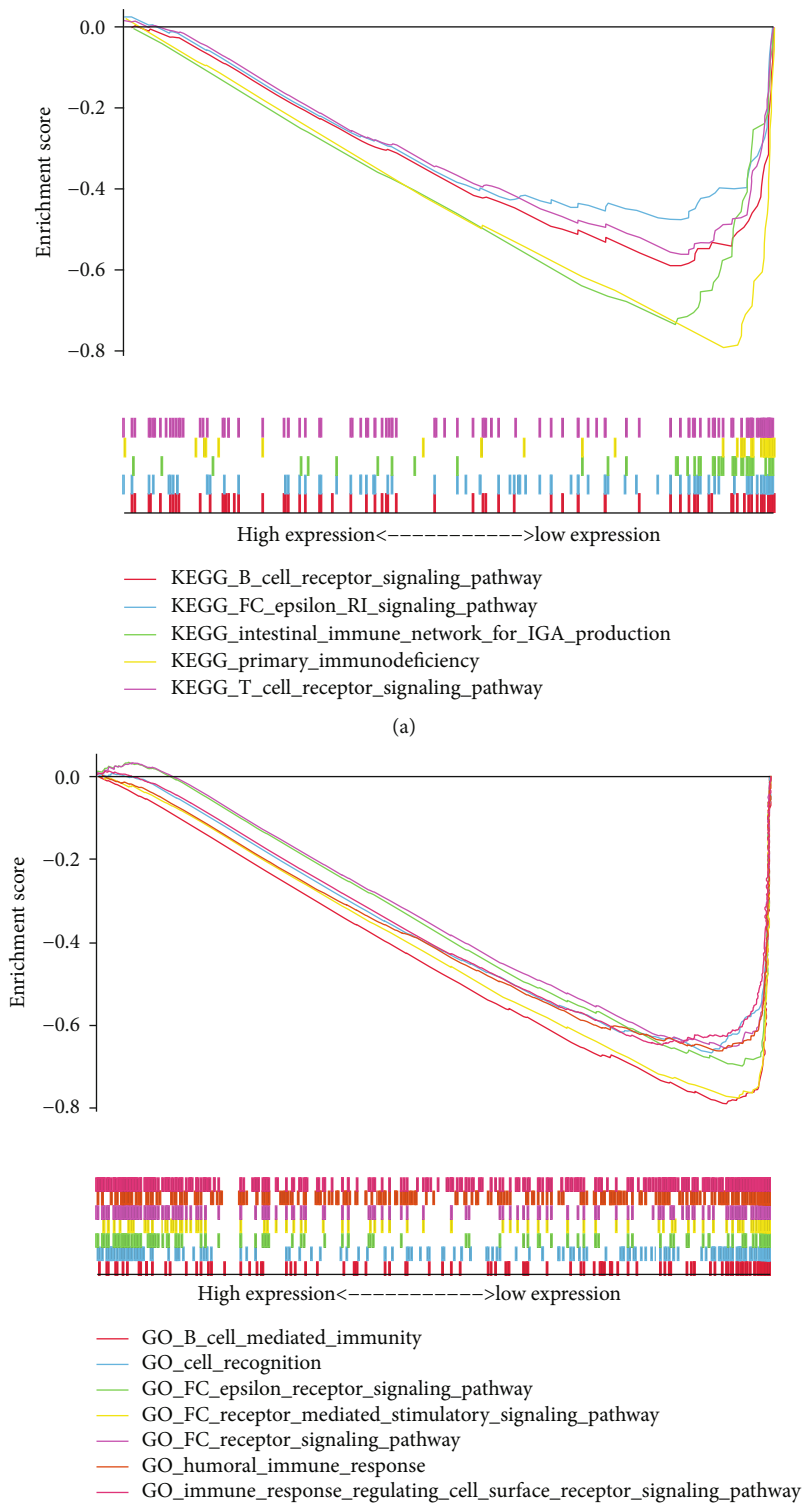

Figure 3: Continued.

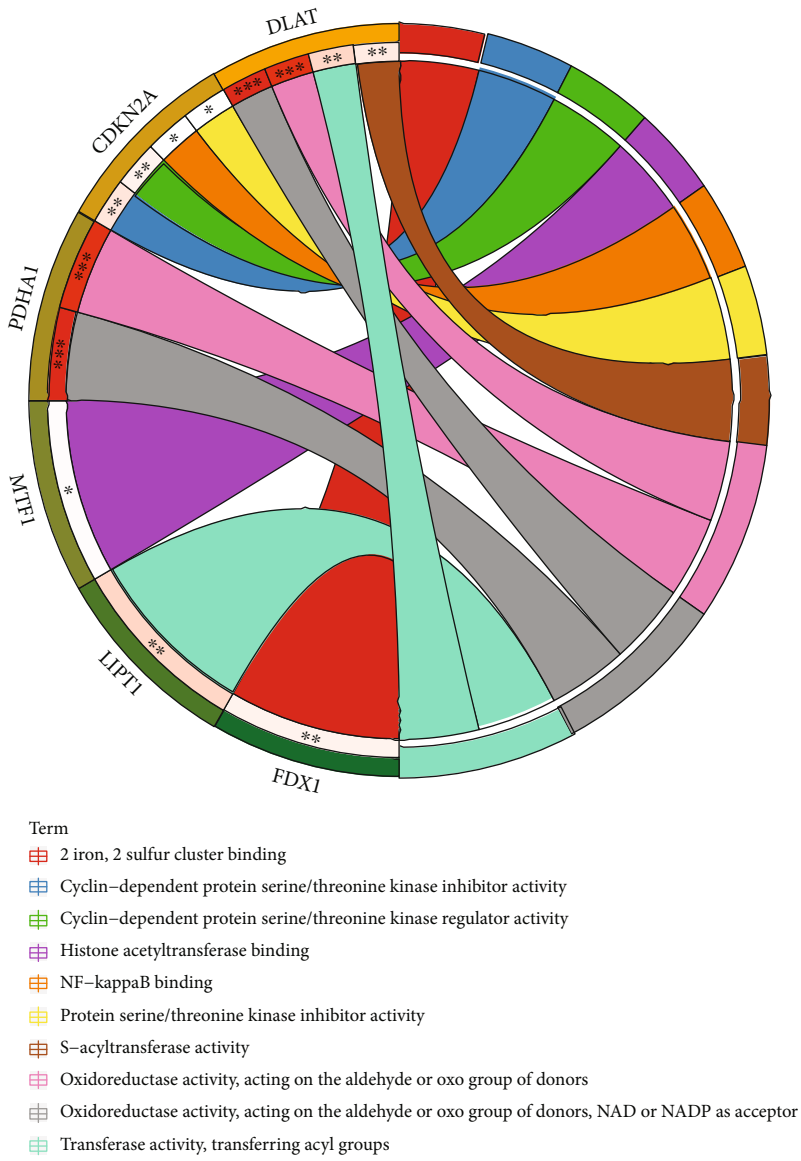

(c)

Figure 3: Continued.

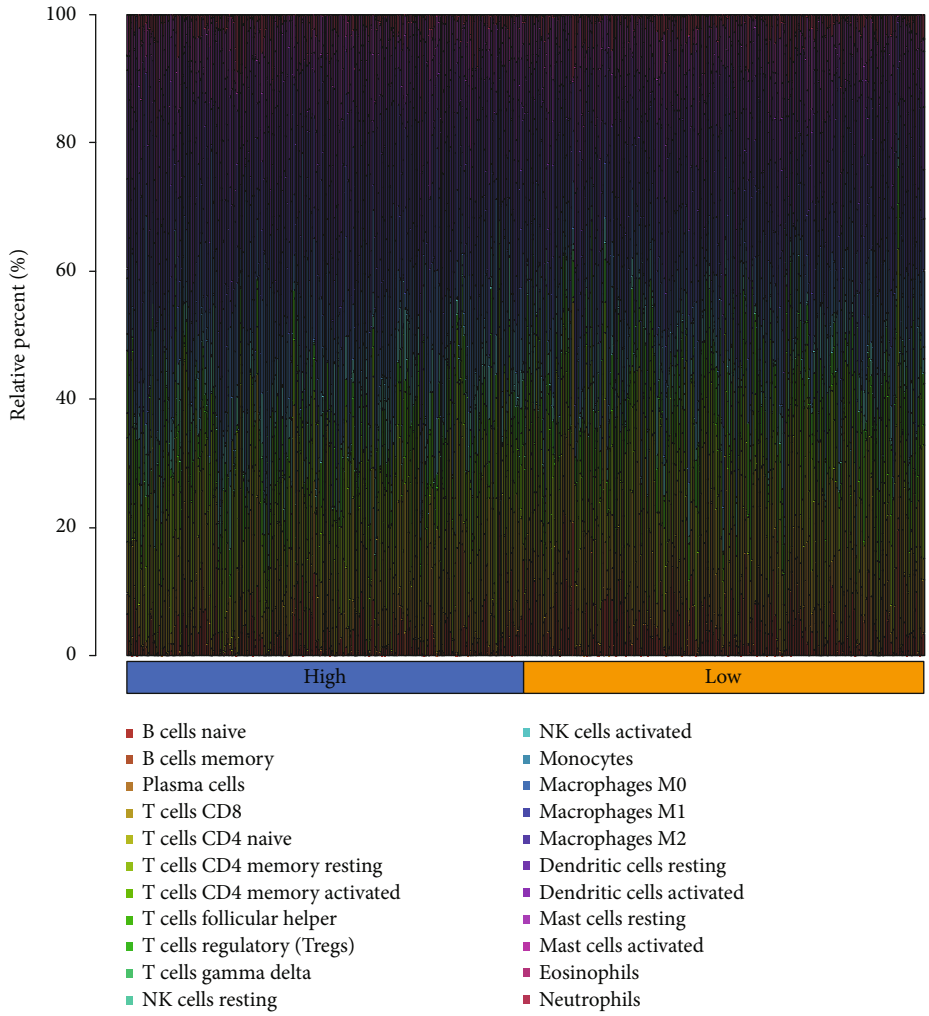

(d)

Figure 3: Continued.

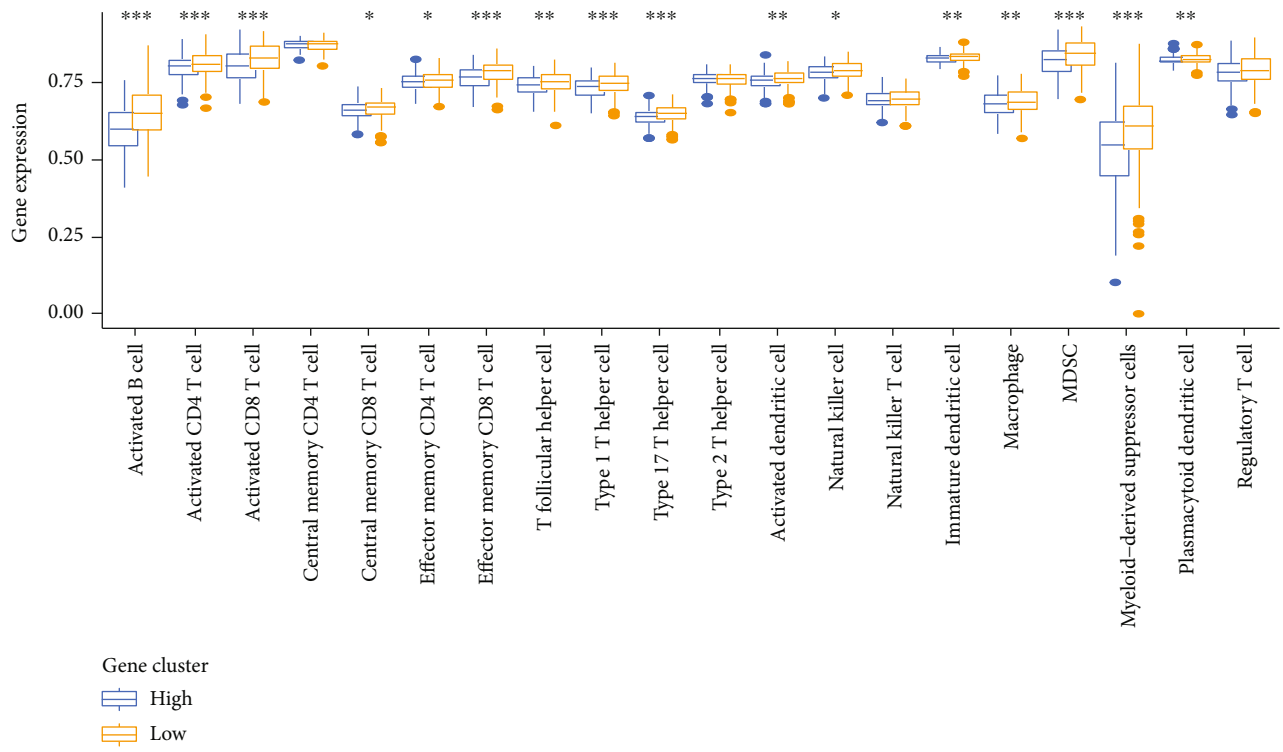

(e)

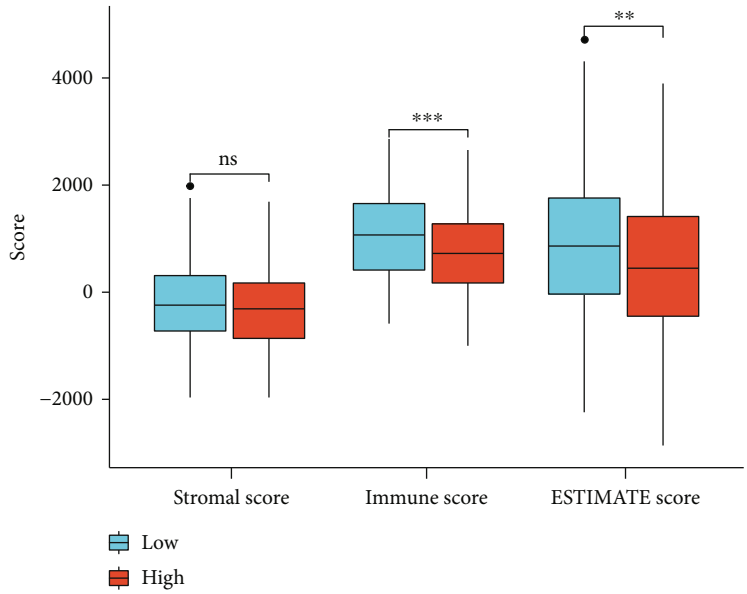

(f)

Figure 3: Continued.

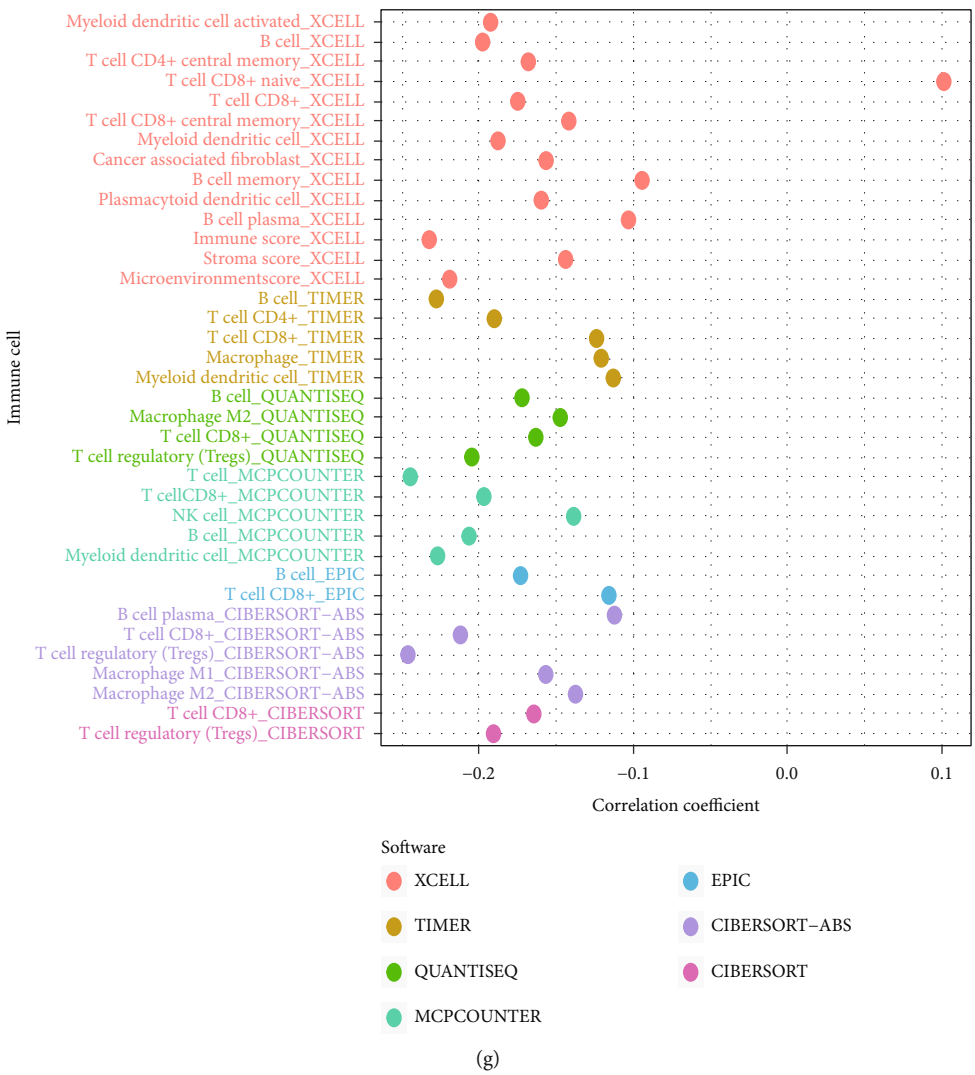

(g)

Figure 3: Correlation between the risk signature and immune microenvironment of HNSCC. (a)–(c) Enrichment plots from gene set enrichment analysis (GSEA). (d) Relative proportion of immune infiltration in HNSCC patients. (e) Box plot shows the differential immune infiltration between low-risk and high-risk groups. (f) Box plot present the differential stromal score, immune score, and ESTIMATE score between low-risk and high-risk groups. (g) Relationship between the risk score and infiltration levels of severe TIICs, as determined by seven separate algorithms.

(gemcitabine: $p = 9.7E6$; cisplatin: $p = 8.0E - 4$; docetaxel: $p = 6.0E - 5$; and doxorubicin, $p = 3.1E3$; (Figures 5(g)–5(h)) and S2(a) and S2(b)).

3.5. Identifying the Cuproptosis-Associated lncRNAs Based on their Prognostic Value in TCGA. Here, we established the CRGs and lncRNA networks (Figure 6(a)). They identified 109 cuproptosis-related lncRNAs using the Pearson correlation analysis ($|\text{cor}| > 0.1, \text{Pp} < 0.05$). Thereafter, they used the univariate Cox regression and identified the 18 lncRNAs which showed an expression level that was associated with the prognosis of the patients, thus demonstrating that they exhibited a prognostic predictive value ($p < 0.05$, Figure 6(b)). The results showed that all cuproptosis-related lncRNAs (11/11, 100%) were expressed differentially between the tumor and adjacent nontumor tissues (Figure 6(c)).

3.6. Classification Subtypes Using the Homogeneous Cuproptosis-Related lncRNAs. We used an unsupervised clustering technique for classifying 501 HNSCC samples into two groups from the TCGA cohort (Figure 6(d)). A survival analysis, depending on the subtype, showed that cluster 2 was associated with a poor prognosis (Figure 6(e)). Figure 6(f) depicts the expression of the 18 lncRNAs, as well as risk scores and clinicopathological variables. In addition, PD-L1 was significantly associated with most of the lncRNAs mentioned above (Figure 6(g)). Patients with TCGA in the cluster 2 had higher ratios of naive B cell ($p = 0.004$), CD8 T cell ($p < 0.001$), and activated resting

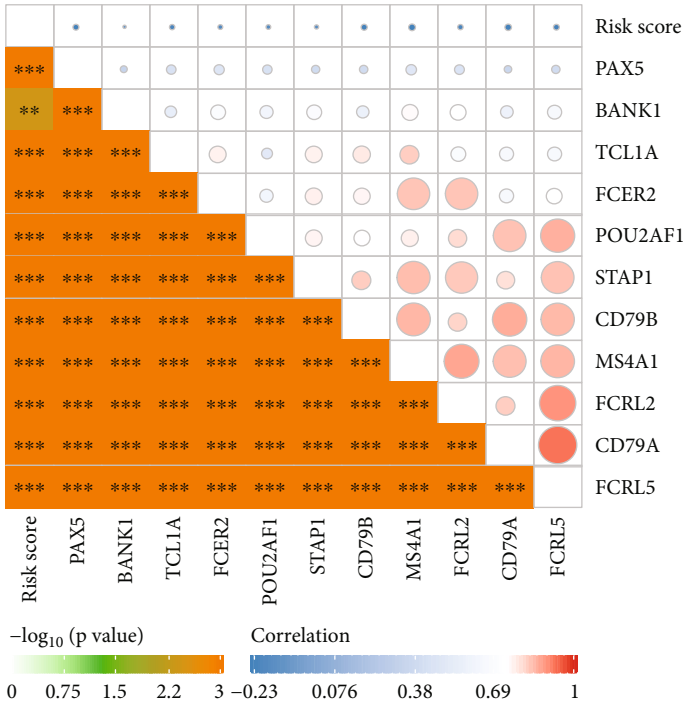

(a)

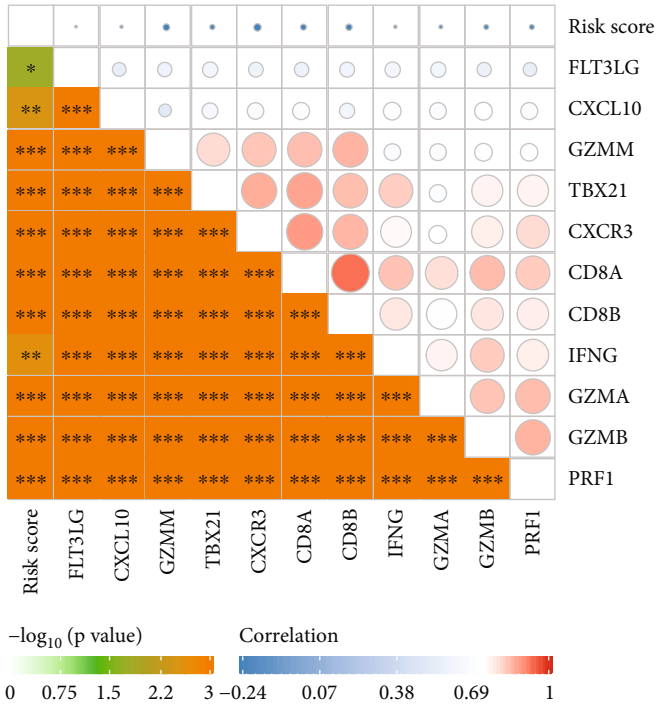

(b)

Figure 4: Continued.

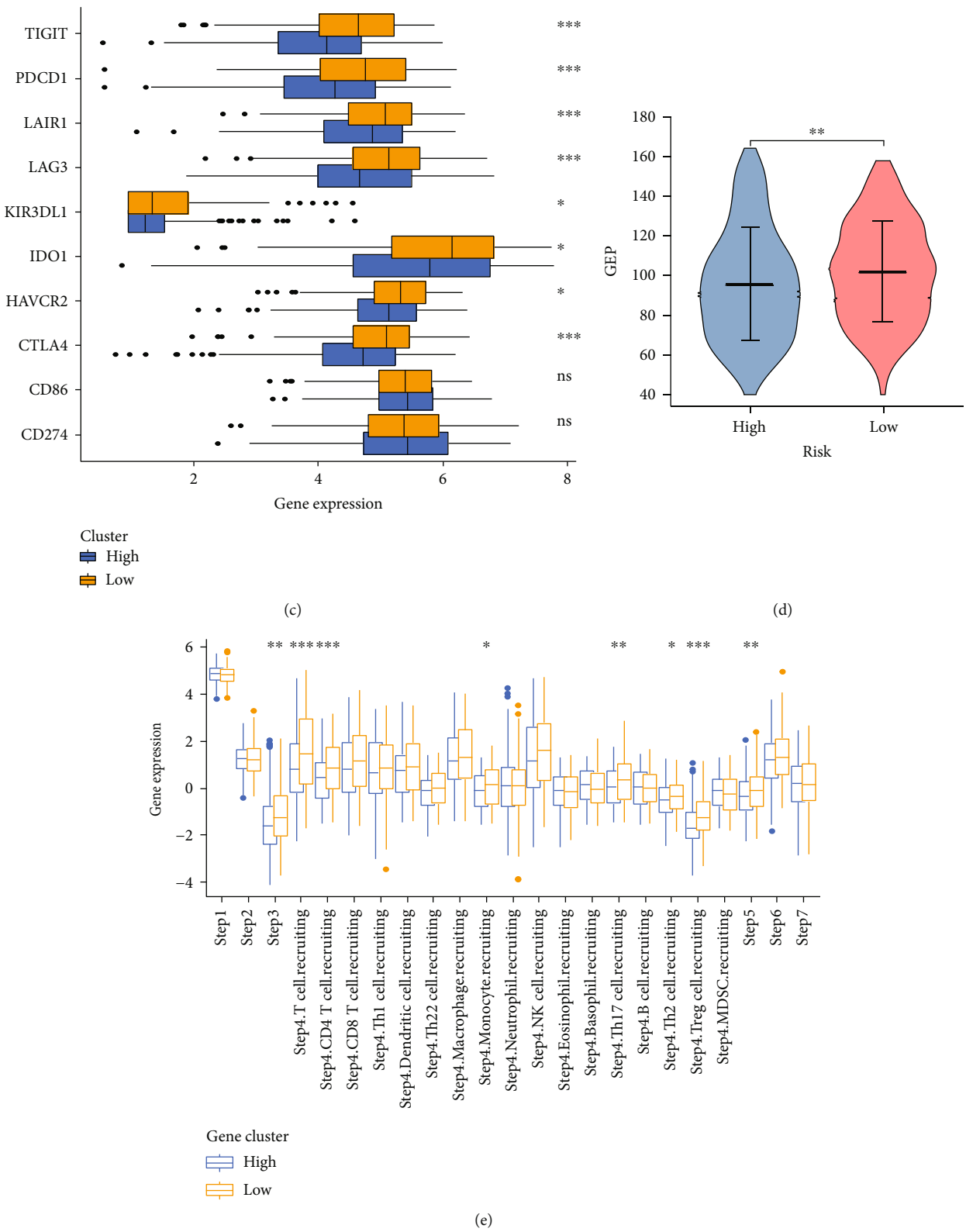

Figure 4: Immune-related functions and in high- and low-risk groups. (a) Relationship between risk score and B cell effector genes. (b) Relationship between risk score and T cell effector genes. (c) Relationship between risk score and 10 inhibitory immune checkpoints. (d) Differences in GEP (T cell-inflamed gene expression profile) between low- and high-risk groups. (e) Difference between low- and high-risk groups at distinct stages of the cancer immunity cycle.

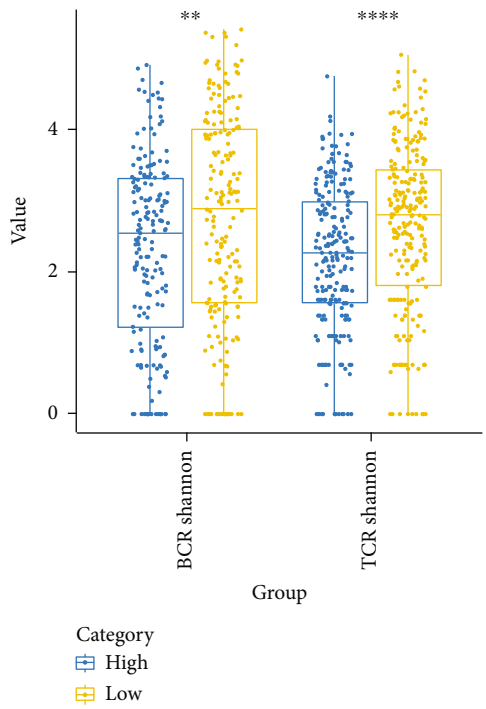

(a)

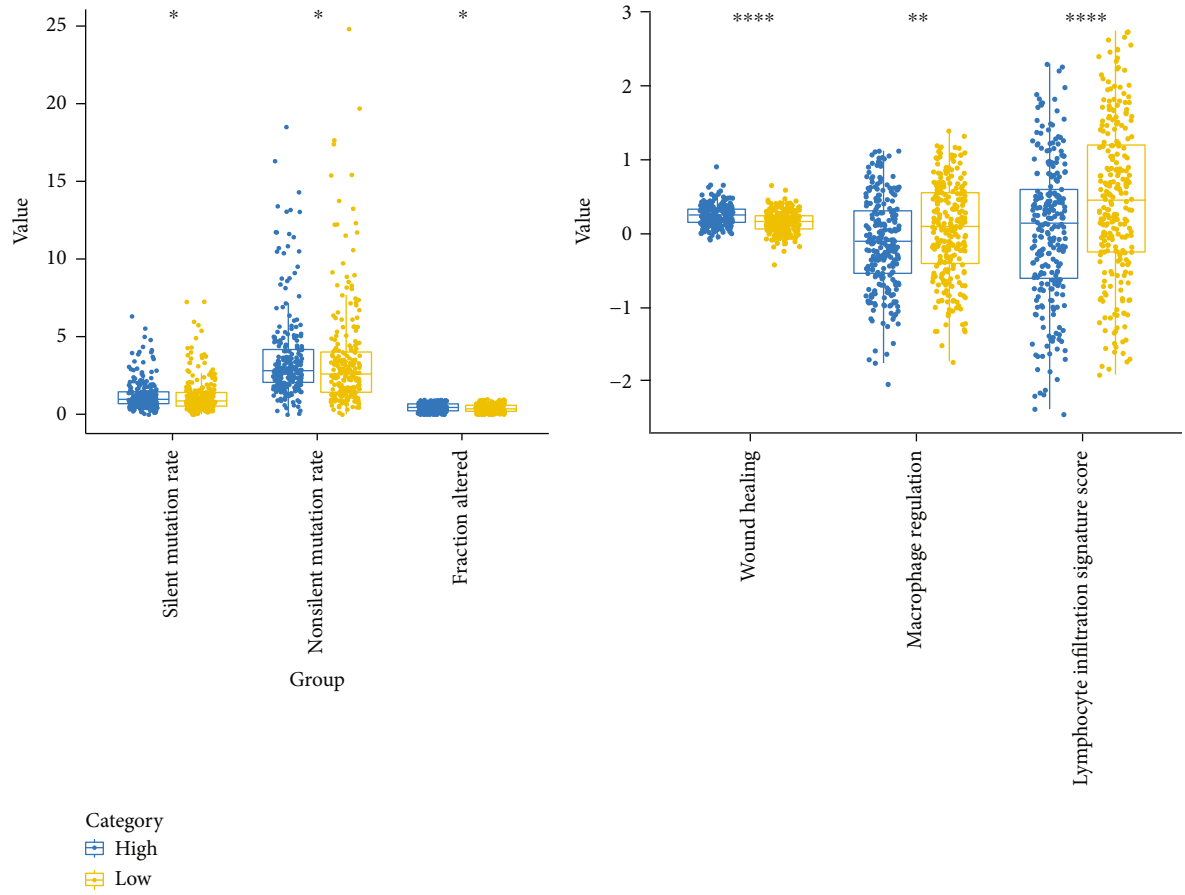

(b)

Figure 5: Continued.

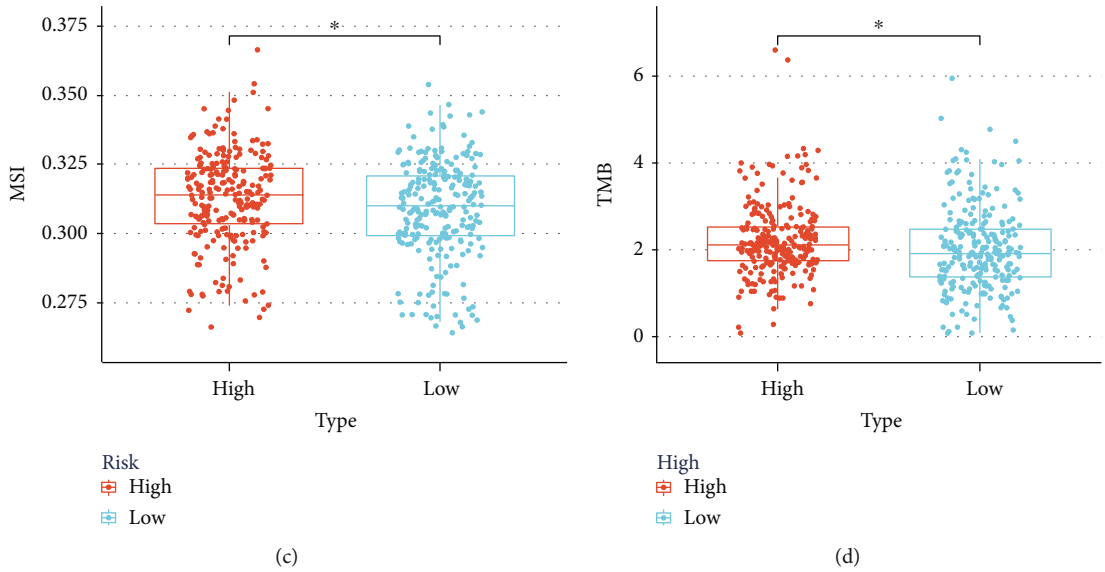

(c) (d)

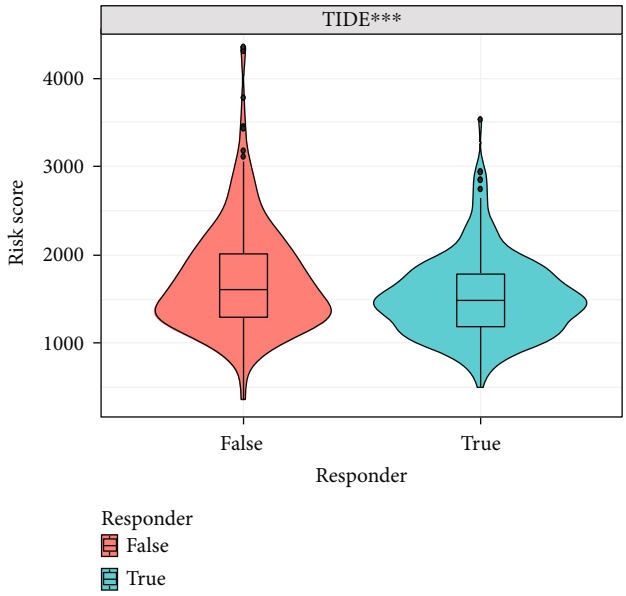

(e)

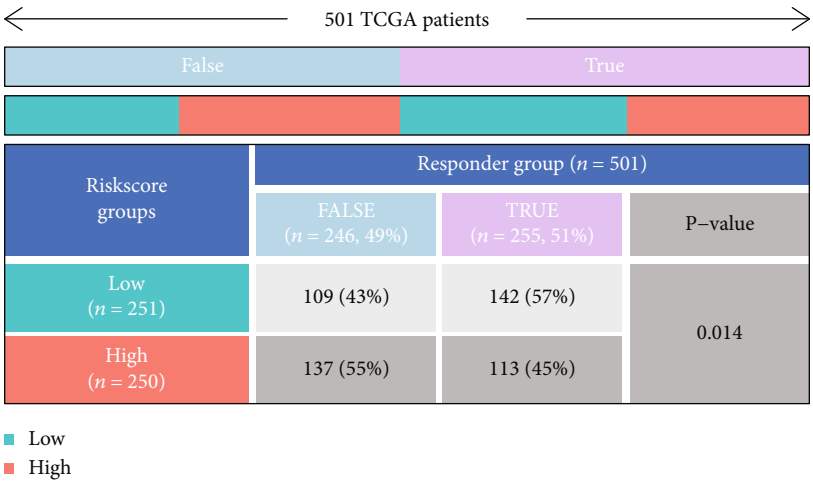

Riskscore groups	Responder group (n = 501)		
	FALSE (n = 246, 49%)	TRUE (n = 255, 51%)	P–value
Low (n = 251)	109 (43%)	142 (57%)	0.014
High (n = 250)	137 (55%)	113 (45%)	

(f)

Figure 5: Continued.

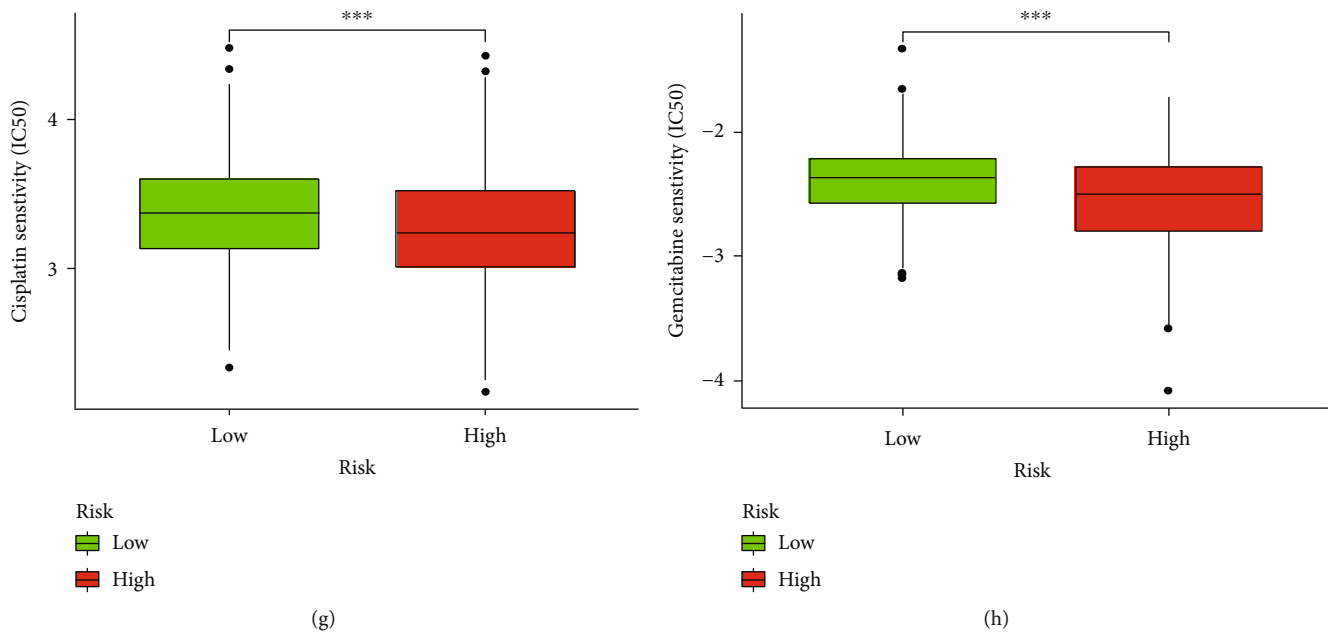

Figure 5: Correlation of the risk score with immune scores, immunotherapy biomarkers, and conventional therapy. (a) Differences in TCR and BCR diversity values between low- and high-risk groups. (b) Differences in MATH (including silent mutation rate, non-silent mutation rate, fraction altered, wound healing macrophage regulation, and lymphocyte infiltration signature score) between low- and high-risk groups. (c)–(d) Differences in MSI and TMB between low- and high-risk groups. (e) Differences in TIDE score between low- and high-risk groups in the TCGA cohort. (f) The anticipated immunotherapy (TRUE/FALSE) response rate to anti-PD-L1 in low- and high-risk groups in the TCGA cohort. (g)–(h) The IC50 of cisplatin and gemcitabine in the low-risk group were higher than those in the high-risk group.

CD4 T cells ($p < 0.001$) (Figures 6(h)–6(i) and S3(a)–S3(e)). The ESTIMATE and stromal scores were lower in cluster 2 (Figures 6(j) and S3(f)).

3.7. Construction of Prognostic Cuproptosis-Related lncRNA Signature. To construct an optimal cuproptosis-related lncRNA risk model for predicting HNSCC prognosis, the 11 cuproptosis-related lncRNA were identified using LASSO regression analysis (Figure 7(a)). Meanwhile, the 501 HNSCC patients were divided into the train group and test group for internal verification. The coefficients of each lncRNA are listed in Table 3.

The results for both the train and the test groups indicated that the low-risk patients experienced a longer OS period in comparison to the high-risk patients (Figures 7(b) and 7(c)). We used the ROC curves for assessing whether the expression profiles of cuproptosis-related lncRNAs could be employed as a potential biomarker for predicting the onset and progression of HNSCC. An AUC of 0.731 was observed in the train group, while the test group showed an AUC of 0.596, implying that this prognostic model is specific and fairly sensitive (Figures 7(d) and 7(e)).

Figure 7(f) depicts the expression of 11 cuproptosis-related lncRNAs, as well as clinicopathological variables, clusters, and risk scores. Then, we carried out the univariate and multivariate Cox regression analyses for determining if the cuproptosis-related lncRNAs could be applied as an independent prognostic model for assessing the OS in HNSCC patients. The results indicated that the cuproptosis-related lncRNA risk model was an effective independent prognostic indicator in the test and the train groups (Figures 7(g)–7(j)). Furthermore, the risk-score values were quantified with the aid of the heat map library, demonstrating that high-risk scores were related to shorter survival times (Figures S3(g)–(h)). According to the survival analysis, the low-risk patients showed a longer survival time than the high-risk patients (Figures 8(a) and 8(b) and S4(a)–(i)). We further observed that the stage, grade, immune scores, and clusters were differently distributed between the high and low-risk groups, which were further demonstrated in Figures 8(c)–8(d) and S5(a)–S5(b). Additionally, we investigated the relationship between the lncRNA risk model and immune cells and observed that the risk model was negatively correlated to the CD8 T cells, CD4 memory-activated T cells, and naive B cells (Figures 8(e)–8(g)). However, it was positively related to the CD4 memory resting T cells (Figure S5(c)).

4. Discussion

In the past decade, reports showed that mammalian cells are harmed by essential trace metals. Metals have emerged as a promising new method of killing cells other than via apoptosis. The new mechanism reported by Tsvetkov et al. suggests that the use of copper may be particularly beneficial for cancer patients that are naturally resistant to apoptosis,

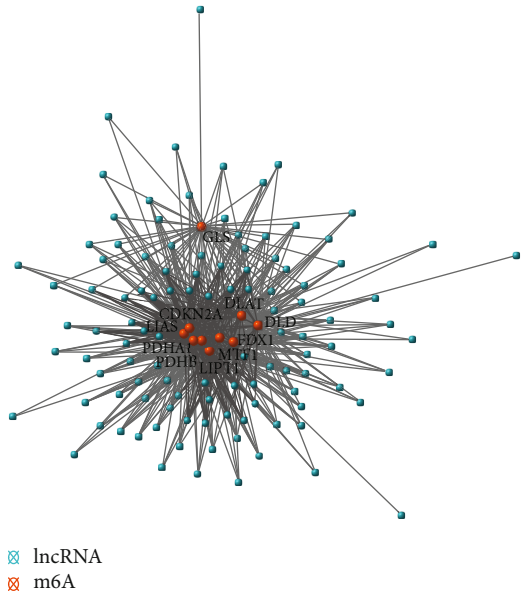

(a)

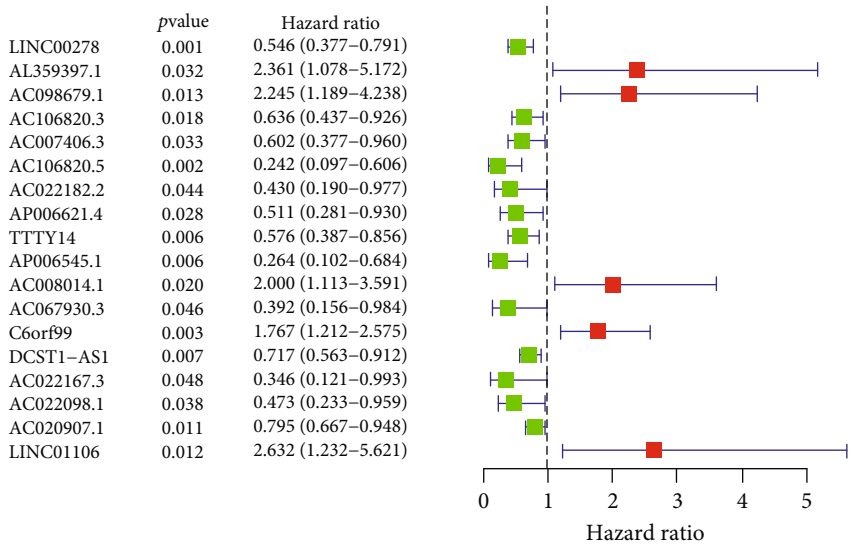

(b)

Figure 6: Continued.

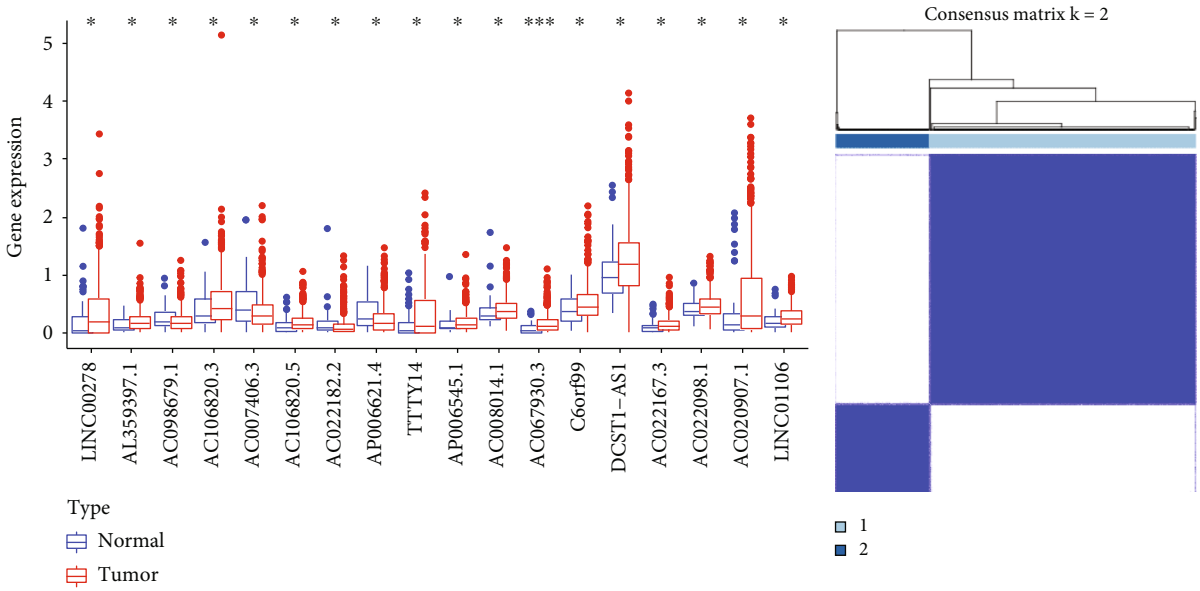

(c) (d)

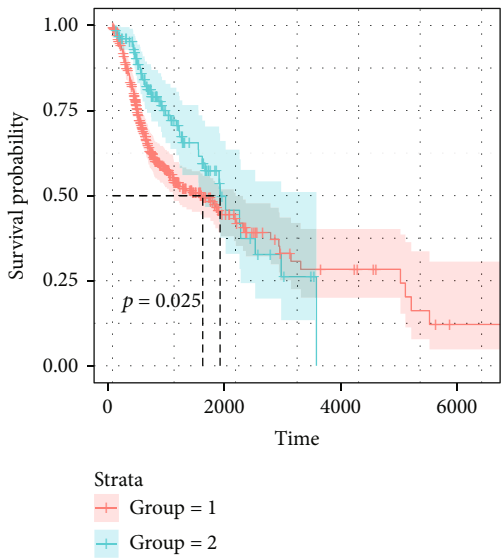

(e)

Figure 6: Continued.

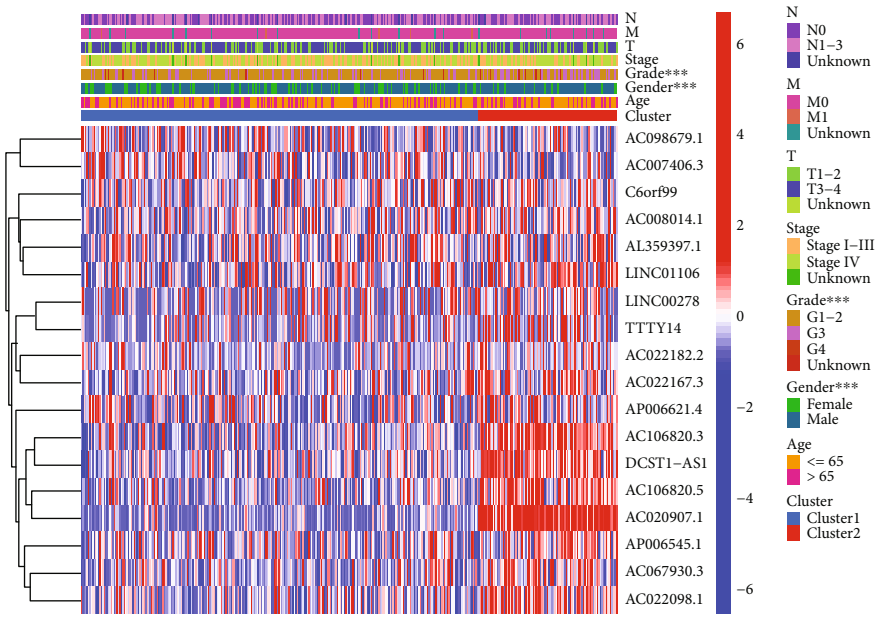

(f)

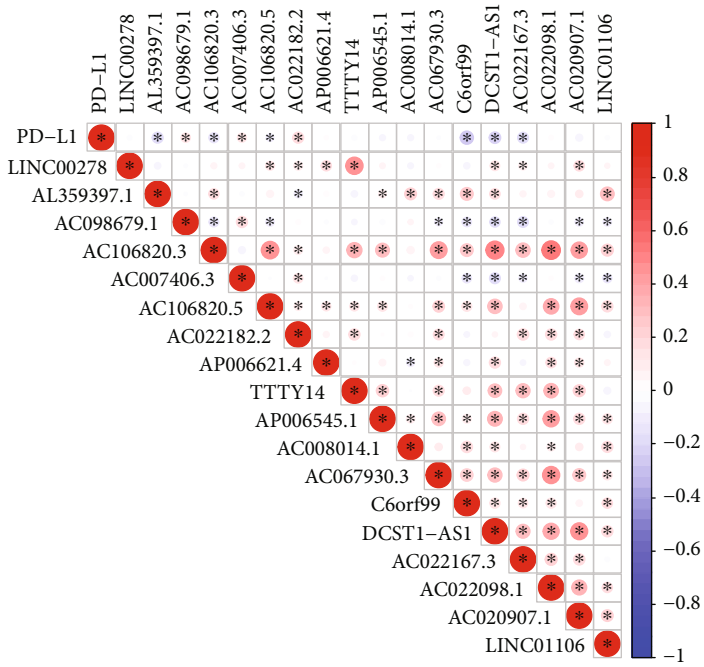

(g)

Figure 6: Continued.

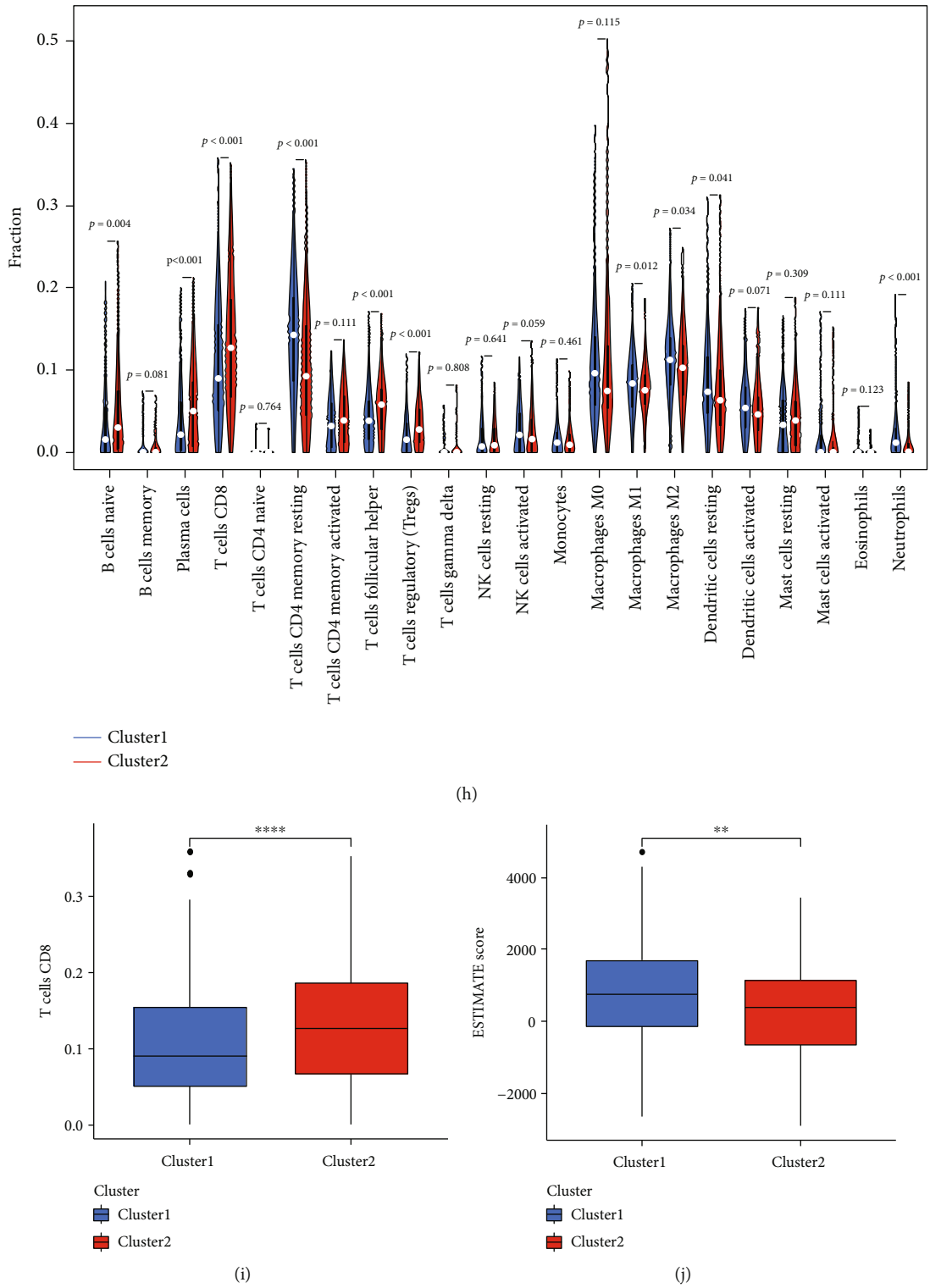

Figure 6: Identification of cuproptosis-associated 18-lncRNAs with prognostic value and immune response in HNSCC patients. (a) A coexpression network of cuproptosis-related lncRNAs and genes was constructed and visualized. (b) 18 independent prognostic predictor lncRNA signatures with different expressions of HNSCC. (c) Box plot presents the differentially expressed cuproptosis-related lncRNAs between HNSCC and normal sample. (d) 501 HNSCC samples from the TCGA cohort were classified into 2 clusters using an unsupervised clustering method. (e) The Kaplan-Meier curve showed that patients in cluster 2 displayed a shorter overall survival than those in cluster 1. (f) Heat map of the prognostic characteristics and clinicopathological correlation of cuproptosis-related lncRNAs. (g) Correlation analysis of PD-L1 expression and 18 independent prognostic predictor lncRNA signatures. (h) Violin plot of immune-infiltrating lymphocytes between cluster 1 and cluster 2. (i) Box plot presents the differentially infiltrated CD8 T cells between cluster 1 and cluster 2. (j) Differences in ESTIMATE score between cluster 1 and cluster 2.

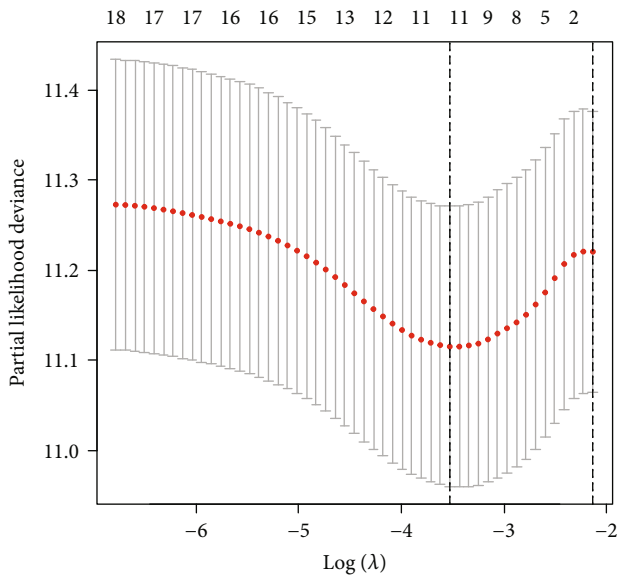

(a)

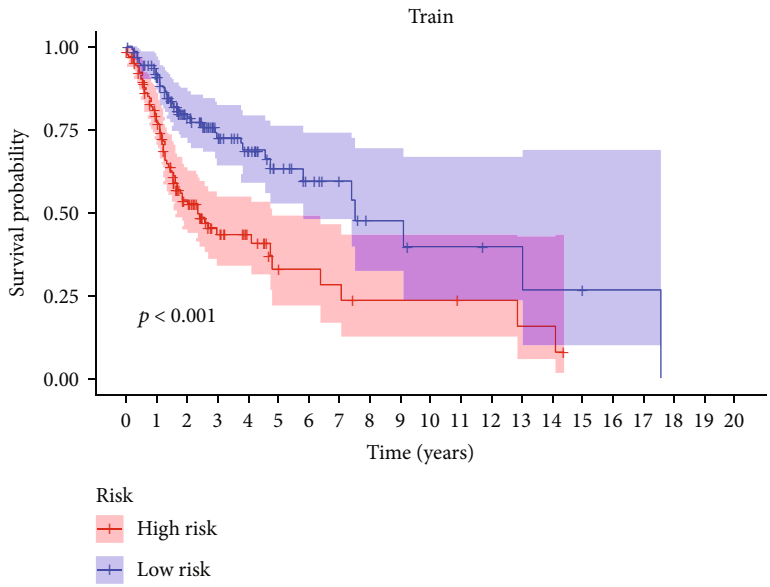

(b)

Figure 7: Continued.

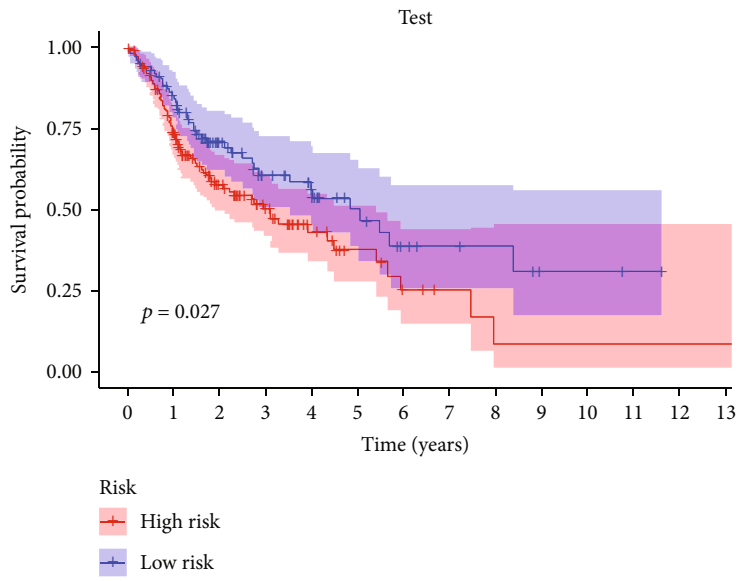

(c)

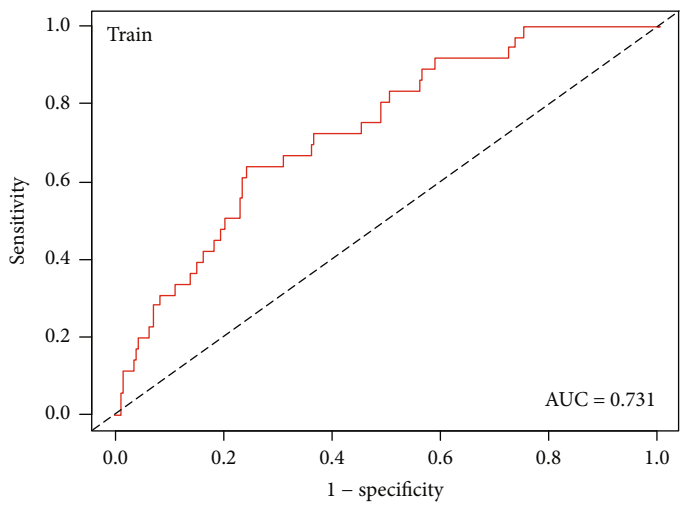

(d)

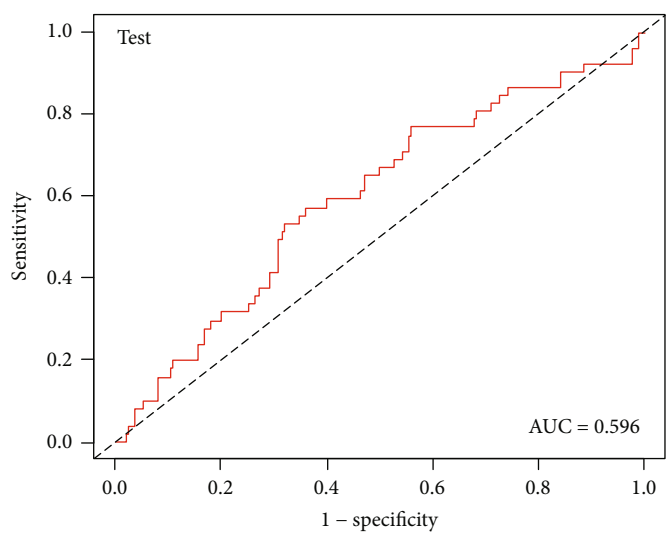

(e)

Figure 7: Continued.

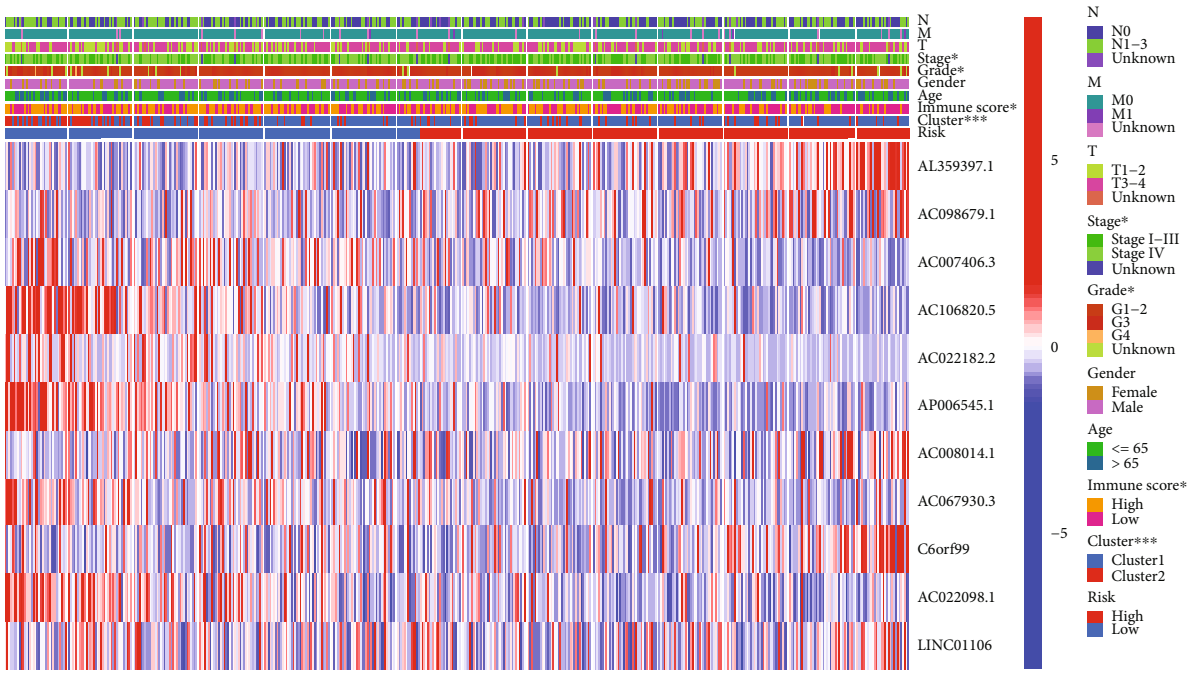

(f)

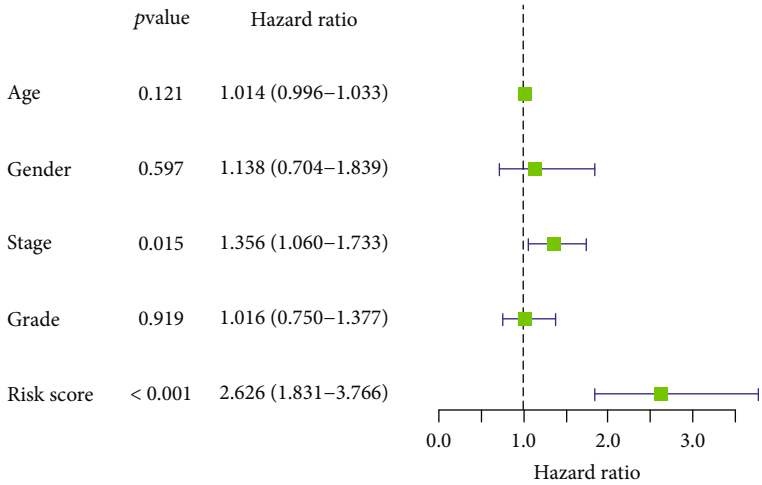

(g)

Figure 7: Continued.

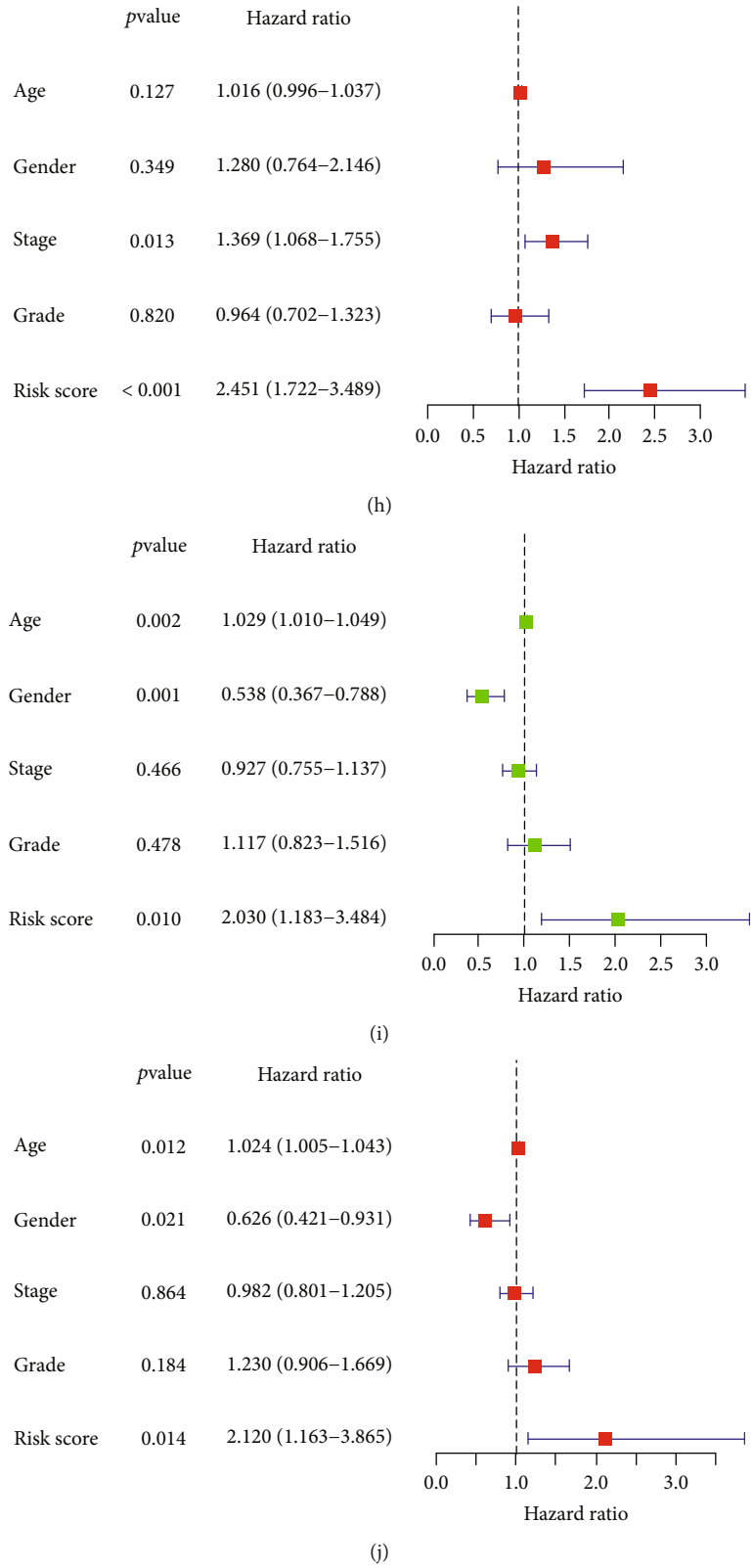

Figure 7: Construction of prognostic cuproptosis-related lncRNA signature. (a) The 11 cuproptosis-related lncRNA used for construction of the gene risk model. (b)–(c) Survival analysis show the prognosis of high-risk and low-risk patients in the train group (b) and the test group (c). (d)–(e) The ROC for risk score with OS for HNSCC cohorts in the train group (d) and the test group (e). (f) Heat map of the prognostic characteristics and clinicopathological correlation based on lncRNA-related risk score. (g)–(j) Univariate and multivariate Cox regression analyses for the lncRNA-related risk score model as an independent prognostic factor both in the train group (g), (h) and the test group (i), (j).

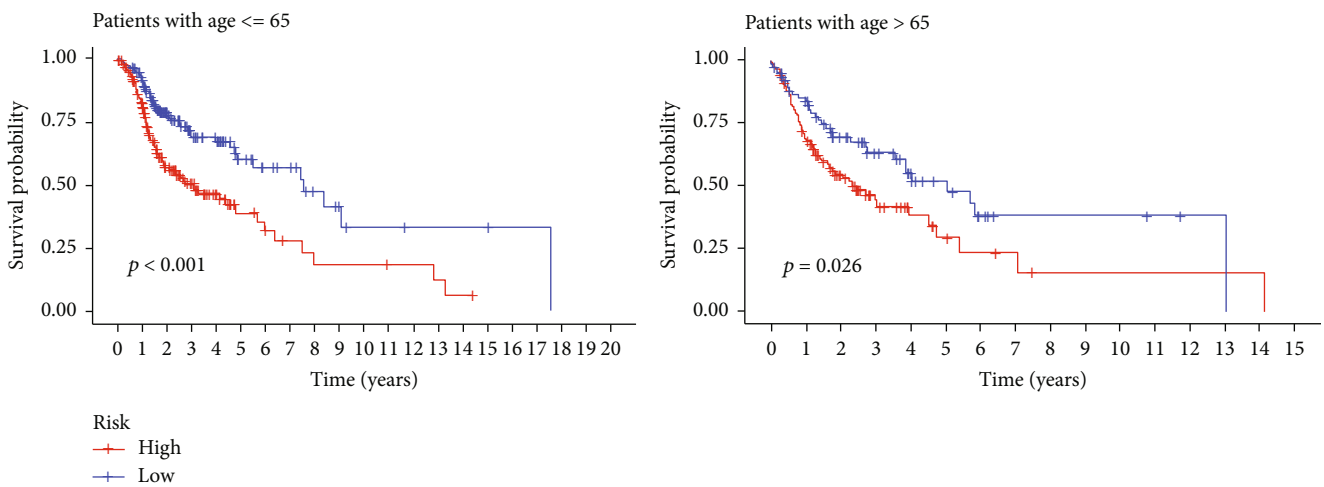

(a)

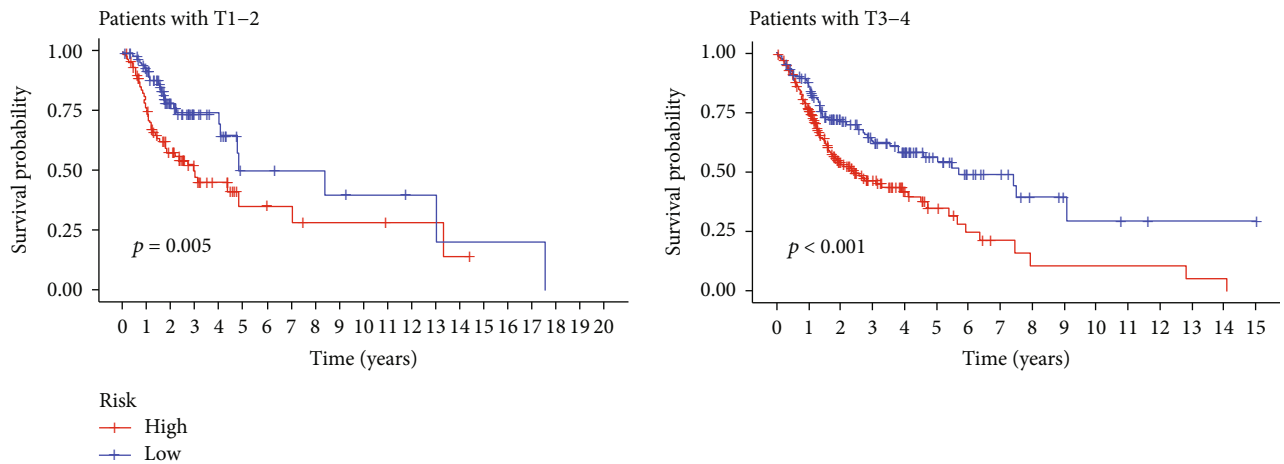

(b)

Figure 8: Continued.

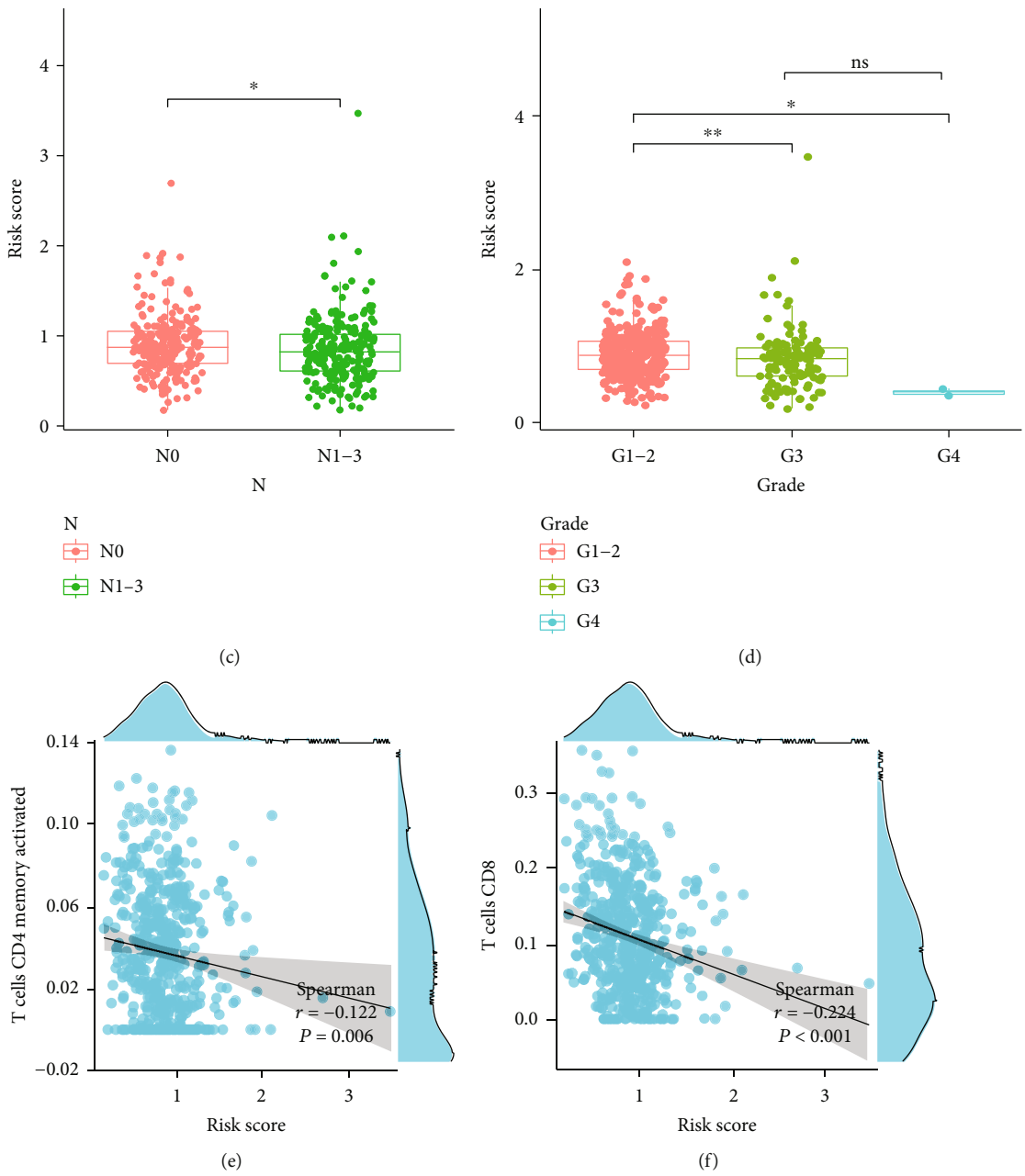

Figure 8: Continued.

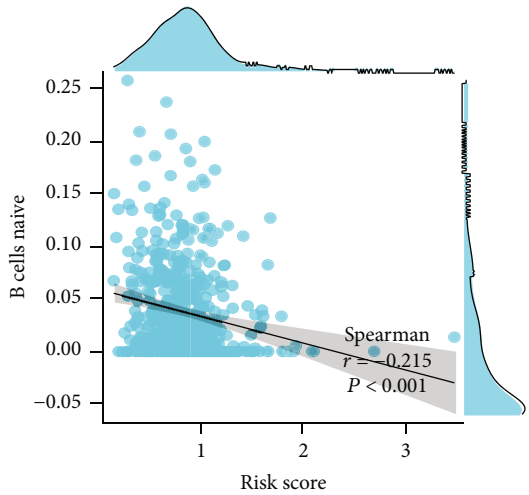

(g)

Figure 8: Prognostic value of cuproptosis-associated lncRNA signature and the correlation with relevant immune cells. (a), (b) The Kaplan-Meier curve showed that patients in different groups ((a) patients with different age; (b) patients with T stage) with high risk displayed a shorter overall survival than those with low risk. (c), (d) Correlation analysis of lncRNA-related risk score and clinical characteristics. (e)–(g) lncRNA-related risk score was inversely correlated with CD4 memory activated T cells (e), CD8 T cells (f), and naive B cells (g).

representing a new method to kill cancer cells as well as offer a potential treatment for tumors [10].

In this study, we investigated the CRG expression profiles and TCGA dataset to determine the cuproptosis-related prognostic gene signatures. A clinical dataset of HNSCC patients from the CPTAC was used for validating the signature. Moreover, we also identified the role of cuproptosis-related genes and constructed a corresponding lncRNAs signature. The study also examined TIICs, TMEs, immune function, immune checkpoints, and immunotherapy as the possible immune responses. Additionally, this study investigated novel therapeutic targets based on the potential and novel biomarkers of the cuproptosis-related pathways in HNSCC.

Recent advances in high throughput DNA sequencing have made it possible to fully characterize the somatic mutations of cancer. As with other cancers associated with solid and smoking-related cancers, HNSCC is formed by the accumulation of a variety of genetic and epigenetic changes [30–32]. Our study demonstrates the mutation of cuproptosis-related genes in HNSCC, with the greatest extent of mutations in CDKN2A, suggesting a possible involvement in the development and progression of HNSCC. A differential expression was noted in eight out of 10 hub CRGs between the tumor and normal tissues, as per the data derived from the TCGA and CPTAC. These results suggested that 10 CRGs were associated with the development of HNSCC.

Then, we validated the accuracy of risk models in predicting the OS of HNSCC patients. The prognostic signature was regarded as a trustworthy technique for anticipating the prognosis of patients with HNSCC and showed satisfactory prognostic discrimination in patients with clinical and pathological T stage, HPV status, positive lymph node number, and clinical outcome.

Analysis of the novel gene signature and its potential functions exhibited that KEGG was primarily enriched in primary immunodeficiency, intestinal immune network for IgA production, B cell receptor signaling pathway, and T cell receptor signaling pathway. Several immune pathways were observed in the low-risk group, indicating that the immune system was activated.

In terms of immune infiltration, the count of the effector memory CD8 T cells, activated B cells, activated CD8 T cells, follicular helper CD8 T cells, activated CD4 T cells, and natural killer cells were significantly different between the high- and low-risk groups. Interestingly, we also noted that the patients in the high-risk group displayed higher TMB and MSI scores. These findings suggested that the infiltration of a few specific immune cell subtypes could considerably affect the prognosis of HNSCC patients.

In HNSC, immune checkpoint blockade therapeutic strategies are of great clinical significance [12]. The negative relationship between risk scores and immune checkpoints, like TIGHT, PDCD1, CTLA4, LAG3, and IDO1, showed that the patients having low-risk scores could have a better immune microenvironment, which made them more likely to respond to ICIs. We also noted that the low-risk group responded to immunotherapy significantly better than the high-risk group, which led to the conclusion that patients with low risk were most likely to benefit from immunotherapy.

LncRNA plays an important regulatory role in several tumor types [33–36]. Most of the lncRNAs have a close association with the genes coded in the vicinity of certain mRNAs, and the interactions between the lncRNA-mRNA pairs [37, 38]. Extensive research has been done on the potential role of lncRNAs as novel biomarkers. Based on the current situation where only a handful of lncRNAs have been reported for HNSCC, our findings will offer a new approach to developing lncRNAs-related therapies for HNSCC. In our study, 109 cuproptosis-related lncRNAs were identified for constructing the lncRNA

signature. 11 hub lncRNAs were selected for designing the model equation for risk assessment. This model was calibrated and validated using internal validation data. We noted that the cuproptosis-related lncRNA risk model was an effective and independent prognostic factor and could be used as an early marker for predicting the onset and progression of HNSCC with a good prediction performance. Additionally, we determined a significant correlation between the clinical-pathological features and risk signature. Furthermore, the lncRNA risk score showed a higher correlation with the tumor cells such as the CD4 memory-activated T cells, CD8 T cells, and naive B cells, which indicated an active anti-tumor immune response.

Cuproptosis, a novel and cryptic cell death model, presents a new therapeutic approach for cancer treatment. However, very few researchers have studied the relationship between cuproptosis and other cell death models [39]. In this study, we have integrated the cuproptosis biomarkers for predicting the treatment outcomes in HNSCC patients as well as identifying the potential therapeutic targets. The risk model we built is a novel cuproptosis-related biomarker for HNSCC prognosis and screening. The risk model demonstrates good prognostic predictive power. It can help clinical doctors to differentiate between high and low risk HNSCC patients to help individualize treatment. Additionally, it also showed tight correlation with TIICs, TME, immune function, immune checkpoints, and immunotherapy as the possible immune responses. The drawbacks of this study include that our prognostic model was both constructed and validated with retrospective data from public databases. A small sample size was used that limited its statistical significance. In addition, the results were not clinically verified. More prospective real-world data should be warranted to verify its clinical utility. Generally, we have identified novel cuproptosis-related biomarkers for HNSCC prognosis. These results could offer insights that could help in developing accurate and robust cancer therapy strategies.

Data Availability

The public dataset used in this study is freely available at https://xenabrowser.net/, https://www.ncbi.nlm.nih.gov/, and https://pdc.cancer.gov/pdc/browse.

Conflicts of Interest

The authors declare that the research was conducted in the absence of any commercial or financial relationships that could be construed as a potential conflict of interest.

Authors' Contributions

The authors declare their contribution as follows. Qin Ding and Xiaochuan Chen conceived and drafted of the manuscript. Wenquan Hong and Li Hua Wang assisted with data curation. Wei Liu analyzed the data. Sunqin Cai and Xin Chen participated in the formal analysis of the study. Jun Lu and Sufang Qiu provided project administration and funding acquisition. All authors have read and agreed to the published version of the manuscript. These authors have contributed equally: Qin Ding and Xiaochuan Chen.

Acknowledgments

The project was funded by the grants of Science and Technology Program of Fujian Province, China (2018Y2003) and Fujian Provincial Clinical Research Center for Cancer Radiotherapy and Immunotherapy (2020Y2012) and supported by the National Clinical Key Specialty Construction Program (2021), Fujian Clinical Research Center for Radiation and Therapy of Digestive, Respiratory and Genitourinary Malignancies and United Fujian Provincial Health and Education Project for Tackling the Key Research, China (2019-WJ-03); National Natural Science Foundation of China (11974077 and 82072986); and Science and Technology Pilot Program of Fujian Province, China (2021Y0053).

Supplementary Materials

Figure S1. Survival analysis of CRG risk model. (a), (b) Survival analysis showed the prognosis of high-risk and low-risk patients. PFS: progression-free-survival; DSS: disease specific survival. (c)–(e) Correlation analysis of risk score and clinical characteristics. (f) Distribution of HNSCC patients based on the risk score. Risk curve and scatter plot for the risk score and survival status of each HNSCC case. The red and green dots represent death and survival, respectively. Heat map showing the expression profiles of cuproptosis-associated seven-genes in the high-risk group and the low-risk group. Figure S2. The IC50 of common chemotherapy agents between gene-related low- and high-risk groups. The IC50 of doxorubicin (a) and docetaxel (b) in the low-risk group were higher than those in the high-risk group. Figure S3. Evaluation of infiltrating immune cells and distribution of HNSCC patients based on the risk scores. (a)–(e) Box plot presents the differentially naive B cells (a), CD4 memory resting T cells (b), follicular helper T cells (c), memory activated CD4 T cells (d), and Tregs (e) between cluster 1 and cluster 2. (f) Differences in stromal score between cluster 1 and cluster 2. (g)–(h) Distribution of HNSCC patients based on the risk score in the train group (g) and the test group (h). Figure S4. Prognostic value of cuproptosis-associated lncRNA signature. The Kaplan-Meier curve showed that patients in different groups ((a) male patients; (b) patients with M0; (c)–(d) patients with different grade; (e)–(f) patients with different N; (g)–(h) patients with different stage) with high risk displayed a shorter overall survival than those with low risk. Figure S5. Prognostic value and correlation of the risk score with immune cells. (a), (b) Correlation analysis of lncRNA-related risk score and clinical characteristics. (c) lncRNA-related risk score was positively correlated with CD4 memory resting T cells. *(Supplementary Materials)*

References

[1] H. Shibata, L. Zhou, N. Xu, A. M. Egloff, and R. Uppaluri, "Personalized cancer vaccination in head and neck cancer," *Cancer Science*, vol. 112, no. 3, pp. 978–988, 2021.

[2] H. Sung, J. Ferlay, R. L. Siegel et al., "Global cancer statistics 2020: GLOBOCAN estimates of incidence and mortality worldwide for 36 cancers in 185 countries," *CA: a Cancer Journal for Clinicians*, vol. 71, no. 3, pp. 209–249, 2021.

[3] V. Chandel, S. Raj, P. Kumar et al., "Metabolic regulation in HPV associated head and neck squamous cell carcinoma," *Life Sciences*, vol. 258, article 118236, 2020.

[4] J. Ferlay, I. Soerjomataram, R. Dikshit et al., "Cancer incidence and mortality worldwide: sources, methods and major patterns in GLOBOCAN 2012," *International Journal of Cancer*, vol. 136, no. 5, pp. E359–E386, 2015.

[5] S. Idris, A. Baqays, A. Isaac, J. K. Chau, K. H. Calhoun, and H. Seikaly, "The effect of second hand smoke in patients with squamous cell carcinoma of the head and neck," *Journal of Otolaryngology-Head & Neck Surgery*, vol. 48, no. 1, pp. 1–6, 2019.

[6] X. M. Zhang, L. J. Song, J. Shen et al., "Prognostic and predictive values of immune infiltrate in patients with head and neck squamous cell carcinoma," *Human Pathology*, vol. 82, pp. 104–112, 2018.

[7] E. Du, A. L. Mazul, D. Farquhar et al., "Long-term survival in head and neck cancer: impact of site, stage, smoking, and human papillomavirus status," *The Laryngoscope*, vol. 129, no. 11, pp. 2506–2513, 2019.

[8] T. Gnanasekaran, H. Low, R. Gupta, K. Gao, and J. Clark, "Prognosis of metastatic head and neck squamous cell carcinoma over the last 30 years," *ANZ Journal of Surgery*, vol. 88, no. 11, pp. 1158–1162, 2018.

[9] D. Tang, X. Chen, and G. Kroemer, "Cuproptosis: a copper-triggered modality of mitochondrial cell death," *Cell Research*, vol. 32, no. 5, pp. 417-418, 2022.

[10] P. Tsvetkov, S. Coy, B. Petrova et al., "Copper induces cell death by targeting lipoylated TCA cycle proteins," *Science*, vol. 375, no. 6586, pp. 1254–1261, 2022.

[11] S. R. Li, L. L. Bu, and L. Cai, "Cuproptosis: lipoylated TCA cycle proteins-mediated novel cell death pathway," *Signal Transduction and Targeted Therapy*, vol. 7, no. 1, pp. 1–3, 2022.

[12] M. Oliva, A. Spreafico, M. Taberna et al., "Immune biomarkers of response to immune-checkpoint inhibitors in head and neck squamous cell carcinoma," *Annals of oncology*, vol. 30, no. 1, pp. 57–67, 2019.

[13] Y. Wang, L. Zhang, and F. Zhou, "Cuproptosis: a new form of programmed cell death," *Cellular & Molecular Immunology*, vol. 19, no. 8, pp. 867-868, 2022.

[14] D. S. Chen and I. Mellman, "Oncology meets immunology: the cancer-immunity cycle," *immunity*, vol. 39, no. 1, pp. 1–10, 2013.

[15] E. Becht, N. A. Giraldo, L. Lacroix et al., "Estimating the population abundance of tissue-infiltrating immune and stromal cell populations using gene expression," *Genome biology*, vol. 17, no. 1, pp. 1–20, 2016.

[16] B. Li, E. Severson, J. C. Pignon et al., "Comprehensive analyses of tumor immunity: implications for cancer immunotherapy," *Genome biology.*, vol. 17, no. 1, pp. 1–6, 2016.

[17] T. Li, J. Fu, Z. Zeng et al., "TIMER2. 0 for analysis of tumor-infiltrating immune cells," *Nucleic acids research*, vol. 48, no. W1, pp. W509–W514, 2020.

[18] B. Ru, C. N. Wong, Y. Tong et al., "TISIDB: an integrated repository portal for tumor–immune system interactions," *Bioinformatics*, vol. 35, no. 20, pp. 4200–4202, 2019.

[19] L. Xu, C. Deng, B. Pang et al., "TIP: A Web Server for Resolving Tumor Immunophenotype Profiling," *Cancer research*, vol. 78, no. 23, pp. 6575–6580, 2018.

[20] A. M. Newman, C. L. Liu, M. R. Green et al., "Robust enumeration of cell subsets from tissue expression profiles," *Nature methods*, vol. 12, no. 5, pp. 453–457, 2015.

[21] J. Hu, A. Yu, B. Othmane et al., "Siglec15 shapes a non-inflamed tumor microenvironment and predicts the molecular subtype in bladder cancer," *Theranostics*, vol. 11, no. 7, pp. 3089–3108, 2021.

[22] P. A. Ott, Y. J. Bang, S. A. Piha-Paul et al., "T-cell–inflamed gene-expression profile, programmed death ligand 1 expression, and tumor mutational burden predict efficacy in patients treated with pembrolizumab across 20 cancers: KEYNOTE-028," *Journal of Clinical Oncology*, vol. 37, no. 4, pp. 318–327, 2019.

[23] M. S. Rooney, S. A. Shukla, C. J. Wu, G. Getz, and N. Hacohen, "Molecular and genetic properties of tumors associated with local immune cytolytic activity," *Cell*, vol. 160, no. 1-2, pp. 48–61, 2015.

[24] V. Thorsson, D. L. Gibbs, S. D. Brown et al., "The immune landscape of cancer," *Immunity*, vol. 48, no. 4, pp. 812–830.e14, 2018.

[25] A. Mayakonda, D. C. Lin, Y. Assenov, C. Plass, and H. P. Koeffler, "Maftools: efficient and comprehensive analysis of somatic variants in cancer," *Genome research*, vol. 28, no. 11, pp. 1747–1756, 2018.

[26] W. Yang, J. Soares, P. Greninger et al., "Genomics of Drug Sensitivity in Cancer (GDSC): a resource for therapeutic biomarker discovery in cancer cells," *Nucleic acids research*, vol. 41, no. D1, pp. D955–D961, 2012.

[27] Z. Bian, R. Fan, and L. Xie, "A Novel Cuproptosis-Related Prognostic Gene Signature and Validation of Differential Expression in Clear Cell Renal Cell Carcinoma," *Genes*, vol. 13, no. 5, p. 851, 2022.

[28] H. Lv, X. Liu, X. Zeng et al., "Comprehensive Analysis of Cuproptosis-Related Genes in Immune Infiltration and Prognosis in Melanoma," *Frontiers in pharmacology*, vol. 13, 2022.

[29] Z. Zhang, X. Zeng, Y. Wu, Y. Liu, X. Zhang, and Z. Song, "Cuproptosis-Related Risk Score Predicts Prognosis and Characterizes the Tumor Microenvironment in Hepatocellular Carcinoma," *Frontiers in immunology*, vol. 13, 2022.

[30] C. Scully, J. K. Field, and H. Tanzawa, "Genetic aberrations in oral or head and neck squamous cell carcinoma 3: clinicopathological applications," *Oral oncology*, vol. 36, no. 5, pp. 404–413, 2000.

[31] P. K. Ha and J. A. Califano, "Promoter methylation and inactivation of tumour-suppressor genes in oral squamous-cell carcinoma," *The lancet oncology*, vol. 7, no. 1, pp. 77–82, 2006.

[32] I. M. Smith, W. K. Mydlarz, S. K. Mithani, and J. A. Califano, "DNA global hypomethylation in squamous cell head and neck cancer associated with smoking, alcohol consumption and stage," *International journal of cancer*, vol. 121, no. 8, pp. 1724–1728, 2007.

[33] C. Mao, X. Wang, Y. Liu et al., "A G3BP1-interacting lncRNA promotes ferroptosis and apoptosis in cancer via nuclear sequestration of p53," *Cancer research*, vol. 78, no. 13, pp. 3484–3496, 2018.

[34] M. Wang, C. Mao, L. Ouyang et al., "Long noncoding RNA LINC00336 inhibits ferroptosis in lung cancer by functioning as a competing endogenous RNA," *Cell Death & Differentiation*, vol. 26, no. 11, pp. 2329–2343, 2019.

[35] Y. Yang, W. Tai, N. Lu et al., "lncRNA ZFAS1 promotes lung fibroblast-to-myofibroblast transition and ferroptosis via functioning as a ceRNA through miR-150-5p/SLC38A1 axis," *Aging (Albany NY)*, vol. 12, no. 10, pp. 9085–9102, 2020.

[36] H. Yu, Z. Han, Z. Xu, C. An, L. Xu, and H. Xin, "RNA sequencing uncovers the key long non-coding RNAs and potential molecular mechanism contributing to XAV939-mediated inhibition of non-small cell lung cancer," *Oncology letters.*, vol. 17, no. 6, pp. 4994–5004, 2019.

[37] A. A. Sigova, A. C. Mullen, B. Molinie et al., "Divergent transcription of long noncoding RNA/mRNA gene pairs in embryonic stem cells," *Proceedings of the National Academy of Sciences of the United States of America*, vol. 110, no. 8, pp. 2876–2881, 2013.

[38] X. P. Kong, J. Yao, W. Luo et al., "The expression and functional role of a FOXC1 related mRNA-lncRNA pair in oral squamous cell carcinoma," *Molecular and cellular biochemistry*, vol. 394, no. 1-2, pp. 177–186, 2014.

[39] M. A. Kahlson and S. J. Dixon, "Copper-induced cell death," *Science*, vol. 375, no. 6586, pp. 1231-1232, 2022.

Hindawi
Disease Markers
Volume 2022, Article ID 4614099, 6 pages
https://doi.org/10.1155/2022/4614099

Research Article

Correlation Study between Levels of Gastrin, Serum IGF-1, and GHBP and Growth and Development in Children with Short Stature Based on Big Data Analysis

Chen Hua[1] and Dan Yu[2]

[1]*Department of Child Healthcare, Yantai Mountain Hospital, Yantai, 264000 Shandong, China*
[2]*Department of Pediatric General Surgery, Qingdao Women and Children's Hospital, Qingdao, 266034 Shandong, China*

Correspondence should be addressed to Dan Yu; yudan@qdfuer.com.cn

Received 11 July 2022; Accepted 10 August 2022; Published 25 August 2022

Academic Editor: Jun Yang

Objective. To analyze the correlation between the levels of gastrin, serum IGF-1, and GHBP and growth and development in children with short stature (SS) using the big data. *Methods*. By means of retrospective analysis, the clinical data of 42 children with SS admitted to our hospital from October 2020 to October 2021 were selected as the study group, while 30 children with the healthy physical examination results in the corresponding period were selected as the control group to measure the growth and development indices and the levels of gastrin, serum IGF-1, and GHBP. The Pearson correlation analysis was used for the relationship between the levels of gastrin, serum IGF-1, and GHBP and growth and development indices in children with SS, and the targeted intervention measures were formulated by the analysis of experimental data. *Results*. Compared with the study group, the height, weight, and bone mineral density (BMD) Z-scores of children in the control group were obviously higher ($P < 0.001$). The levels of gastrin, serum IGF-1, and GHBP in the study group were markedly lower than those in the control group ($P < 0.05$). The Pearson correlation analysis showed that the gastrin, serum IGF-1, and GHBP of children were positively correlated with growth and development indices ($P < 0.001$). The levels of gastrin, serum IGF-1, and GHBP in children were distinctly improved after treatment ($P < 0.05$). *Conclusion*. The gastrin, serum IGF-1, and GHBP are closely related to the SS, and the effective clinical intervention can better improve the above indicators of children to promote their growth and development.

1. Introduction

Short stature (SS), a more common disease in children, refers to a child whose height is 2 standard deviations below the average height for the same age, gender, and race or below the 3rd percentile of normal children growth curve [1]. The specific etiology of children with SS that have no potential pathological condition is not clear, speculating that SS is a multigenic disease, and it is less likely to reach normal height after adulthood without timely treatment. The occurrence of SS will seriously affect the physiological, psychological, and intellectual abilities of children and bring heavy psychological and economic burden to their families, so that the active exploration of its pathogenesis can benefit these children. The disorder of skeletal development is one of the main causes of SS, and hereditary metabolic diseases, malnutrition, and other chronic diseases are also the risk factors for SS [2]. Insulin-like growth factor-1 (IGF-1) and growth hormone binding protein (GHBP) are closely related to the growth and development of young children. Among them, IGF-1 as a kind of peptide for promoting cells growth is similar to structure and function of insulin, which has an important promotion in cell proliferation and differentiation and individual growth and development [3, 4]. GHBP is formed by the decomposition of extracellular components of growth hormone receptor (GHR) by proteolytic enzymes, which plays an important regulatory role in human growth [5]. Gastrin is a newly discovered natural endogenous ligand

for the growth hormone secretagogue receptor (GHS-R), which acts on pituitary and hypothalamus. It not only has an endocrine function but also promotes the appetite and enhances the gastrointestinal motility [6, 7]. Big data analysis is a method that predicts the possibility of events by comparing and analyzing the data obtained from the experiments and studies the correlation between data and data, with the instructive and representative analysis results [8]. At present, there are few studies on gastrin, serum IGF-1, and GHBP in children with SS. This study analyzed the correlation between the above indexes and the growth and development in children with SS by the big data, in order to provide a reference for the clinical diagnosis and treatment of the disease. The reports were as follows.

2. Materials and Methods

2.1. General Information. 42 children with SS admitted to our hospital from October 2020 to October 2021 were selected as the study group with the age range of 2-13 years old and the average age of (7.02 ± 3.32) years old, including 23 males and 19 females. At the same time, 30 children with the healthy physical examination results in the corresponding period were selected as the control group with the age range of 2-13 years old and the average age of (7.13 ± 3.84) years old, including 17 males and 13 females. The study was approved by the hospital ethics committee and in line with the Declaration of Helsinki (2013) [9].

2.2. Inclusion and Exclusion Criteria. Inclusion criteria. (1) Children were in accordance with the relevant diagnostic criteria of SS, with the age less than 13 years old. (2) Children had the symmetrical stature and no chronic organic disease. (3) Children had the normal intelligence development.

Exclusion criteria. (1) Children with the liver, kidney and intestinal diseases; (2) children with the abnormal thyroid function; and (3) children with the tumor, mental disorders, and obesity.

2.3. Methods

2.3.1. Detection of Laboratory Indexes. The fasting venous blood of children (6 ml) was collected from 8 : 00 to 10 : 00 in the morning and placed in three tubes without anticoagulation.

(1) *Determination of Gastrin.* 10 g/L of ethylenediamine tetraacetic acid (EDTA) at a dose of 30 μL and trypsin inhibitor at a dose of 20 μL were injected into the test tube. After the sufficient mixing, the mixture was in static condition for 4 h and then centrifuged at 3000 r/min for 15 min to separate the plasma, using an ultralow temperature refrigerator at −80°C to freeze and store. The freeze-thaw was taken out during the determination, using the same test kits (manufacturer: Shanghai Shuangying Biotechnology Co., Ltd.) to determine

(2) *Determination of IGF-1 and GHBP.* After the blood was fully solidified, it was centrifuged at 3000 r/min for 5 min by a centrifuge to obtain the serum using a refrigerator at -20°C to store. After all samples were collected, the IGF-1 was determined by chemiluminescence immunoassay, and the GHBP was measured by enzyme-linked immunosorbent assay. All operations were carried out according to the relevant instructions of the kits (manufacturer: Beijing Kerui Mei Technology Co., Ltd.)

Table 1: Comparison of growth and development indices in children between the two groups (Mean ± SD).

Groups	n	Height (cm)	Weight (kg)	BMD Z-scores
Study group	42	103.36 ± 6.02	18.40 ± 2.89	−1.18 ± 0.54
Control group	30	114.67 ± 7.94	26.05 ± 6.60	0.44 ± 0.07
t		6.876	7.075	7.446
P		<0.001	<0.001	<0.001

2.3.2. Detection of Growth and Development Indices

(1) *Measurement of Height and Weight.* The subjects kept standing in attention position on the floor of the height and weight measuring instrument, with the naturally upright body. The heels, shoulders, and sacral tail were in contact with the column, with the head in frontal position, while children kept looking straight ahead. The height and weight were measured three times in order to obtain the average value

(2) *Measurement of BMD Z -Scores.* The BMD Z-scores were measured by an ultrasound bone densitometer (manufacturer: Xuzhou Pinyuan Electronic Technology Co., Ltd.; model: BMD-A1). 1/3 of the left distal tibia as the measurement site was taken three times to obtain the average value. The determination criteria were as follows. If the measurement value was $-2.0 \leq Z < -1.0$, the BMD was mild deficiency. If the measurement value was $-3.0 \leq Z < -2.0$, the BMD was moderate deficiency. If the measurement value was $Z < -3.0$, the BMD was severe deficiency

2.4. Intervention Methods. Children in the study group were treated with the recombinant human growth hormone (manufacturer: Shenzhen Kexing Biotech Co., Ltd.; NMPA approval no.: S20063087; specification: 0.65 mg/piece) by the subcutaneous injection at a dose of 0.05 mg/time every day and lysine hydrochloride tablets (manufacturer: Anqiu Lu'an Pharmaceutical Co., Ltd.; NMPA approval No.: H37023859; specification: 0.2 g) by oral administration at a dose of 200 mg/time every day.

2.5. Observation Indices. The growth and development indices (height, weight and BMD Z-scores) and the levels of gastrin, serum IGF-1, and GHBP were compared between the two groups, and the correlation between the levels of gastrin, serum IGF-1, and GHBP and the growth and development indices was analyzed.

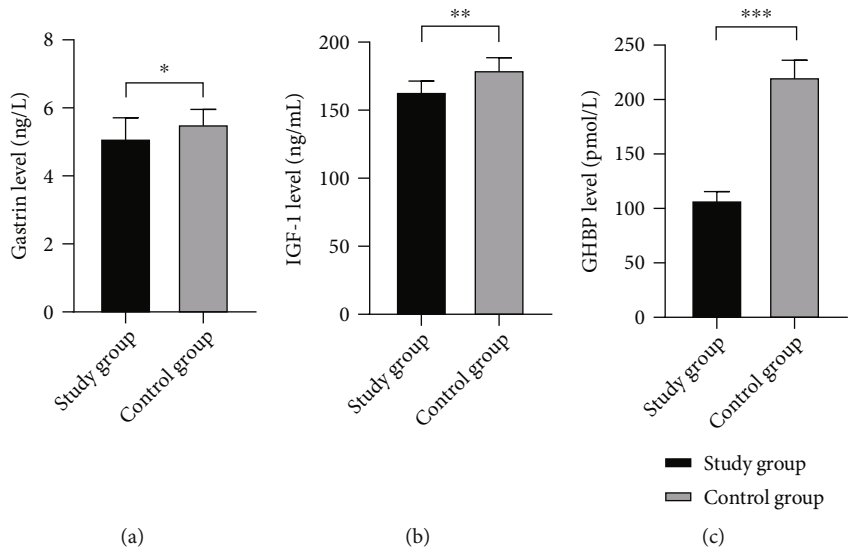

Figure 1: Comparison of levels of gastrin, serum IGF-1, and GHBP in children between the two groups (Mean ± SD). Notes. (a) was the comparison of the gastrin levels between the two groups. The transverse axis represented the study group and the control group, and the vertical axis represented the gastrin level (ng/mL). The gastrin levels in the study group and the control group were (5.11 ± 0.60) ng/mL and (5.53 ± 0.43) ng/mL, respectively. * represented a significant difference in the gastrin levels between the two groups in children ($t = 3.277$, $P < 0.05$). (b) was the comparison of the IGF-1 levels between the two groups. The transverse axis represented the study group and the control group, and the vertical axis represented the IGF-1 level (ng/mL). The IGF-1 levels in the study group and the control group were (163.80 ± 7.64) ng/mL and (179.73 ± 8.81) ng/mL, respectively. ** represented a significant difference in the IGF-1 levels between the two groups in children ($t = 8.182$, $P < 0.001$). (c) was the comparison of the GHBP levels between the two groups. The transverse axis represented the study group and the control group, and the vertical axis represented the GHBP level (pmol/L). The GHBP levels in the study group and the control group were (108.92 ± 4.43) pmol/L and (222.07 ± 15.36) pmol/L, respectively. *** represented a significant difference in the GHBP levels between the two groups in children ($t = 45.289$, $P < 0.001$).

Table 2: Correlation between the levels of gastrin, serum IGF-1, and GHBP and growth and development indices.

Observation indices	Gastrin		Serum IGF-1		Serum GHBP	
	r values	*P* values	*r* values	*P* values	*r* values	*P* values
Height	0.822	<0.001	0.673	<0.001	0.758	<0.001
Weight	0.653	<0.001	0.520	<0.001	0.706	<0.001
BMD *Z*-scores	0.621	<0.001	0.544	<0.001	0.686	<0.001

The levels of gastrin, serum IGF-1, and GHBP before and after treatment in children with SS were compared.

2.6. Statistical Methods. The data included in this study were processed by the professional statistical software SPSS26.0, and the pictures were drawn by the GraphPad Prism 7 (GraphPad Software, San Diego, USA). The enumeration data and measurement data were tested by x^2 and t test, indicated by (n (%)) and Mean ± SD. The Pearson correlation coefficient method was used to analyze the correlation between the levels of gastrin, serum IGF-1, and GHBP and growth and development indices in children. When $P < 0.05$, the differences were considered to be statistically significant.

3. Results

3.1. Comparison of Growth and Development Indices. Compared with the study group, the height, weight, and BMD *Z*-scores of children in the control group were obviously higher ($P < 0.001$), see details in Table 1.

3.2. Comparison of Levels of Gastrin, Serum IGF-1, and GHBP. The results showed that the levels of gastrin, serum IGF-1, and GHBP of children in the study group were markedly lower than those in the control group ($P < 0.05$), see details in Figure 1.

3.3. Correlation between the Levels of Gastrin, Serum IGF-1, and GHBP and Growth and Development Indices. The Pearson correlation analysis showed that the gastrin, serum IGF-1, and GHBP of children were positively correlated with growth and development indices ($P < 0.001$), see details in Table 2.

3.4. Comparison of Levels of Gastrin, Serum IGF-1, and GHBP in Children before and after Treatment. The study results showed that the levels of gastrin, serum IGF-1, and GHBP were significantly improved after treatment in children ($P < 0.05$), see details in Figure 2.

4. Discussion

There are many factors affecting the growth and development of children, with a relatively complex mechanism, and SS has been discussed by many researchers [10, 11]. Some studies have shown that the function abnormality of hypothalamus-pituitary and its IGF axis is the main reason affecting the growth and development of children [12].

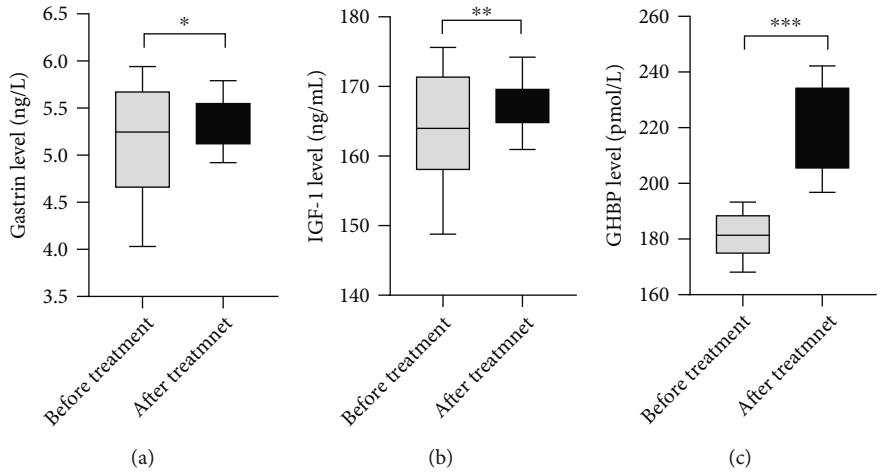

Figure 2: Comparison of levels of gastrin, serum IGF-1, and GHBP in children before and after treatment (Mean ± SD). Notes. (a) showed the comparison of gastrin levels in children before and after treatment. The transverse axis represented before and after treatment, and the vertical axis represented the gastrin level (ng/mL). The gastrin levels in children before and after treatment were (5.11 ± 0.60) ng/mL and (5.34 ± 0.27) ng/mL, respectively. * represented a significant difference in the gastrin levels of children before and after treatment ($t = 2.265$, $P < 0.05$). (b) showed the comparison of IGF-1 levels in children before and after treatment. The transverse axis represented before and after treatment, and the vertical axis represented the IGF-1 level (ng/mL). The IGF-1 levels in children before and after treatment were (163.80 ± 7.64) ng/mL and (167.18 ± 3.67) ng/mL, respectively. ** represented a significant difference in the IGF-1 levels of children before and after treatment ($t = 2.584$, $P < 0.05$). (c) showed the comparison of GHBP levels in children before and after treatment. The transverse axis represented before treatment and after treatment, and the vertical axis represented the GHBP level (pmol/L). The GHBP levels in children before and after treatment were (181.53 ± 7.45) pmol/L and (220.92 ± 15.31) pmol/L, respectively. *** represented a significant difference in the GHBP levels of children before and after treatment ($t = 14.993$, $P < 0.001$).

IGF-1, a peptide and protein whose structure is similar to the insulin factor, is secreted by kidney, liver, and spleen cells. The growth hormone (GH)/IGF-1 axis, as a study hotspot in recent years, can regulate the bone balance in human body and determine the growth length, maturity of bone, and the obtained maximum bone mass before puberty [13], and its main manifestation is to maintain the bone mass at adult stage. IGF-1 can directly promote the cell differentiation and proliferation as a target cell, and GH can stimulate the IGF-1 produced by peripheral tissues especially liver. In addition, IGF-1 promotes the growth mediated by GH [14] and induces the occurrence of chondrocyte mitosis, both of which participate in the growth and development of children. Animal experiments have found [15, 16] that GHBP, a specific binding protein of GH in plasma, can bind to the GH, which can reduce the fluctuation of GH level caused by the pulsatile secretion of GH in hypophysis and prolong the half-life of GH, thus regulating the GH. GHBP in human is generated by the protein cleavage mechanism of growth hormone receptor (GHR), which can be used to reflect the status of GHR in the body. Therefore, in a sense, GHBP is able to provide a theoretical basis for the clinical treatment of children with SS [17, 18]. In addition, the related studies of GHBP have achieved remarkable results in other areas. Some scholars [19] have proposed that serum GHBP can be used as an important biological marker for screening of Down syndrome in the early pregnant stage, and its level is also positively correlated with the risk of breast cancer in women [20].

Gastrin is a peptide hormone released into the blood by the secretion of gastric fundus, with the element of 28 amino acids [21]. After acylation, it is able to combine with the growth hormone secretagogue receptor to across the blood-brain barrier, which is the only known hormone in the blood to stimulate appetite, with an unclear mechanism on promoting the GH secretion. Current studies have shown that [22] gastrin can increase the circulating level of GH by at least two pathways. A pathway is to increase the cycle of phosphoric acid and activate the protein kinase C by activating the signaling pathway of phospholipase C, which can cause the increase of intracellular Ca^{2+} level and the release of diacylglycerol, thereby increasing the secretion of growth hormone-releasing hormone. The second pathway is that gastrin directly increases the GH secreted by pituitary cells, and the specific regulation pathway remains to be further studied.

In recent years, the real world study based on daily practice data in clinical care has been paid more and more attention, and big data application in medical field has been listed as the key development direction in China [23, 24]. In this study, the laboratory tests were used to analyze the differences of growth and development indices, gastrin, serum IGF-1, and GHBP between children with SS and healthy children by big data, hoping to determine the correlation between the levels of gastrin, serum IGF-1, and GHBP and growth and development in children with SS by comparing the clinical data. The result showed that the levels of gastrin, serum IGF-1, and GHBP of children in the study group were significantly lower than those in the control group ($P < 0.05$), and the result enabled people to have a new understanding of SS, which was obviously better than that of Motta Felipe et al. [25]. The Pearson

correlation analysis showed that there were significant correlations between gastrin, serum IGF-1, and GHBP and growth and development indices in children ($P < 0.001$). The results of the proposed method in this study were compared with those of the traditional methods, which exceeded the previous reports, indicating that the experiment had a higher clinical value. The contributions of this study were as below. The relationship between serological indicators and growth and development indices in children with SS was analyzed to more deeply understand the pathogenesis of SS, which was a major progress and development in clinic undoubtedly, with extensive guiding significance in the treatment of SS and as the development direction of future medicine. The advantages of this study were that the relationship between serological indicators and growth and development indices of children in the two groups was detected, and the relation of test variables was explored using the Pearson correlation analysis, which was innovative undoubtedly. The limitation of this study was as follows. Only 42 cases were included in this study, with a small sample size, so that there must be a deviation in sample selection, and the large-sample and multicenter studies are needed in the subsequent studies.

Data Availability

Data to support the findings of this study is available on reasonable request from the corresponding author.

Conflicts of Interest

The authors do not have conflicts of interest to declare.

References

[1] E. Aurora, G.-P. Montserrat, and C. Raquel, "A 10-year-old boy with short stature and microcephaly, diagnosed with moyamoya syndrome and microcephalic osteodysplastic primordial dwarfism type II (MOPD II)," *The American Journal of Case Reports*, vol. 22, article e933919, 2021.

[2] X. Li, R. Yao, G. Chang et al., "Clinical profiles and genetic spectra of 814 Chinese children with short stature," *The Journal of Clinical Endocrinology and Metabolism*, vol. 107, no. 4, pp. 972–985, 2022.

[3] Y. Wan, X. Gong, S. Cheng et al., "Short stature in patients with diamond-blackfan anemia: a cross-sectional study," *The Journal of Pediatrics*, vol. 240, pp. 177–185, 2022.

[4] B. Xu, Y. Feng, L. Gan et al., "Vitamin D status in children with short stature: accurate determination of serum vitamin D components using high-performance liquid chromatography-tandem mass spectrometry," *Frontiers in Endocrinology*, vol. 12, article 707283, 2021.

[5] S. Gürsoy, F. Hazan, A. Aykut et al., "Detection of SHOX gene variations in patients with skeletal abnormalities with or without short stature," *Journal of Clinical Research in Pediatric Endocrinology*, vol. 12, no. 4, pp. 358–365, 2020.

[6] J. Hoover-Fong, A. Y. Alade, M. Ain et al., "Blood pressure in adults with short stature skeletal dysplasias," *American Journal of Medical Genetics Part A*, vol. 182, pp. 150–161, 2020.

[7] J.-S. Lee, H. Y. Kim, Y. A. Lee, S. Y. Lee, T. J. Cho, and J. M. Ko, "Clinical and genetic characteristics of 23 Korean patients with haploinsufficiency of the short-stature homeobox-containing gene," *Experimental and Clinical Endocrinology & Diabetes*, vol. 129, no. 8, pp. 611–620, 2021.

[8] H. S. Kim, D. K. Ng, M. B. Matheson et al., "Delayed menarche in girls with chronic kidney disease and the association with short stature," *Pediatric Nephrology*, vol. 35, pp. 1471–1475, 2020.

[9] World Medical Association, "World Medical Association Declaration of Helsinki: ethical principles for medical research involving human subjects," *Journal of the American Medical Association*, vol. 310, no. 20, pp. 2191–2194, 2013.

[10] Q. Zeng, L. Ou, W. Wang, and D. Y. Guo, "Gastrin, cholecystokinin, signaling, and biological activities in cellular processes," *Frontiers in Endocrinology*, vol. 11, p. 112, 2020.

[11] P. Xu, J. J. Gildea, C. Zhang et al., "Stomach gastrin is regulated by sodium via PPAR-α and dopamine D1 receptor," *Journal of Molecular Endocrinology*, vol. 64, pp. 53–65, 2020.

[12] Y. J. Kim, C. N. Paik, I. H. Jo, D. B. Kim, and J. M. Lee, "Serum gastrin predicts hydrogen-producing small intestinal bacterial overgrowth in patients with abdominal surgery: a prospective study," *Clinical and Translational Gastroenterology*, vol. 12, article e00291, 2020.

[13] J. Fu, Y. Tang, Z. Zhang, L. Tong, R. Yue, and L. Cai, "Gastrin exerts a protective effect against myocardial infarction via promoting angiogenesis," *Molecular Medicine*, vol. 27, p. 90, 2021.

[14] R. Veysey-Smith, A. R. Moore, S. V. Murugesan et al., "H. pylori effects of proton pump inhibitor therapy, infection and gastric preneoplastic pathology on fasting serum gastrin concentrations," *Frontiers in Endocrinology*, vol. 12, article 741887, 2021.

[15] I. S. Ferraz, D. M. C. Vieira, L. A. D. Ciampo Jr. et al., "Vitamin A deficiency and association between serum retinol and IGF-1 concentrations in Brazilian children with Down syndrome," *Jornal de Pediatria*, vol. 98, no. 1, pp. 76–83, 2022.

[16] S. Hata, H. Mori, T. Yasuda et al., "A low serum IGF-1 is correlated with sarcopenia in subjects with type 1 diabetes mellitus: findings from a post-hoc analysis of the iDIAMOND study," *Diabetes Research and Clinical Practice*, vol. 179, article 108998, 2021.

[17] J. Pyo, K. Hare, S. Pletts et al., "Feeding colostrum or a 1:1 colostrum:milk mixture for 3 days postnatal increases small intestinal development and minimally influences plasma glucagon-like peptide-2 and serum insulin-like growth factor-1 concentrations in Holstein bull calves," *Journal of Dairy Science*, vol. 103, no. 5, pp. 4236–4251, 2020.

[18] E. Kjellberg, J. Roswall, S. Bergman, B. Strandvik, and J. Dahlgren, "Serum n-6 and n-9 fatty acids correlate with serum IGF-1 and growth up to 4 months of age in healthy Infants," *Journal of Pediatric Gastroenterology and Nutrition*, vol. 66, no. 1, pp. 141–146, 2018.

[19] A. Hameed, L. B. Gallagher, E. Dolan et al., "Insulin-like growth factor-1 (IGF-1) poly (lactic-co-glycolic acid)(PLGA) microparticles–development, characterisation, and in vitro assessment of bioactivity for cardiac applications," *Journal of Microencapsulation*, vol. 36, pp. 267–277, 2019.

[20] A. J. Fischer-Tlustos, J. Pyo, Y. Song, D. L. Renaud, L. L. Guan, and M. A. Steele, "Short communication: effect of delaying the first colostrum feeding on small intestinal histomorphology and serum insulin-like growth factor-1 concentrations in

neonatal male Holstein calves," *Journal of Dairy Science*, vol. 103, no. 12, pp. 12109–12116, 2020.

[21] L. Huang, Z. Wang, Z. Shan et al., "Nasal asymmetry changes during growth and development in 6- to 12-year-old children with repaired unilateral cleft lip and palate: a 3D computed tomography analysis," *Journal of Anatomy*, vol. 240, pp. 155–165, 2022.

[22] T. D. Tran, S. Holton, H. Nguyen, and J. Fisher, "Physical growth: is it a good indicator of development in early childhood in low- and middle-income countries?," *BMC Pediatrics*, vol. 19, p. 276, 2019.

[23] D. Xu and Z. Haolin, "Correlation between hypothyroidism during pregnancy and glucose and lipid metabolism in pregnant women and its influence on pregnancy outcome and fetal growth and development," *Frontiers in Surgery*, vol. 9, article 863286, 2022.

[24] X. Zeng, X. Xu, Q. Qin, K. Ye, W. Wu, and X. Huo, "Heavy metal exposure has adverse effects on the growth and development of preschool children," *Environmental Geochemistry and Health*, vol. 41, no. 1, pp. 309–321, 2019.

[25] F. Motta, A. P. Eisencraft, and L. G. Crisostomo, "Influence of growth hormone replacement on neurological and psychomotor development. Case report," *Einstein (Sao Paulo)*, vol. 16, article eRC3961, 2018.

Hindawi
Disease Markers
Volume 2022, Article ID 2081590, 8 pages
https://doi.org/10.1155/2022/2081590

Research Article

Exploring Key Genes and Pathways of Cardiac Hypertrophy Based on Bioinformatics

Zhenzhen Zhang and Chunxiao Wang

Department of Cardiology, The Affiliated Yantai Yuhuangding Hospital of Qingdao University, Yantai 264000, China

Correspondence should be addressed to Chunxiao Wang; wangchunxiao@ytyhdyy.com.cn

Received 28 June 2022; Revised 21 July 2022; Accepted 4 August 2022; Published 22 August 2022

Academic Editor: Chang Gu

Objective. This research is aimed at identifying the key genes and pathways of cardiac hypertrophy using bioinformatics and at providing a new target for the identification of cardiac hypertrophy. *Methods*. Microarray data GSE1621 and GSE18801 were acquired from the GEO database. The DEGs of GSE1621 and GSE18801 were analyzed using the online tool GEO2R. "ggplot2" package of R software was utilized to generate the volcano plots. The top and bottom 10 genes were mapped as a heat map. GO functional annotation analysis and KEGG pathway enrichment analysis were performed separately for DEGs using the online software DAVID. Histograms were plotted using the R "ggplot2" package. The DEGs were imported into the STRING online database for constructing PPI networks and analyzing the DEG interaction relationships. *Results*. In the present study, 469 DEGs were screened in GSE1621 and a total of 793 DEGs were screened in GSE18801. GO analyses indicate that DEGs were mainly involved in cardiac muscle contraction, regulation of blood circulation, regulation of muscle contraction, muscle contraction, striated muscle contraction, regulation of heart contraction, regulation of striated muscle contraction, and tissue remodeling. KEGG analyses indicate that DEGs were mainly involved in Th17 cell differentiation, Th1 and Th2 cell differentiation, HIF-1 signaling pathway, pathways in cancer, hematopoietic cell lineage, Chagas disease and cell adhesion molecules, viral myocarditis, central carbon metabolism in cancer, acute myeloid leukemia, and JAK-STAT signaling pathway. Eight hub genes were screened, including Akt1, Lox, Timp1, Col1al, Spp1, Ccnd1, Mmp3, and Egfr. *Conclusions*. The DEGs associated with cardiac hypertrophy were screened via bioinformatics analysis, and eight hub genes were identified, including Akt1, Lox, Timp1, Col1al, Spp1, Ccnd1, Mmp3, and Egfr, which might be a new target for the identification of cardiac hypertrophy.

1. Introduction

Cardiac hypertrophy is an adaptive response of the myocardium to increased sustained load and often leads to cardiovascular disease [1]. Patients with cardiac hypertrophy clinically show fatigue, dizziness, chest pain, and dyspnea, which seriously harm human health [2]. In developing countries, cardiac hypertrophy ultimately induced heart failure for approximately 25% of all deaths in the population [3, 4].

Cardiac hypertrophy is mainly characterized by hypertrophy of cardiomyocytes and alterations in interstitial components [1]. Pathological myocardial hypertrophy is characterized by protein accumulation, new formation of myogenic fibers, increased expression of embryonic genes, proliferation of myocardial interstitial cells, an increase in the size of cardiomyocytes, and proliferation of connective tissue such as collagen [5, 6]. These pathological changes cause structural disorders of the myocardium, reduced contractility, impaired blood supply, and increased oxygen consumption, resulting in cardiac systolic and diastolic insufficiency, leading to heart failure, arrhythmias, and sudden death. Many cardiovascular diseases such as hypertension, myocardial infarction, heart valve disease, and hyperthyroidism can trigger myocardial hypertrophy, which is mostly considered to be irreversible [5]. The pathogenesis of pathological cardiac hypertrophy is complex and is regulated by various cellular signals [7]. For half a century, although cardiac hypertrophy has been extensively studied

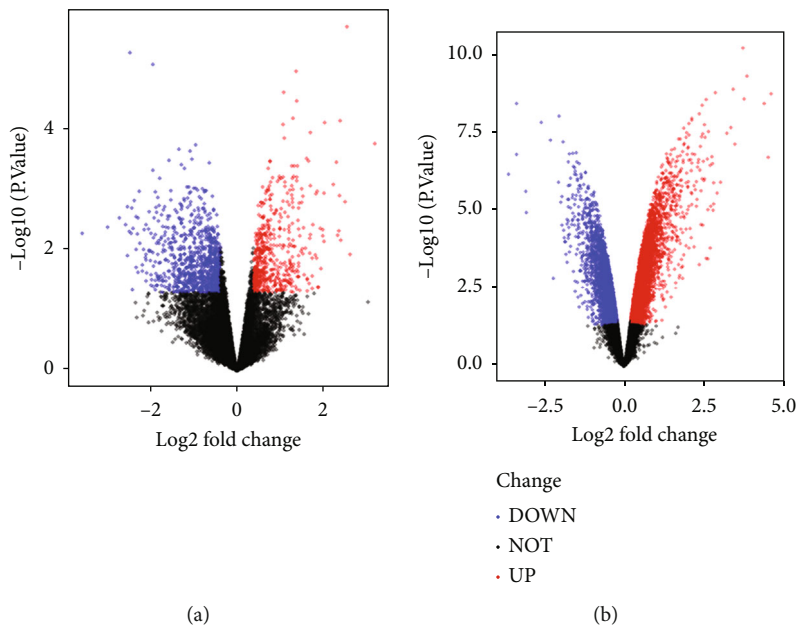

Figure 1: Volcano plots of DEGs in (a) GSE1621 and (b) GSE18801.

at the global, cellular, and molecular levels, the formation process of cardiac hypertrophy remains a mystery.

With the development of bioinformatics, genomics, transcriptomics, proteomics, and metabolomics have generated big data, which can be analyzed by combining bioinformatics and computer science, providing new methods to study the molecular mechanisms of diseases [8]. With the rapid development of gene chips, screening differentially expressed genes (DEGs) and analyzing their functions based on gene chips are currently a new and effective method to study the molecular mechanisms of disease development [9]. Meng et al. obtained GSE129090 dataset and found Bcl-2 participate in progression of cardiac hypertrophy [10]. Katja et al. constructed left ventricular hypertrophy model and screened Efcab6 as new potential candidate gene in left ventricular hypertrophy [11]. The present study is aimed at screening hub genes that participate in cardiac hypertrophy based on GEO database.

In this study, the gene microarray of myocardial hypertrophy in GEO database was used to screen out DEGs, and online databases such as GO and KEGG were utilized to annotate differential gene functions and analyze gene enriched signaling pathways, which provided ideas for identifying new biomarkers of myocardial hypertrophy and revealing potential mechanisms of the disease.

2. Material and Methods

2.1. Data Collection. Microarray data GSE1621 and GSE18801 were downloaded from the GEO database. GSE1621 included 4 myocardial hypertrophy mice caused by coarctation of aortic arch and 3 sham mice, and the platform was Affymetrix Murine Genome U74A Version 2 Array. GSE18801 included 3 isoproterenol-induced cardiac hypertrophy subjects and 3 normal subjects, and the platform was Affymetrix Mouse Genome 430 2.0 Array.

2.2. Identification of DEGs. The DEGs of GSE1621 and GSE18801 were analyzed using the online tool GEO2R. The screening criteria for DEGs were adjusted P value $<$ 0.05 and $|\mathrm{Log}_2$ fold change (LogFC)$| > 1.5$. "ggplot2" package was utilized to generate the volcano plots. The top and bottom 10 genes were mapped as a heat map.

2.3. Functional and Pathway Enrichment Analyses. GO functional annotation analysis and KEGG pathway enrichment analysis were performed separately for DEGs using the online software DAVID (https://david.ncifcrf.gov/tools.jsp). Histograms were plotted using the R "ggplot2" package.

2.4. PPI Network Construction. The DEGs were first imported into the STRING online database (https://cn.string-db.org/) for analysis. Cytoscape software was used to construct PPI networks and analyze the DEG interaction relationships. Finally, the "MCC" algorithm of "Cytohubba" plugin was used to build the module and screen the candidate hub genes.

3. Results

3.1. Identification of DEGs. 153 upregulated DEGs and 316 downregulated DEGs were screened in GSE1621 in the heart tissues of mouse with cardiac hypertrophy (Figure 1(a)). 527 upregulated DEGs and 266 downregulated DEGs were screened in GSE18801 (Figure 1(b)). 38 co-DEGs, including 17 upregulated genes (Figure 2(c)) and 21 downregulated genes (Figure 2(d)), were obtained by taking the intersection from DEGs of GSE1621 and GSE18801. The heat map was generated based on the top and bottom 10 DEGs (Figures 2(a) and 2(b)).

3.2. GO Annotation Analyses of DEGs. The DEGs of GSE1621 participated in positive regulation of cell adhesion, phenol-containing compound biosynthetic process,

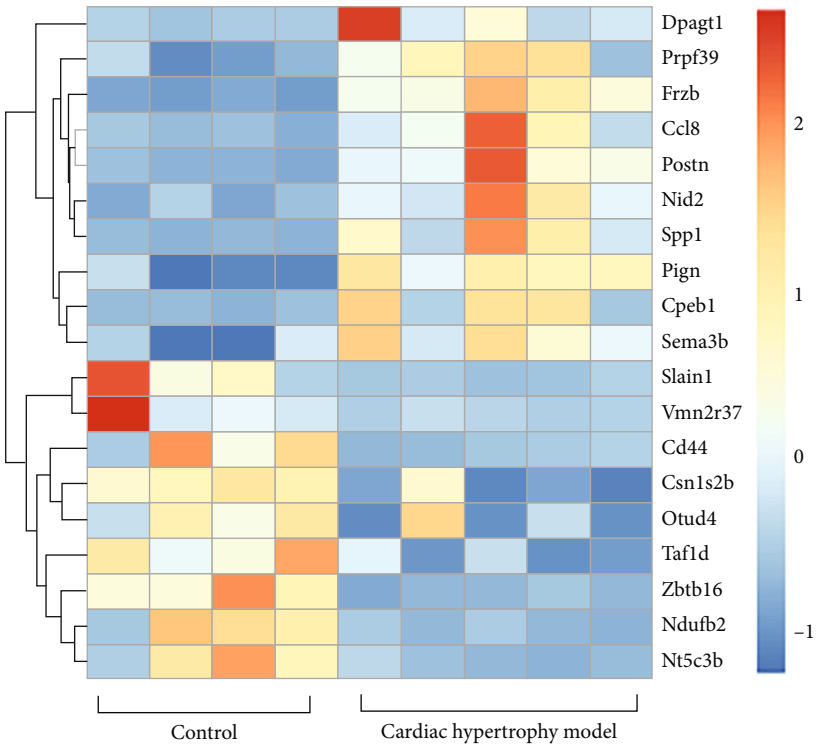

(a)

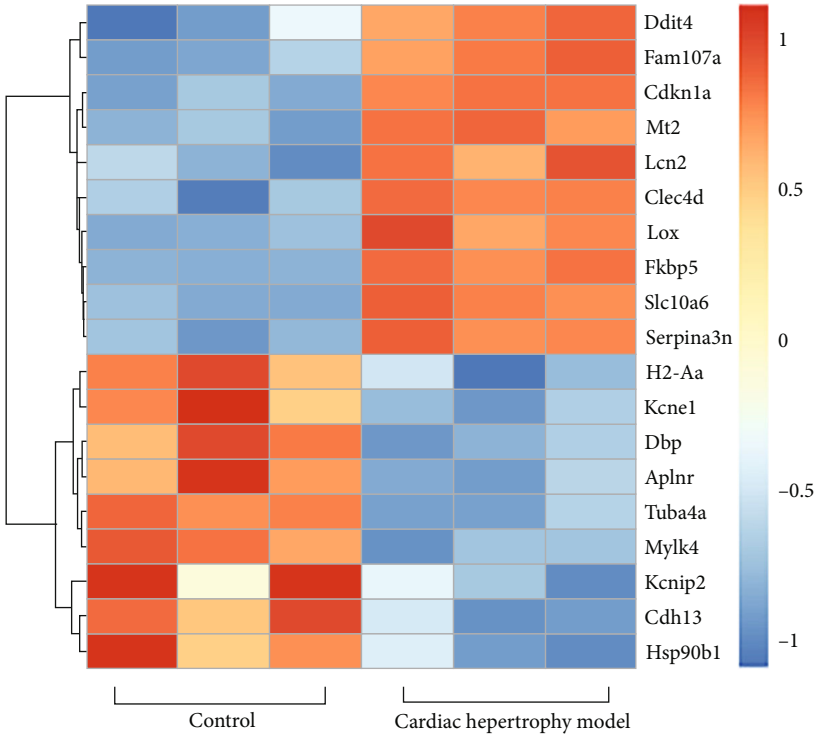

(b)

Figure 2: Continued.

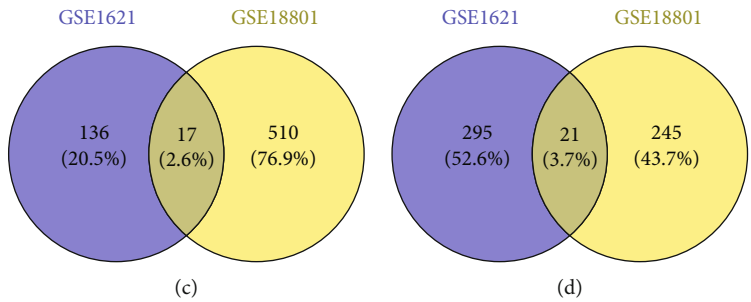

Figure 2: The heat map plots of the top 10 genes and Venn diagrams. (a) The heat map plots of GSE1621. (b) The heat map plots of GSE18801. Venn diagrams illustrated the number of (c) up- and (d) downregulated genes in both datasets, respectively.

activation of immune response, mononuclear cell differentiation, response to ketone, regulation of T cell activation, and negative regulation of T cell proliferation and activation (Figure 3(a)). The DEGs of GSE18801 participated in positive regulation of epithelial cell proliferation, tissue remodeling, regulation of epithelial cell proliferation, regulation of tissue remodeling, regulation of endothelial cell proliferation, epithelial cell proliferation, positive regulation of epithelial cell proliferation, and cell chemotaxis (Figure 3(b)). The co-DEGs participated in cardiac muscle contraction, regulation of blood circulation, regulation of muscle contraction, muscle contraction, striated muscle contraction, regulation of heart contraction, regulation of striated muscle contraction, and tissue remodeling (Figure 3(c)).

3.3. KEGG Pathway Enrichment Analyses of DEGs. The DEGs of GSE1621 were related to Th17 cell differentiation, pathways in cancer, hematopoietic cell lineage, Chagas disease and cell adhesion molecules, and Th1 and Th2 cell differentiation (Figure 4(a)). The DEGs of GSE18801 were related to viral myocarditis, thyroid hormone signaling pathway, FoxO signaling pathway, JAK-STAT signaling pathway, apelin signaling pathway, thyroid cancer, focal adhesion, HIF-1 signaling pathway, chemical carcinogenesis-receptor activation, proteoglycans in cancer, Epstein-Barr virus infection, influenza A, alcoholic liver disease, prostate cancer, lipid and atherosclerosis, IL-17 signaling pathway, PI3K-Akt signaling pathway, MAPK signaling pathway, human T cell leukemia virus 1 infection, pathways in cancer, hepatocellular carcinoma, hepatitis C, melanoma, fluid shear stress and atherosclerosis, and acute myeloid leukemia (Figure 4(b)). The co-DEGs of GSE1621 and GSE18801 were related to the HIF-1 signaling pathway (Figure 4(c)).

3.4. PPI Network and Hub Genes. DEGs were uploaded to STRING online software, and PPI network was constructed. The module analysis of GSE1621 using the MCODE plugin found three functional modules (Figure 5(a)), and Col1al was identified as hub genes. The module analysis of GSE18801 using the MCODE plugin found three functional modules (Figure 5(b)), and Ccnd1, Mmp3, Egfr, and Akt1 were identified as hub genes. The module analysis of co-DEGs using the MCODE plugin found one functional module (Figure 5(c)), and Lox, Timp1, and Spp1 were identified as hub genes.

4. Discussion

Cardiac hypertrophy is the cellular response of the heart to physiological stimuli (exercise, pregnancy, etc.) and pathological stimuli (increased pressure or volume load, valvular heart disease, etc.) [1]. Pathological cardiac hypertrophy causes enlargement of cardiomyocytes along the longitudinal axis, upregulation of embryonic gene expression, decreased myocardial contractile function, and irreversible processes such as apoptosis and myocardial fibrosis, which can eventually lead to heart failure [2]. Cardiac hypertrophy is traditionally considered to be a compensatory response to increased workload, to reduce ventricular wall pressure and to maintain cardiac systolic function. However, studies have shown that left ventricular hypertrophy is an independent risk factor for increased cardiovascular morbidity and mortality, even more so than other risk factors. In this experiment, two microarray data related to cardiac hypertrophy in GEO database were mined by bioinformatics, and their common DEGs were screened. Then, the data were analyzed secondarily by biofunctional enrichment, signal pathway enrichment analysis, and protein interaction, in order to provide new therapeutic targets of cardiac hypertrophy.

In the present study, 469 DEGs were screened in GSE1621 and a total of 793 DEGs were screened in GSE18801. GO analyses indicate that DEGs were mainly involved in cardiac muscle contraction, regulation of blood circulation, regulation of muscle contraction, muscle contraction, striated muscle contraction, regulation of heart contraction, regulation of striated muscle contraction, and tissue remodeling. KEGG analyses indicate that DEGs were mainly involved in Th17 cell differentiation, Th1 and Th2 cell differentiation, HIF-1 signaling pathway, pathways in cancer, hematopoietic cell lineage, Chagas disease and cell adhesion molecules, viral myocarditis, central carbon metabolism in cancer, JAK-STAT signaling pathway, and acute myeloid leukemia. HIF-1 is a dimeric transcription factor composed of two subunits, including HIF-1α and HIF-1β. HIF-1α expression induced by pressure load will lead to a significant increase in heart mass to body weight ratio and increased BNP expression and promote the occurrence of myocardial hypertrophy [12]. PI3K is an intracellular phosphatidylinositol kinase. Yu et al. found PI3K could participate in regulating progression of cardiac hypertrophy to heart failure by prolonging autophagic activation, which

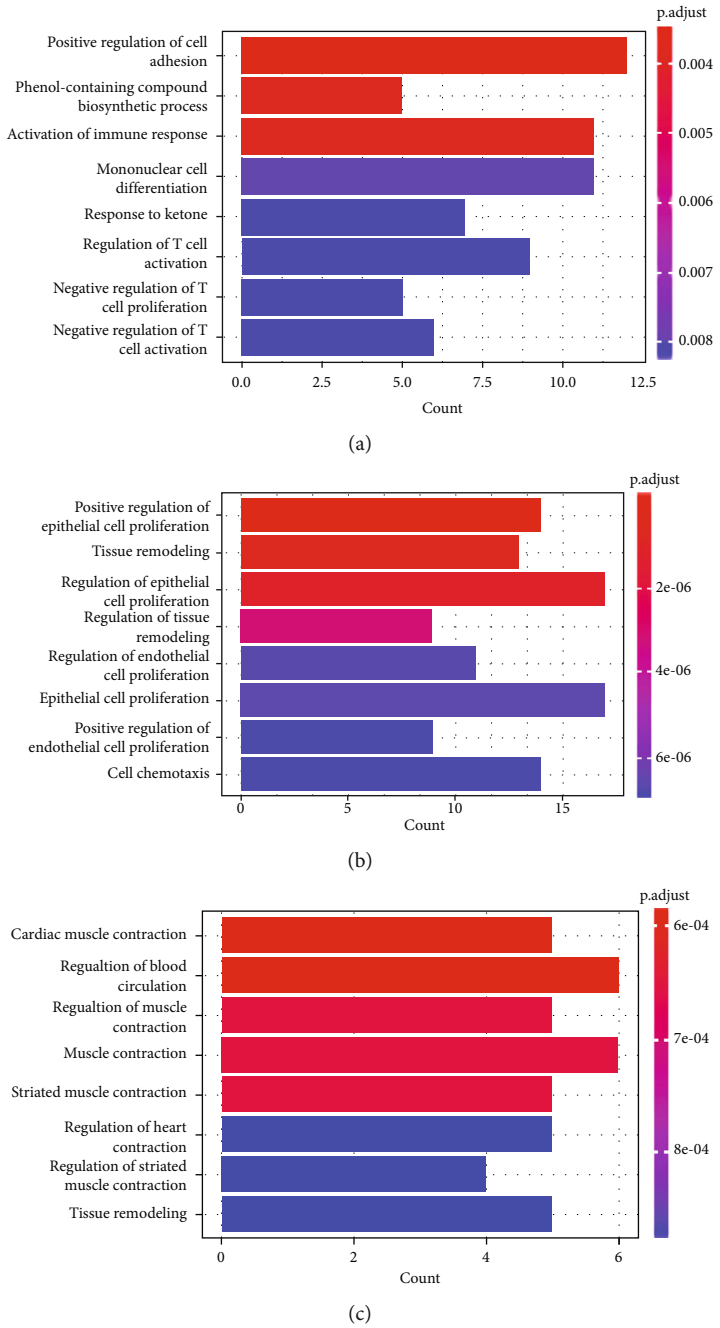

Figure 3: Gene Ontology (GO) analyses of DEGs in (a) GSE1621, (b) GSE18801, and (c) co-DEGs.

may be a potential target for the treatment of decompensated myocardial hypertrophy [13]. JAK-STAT is mainly found in cardiomyocytes and is activated by cytokines and growth factors and is a direct signaling pathway linking cell surface receptors to nuclear transcription. Alrasheed et al. suggested simvastatin prevented isoprenaline-induced myocardial hypertrophy by modulating the JAK-STAT signaling pathway [14]. The MAPK signaling pathway is activated by cardiotrophin-1, transforming growth factor-β, mechanical stretch, and tyrosine kinase receptors and is involved in a series of protein kinase phosphorylations which is essential in the progression of myocardial pathological hypertrophy [15]. Eight hub genes were screened, including Akt1, Lox, Timp1, Col1al, Spp1, Ccnd1, Mmp3, and Egfr.

Serine/threonine kinase (Akt), also known as PKB, is a direct downstream target protein of PI3K [16]. Akt activation is antiapoptotic and promotes cell proliferation and has roles in regulating cardiomyocyte growth and coronary angiogenesis. Akt is a major effector of PI3K, and only Akt1 and Akt2 of the three Akt genes are expressed in the myocardium. Akt1 knockout mice weighed 20% less than those born in the same litter and had a corresponding reduction in the weight of all tissues, including the heart [17]. The downstream target proteins of the EGFR signaling pathway

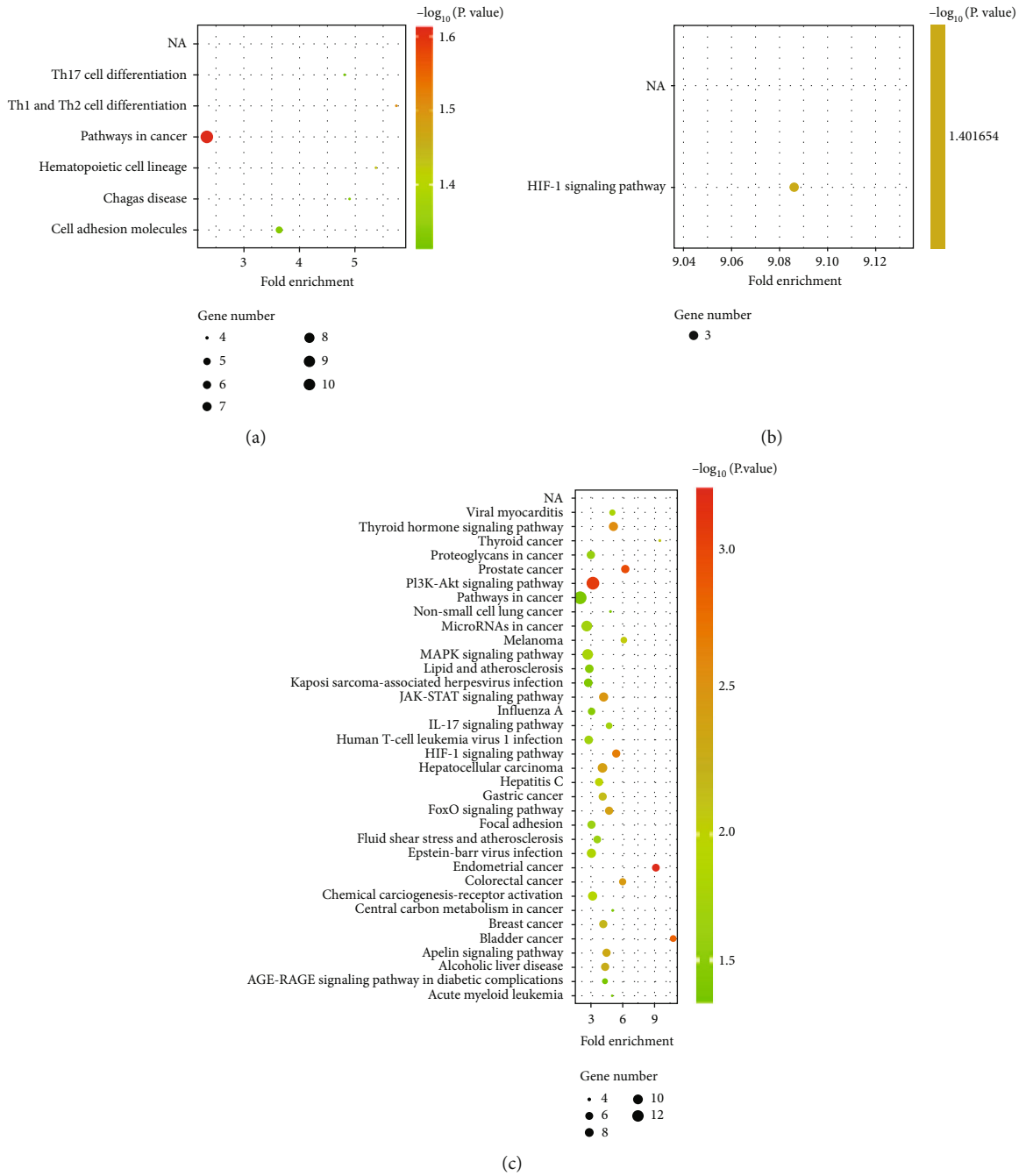

Figure 4: KEGG analyses of DEGs. KEGG analysis of DEGs in (a) GSE1621, (b) GSE18801, and (c) co-DEGs.

include AKT, ERK, and STAT3. The EGFR signaling pathway is participated in biological activities like cycle regulation, division, and cell proliferation and is closely associated with the development of cardiovascular diseases such as cardiomyopathy and cardiovascular injury [18]. Kenigsberg et al. found that the EGFR signaling pathway was participated in cell cycle regulation [19]. The cell cycle progresses to the midmitotic phase with the formation of spindle filaments, and microfilaments are formed in large numbers at this stage, resulting in an increase in cell size.

The extracellular matrix (ECM), which surrounds the cardiomyocytes, protects the functional and structural integrity of the heart. Alterations in the extracellular matrix, particularly abnormal alterations in type 1 collagen fibers and type 2 collagen fibers, play an important role in myocardial remodeling. Alterations in the extracellular matrix of the myocardium, particularly the deposition of myocardial collagen that develops asynchronously with cardiomyocyte hypertrophy, are important in contributing to the progression of myocardial hypertrophy. Matrix metalloproteinases (MMPs) of myocardial hypertrophy are protein-cleaving enzymes that hydrolyze the extracellular matrix and consist mainly of collagenases [20]. MMPs can increase abnormal collagen synthesis by degrading the extracellular matrix,

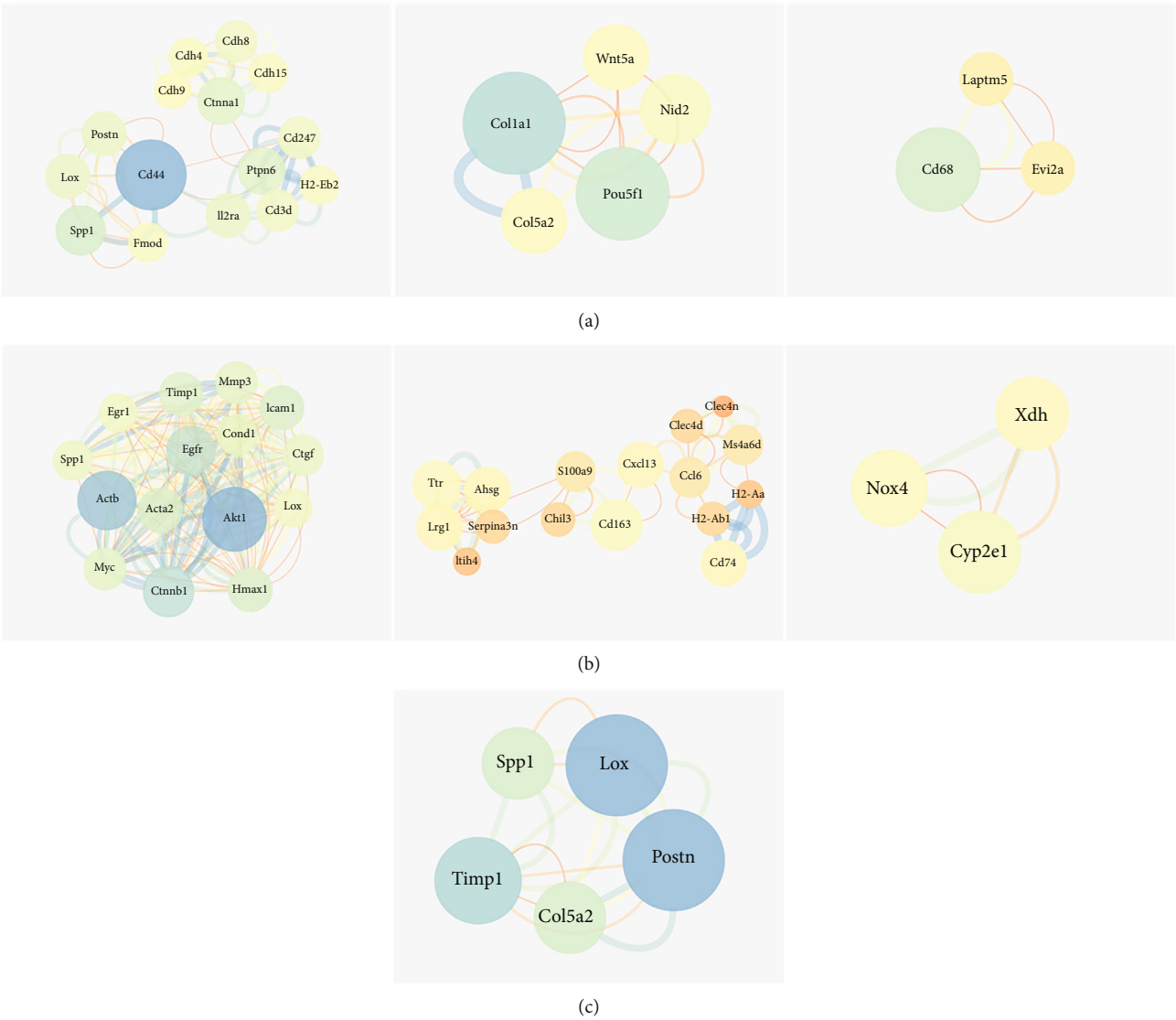

Figure 5: PPI networks based on the screened DEGs in (a) GSE1621, (b) GSE18801, and (c) co-DEGs.

stimulating the continuous emergence of new connective tissue and eventually leading to myocardial interstitial fibrosis, ventricular enlargement, and loss of contractile function of the myocardium [21]. MMP3 is a member of the matrix metalloproteinase family that degrades the extracellular matrix and can degrade denatured collagen [22]. In cultured neonatal rat cardiac fibroblasts, TGF-β1 upregulated collagen type 1, col1a1, and col3a1. Col1a1 and col3a1 are closely related to the formation of myocardial hypertrophy.

In conclusion, in this study, the DEGs associated with cardiac hypertrophy were screened via bioinformatics analysis, and eight hub genes were identified, including Akt1, Lox, Timp1, Col1al, Spp1, Ccnd1, Mmp3, and Egfr, which might play an important role in the development of cardiac hypertrophy induced by pressure overload, further providing more information for studies on pathogenesis and screening of potential biomarkers of cardiac hypertrophy.

Data Availability

Data to support the findings of this study is available on reasonable request from the corresponding author.

Conflicts of Interest

The authors have no conflicts of interest to declare.

References

[1] I. Shimizu and T. Minamino, "Physiological and pathological cardiac hypertrophy," *Journal of Molecular and Cellular Cardiology*, vol. 97, pp. 245–262, 2016.

[2] Y. K. Tham, B. C. Bernardo, J. Y. Y. Ooi, K. L. Weeks, and J. R. McMullen, "Pathophysiology of cardiac hypertrophy and heart failure: signaling pathways and novel therapeutic targets," *Archives of Toxicology*, vol. 89, no. 9, pp. 1401–1438, 2015.

[3] H. N. Sabbah, "Silent disease progression in clinically stable heart failure," *European Journal of Heart Failure*, vol. 19, no. 4, pp. 469–478, 2017.

[4] M. Michels, I. Olivotto, F. W. Asselbergs, and J. van der Velden, "Life-long tailoring of management for patients with hypertrophic cardiomyopathy : awareness and decision-making in changing scenarios," *Netherlands Heart Journal*, vol. 25, no. 3, pp. 186–199, 2017.

[5] M. Nakamura and J. Sadoshima, "Mechanisms of physiological and pathological cardiac hypertrophy," *Nature Reviews. Cardiology*, vol. 15, no. 7, pp. 387–407, 2018.

[6] M. Tian, X. Jiang, X. Li, J. Yang, C. Zhang, and W. Zhang, "LKB1IP promotes pathological cardiac hypertrophy by targeting PTEN/Akt signalling pathway," *Journal of Cellular and Molecular Medicine*, vol. 25, no. 5, pp. 2517–2529, 2021.

[7] C. J. Oldfield, T. A. Duhamel, and N. S. Dhalla, "Mechanisms for the transition from physiological to pathological cardiac hypertrophy," *Canadian Journal of Physiology and Pharmacology*, vol. 98, no. 2, pp. 74–84, 2020.

[8] Z. Tao, A. Shi, R. Li, Y. Wang, X. Wang, and J. Zhao, "Microarray bioinformatics in cancer- a review," *Journal of BUON*, vol. 22, no. 4, pp. 838–843, 2017.

[9] W. Yan, P. Wang, C. X. Zhao, J. Tang, X. Xiao, and D. W. Wang, "Decorin gene delivery inhibits cardiac fibrosis in spontaneously hypertensive rats by modulation of transforming growth factor-beta/Smad and p38 mitogen-activated protein kinase signaling pathways," *Human Gene Therapy*, vol. 20, no. 10, pp. 1190–1200, 2009.

[10] X. Meng, J. Cui, and G. He, "Bcl-2 is involved in cardiac hypertrophy through PI3K-Akt pathway," *BioMed Research International*, vol. 2021, Article ID 6615502, 2021.

[11] K. Grabowski, M. Riemenschneider, L. Schulte et al., "Fetal-adult cardiac transcriptome analysis in rats with contrasting left ventricular mass reveals new candidates for cardiac hypertrophy," *PLoS One*, vol. 10, no. 2, article e0116807, 2015.

[12] M. Hölscher, K. Schäfer, S. Krull et al., "Unfavourable consequences of chronic cardiac HIF-1α stabilization," *Cardiovascular Research*, vol. 94, no. 1, pp. 77–86, 2012.

[13] P. Yu, Y. Zhang, C. Li et al., "Class III PI3K-mediated prolonged activation of autophagy plays a critical role in the transition of cardiac hypertrophy to heart failure," *Journal of Cellular and Molecular Medicine*, vol. 19, no. 7, pp. 1710–1719, 2015.

[14] N. M. Al-Rasheed, M. M. Al-Oteibi, R. Z. Al-Manee et al., "Simvastatin prevents isoproterenol-induced cardiac hypertrophy through modulation of the JAK/STAT pathway," *Drug Design, Development and Therapy*, vol. 9, pp. 3217–3229, 2015.

[15] Q. Xu, H. Ding, S. Li et al., "Sleeve gastrectomy ameliorates diabetes-induced cardiac hypertrophy correlates with the MAPK signaling pathway," *Frontiers in Physiology*, vol. 12, article 785799, 2021.

[16] L. Ba, J. Gao, Y. Chen et al., "Allicin attenuates pathological cardiac hypertrophy by inhibiting autophagy via activation of PI3K/Akt/mTOR and MAPK/ERK/mTOR signaling pathways," *Phytomedicine*, vol. 58, article 152765, 2019.

[17] H. Cho, J. L. Thorvaldsen, Q. Chu, F. Feng, and M. J. Birnbaum, "Akt1/PKBα is required for normal growth but dispensable for maintenance of glucose homeostasis in mice∗," *The Journal of Biological Chemistry*, vol. 276, no. 42, pp. 38349–38352, 2001.

[18] W. Ai, Y. Zhang, Q. Z. Tang et al., "Silibinin attenuates cardiac hypertrophy and fibrosis through blocking EGFR- dependent signaling," *Journal of Cellular Biochemistry*, vol. 110, no. 5, pp. 1111–1122, 2010.

[19] B. Kenigsberg, V. Jain, and A. Barac, "Cardio-oncology related to heart failure: epidermal growth factor receptor target-based therapy," *Heart Failure Clinics*, vol. 13, no. 2, pp. 297–309, 2017.

[20] G. Euler, F. Locquet, J. Kociszewska et al., "Matrix metalloproteinases repress hypertrophic growth in cardiac myocytes," *Cardiovascular Drugs and Therapy*, vol. 35, no. 2, pp. 353–365, 2021.

[21] S. Wang, M. Cheng, Z. Hu et al., "Angiotensin II facilitates matrix metalloproteinase-9-mediated myosin light chain kinase degradation in pressure overload-induced cardiac hypertrophy," *Cellular Physiology and Biochemistry*, vol. 44, no. 6, pp. 2281–2295, 2018.

[22] M. Matusiewicz, M. Rachwalik, M. Krzystek-Korpacka et al., "Upregulated sulfatase and downregulated MMP-3 in thoracic aortic aneurysm," *Advances in Clinical and Experimental Medicine*, vol. 29, no. 5, pp. 565–572, 2020.

Hindawi
Disease Markers
Volume 2022, Article ID 4688203, 6 pages
https://doi.org/10.1155/2022/4688203

Research Article

Inhibitory Effect of Trihydroxy Isoflavone on Neuronal Apoptosis in Natural Aging Rats

Ke Zhao,[1] Shenghui Li,[2] Jianzhou Chen,[2] and Qinghua Jin[2]

[1]*Department of Physiology, Baicheng Medical College, Baicheng, 137000 Jilin, China*
[2]*Department of Physiology and Pathophysiology, College of Medicine, Yanbian University, Yanji, 133000 Jilin, China*

Correspondence should be addressed to Qinghua Jin; qinghuajin@163.com

Received 24 June 2022; Revised 29 July 2022; Accepted 1 August 2022; Published 21 August 2022

Academic Editor: Jianxin Shi

Objective. To explore the impact of genistein (Gen) on the apoptosis of neuronal cells in naturally aged rats and its mechanism. *Methods*. Fifty SD male rats were allocated into five groups at random, including youth group (3M group), natural aging group (24M group), and Gen low-, medium-, and high-dose groups. Starting from 18 months of age, Gen 10, 30, and 60 mg-kg^{-1} were administered via gavage to the Gen low-, medium-, and high-dose groups, respectively, while the rats in the natural aging group was given saline by gavage until 24 months of age, and the drug was stopped for 1 d per week for 6 months. The protein expression of target genes was examined using western blotting. *Results*. In contrast to the 3M group, the 24M group rats showed disturbed neuronal cell arrangement and massive cell degeneration. After 6 months of Gen intervention, in contrast to the 24M group, the neural cell pathology in the CA3 area of the hippocampus improved and cell apoptotic decreased observably. In contrast to the 3M group, the protein expression of c-Jun amino-terminal kinase (p-JNK), C/EBP homologous protein (CHOP), inflammatory vesicle 3-associated factor (NLRP3), cysteine protease-1 (Caspase-1), and apoptosis-related punctate protein (ASC) and downstream inflammatory factors in the hippocampus was obviously increased in the 24M group. In contrast to the 24M group, the protein expression of p-JNK, CHOP, NLRP3, Caspase-1, and ASC and downstream inflammatory factors in the hippocampus was observably declined in Gen groups. *Conclusion*. Gen has a protective effect on hippocampal neurons in aging rat brain tissue via the inhibition of the ERS apoptotic signaling pathway and NLRP3 inflammatory vesicle activation.

1. Introduction

Aging is a natural and complex process that is inevitable in the organism; neurodegenerative diseases are its main clinical manifestations [1–3]. With the intensive research on neurodegenerative diseases associated with brain aging, it has been confirmed that oxidative stress, inflammation, and other induced neuroapoptosis are essential in these diseases [4, 5]. Endoplasmic reticulum stress- (ERS-) induced apoptosis is a factor in the development of many neurodegenerative diseases and causes neurological disorders mainly due to oxidative stress and metabolic disorders caused by the accumulation of unfolded proteins [6]. There is evidence that excessive activation of ERS pathway unfolded protein signaling is detected in the brains of AD, PD, and HD patients, inducing apoptosis [7]. Mercado et al. found significantly elevated expression of genes related to the ERS signaling pathway in PD patients [8]. Neuroinflammation-induced apoptosis is involved in aging and neurodegenerative diseases. Increased release of inflammatory factors and other neurotoxic factors has been reported in naturally aging individuals and AD and PD brains [9]. Griffioen et al. found that inhibition of neuroinflammation-related genes significantly prolonged the lifespan of HD mice and that expression of ERS and neuroinflammatory response-related factors was significantly increased in the brains of naturally aging APP/PS1 mice [10].

Genistein (Gen) is an isoflavone rich in soybeans and possesses a variety of biological activities and pharmacological effects, such as antitumor, antifungal, hypolipidemic, and hypoglycemic activities [11]. Numerous studies proved that Gen has a protective effect on nerve cells [12]. Xu et al. found

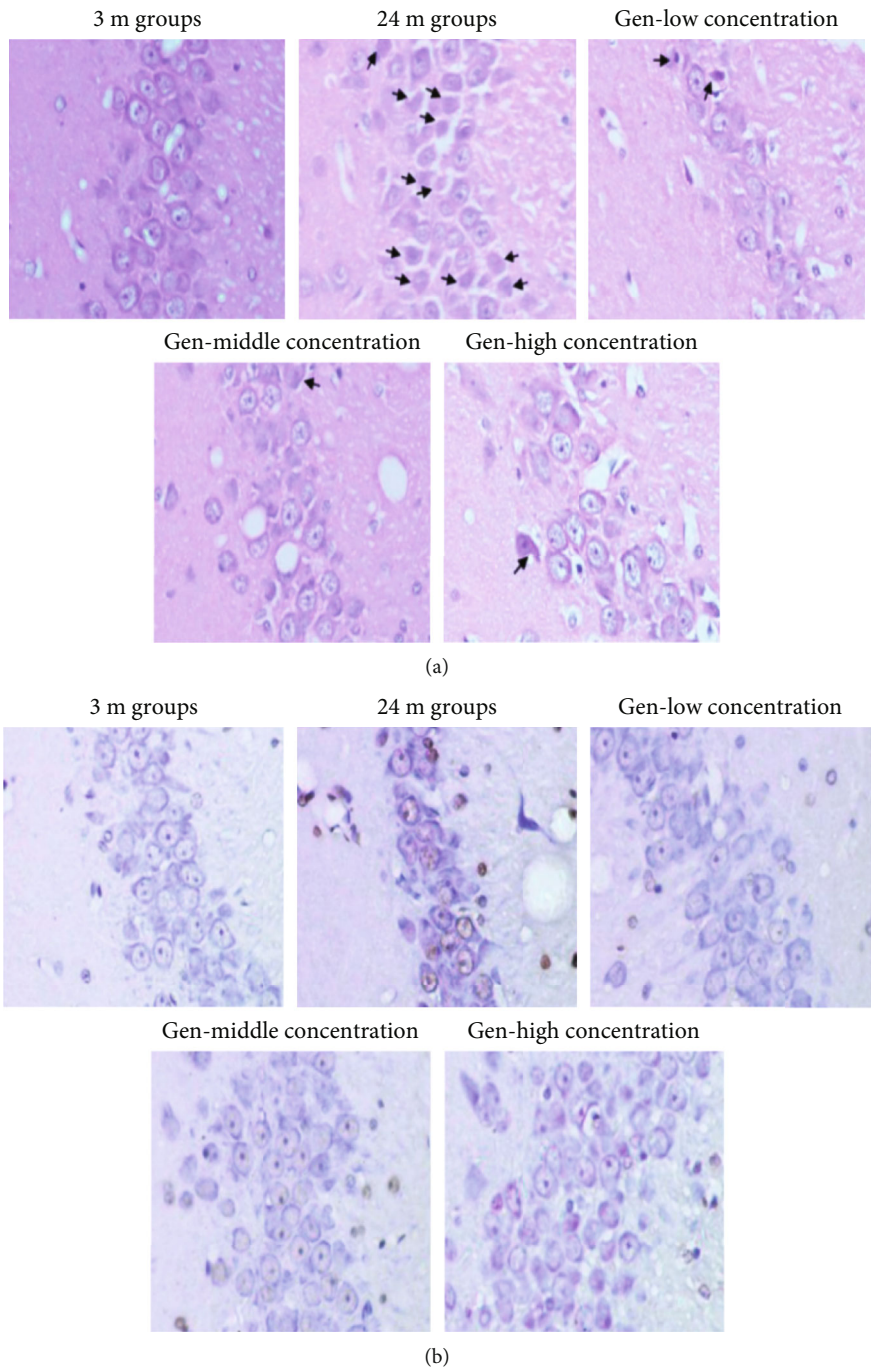

Figure 1: Effect of Gen on the morphology and apoptosis of rat hippocampal neurons (×400). Note: (a) HE staining and (b) Tunel staining. The arrows meant the degenerated cells.

that Gen significantly improved the morphology of vertebral cells in the CA1 region of the hippocampus of mice with cerebral ischemia-reperfusion, declined cell apoptosis, and significantly inhibited apoptosis-related proteins such as TNF-α inflammatory factor and p-JNK1/2 in brain tissue, exerting a neuroprotective effect [13]. However, whether Gen can reduce apoptosis in naturally aged rats by inhibiting apoptosis-related proteins of the ERS signaling pathway and inhibiting the inflammatory response activated by NLRP3 inflammatory vesicles remains to be further investigated.

2. Materials and Methods

2.1. Animals. SPF male SD rats (200 ± 20 g) were acquired from the Laboratory Animal Center of Three Gorges University, Yichang, Hubei, China. The animal production

Table 1: Effect of Gen on p-JNK and CHOP protein expression levels ($\bar{x} \pm s$, $n = 10$).

Group	Dose (mg-kg^{-1})	p-JNK	CHOP
3M group	—	0.82 ± 0.06	0.42 ± 0.04
24M group	—	$1.05 \pm 0.04^{*}$	$0.74 \pm 0.05^{***}$
Gen low-dose group	10	$0.81 \pm 0.08^{\#}$	$0.62 \pm 0.04^{\#}$
Gen medium-dose group	30	$0.78 \pm 0.12^{\#}$	$0.55 \pm 0.01^{\#\#}$
Gen high-dose group	60	$0.75 \pm 0.16^{\#}$	$0.34 \pm 0.05^{\#\#\#}$

Note: in contrast to the 3M group, $^{*}P < 0.05$ and $^{***}P < 0.001$; in contrast to the 24M group, $^{\#}P < 0.05$, $^{\#\#}P < 0.01$, and $^{\#\#\#}P < 0.001$. The following table is the same.

license number is (SCXK)(E) 2011-0012. The feeding environment was 23 ± 3°C, 60 ± 5% relative humidity, 12 h/12 h alternating light and dark, and free feeding and drinking.

2.2. Drugs and Reagents. Gen (purity > 95%), Chengdu Phytobiotech Co., Ltd., Lot No. PCS0841; rabbit multiple antibodies JNK (Lot No. #9252), rabbit multiple antibodies p-JNK (Lot No. #9251), rabbit multiple antibodies β-actin (Lot No. 4970L), Cell Signaling, USA; Rabbit Multi-Anti-ASC (Lot #: sc-22514-R), Rabbit Multi-Anti-IL-18 (Lot #: sc-7954), Rabbit Multi-Anti-IL-1β (Lot #: sc-7884), Sheep Multi-Anti-TNF-α (Lot #: sc-1350), Mouse Monoclonal Anti-CHOP (Lot #: sc-56107), Santa Cruz, USA; Rabbit Multi-Anti-NLRP3 (Lot: ab214185), Abcam, USA; Mouse Monoclonal Antibody Caspase-1 (Lot No. NB100-56565), Novus Corporation, USA; and goat anti-rabbit, goat anti-mouse secondary antibody, and donkey anti-goat secondary antibody, Wuhan Corey Co., were used.

2.3. Apparatus. PowerPac200 Western Blotting Electrophoresis Instrument, Bio-Rad, USA; BioshineChemiQ4800 Chemiluminescent Gel Imaging Automated Developer, Shanghai OXO Scientific Instruments Co. Ltd.; TP1020 automatic dehydrator, EG1150H paraffin embedding machine, EG1150C ultrathin slicer, Leica, Germany; and BX53 microscope, Olympus, Japan, were used.

2.4. Methodology

2.4.1. Animal Grouping and Drug Administration. Ten 3-month-old rats were utilized as the young control group (3M group), and 40 18-month-old rats were allocated into the aging group (24M group), with the Gen low-, medium-, and high-dose groups at random. Starting from 18 months of age, Gen 10, 30, and 60 mg-kg^{-1} were administered by gavage to the Gen low-, medium-, and high-dose groups, respectively, while the natural aging group was given saline by gavage until 24 months of age, and the drug was stopped for 1 d per week for 6 months. The aging group was gavaged with the same amount of saline.

2.4.2. Morphological Changes Observed via HE Staining. The rats were anesthetized with 2.5% pentobarbital sodium through intraperitoneal injection, the blood was flushed by perfusion of saline into the thoracic aorta and then perfused with 4% paraformaldehyde, and the brain was fixed in 4% paraformaldehyde by severing the head. After dehydration, the tissue was paraffin-embedded, 4 μm sections were stained using HE, and the morphology was analyzed microscopically.

2.4.3. Measurement of Apoptosis in Hippocampal Neurons of Aging Rats Using Tunel Method. The cells with brown granules in the nucleus were considered as apoptotic cells, and the results were observed under the microscope.

2.4.4. Detection of ERS- and Neuroinflammation-Induced Apoptosis Using Western Blot. The protein expression of ERS-associated proteins CHOP and p-JNK and neuroinflammation-associated factors was detected. Total proteins were extracted from rat hippocampal tissues, denatured in a water bath at 95°C for 10 minutes, separated through SDS-PAGE gel electrophoresis, and transferred to a membrane, which was incubated using primary antibodies overnight at 4°C. Secondary antibody was put in and incubated at 25°C. Protein bands were developed in ECL and were analyzed by grayscale scanning using ImageJ software.

2.5. Statistical Methods. Data analysis was conducted via SPSS 18.0 software. The difference between groups was analyzed using one-way ANOVA. $P < 0.05$ indicated obvious difference between the groups.

3. Results

3.1. Effect of Gen on the Morphology and Apoptosis of Neuronal Cells in the Hippocampal Region of Naturally Aged Rats. HE (Figure 1(a)) and Tunel (Figure 1(b)) staining was used to observe the pathological changes and apoptosis of neuronal cells in the CA3 region of the hippocampus of rats in each group. The results showed the neuronal cells in the CA3 region of the hippocampus of rats in the 3M group were neatly arranged and tightly packed, with clear nuclei and large, round nuclei; the neuronal cells in the hippocampus of rats in the 24M group were disorganized, with numerous degenerated cells (arrow), and the nuclei of degenerated neuronal cells were solidly and deeply stained in a triangular or irregular shape, and the number of apoptotic cells was high. After 6 months of Gen intervention, in contrast to the 24M group, the neural cell pathology in the CA3 area of the hippocampus improved and the number of apoptotic cells observably declined.

3.2. Effect of Gen on ERS-Related Proteins p-JNK and CHOP. The protein expression of p-JNK and CHOP in hippocampal tissues was observed via western blot method. In contrast to those in the 3M group, the protein expression of p-JNK and CHOP was observably raised in the 24M group ($P < 0.05$ and $P < 0.001$, Table 1 and Figure 2). After 6 months of Gen intervention, the protein expression of p-JNK and CHOP was observably downregulated in all Gen dose groups in contrast to the 24M group ($P < 0.05$, $P < 0.01$, and $P < 0.001$; Table 1 and Figure 2).

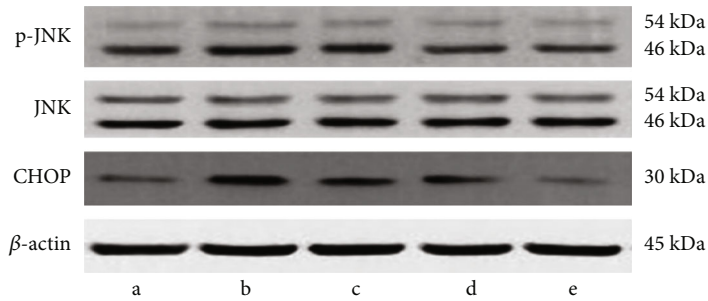

Figure 2: Effect of Gen on p-JNK and CHOP protein expression. Note: (a) 3M group; (b) 24M group; (c) Gen low-dose group; (d) Gen medium-dose group; (e) Gen high-dose group.

Table 2: Effect of Gen on protein expression of IL-1β and TNF-α ($\bar{x} \pm s$, $n = 10$).

Group	Dose (mg-kg^{-1})	IL-1β	TNF-α
3M group	—	0.59 ± 0.06	0.47 ± 0.16
24M group	—	$0.91 \pm 0.17^{**}$	$1.11 \pm 0.14^{***}$
Gen low-dose group	10	$0.63 \pm 0.06^{**}$	$0.85 \pm 0.061^{\#}$
Gen medium-dose group	30	$0.57 \pm 0.08^{\#}$	$0.76 \pm 0.07^{\#\#}$
Gen high-dose group	60	$0.53 \pm 0.04^{\#\#\#}$	$043 \pm 0.17^{\#\#\#}$

3.3. Effect of Gen on the Protein Expression of Inflammatory Factors. IL-1β and TNF-α expression was markedly raised in the hippocampus of the 24M group compared with the 3M group ($P < 0.01$ and $P < 0.001$, Table 2 and Figure 3). All Gen dose groups significantly downregulated IL-1β and TNF-α in contrast to the 24M group ($P < 0.05$, $P < 0.01$, and $P < 0.001$; Table 2 and Figure 3).

3.4. Effect of Gen on the Expression of NLRP3, ASC, Caspase-1, and IL-18. In contrast to the 3M group, the protein expression of NLRP3, ASC, Caspase-1, and IL-18 in hippocampal tissues was apparently raised in the 24M group ($P < 0.05$ and $P < 0.01$, Table 3 and Figure 4). After 6 months of Gen intervention, the protein expression of NLRP3, ASC, Caspase-1, and IL-18 was observably downregulated in all Gen dose groups in contrast to the 24M group ($P < 0.05$, $P < 0.01$, and $P < 0.001$; Table 3 and Figure 4).

4. Discussion

Aging puts the body in a state of chronic stress, and excessive activation of unfolded protein signaling in the ERS pathway triggers apoptosis and neuroinflammation, which are essential in many neurodegenerative diseases [14, 15]. ERS is a cellular response process triggered by various stimuli that disrupt protein folding in the endoplasmic reticulum. However, prolonged and sustained ERS can lead to cell damage and eventually apoptosis. JNK is a downstream apoptotic molecule activated by the IRE1 apoptotic pathway of the three UPR pathways, which mediates the stress response and the apoptotic response induced by inflammatory factors such as TNF-α [16]. CHOP is an ERS-specific transcription factor and is one of the most important mediators of the ERS-induced apoptotic pathway [17]. It was found that JNK and CHOP are also involved in regulating apoptosis in neuronal cells. In the literature, it has been reported that neuronal cells in the CA1 region of the hippocampus of aged rats are heavily degenerated and ERS pathway-related proteins such as CHOP and p-JNK are upregulated in the hippocampus and cortex. The present study demonstrated that neuronal cells in the hippocampus of naturally aged rats were heavily degenerated and cell apoptotic was raised, and the expression of p-JNK and CHOP was obviously raised, while Gen significantly improved the morphology of hippocampal tissue, inhibited the expression of apoptotic cytokines p-JNK and CHOP, and reduced the number of apoptotic cells. This suggests that Gen can reduce aging-induced neuronal apoptosis by inhibiting the activation of JNK and CHOP, which are related to the ERS apoptotic signaling pathway.

NLRP3 inflammatory vesicles usually consist of the pattern recognition receptor NLRP3, the junctional protein ASC, and the effector molecule Caspase-1. Upon pathogen invasion, NLRP3 recruits Caspase-1 precursors via the junctional protein ASC and promotes the activation of Caspase-1, which further enhances the inflammatory factor secretion [18]. In turn, the release of inflammatory factors can further promote the release of TNF-α, and the activation of excessive inflammatory factors further induces cell death. It has been widely reported in the literature that NLRP3 inflammatory vesicles are extensively involved in the onset and development of aging and neurological diseases. It was found that NLRP3 inflammatory vesicle activation was significantly increased in hippocampal tissue of decompensated rats, and the protein expression of inflammatory factors was also markedly raised, and the apoptosis of neuronal cells was significantly raised. Lee et al. found that toxic β-amyloid activates NLRP3 inflammatory vesicles and leads to AD pathology and tissue damage [19], and inhibition of Caspase-1 reduces the activation of RAW264.7. Inhibition of Caspase-1 reduced the activation of BV2 microglia by activated RAW264.7 macrophage inflammatory response and significantly raised the protein expression of NLRP3 inflammatory vesicles and inflammatory factors in the brain of PD model rats. The present study demonstrated the protein expression of NLRP3 inflammatory vesicles and

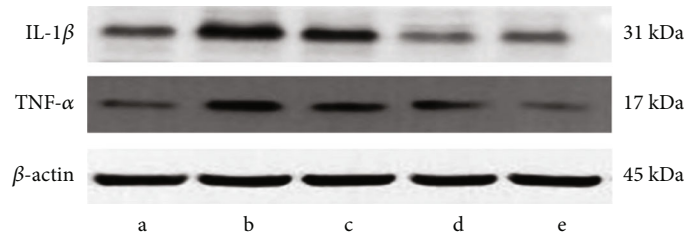

Figure 3: Effect of Gen on the protein expression of inflammatory factors. Note: (a) 3M group; (b) 24M group; (c) Gen low-dose group; (d) Gen medium-dose group; (e) Gen high-dose group.

Table 3: Effect of Gen on NLRP3 inflammatory vesicle-associated protein expression ($\bar{x} \pm s$, $n = 10$).

Group	Dose (mg-kg^{-1})	NLRP3	ASC	Caspase-1	IL-18
3M group	—	0.35 ± 0.04	0.83 ± 0.17	1.03 ± 0.07	0.78 ± 0.11
24M group	—	$0.57 \pm 0.02^{**}$	$1.21 \pm 0.03^{*}$	$1.35 \pm 0.20^{*}$	$1.07 \pm 0.13^{*}$
Gen low-dose group	10	$0.42 \pm 0.02^{*}$	$0.85 \pm 0.10^{\#}$	$1.05 \pm 0.05^{\#}$	$0.78 \pm 0.09^{\#}$
Gen medium-dose group	30	$0.32 \pm 0.05^{\#\#}$	$0.88 \pm 0.16^{\#\#}$	$0.94 \pm 0.02^{\#\#}$	$0.79 \pm 0.12^{\#}$
Gen high-dose group	60	$0.33 \pm 0.10^{\#\#}$	$0.54 \pm 0.14^{\#\#\#}$	$0.96 \pm 0.02^{\#\#}$	$0.59 \pm 0.07^{\#\#}$

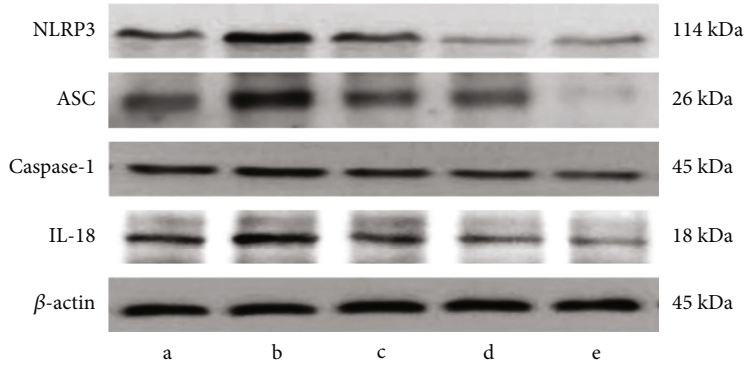

Figure 4: Effect of Gen on the expression of NLRP3 inflammatory vesicle-associated protein. Note: (a) 3M; (b) 24M; (c) Gen low-dose group; (d) Gen medium-dose group; (e) Gen high-dose group.

inflammatory factors were observably higher in hippocampal tissues of naturally aged rats in contrast to those of young rats, and Gen significantly downregulated the protein expression of NLRP3 inflammatory vesicles and downstream inflammatory factors. This suggested Gen may play a protective role in inhibiting neuronal apoptosis by suppressing the activation of NLRP3 inflammatory vesicles and reducing the release of inflammatory factors. In conclusion, aging can cause apoptosis in rat hippocampal tissue, and the protective effect of Gen on neuronal cells may be related to the inhibition of the expression of p-JNK and CHOP, the proteins related to the ERS apoptotic signaling pathway, and the inhibition of NLRP3 inflammatory vesicles, thus reducing neuronal apoptosis. There were some limitations in our study. (1) All test indicators were at the end of this experiment, but the aging kinetics has not been confirmed. (2) This study focused on the detection of apoptotic proteins and pathways and lacks the detection of other methods. (3) The limited number of research animals may affect the experimental results. We will consider all the above points in the future.

Data Availability

Data to support the findings of this study is available on reasonable request from the corresponding author.

Conflicts of Interest

The authors do not have conflicts of interest to declare.

Acknowledgments

This research was funded by the National Nature Fund, grant numbers 81760158 and 31560278.

References

[1] Y. Fujino, T. Kasai, F. Kitani-Morii et al., "Impaired age-dependent increases in phosphoglycerate kinase activity in red blood cells of Parkinson's disease patients," *Parkinsonism & Related Disorders*, vol. 91, pp. 128–134, 2021.

[2] X. Zhang, X. Wei, Y. Mei et al., "Modulating adult neurogenesis affects synaptic plasticity and cognitive functions in mouse

models of Alzheimer's disease," *Stem Cell Reports*, vol. 16, no. 12, pp. 3005–3019, 2021.

[3] N. Zarate, T. A. Intihar, D. Yu et al., "Heat shock factor 1 directly regulates postsynaptic scaffolding PSD-95 in aging and Huntington's disease and influences striatal synaptic density," *International Journal of Molecular Sciences*, vol. 22, no. 23, p. 13113, 2021.

[4] M. Jové, N. Mota-Martorell, P. Torres et al., "The causal role of lipoxidative damage in mitochondrial bioenergetic dysfunction linked to Alzheimer's disease pathology," *Life*, vol. 11, no. 5, p. 388, 2021.

[5] A. Ishtiaq, T. Ali, A. Bakhtiar et al., "Melatonin abated bisphenol A-induced neurotoxicity via p53/PUMA/Drp-1 signaling," *Environmental Science and Pollution Research International*, vol. 28, no. 14, pp. 17789–17801, 2021.

[6] H. Wu, S. Zheng, J. Zhang, S. Xu, and Z. Miao, "Cadmium induces endoplasmic reticulum stress-mediated apoptosis in pig pancreas via the increase of Th1 cells," *Toxicology*, vol. 457, article 152790, 2021.

[7] X. Li, Y. Cheng, Y. Qin et al., "Chrysophanol exerts neuroprotective effects via interfering with endoplasmic reticulum stress apoptotic pathways in cell and animal models of Alzheimer's disease," *The Journal of Pharmacy and Pharmacology*, vol. 74, no. 1, pp. 32–40, 2022.

[8] G. Mercado, V. Castillo, P. Soto et al., "Targeting PERK signaling with the small molecule GSK2606414 prevents neurodegeneration in a model of Parkinson's disease," *Neurobiology of Disease*, vol. 112, pp. 136–148, 2018.

[9] R. J. Ward, D. T. Dexter, and R. R. Crichton, "Ageing, neuroinflammation and neurodegeneration," *Frontiers in Bioscience (Scholar Edition)*, vol. 7, no. 1, pp. 189–204, 2015.

[10] K. Griffioen, M. P. Mattson, and E. Okun, "Deficiency of Toll-like receptors 2, 3 or 4 extends life expectancy in Huntington's disease mice," *Heliyon*, vol. 4, no. 1, article e00508, 2018.

[11] Y. Gu, C. F. Zhu, H. Iwamoto, and J. S. Chen, "Genistein inhibits invasive potential of human hepatocellular carcinoma by altering cell cycle, apoptosis, and angiogenesis," *World Journal of Gastroenterology*, vol. 11, no. 41, pp. 6512–6517, 2005.

[12] T. Ohgomori and S. Jinno, "Cuprizone-induced demyelination in the mouse hippocampus is alleviated by phytoestrogen genistein," *Toxicology and Applied Pharmacology*, vol. 363, pp. 98–110, 2019.

[13] J. Xu, J. Zhu, C. Shi, K. Guo, and D. T. Yew, "Effects of genistein on hippocampal neurodegeneration of ovariectomized rats," *Journal of Molecular Neuroscience*, vol. 31, no. 2, pp. 101–112, 2007.

[14] Y. Gerakis and C. Hetz, "Emerging roles ofERstress in the etiology and pathogenesis of Alzheimer's disease," *The FEBS Journal*, vol. 285, no. 6, pp. 995–1011, 2018.

[15] S. Di Benedetto, L. Müller, E. Wenger, S. Düzel, and G. Pawelec, "Contribution of neuroinflammation and immunity to brain aging and the mitigating effects of physical and cognitive interventions," *Neuroscience and Biobehavioral Reviews*, vol. 75, pp. 114–128, 2017.

[16] C. J. Dougherty, L. A. Kubasiak, D. P. Frazier et al., "Mitochondrial signals initiate the activation of c-Jun N-terminal kinase (JNK) by hypoxia-reoxygenation," *The FASEB Journal*, vol. 18, no. 10, pp. 1060–1070, 2004.

[17] F. Walter, A. O'brien, C. G. Concannon, H. Düssmann, and J. H. Prehn, "ER stress signaling has an activating transcription factor 6α (ATF6)-dependent "off-switch"," *The Journal of Biological Chemistry*, vol. 293, no. 47, pp. 18270–18284, 2018.

[18] Z. Wang, S. Meng, L. Cao, Y. Chen, Z. Zuo, and S. Peng, "Critical role of NLRP3-caspase-1 pathway in age-dependent isoflurane-induced microglial inflammatory response and cognitive impairment," *Journal of Neuroinflammation*, vol. 15, no. 1, p. 109, 2018.

[19] Y. Cai, Y. Chai, Y. Fu et al., "Salidroside ameliorates Alzheimer's disease by targeting NLRP3 inflammasome-mediated pyroptosis," *Frontiers in Aging Neuroscience*, vol. 13, article 809433, 2022.

Hindawi
Disease Markers
Volume 2022, Article ID 9376608, 8 pages
https://doi.org/10.1155/2022/9376608

Research Article

Identification of Potential miRNA-mRNA Regulatory Network in the Development of Oral Cancer

Yun Yang,[1] Xin Xin,[2] and Ting Xu[3]

[1]*Department of Stomatology, The Affiliated Yantai Yuhuangding Hospital of Qingdao University, Yantai 264000, China*
[2]*Department of Stomatology, North China Medical and Health Group XingTai General Hospital, Xingtai 054000, China*
[3]*Department of Stomatology, The Affiliated Yantai Yuhuangding Hospital of Qingdao University Laishan Branch, Yantai 264000, China*

Correspondence should be addressed to Ting Xu; xuting@yhdyylsfy.org.cn

Received 20 June 2022; Revised 22 July 2022; Accepted 29 July 2022; Published 18 August 2022

Academic Editor: Chang Gu

Background. Oral cancer is a difficult question in modern medical system, and there are few effective strategies to completely heal these diseases. This research investigated the miRNA-mRNA network in oral cancer development via bioinformatics excavation. *Methods*. GSE28100 and GSE23558 in the GEO database were selected for bioinformatics analysis. The datasets were analyzed with GEO2R to obtain the related matrix files. The hot plot and heatmap of the matrix files were drawn with R language. The MiRDIP database was applied to predict and screen the targets of miRNAs. The DEGs in the matrix files were analyzed with the DAVID database and visualized with R language for enrichment analysis. The PPI-network of the DEGs was established with the STRING database and Cytoscape. Besides, the miRNA-mRNA was visualized by Cytoscape. *Results*. 35 genes were identified as the DEGs in GES28100. 1651 genes were identified as the DEGs in GSE23558. 143 common genes in the targets of miRNAs in GSE28100 and the DEGs in GSE the targets of DEGs in GES28100 and common genes were enriched in the PI3K/AKT pathway, MAPK pathway, etc. The DEGs in GSE28100 and GSE23558 were involved in the regulations of transcription from RNA polymerase II promoter and DNA transcription. The DEGs in GSE28100 and GSE23558 were established with the miRNA-mRNA network. *Conclusion*. This research identified miR-15b-5p, miR-199a-3p, miR-21-5p, miR-424-5p, and miR-454-3p as the biomarker of oral cancer and established the miRNA-mRNA network in oral progression.

1. Introduction

Oral cancer is a widely prevalent disease in the world, which is one of intractable issues for model society [1, 2]. At present, surgical operation, chemotherapy, and radiotherapy are major therapeutic strategies for oral cancer. However, even with the various clinical intervention, the prognosis of the patients remains unsatisfactory [3]. Statistically, less 50% patients with oral cancer have survival regions more than five years [4]. Increasing studies have indicated that the mRNA profiles of the oral cancer tissues popularly exhibit significant difference compared with the normal tissues [5]. For one side, mRNA disorder is closely related with the deterioration of the cancer, and some genes also exhibit extremely carcinogenic activity to drive the malignant phenotype of the tumor cells [6]. The oral cancer is characterized with a high risk of lymphatic metastasis, which is the major reason leading the rapid progression and worse prognosis of the symptom [7, 8].

miRNAs serve critical roles in cellular metabolism, and the disorder of miRNA profile has also been confirmed as the direct reason causing the development and progression of multiple diseases [9]. For oral cancer, accumulating researches have revealed that the development of this disease is also closely associated with the cellular metabolic disturbance mediated by aberrant expression of some miRNAs [8, 10]. Bioinformatics analysis based on public data of microarray analysis has been gradually recognized as a useful way to investigate potential molecular relationship in disease development [11]. Abundant researches are concentrated on identifying potential drug targets and revealing complex cellular conduction via analyzing the global gene profiles [10]. For oral

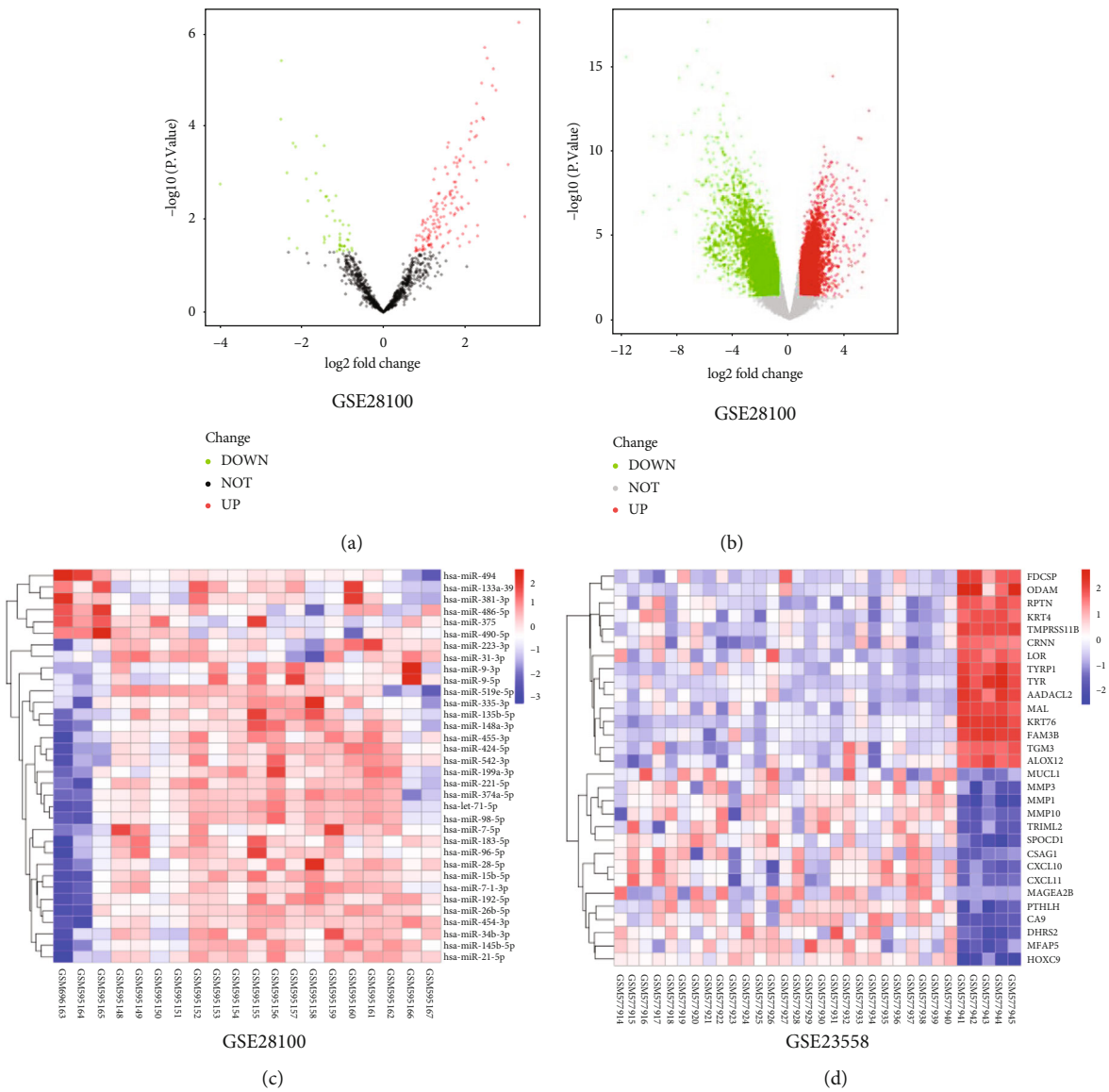

Figure 1: The DEGs in GES28100 and GSE23558. (a, b) The hot plots of DEGs in GES28100 and GSE23558. (c, d) The heatmaps of DEGs in GES28100 and GSE23558.

cancer, an obvious difference of miRNA and mRNA profile is also observed by abundant reports [12]. Some genes may have great value in clinical diagnosis and treatment.

In this study, the potential regulation of oral cancer was investigated via excavating the public cancer database, in order to identify the biomarkers in the development of oral cancer and thus provide some new reference for the treatment of this disease.

2. Materials and Method

2.1. Data Source. GSE28100 and GSE23558 were obtained from the GEO database (https://www.ncbi.nlm.nih.gov/geo/), and the datasets were analyzed with GEO2R to obtain matrix profiles. GSE28100 was the miRNA expression matrix based on the GPL10850 platform, which included 17 oral cancer tissues and 3 normal tissues. GSE23558 was the mRNA expression matrix based on the GPL6480 platform, which included 27 oral cancer tissues and 5 normal tissues.

2.2. Differential Expression Genes (DEGs). The raw data of GSE28100 and GSE23558 were analyzed with GEO2R tool, and the related matrix files were normalized with the R language. The genes in GSE28100 and GSE23558 with $|\text{LogFC}| \geq 2$ and $P < 0.05$ were selected as the DEGs.

2.3. Function and Pathway Enrichment Analysis. The annotation and enrichment analysis of the DEGs was performed by DAVID database (https://david.ncifcrf.gov/home.jsp). The GO term and KEGG pathways with $P < 0.05$ in the results were screened and then visualized with R language.

2.4. Identification of the Hub Nodes. The protein interaction network was analyzed with the STRING database (https://cn

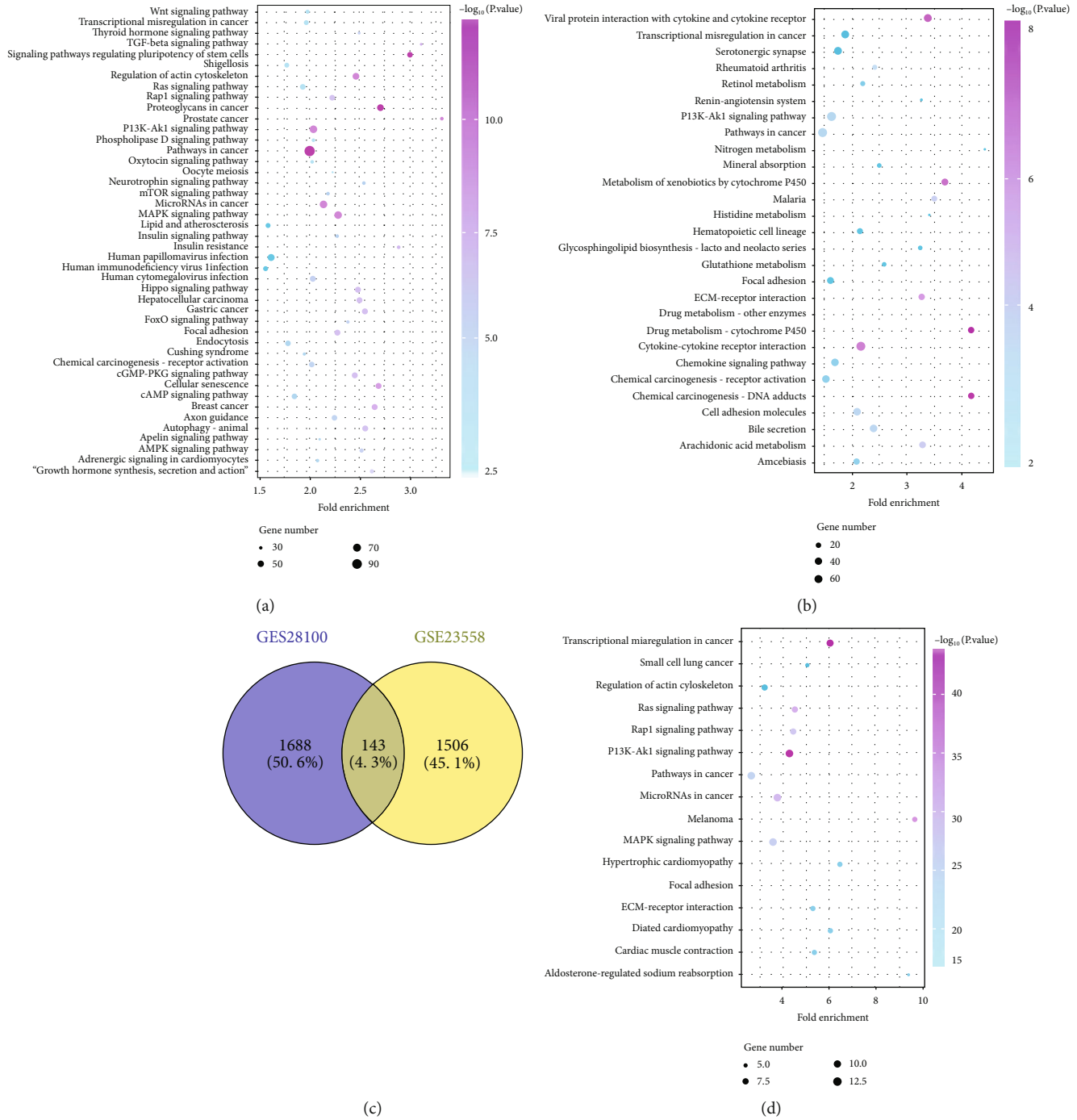

Figure 2: The related KEGG pathways of the DEGs. (a) The KEGG analysis of the DEGs in GES28100. (b) The KEGG analysis of the DEGs in GSE23558. (c) The common genes of GES28100 and GSE23558. (d) The KEGG analysis of the common genes.

.string-db.org/). After that, the results were analyzed and figured with Cytoscape software. For the miRNA-mRNA network, the related miRNAs with differential expression and their targets were figured with Cytoscape software.

3. Results

3.1. Identification of DEGs. For GES28100, the abundances of 7 downregulated genes and 28 upregulated genes were identified as the DEGs. For GSE23558, the 1237 downregulated genes and 414 upregulated genes were identified as the DEGs (Figures 1(b) and 1(d)). Moreover, there were 143 common genes in the targets of miRNAs in GSE28100 and the DEGs in GSE (Figures 1(a) and 1(c)).

3.2. KEGG Enrichment Analysis. The genes were uploaded on the DAVID database to analyze the related pathways. The results showed that targets of DEGs in GES28100 were

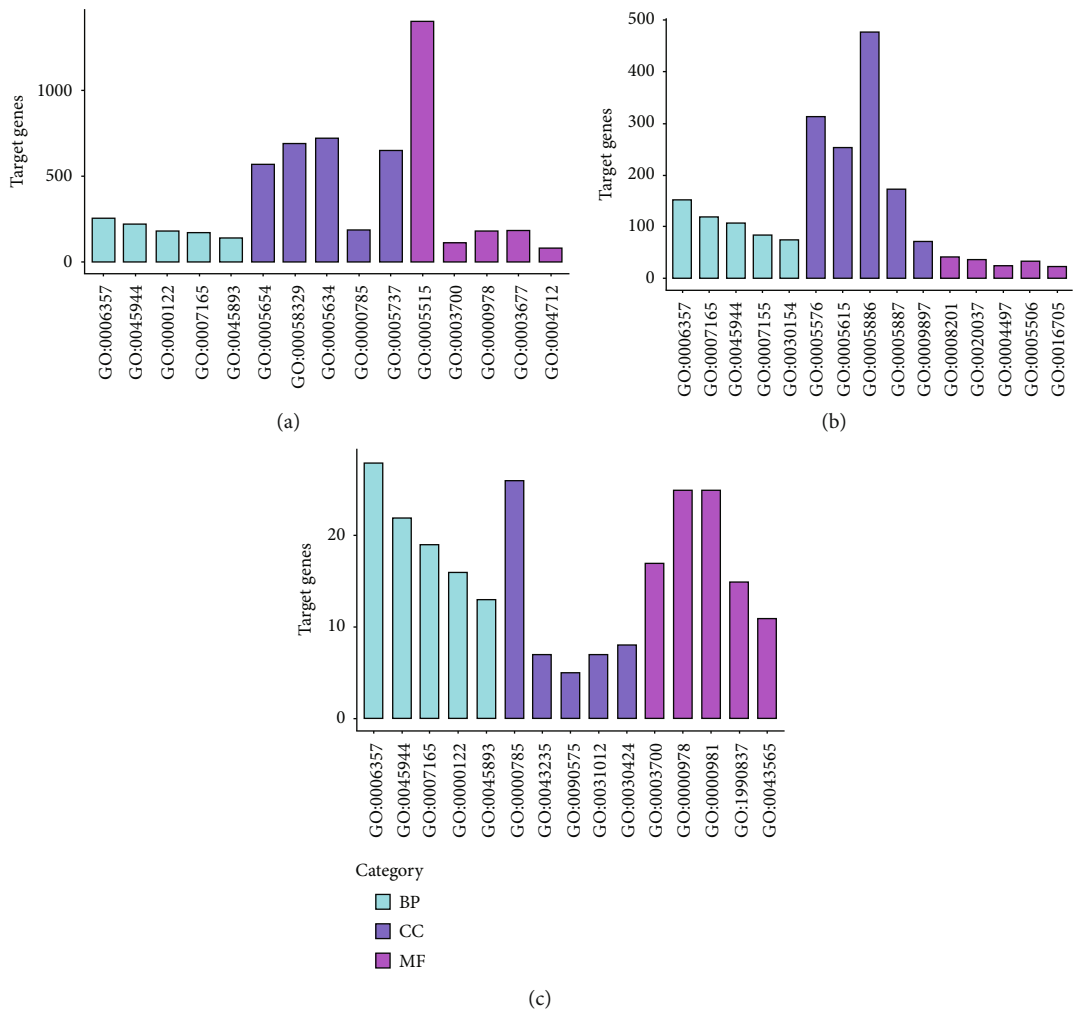

Figure 3: The GO analysis of the DEGs. (a) The GO analysis of the DEGs in GES28100. (b) The GO analysis of the DEGs in GSE23558. (c) The GO analysis of the common genes.

associated with PI3K/AKT, MAPK, Wnt, Hippo, and APMK pathways (Figure 2(b)). The DEGs in GSE23558 were also related with the PI3K/AKT, MAPK, Wnt, Hippo, and APMK pathway (Figure 2(c)). Moreover, the common genes were enriched in the PI3K/AKT, MAPK pathway, and so on (Figures 2(a) and 2(d)).

3.3. GO Enrichment Analysis. For GSE28100, the molecular functions of the targets were majorly located in nucleus, cytosol, cytoplasm, nucleoplasm, and plasma membrane, and they were related with protein binding, metal ion binding, ATP binding, identical protein binding, and RNA binding and involved in biological processes including the regulation of transcription from RNA polymerase II promoter, signal transduction, and the regulation of DNA transcription (Figure 3(a)). For GSE23558, the DEGs were majorly located in protein binding, plasma membrane, integral component of membrane, extracellular region, and identical protein binding, and they were related with the extracellular space, regulation of RNA polymerase II, and signal transduction and involved in the exosome secretion, integral component of plasma membrane, calcium ion binding, and endoplasmic reticulum membrane (Figure 3(b)). Moreover, the common genes were located in nucleus chromatin, extracellular region, extracellular space, and perinuclear region of cytoplasm, and they were involved in regulation of RNA polymerase II and signal transduction (Figure 3(c)).

3.4. PPI and miRNA-mRNA Network. For the targets of GES28100, three clusters were found, containing cluster 1 with 31 nodes and 724 edges, cluster 2 with 54 nodes and 828 edges, and cluster 3 with 65 nodes and 504 edges (Figures 4(a)–4(c)). Three clusters were found in GSE23558, containing cluster 1 with 52 nodes and 1222 edges, cluster 2 with 53 nodes and 808 edges, and cluster 3 with 44 nodes and 566 edges (Figures 4(d) and 4(e)). Moreover, a cluster with 8 nodes and 48 edges was found in the common genes of the DEGs in GSE23558 and the targets of the DEGs in GSE28100; the miRNA-mRNA network was established (Figures 5(a) and 5(b)).

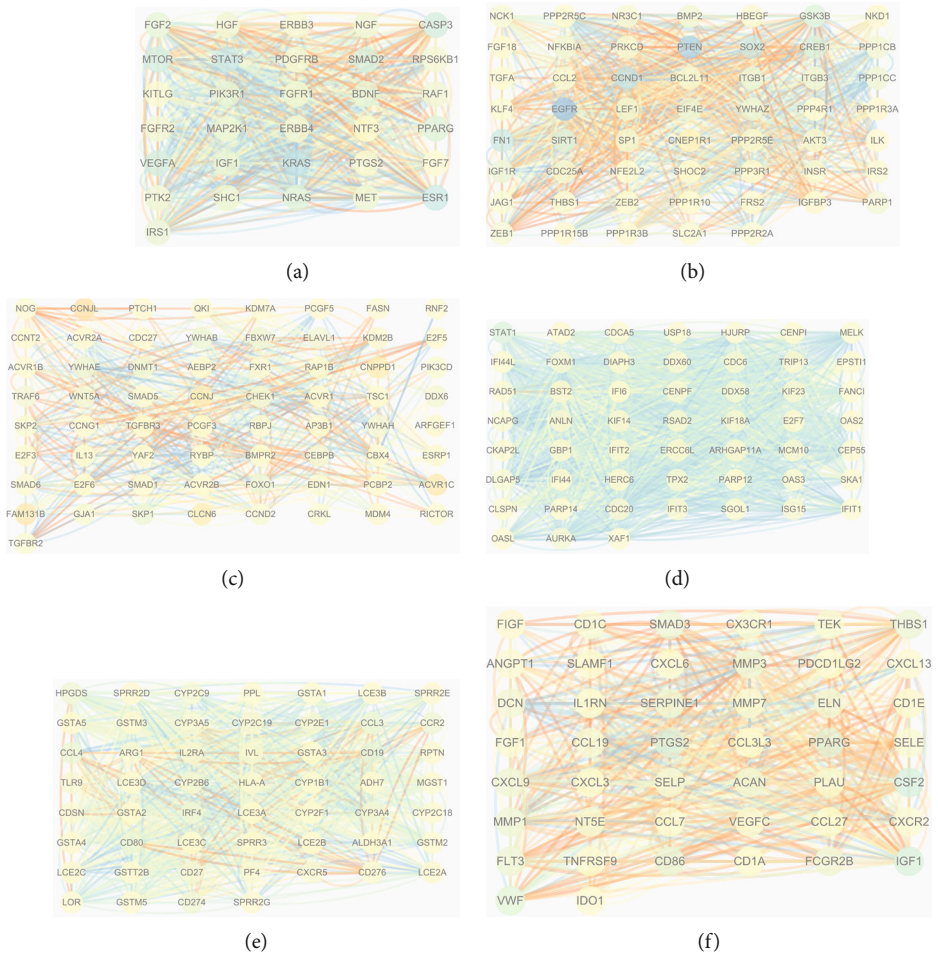

Figure 4: The PPI network of the DEGs in GES28100 and GES23558. (a–c) The PPI network of the DEGs in GES28100. (d, e) The PPI network of the DEGs in GES23558.

4. Discussion

Oral cancer is still a stubborn malignant disease with complicated pathological mechanism. The expression disorder of the genes has been gradually recognized as the major reason leading the malignant progression of the cancer [10]. This study investigated the potential regulation mechanism of oral cancer via excavating the public database and thus found some biomarker genes and the related regulation network.

Compared with the normal tissues, the miRNA profiles of the tumor tissues generally exhibited significant change [13]. Accumulating researches have indicated that some miRNAs serve critical roles in the deterioration of the tumors [14]. In the research, it was also found that the miRNA profiles were dramatically difference in the tumor tissues and adjacent healthy tissues, and 7 downregulated genes and 28 upregulated were identified as the DEG miRNAs which may serve as critical roles in oral cancer. Moreover, miR-15b-5p, miR-199a-3p, miR-21-5p, miR-424-5p, and miR-454-3p were related with the hub nodes screened in GSE23558 and the targets in GES28100. miR-199a-3p has been confirmed to drive the development of multiple types of cancer. Song et al. has observed the elevated miR-199a-3p in gastric cancer, and miR-199a-3p silence can obviously force the apoptosis of the cancer cells [15]. The research has mirrored that miR-21-5p is dramatically enriched in the exosome secreted from cancer cells which can induce the angiogenesis of tumor and thus induced the focus metastasis [16]. The research has proved that miR-15b-5p is dramatically elevated in colorectal cancer and reduced miR-15b-5p can remarkably impede the malignant behaviors of the cancer cells [17]. In oral cancer, increased miR-424-5p has been confirmed to induce the phosphorylation of STAT5 and thus drive the cellular aberrant invasion [18]. The report has indicated that miR-454-3p can induce the metastasis of breast cancer via inducing the aberrant activation of Wnt pathway [19]. However, the related research has also revealed that miR-454-3p serves as a tumor suppressor in glioma [20].

In this research, the DEGs in GSE23558, including SMAD3, PTGS2, PPARG, MMP3, THBS1, and SERPINE1, were identified as the hub nodes. Being regulated by the TGF-β pathway, SMAD3 has been widely proved to be involved in the deterioration of multiple tumors. Shinriki et al. have observed that the abnormal phosphorylation of

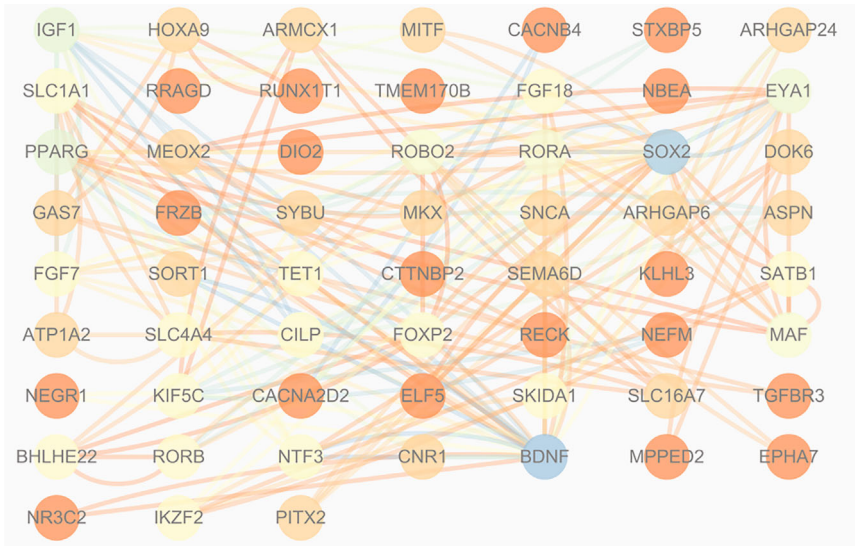

(a)

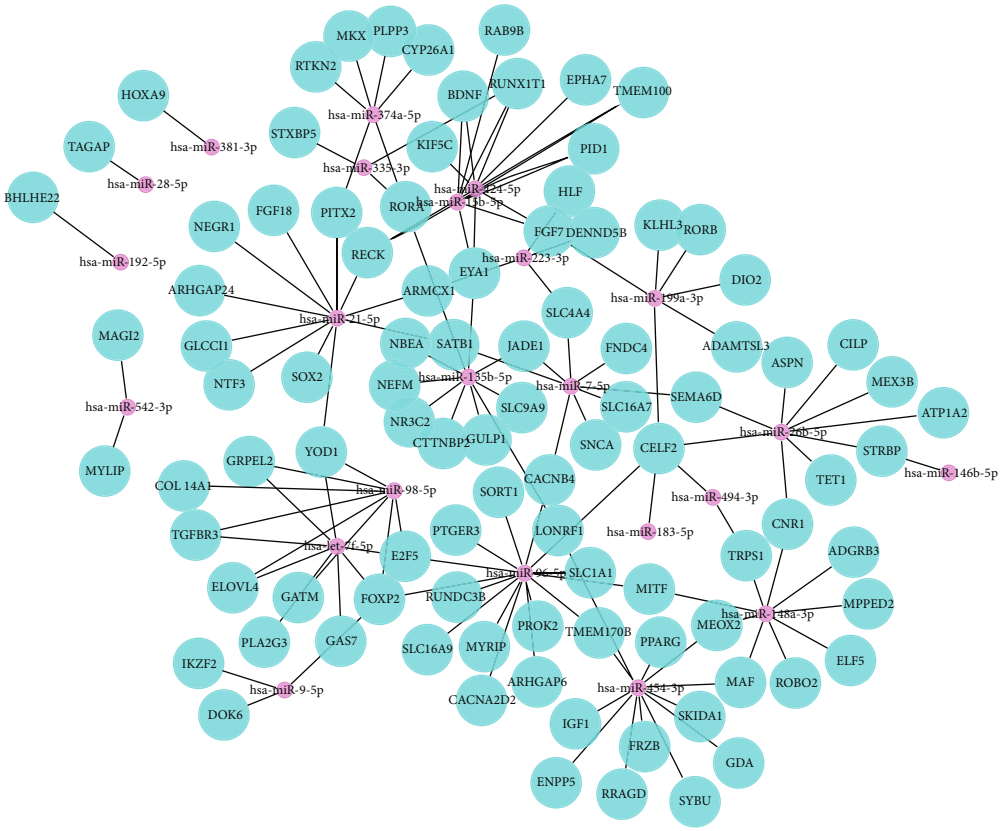

(b)

Figure 5: The miRNA-mRNA network related to oral cancer. (a) The PPI network of the common genes in GES28100 and GES23558. (b) The miRNA-mRNA network.

SMAD3 is dramatically elevated in oral cancer cells [21]. As well as other types of cancer, oral cancer also has high invasive and migration abilities. Aberrant abundance of MMP3 is a general event which has been observed in multiple tumors, and high abundance of MMP3 is also associated with malignant phenotype of tumor cells such as invasion and migration. The research has indicated that increased MMP3 can extremely drive the metastasis of esophageal cancer cells [22]. Besides, reduced SERPINE1 can obviously impede the resistance of breast cancer cells to paclitaxel via inducing the inactivation of VEGFA [23]. In oral cancer, SERPINE1 can also induce the aberrant proliferation of the cancer cells [24]. THBS1 serves as a critical role in the angiogenesis of cancer cells and thus promotes the metastasis of

oral cancer cells [25, 26]. Hence, it suggests that SMAD3, MMP3, SERPINE1, and THBS1 serve as tumor promoters in oral cancer.

Abundant researches have revealed that the aberrant changes in the activities of cellular pathways are major reasons leading the deterioration of tumor focus. The disturbances of the pathways, such as PI3K/AKT, P53, and Wnt, can directly force the malignant behaviors of tumor cells and thus have been recognized as the potential intervention target in clinical. In this research, the DEGs in both GSE23558 and GES28100 were observed to be related with the PI3K/AKT pathway, MAPK pathway, and so on. Moreover, the DEGs in GSE23558 and GES28100 were also enriched in PI3K/AKT and MAPK pathway. In oral cancer, targeting PI3K/AKT has also been recognized as a promising way in drug development. Wei et al. has found that salvianolic acid B can impede the glycolysis of oral cancer via blocking PI3K/AKT [27]. Besides, aberrant-activated MAPK pathway is also a biomarker event in the deterioration of oral cancer. Chen et al. has proved that the dysfunction of MAPK pathway can induce the TGF-β pathway activation and thus mediate the malignant behaviors of oral cancer cells.

In conclusion, this research identified miR-15b-5p, miR-199a-3p, miR-21-5p, miR-424-5p, and miR-454-3p as the biomarker of oral cancer and established the miRNA-mRNA network in oral progression.

Data Availability

Data to support the findings of this study is available on reasonable request from the corresponding author.

Conflicts of Interest

The authors have no conflicts of interest to declare.

Authors' Contributions

Yun Yang and Xin Xin contributed equally to this work.

References

[1] J. Kaur, R. Srivastava, and V. Borse, "Recent advances in point-of-care diagnostics for oral cancer," *Biosensors and Bioelectronics*, vol. 178, p. 112995, 2021.

[2] S. K. Gangwar, A. Kumar, S. Jose et al., "Nuclear receptors in oral cancer-emerging players in tumorigenesis," *Cancer Letters*, vol. 536, p. 215666, 2022.

[3] C. Saka-Herrán, E. Jané-Salas, A. Mari-Roig, A. Estrugo-Devesa, and J. López-López, "Time-to-treatment in oral cancer: causes and implications for survival," *Cancers*, vol. 13, no. 6, p. 1321, 2021.

[4] R. Mishra, "Glycogen synthase kinase 3 beta: can it be a target for oral cancer," *Molecular Cancer*, vol. 9, no. 1, p. 144, 2010.

[5] J. Bouaoud, P. Bossi, M. Elkabets et al., "Unmet needs and perspectives in oral cancer prevention," *Cancers*, vol. 14, no. 7, p. 1815, 2022.

[6] T. Khan, N. Relitti, M. Brindisi et al., "Autophagy modulators for the treatment of oral and esophageal squamous cell carcinomas," *Medicinal Research Reviews*, vol. 40, no. 3, pp. 1002–1060, 2020.

[7] A. Capote-Moreno, E. Ramos, J. Egea, F. López-Muñoz, E. Gil-Martín, and A. Romero, "Potential of melatonin as adjuvant therapy of oral cancer in the era of Epigenomics," *Cancers*, vol. 11, no. 11, p. 1712, 2019.

[8] M. Dioguardi, G. A. Caloro, L. Laino et al., "Circulating miR-21 as a potential biomarker for the diagnosis of oral cancer: a systematic review with meta-analysis," *Cancers*, vol. 12, no. 4, p. 936, 2020.

[9] H. A. Adeola, I. O. Bello, R. T. Aruleba et al., "The practicality of the use of liquid biopsy in early diagnosis and treatment monitoring of oral cancer in resource-limited settings," *Cancers*, vol. 14, no. 5, p. 1139, 2022.

[10] W. D'Souza and A. Kumar, "microRNAs in oral cancer: moving from bench to bed as next generation medicine," *Oral Oncology*, vol. 111, article 104916, 2020.

[11] S. Yete and D. Saranath, "MicroRNAs in oral cancer: biomarkers with clinical potential," *Oral Oncology*, vol. 110, article 105002, 2020.

[12] S. C. Tsai, S. F. Huang, J. H. Chiang et al., "The differential regulation of microRNAs is associated with oral cancer," *Oncology Reports*, vol. 38, no. 3, pp. 1613–1620, 2017.

[13] W. N. William, V. Papadimitrakopoulou, J. J. Lee et al., "Erlotinib and the risk of oral cancer: the erlotinib prevention of oral cancer (EPOC) randomized clinical trial," *JAMA Oncology*, vol. 2, no. 2, pp. 209–216, 2016.

[14] L. L. Leung, M. K. Riaz, X. Qu, J. Chan, and K. Meehan, "Profiling of extracellular vesicles in oral cancer, from transcriptomics to proteomics," *Seminars in Cancer Biology*, vol. 74, pp. 3–23, 2021.

[15] R. Song, Y. Li, W. Hao et al., "Circular RNA MTO1 inhibits gastric cancer progression by elevating PAWR via sponging miR-199a-3p," *Cell Cycle*, vol. 19, no. 22, pp. 3127–3139, 2020.

[16] Q. He, A. Ye, W. Ye et al., "Cancer-secreted exosomal miR-21-5p induces angiogenesis and vascular permeability by targeting KRIT1," *Cell Death & Disease*, vol. 12, no. 6, p. 576, 2021.

[17] L. N. Sun, Z. Zhi, L. Y. Chen et al., "SIRT1 suppresses colorectal cancer metastasis by transcriptional repression of miR-15b-5p," *Cancer Letters*, vol. 409, pp. 104–115, 2017.

[18] H. Y. Peng, S. S. Jiang, J. R. Hsiao et al., "IL-8 induces miR-424-5p expression and modulates SOCS2/STAT5 signaling pathway in oral squamous cell carcinoma," *Molecular Oncology*, vol. 10, no. 6, pp. 895–909, 2016.

[19] L. Ren, H. Chen, J. Song et al., "MiR-454-3p-mediated Wnt/β-catenin signaling antagonists suppression promotes breast cancer metastasis," *Theranostics*, vol. 9, no. 2, pp. 449–465, 2019.

[20] N. Shao, L. Xue, R. Wang, K. Luo, F. Zhi, and Q. Lan, "miR-454-3p is an exosomal biomarker and functions as a tumor suppressor in glioma," *Molecular Cancer Therapeutics*, vol. 18, no. 2, pp. 459–469, 2019.

[21] S. Shinriki, H. Jono, M. Maeshiro et al., "Loss of CYLD promotes cell invasion via ALK5 stabilization in oral squamous cell carcinoma," *The Journal of Pathology*, vol. 244, no. 3, pp. 367–379, 2018.

[22] H. F. Hu, W. W. Xu, W. X. Zhang et al., "Identification of miR-515-3p and its targets, vimentin and MMP3, as a key regulatory mechanism in esophageal cancer metastasis: functional and clinical significance," *Signal Transduction and Targeted Therapy*, vol. 5, no. 1, p. 271, 2020.

[23] Q. Zhang, L. Lei, and D. Jing, "Knockdown of SERPINE1 reverses resistance of triple-negative breast cancer to paclitaxel via suppression of VEGFA," *Oncology Reports*, vol. 44, no. 5, pp. 1875–1884, 2020.

[24] C. Zhao and Z. Liu, "MicroRNA 617 targeting SERPINE1 inhibited the progression of oral squamous cell carcinoma," *Molecular and Cellular Biology*, vol. 41, no. 6, article e0056520, 2021.

[25] H. J. Shih, C. L. Chen, and P. L. Torng, "IGFBP3 inhibits angiogenesis through intracellular regulation of THBS1 expression," *American Journal of Cancer Research*, vol. 10, no. 6, pp. 1728–1744, 2020.

[26] M. Xiao, J. Zhang, W. Chen, and W. Chen, "M1-like tumor-associated macrophages activated by exosome-transferred THBS1 promote malignant migration in oral squamous cell carcinoma," *Journal of Experimental & Clinical Cancer Research*, vol. 37, no. 1, p. 143, 2018.

[27] J. Wei, J. Wu, W. Xu et al., "Salvianolic acid B inhibits glycolysis in oral squamous cell carcinoma via targeting PI3K/AKT/HIF-1α signaling pathway," *Cell Death & Disease*, vol. 9, no. 6, p. 599, 2018.

Hindawi
Disease Markers
Volume 2022, Article ID 4506350, 6 pages
https://doi.org/10.1155/2022/4506350

Research Article

Effect of Bicalutamide Combined with Docetaxel on Serum PSA and VEGF Levels in Patients with Advanced Prostate Carcinoma

Zhaoxin Guo,[1] Xiaolin Hu,[2] Renguang Lv,[3] Yongzhen Zhang,[1] Liwei Meng,[1] Zhaoxu Liu,[1] and Lei Yan[1]

[1]*Department of Urology, Qilu Hospital of Shandong University, Jinan, 250012 Shandong, China*
[2]*Department of Endocrinology, Jinan Central Hospital, Jinan, 250033 Shandong, China*
[3]*Department of Urology, Jinan Seventh People's Hospital, Jinan, 251400 Shandong, China*

Correspondence should be addressed to Lei Yan; yanlei@sdqiluhospital.cn

Received 29 June 2022; Accepted 4 August 2022; Published 17 August 2022

Academic Editor: Jun Yang

Objective. To investigate the effect of bicalutamide combined with docetaxel on the levels of prostate-specific antigen (PSA) in serum and vascular endothelial growth factor (VEGF) in patients with advanced prostate carcinoma (PCa). *Methods*. The clinical data of 103 patients with advanced PCa at our hospital between Feb. 2020 and Feb. 2021 were retrospectively analyzed, the 90 of whom screened by inclusion and exclusion criteria were finally chosen as research objects. They were divided into a control group and an experimental group according to the order of admission, with 45 cases in each group. The control group was treated with conventional treatment, while the experimental group underwent the combination of bicalutamide and docetaxel, and the clinical indices of the two groups were compared. *Results*. After treatment, the serum indices in the experimental group were remarkably lower than those in the control group ($P < 0.001$), with remarkably lower incidence of toxic and side effects ($P < 0.05$) and higher Expanded Prostate Cancer Index Composite (EPIC) scores ($P < 0.001$) in the experimental group than in the control group. *Conclusion*. The implementation of bicalutamide combined with docetaxel in patients with advanced PCa is effective in reducing the inflammatory expression and improving quality of life and has a higher safety profile. Compared with conventional treatment, this method is of high application value, and further studies will help establish a better solution for such patients.

1. Introduction

As a common disease in urology, prostate carcinoma (PCa) is the epithelial malignant tumor occurring in the prostate [1]. According to statistics, there were nearly 1.29 million new cases of PCa in 2018, accounting for 6.98% of all tumors, and the number of death cases was as high as 35,4800 [2]. Relevant literature has suggested that PCa is the second most common malignant tumor and the fifth most common mortality among men worldwide [3]. Castellucci et al. [4] have pointed out that there are distinct ethnic regional differences in the incidence and mortality of PCa which ranks as the leading male malignancy in Europe, New Zealand, the Americas, Australia, and most of sub-Saharan Africa, with a disease incidence of 70-85 per 100,000. It is a major contributor to cancer deaths in men in 46 countries, particularly in the Caribbean and sub-Saharan Africa [5]. It is reported that the incidence of PCa in China is eminently lower than that in Western countries but is increasing with changing diets, an aging population, and the development of early screening [6]. Xu et al. [7] have noted that approximately 1.09 million men are diagnosed with PCa and 290,000 die from it each year. It is estimated that the number of new cases of PCa will increase to 1.65 million and deaths will increase to 495,000 by 2030 due to global population growth and aging [8]. Compared to western countries such as the US, China has a lower incidence rate but accounts for 4.99% of deaths from PCa worldwide [9]. PCa can lead to urination disorders and induce systemic damage, such as renal failure and digestive failure, and can also metastasize to other parts of the body through blood and lymph nodes, seriously threatening the health of

patients. The cause of this tumor is currently unknown and is presumed to be related to age, genetics, diet, and environmental factors. Therefore, it has become the focus of current medical research to improve the detection rate, reduce the mortality rate, and find reasonable treatments of PCa.

Surgery, radiotherapy, chemotherapy, and androgen deprivation therapy (ADT) are the main clinical treatments for PCa [10]. Surgery is the standard protocol for PCa owing to its ability to rapidly reduce androgen in the patients' body, but surgical castration alone has a high recurrence rate and poor efficacy. In addition, PCa patients are usually diagnosed at an advanced stage and the body functions of the elderly decline, for which reason most of them are intolerant and difficult to undergo surgical treatment, and therefore, palliative therapies based on endocrine treatment are mainly adopted in clinic [11]. Although conventional treatment can obviously improve the clinical symptoms of patients, the therapeutic effect does not reach the expectation and barely meet the clinical demand. Bicalutamide is an antihormone drug with strong specificity that can effectively reduce androgen in the body, and docetaxel enhances the polymerization and inhibits the depolymerization of tubulin and disrupts mitosis of tumor cells [12]; the combined effect of the two is remarkable. Meanwhile, a study has shown that prostate-specific antigen (PSA) can be used to diagnose PCa and determine the effect and prognosis of endocrine treatment, which is a common clinical detection index [13]. Vascular endothelial growth factor (VEGF) can promote the angiogenesis of tumors, which is also an important index factor to judge the prognosis of PCa [14]. Thus, in order to further investigate the effect of bicalutamide combined with docetaxel on serum PSA and VEGF levels in patients with advanced PCa, this paper adopts this scheme and carries out a combined clinical intervention for the research objects, aiming to provide more evidence-based clinical proof for such patients.

2. Materials and Methods

2.1. General Data. The clinical data of 103 patients with advanced PCa at our hospital between Feb. 2020 and Feb. 2021 were retrospectively analyzed. Among them, 90 cases met the inclusion criteria and 13 cases were excluded. They were divided into a control group and an experimental group according to the order of admission, with 45 cases in each group. The study was in accordance with the Declaration of Helsinki [15].

2.2. Recruitment of Research Objects. Inclusion criteria. ① The patients met the diagnostic criteria of PCa in the Diagnosis and Treatment of Prostate Cancer [16] and confirmed by imaging and pathological diagnosis and were identified as advanced PCa by the TNM staging method, with clinical symptoms such as slow urine stream, urinary incontinence, and hematuria; ② the patients had an expected survival period of >1 year and no distant metastasis; ③ the patients were able to better cooperate with the study, related inspection, and follow-up with independent consciousness; ④ the patients had been diagnosed with PCa breaking through the capsule 30 d before inclusion; and ⑤ the patients were treated according to the scheme given by the hospital and had the corresponding treatment indications during the whole process of treatment.

Exclusion criteria. ① Patients who had received chemotherapy or other treatment regimens before; ② patients with psychiatric abnormalities or cognitive impairments that affected treatment and communication; ③ patients with contraindications to treatment or drug allergies; ④ patients with severe cardiac, cerebral, hepatic, or renal insufficiency; ⑤ patients with other malignant tumors; and ⑥ patients with pituitary or adrenal cortical dysfunction.

2.3. Methods

2.3.1. Control Group. Patients in the control group were given abiraterone acetate tablets (manufacture: Jiangxi Shanxiang Pharmaceutical Co., Ltd.; NMPA Approval No. H20193276; specification: 0.25 g ∗ 120 tablets/box), once a day, 1000 mg. On this basis, prednisone acetate tablets (manufacture: Xianju Pharmaceutical Co., Ltd.; NMPA Approval No. H33021207; specification: 5 mg ∗ 100 tablets) were introduced, 5 mg-10 mg each time and 10 mg-60 mg per day orally.

2.3.2. Experimental Group. Patients in the experimental group received bicalutamide capsules (manufacture: Shanxi Zhendong Pharmaceutical Co., Ltd.; NMPA Approval No. H20060983; specification: 50 mg ∗ 30 s) with 50 mg each time, once a day. On this basis, an intravenous drip of docetaxel (manufacture: Beijing Eastern Union Biopharmaceuticals, Ltd.; NMPA Approval No. H20050879; specification: 0.5 ml: 20 mg) was administrated. Based on the calculated amount of medication for the patients, the required dose was inhaled with a syringe and diluted into 5% glucose injection or 0.9% sodium chloride injection, gently shaken, and mixed well to a final concentration of ≤0.74 mg/ml. The docetaxel dosage was 70 mg/m^2-75mg/m^2, with an intravenous drip of 1 h, once every 3 weeks.

2.3.3. Period of Treatment. Patients in both groups were reviewed once every 30 d. When the PSA index was <0.2 ng/ml, the medication could be stopped, and when the PSA index was >4 ng/ml, the medication needed to be continued, for 12 months.

2.4. Observation Indices. After treatment, 5 ml of fasting venous blood was collected from both groups, which was centrifuged at 3000 r/min for 10 min by a centrifuge (model: TD4ZB; manufacturer: Changsha Xiangrui Centrifuge Co., Ltd.), with the upper layer of serum preserved. Serum PSA indices were detected by the electrochemiluminescence method, with VEGF indices detected by enzyme-linked immunosorbent assay. All operations were carried out strictly according to the instructions of the kit (purchased from Wuhan Saipei Biotechnology Co., Ltd.).

The incidence of toxic and side effects was compared between both groups, including gastrointestinal reactions, abnormal liver function, sexual dysfunction, and sensory abnormalities.

Table 1: Comparison of baseline data.

Items	Experimental group ($n = 45$)	Control group ($n = 45$)	x^2/t	P
Age ($\bar{x} \pm s$, years)	65.44 ± 6.18	66.42 ± 6.46	0.735	0.464
BMI (kg/m^2)	19.98 ± 0.53	20.13 ± 0.65	1.199	0.234
Mean disease duration (years)	2.84 ± 1.00	2.80 ± 0.99	0.191	0.849
Clinical stages			0.049	0.824
Stage C	30 (66.67%)	29 (64.44%)		
Stage D	15 (33.33%)	16 (35.56%)		
Number of comorbidities (types)	2.47 ± 1.52	2.33 ± 1.51	0.438	0.662
Education levels			0.048	0.827
High school and above	29 (62.22%)	28 (64.44%)		
Middle school and below	16 (37.78%)	17 (35.56%)		
Career				
Civil servants	9 (20.00%)	10 (22.22%)	0.067	0.796
Workers	8 (17.78%)	9 (20.00%)	0.073	0.788
Farmers	6 (13.33%)	7 (15.56%)	0.089	0.764
Individual business owners	7 (15.56%)	5 (11.11%)	0.385	0.535
Other	15 (33.33%)	14 (31.11%)	0.051	0.822
Religious beliefs			0.062	0.803
Yes	10 (22.22%)	11 (24.44%)		
No	35 (77.78%)	34 (75.56%)		
Family income			0.045	0.832
(≥3000 yuan/man·month)	21 (46.67%)	20 (44.44%)		
(<3000yuan/man·month)	24 (53.33%)	25 (55.56%)		
Smoking			0.216	0.642
Yes	33 (73.33%)	31 (68.89%)		
No	12 (26.67%)	14 (31.11%)		
Drinking			0.073	0.788
Yes	36 (80.00%)	37 (82.22%)		
No	9 (20.00%)	8 (17.78%)		
Residence			0.178	0.673
Urban areas	21 (46.67%)	23 (51.11%)		
Rural areas	24 (53.33%)	22 (48.89%)		

The quality of life was assessed by the Expanded Prostate Cancer Index Composite (EPIC) [17], whose evaluation items were sexual function (observing whether the sexual initiative, erectile function, and psychophysiological responsiveness to sex were normal), urinary function (observing the disorders of the ureter, kidneys, urethra, and bladder function), intestinal function (observing the disorders of the intestinal absorption, digestion, and secretion), and hormonal function (observing the levels of the hormone, androgen, and adrenal cortical hormone). The higher the function score, the better the quality of life; the higher the symptom score, the more obvious the symptoms; total score = function score − symptom score, followed by linear conversion, with scores ranging from 0 to 100 and higher scores representing better quality of life.

2.5. Statistical Disposal. The data of the study were statistically analyzed by SPSS21.0. The count data were tested with the x^2 test and expressed by ((n%)), with measurement data by the t test and ($\bar{x} \pm s$). $P < 0.05$ suggested a statistically remarkable difference.

3. Results

3.1. Comparison of Baseline Data. No remarkable differences were found in the age, BMI, mean disease duration, clinical stages, number of comorbidities, education levels, career, religious beliefs, family income, smoking, drinking, and residence between both groups ($P > 0.05$), see Table 1.

3.2. Comparison of Serum Indices after Treatment. After treatment, the serum indices in the experimental group were remarkably lower than those in the control group ($P < 0.001$), see Table 2.

3.3. Incidence of Toxic and Side Effects. The incidence of toxic and side effects in the experimental group was

Table 2: Comparison of serum indices after treatment ($\bar{x} \pm s$).

Groups	n	PSA (ng/ml)	VEGF (pg/ml)
Experimental group	45	5.21 ± 0.55	84.05 ± 6.00
Control group	45	9.36 ± 1.47	94.52 ± 13.35
t		17.737	4.799
P		<0.001	<0.001

Table 3: Incidence of toxic and side effects (n(%)).

Groups	n	Gastrointestinal reactions	Abnormal liver function	Sexual dysfunction	Sensory abnormalities	Total incidence
Experimental group	45	2 (4.44%)	1 (2.22%)	1 (2.22%)	2 (4.44%)	6 (13.33%)
Control group	45	4 (8.89%)	3 (6.67%)	3 (6.67%)	4 (8.89%)	14 (31.11%)
x^2						4.114
P						<0.05

Table 4: Comparison of EPIC scores after treatment ($\bar{x} \pm s$).

Groups	n	Sexual function	Urinary function	Intestinal function	Hormonal function
Experimental group	45	85.76 ± 2.19	41.63 ± 2.78	87.93 ± 2.56	77.95 ± 4.49
Control group	45	78.99 ± 2.49	31.84 ± 1.74	79.67 ± 3.49	67.39 ± 4.44
t		13.695	20.025	12.802	11.218
P		<0.001	<0.001	<0.001	<0.001

remarkably lower than that in the control group ($P < 0.05$), see Table 3.

3.4. Comparison of EPIC Scores after Treatment. After treatment, the EPIC scores in the experimental group were remarkably higher than those in the control group ($P < 0.001$), see Table 4.

4. Discussion

Significant racial and geographic differences in the incidence of PCa have been reported, and in the US, the incidence of PCa has surpassed lung cancer as the number one tumor endangering men's health [18]. The incidence of PCa in Asia is much lower than that in Europe and the US, but it has been on the rise in recent years and is growing more rapidly than in the latter. Patients with advanced PCa have a poor prognosis with short survival time, and most of them are accompanied by bone metastasis symptoms. Therefore, clinical treatment is aimed at controlling disease progression and improving the survival time and quality of patients as well as their quality of life. Studies have shown that PCa patients lean more on androgen, whose bond with receptors can stimulate the prostate cancer cells to divide and proliferate [19]. Meanwhile, Li et al. [20] have found that the blocking of sources of dihydrotestosterone, of which about 89% originates from the testis and 11% from the adrenal gland, can effectively inhibit the growth of prostate cancer cells. Bicalutamide is a competitive inhibitor of male receptors, which inhibits androgen receptors and induces apoptosis in prostate cancer cells, thus effectively inhibiting their function and growth. Docetaxel is a cytotoxic antitumor drug that achieves the purpose of antitumor by disrupting the equilibrium state of microtubule and tubulin dimer [21]. PSA, a glycoprotein secreted by tissues with prostate cancer, is an important serum index for the evaluation and screening of PCa and is closely related to its occurrence and progression. VEGF is a multifunctional cell growth factor that can promote neovascularization and plays an important role in the formation and maintenance of neovascularization in PCa [22]. The results of this study showed that all serum indices were remarkably lower in the experimental group than those in the control group after treatment ($P < 0.001$), indicating that the continuous implementation of this treatment scheme significantly reduced and maintained serum PSA and VEGF levels. The reasons were analyzed as follows. As an antiandrogen drug, bicalutamide can bind to the androgen receptor in the body with high intensity, thus reducing the growth-promoting effect of testosterone and dihydrotestosterone on cancer cells, maximally controlling

the metastasis of prostate cancer cells and consolidating the therapeutic effect. In addition, this treatment can effectively reduce testosterone. Docetaxel, an antitumor drug of taxane compounds, can destroy the mitosis of tumor cells by enhancing tubulin polymerization and inhibiting tubulin depolymerization, thereby inhibiting the division and proliferation of tumor cells, and also reducing the serum PSA and VEGF levels of patients. The combination of the two greatly reduces the serum PSA and VEGF levels of advanced PCa patients, which is positive for the improvement of the disease. Meanwhile, Yang et al. [23] have found that the application of intermittent endocrine treatment in elderly patients with advanced PCa is effective in reducing serum PSA and VEGF levels, regulating immune function, and promoting patients' quality of life, which is consistent with the results of this study.

The incidence of toxic and side effects is an important evaluation index of treatment safety. Gastrointestinal reactions, abnormal liver function, sexual dysfunction, and sensory abnormalities are common adverse reactions in PCa patients, which seriously affect their quality of life. In this study, the overall incidence of toxic and side effects in the experimental group was remarkably lower than that in the control group ($P < 0.05$), indicating that bicalutamide combined with docetaxel is safer than conventional treatment. Moreover, it has been shown that intermittent endocrine treatment for advanced PCa in the elderly can arrest the progression of PCa to the androgen-independent phase, significantly improve the prognosis of patients, and improve their quality of life [24]. The EPIC scale, which is suitable for PCa patients at different stages of development and treatments (mainly surgery, chemotherapy, radiotherapy, and hormonal therapy), is widely used in various countries and regions. The scale is short, is easy to use, and can help clinicians to comprehensively, accurately, rapidly, and specifically assess the quality of life of PCa patients with good reliability and validity, serving as a powerful tool to synthetically assess the quality of health and life related to PCa. Hashimoto et al. [25] have found that the quality of life of most patients with localized PCa within 1 year of treatment tended to decline, and the effect of different treatments on quality of life varied considerably. The results of this study have shown that the scores of sexual function, urinary function, intestinal function, and hormonal function in the experimental group were higher than those in the control group, which fully explains that the combination of bicalutamide and docetaxel is effective in improving the quality of life of patients and is beneficial to their prognosis. Inadequacy of this study: first of all, the selected cases were patients in local hospitals and the source of cases was single; secondly, the study was limited by the observation time, which did not include a sufficient sample size, resulting in bias in the study results; finally, there was a lack of long-term follow-up observation on the intervention effect of patients. Therefore, multicenter clinical research should be conducted to further explore the therapeutic characteristics of bicalutamide combined with docetaxel and assessment tools for bladder function should be added, so as to better exploit the therapeutic advantages of drug combination and benefit more PCa patients.

In summary, bicalutamide combined with docetaxel is a reliable regimen for the treatment of advanced PCa, and the application of this regimen can benefit the patients by effectively reducing serological indexes and improving quality of life. Therefore, it is recommended for the clinical treatment of PCa.

Data Availability

Data to support the findings of this study is available on reasonable request from the corresponding author.

Conflicts of Interest

The authors do not have conflicts of interest to declare.

Acknowledgments

This research was funded by the Key R & D Plan of Shandong Province (histone methyltransferase setd2 regulates Wnt/β-molecular mechanism of catenin signaling pathway inhibiting proliferation and metastasis of renal clear cell carcinoma), grant number 2019GSF108255.

References

[1] G. Hanan, E. Ahmad Ardalan, C. Thenappan et al., "Comparison of magnetic resonance imaging and transrectal ultrasound informed prostate biopsy for prostate cancer diagnosis in biopsy naïve men: a systematic review and meta-analysis," *The Journal of Urology*, vol. 203, no. 6, pp. 1085–1093, 2020.

[2] J. Marlena, S. Łukasz, A. Paulina, A. Kasperska, and A. Marszałek, "Expression levels of IL-17A, IL-17F, IL-17RA, and IL-17RC in prostate cancer with taking into account the histological grade according to Gleason scale in comparison to benign prostatic hyperplasia: in search of new therapeutic options," *Journal of Immunology Research*, vol. 2020, Article ID 4910595, 2020.

[3] S. Tahlia, K. James, S. Martin et al., "Pharmacodynamics effects of CDK4/6 inhibitor LEE011 (ribociclib) in high-risk, localised prostate cancer: a study protocol for a randomised controlled phase II trial (LEEP study: LEE011 in high-risk, localised prostate cancer)," *BMJ Open*, vol. 10, no. 1, article e033667, 2020.

[4] C. Roberto, I. Linares Quevedo Ana, J. Sánchez Gómez Francisco et al., "A non-randomized prospective study on the diagnostic performance of perineal prostatic biopsy, directed via diffusion nuclear resonance, in patients with suspected prostate cancer and previous negative transrectal prostate biopsy," *Urologia*, vol. 88, no. 1, pp. 69–76, 2021.

[5] A. Vertosick Emily, H. Christel, D. Sjoberg Daniel et al., "Prespecified 4-Kallikrein marker model at age 50 or 60 for early detection of lethal prostate cancer in a large population based cohort of asymptomatic men followed for 20 years," *The Journal of Urology*, vol. 204, no. 2, pp. 281–288, 2020.

[6] P. K. Jin, C. Sang, L. J. Sung, J. K. Kim, M. H. Kim, and I. G. Jeong, "Risk stratification of prostate cancer according to PI-RADS® version 2 categories: meta-analysis for prospective studies," *The Journal of Urology*, vol. 204, no. 6, pp. 1141–1149, 2020.

[7] X. Xing, F. Mahdi, Y. Tian et al., "Risk of invasive prostate cancer and prostate cancer death in relatives of patients with prostatic borderline or in situ neoplasia: a nationwide cohort study," *Cancer*, vol. 126, no. 19, pp. 4371–4378, 2020.

[8] A. Bjurlin Marc, R. Carroll Peter, E. Scott et al., "Update of the standard operating procedure on the use of multiparametric magnetic resonance imaging for the diagnosis, staging and management of prostate cancer," *The Journal of Urology*, vol. 203, no. 4, pp. 706–712, 2020.

[9] S. Johanna, L. I. Franck, G. Oskar et al., "Time spent in hormone-sensitive and castration-resistant disease states in men with advanced prostate cancer, and its health economic impact: registry-based study in Sweden," *The Journal of Urology*, vol. 55, no. 1, pp. 1–8, 2021.

[10] L.-B. Sami-Ramzi, K. Mykyta, B. Dirk et al., "Minimum magnetic resonance imaging-ultrasound fusion targeted biopsy cores needed for prostate cancer detection: multivariable retrospective, lesion based analyses of patients treated with radical prostatectomy," *The Journal of Urology*, vol. 203, no. 2, pp. 299–303, 2020.

[11] H. Gaofei, S. Chengfang, S. Yuanyuan et al., "The diagnostic value of prostate cancer between holmium laser enucleation of the prostate and transurethral resection of the prostate for benign prostatic hyperplasia: a retrospective comparative study," *International Journal of Surgery*, vol. 79, pp. 217–221, 2020.

[12] K. H. Won, L. H. Youn, B. Y. Joon et al., "A novel urinary mRNA signature using the droplet digital polymerase chain reaction platform improves discrimination between prostate cancer and benign prostatic hyperplasia within the prostate-specific antigen gray zone," *Investigative And Clinical Urology*, vol. 61, no. 4, pp. 411–418, 2020.

[13] R. Setareh, M. Emadoddin, S. Farzin, S. Khafri, T. A. Kopi, and H. Parsian, "Evaluation of the plasma level of long non-coding RNA PCAT1 in prostatic hyperplasia and newly diagnosed prostate cancer patients," *The Journal of Gene Medicine*, vol. 22, no. 10, p. e 3239, 2020.

[14] S. Karim, S. Wettstein Marian, L. Laura et al., "External validation and comparison of prostate cancer risk calculators incorporating multiparametric magnetic resonance imaging for prediction of clinically significant prostate cancer," *The Journal of Urology*, vol. 203, no. 4, pp. 719–726, 2020.

[15] World Medical Association, "World Medical Association Declaration of Helsinki," *Journal of the American Medical Association*, vol. 310, no. 20, pp. 2191–2194, 2013.

[16] A. Markin Pavel, B. Alex, M. Natalia et al., "Plasma sarcosine measured by gas chromatography-mass spectrometry distinguishes prostatic intraepithelial neoplasia and prostate cancer from benign prostate hyperplasia," *Laboratoriums Medizin*, vol. 51, no. 6, pp. 566–573, 2020.

[17] S. Gang, R. Mingjian, W. He et al., "How many targeted biopsy cores are needed for clinically significant prostate cancer detection during transperineal magnetic resonance imaging ultrasound fusion biopsy?," *The Journal of Urology*, vol. 204, no. 6, pp. 1202–1208, 2020.

[18] N. Costa Daniel, J. Liwei, S. Naveen et al., "Prospective PI-RADS v2.1 atypical benign prostatic hyperplasia nodules with marked restricted diffusion: detection of clinically significant prostate cancer on multiparametric MRI," *AJR. American Journal of Roentgenology*, vol. 217, no. 2, pp. 395–403, 2021.

[19] A. Joosse Simon, B. Burkhard, G. Christin et al., "Tumor-associated release of prostatic cells into the blood after transrectal ultrasound-guided biopsy in patients with histologically confirmed prostate cancer," *Clinical Chemistry*, vol. 66, no. 1, pp. 161–168, 2020.

[20] L. Qi, S. Yibo, S. Rigai et al., "Altered staining patterns and expression level of engrailed-2 in benign prostatic hyperplasia and prostate cancer predict prostatic disease progression," *BMC Cancer*, vol. 20, no. 1, p. 555, 2020.

[21] T. Tadashi, T. Masataka, S. Naoki et al., "Does screening for prostate cancer improve cancer-specific mortality in Asian men? Real-world data in Yokosuka City 15 years after introducing PSA-based population screening," *Prostate*, vol. 80, no. 11, pp. 824–830, 2020.

[22] C. E. David, A. Gerald, J. Freedland Stephen et al., "Evolving understanding and categorization of prostate cancer: preventing progression to metastatic castration-resistant prostate cancer: RADAR IV," *The Canadian Journal of Urology*, vol. 27, pp. 10352–10362, 2020.

[23] Y. Tingting, Z. Yi, W. Haiyan et al., "Insulin exacerbated high glucose-induced epithelial-mesenchymal transition in prostatic epithelial cells BPH-1 and prostate cancer cells PC-3 via MEK/ERK signaling pathway," *Experimental Cell Research*, vol. 394, no. 1, article 112145, 2020.

[24] S. Butler Santino, M. Vinayak, G. Zhao Shuang et al., "Prostate cancer incidence across stage, NCCN risk groups, and age before and after USPSTF grade D recommendations against prostate-specific antigen screening in 2012," *Cancer*, vol. 126, no. 4, pp. 717–724, 2020.

[25] H. Takeshi, N. Jun, K. Takeshi et al., "Predicting factors for progression to castration resistance prostate cancer after biochemical recurrence in patients with clinically localized prostate cancer who underwent radical prostatectomy," *International Journal of Clinical Oncology*, vol. 25, no. 9, pp. 1704–1710, 2020.

Hindawi
Disease Markers
Volume 2022, Article ID 5069918, 7 pages
https://doi.org/10.1155/2022/5069918

Research Article

Effects of Pamidronate Disodium Combined with Calcium on BMD Values and Severity of Pain in Elderly Patients with Osteoporosis Based on Mobile Terminal Platform for Internet of Things

Zuoming Bai, Jianguo Wang, Mingming Kang, Peng Guo, and Dong Wang

Department of Orthopedics, The Second Hospital of Shanxi Medical University, Taiyuan, 030001 Shanxi, China

Correspondence should be addressed to Dong Wang; wangdong@sydey.org.cn

Received 29 June 2022; Revised 5 August 2022; Accepted 8 August 2022; Published 16 August 2022

Academic Editor: Jun Yang

Objective. To explore the effects of pamidronate disodium combined with calcium on BMD values and the severity of pain in elderly patients with osteoporosis based on the mobile terminal platform for the Internet of Things. *Methods*. The data of 120 patients admitted to our hospital from January 2019 to December 2020 were retrospectively analyzed. According to the patients' condition and medication wills, they were divided into the experimental group ($n = 68$) and the control group ($n = 52$). All patients were given chronic disease management based on the mobile terminals for the Internet of Things, and they received the treatment of bisphosphonates and calcium, with the supplement of calcium at a daily dose of 1000 mg. The control group was given alendronate sodium once a week, and the experimental group was given pamidronate disodium by intravenous infusion three times a month, with the treatment cycle as 1 year. The patients' bone mineral density (BMD) values and the pain indexes were compared after treatment. *Results*. There was no statistical difference in general information between the two groups ($p > 0.05$). The BMD values of the lumbar vertebrae $L_{2\text{-}4}$, total hip, and femur neck at 6 months and 1 year after treatment in the experimental group were significantly higher than those in the control group ($p < 0.001$). The pain scores at 6 months and 1 year after treatment in the experimental group were significantly lower than those in the control group ($p < 0.001$). *Conclusion*. The treatment of pamidronate disodium combined with calcium based on the mobile terminal platform for the Internet of Things can reduce the severity of pain in elderly patients with osteoporosis and improve the BMD, which has a generalization value.

1. Introduction

Osteoporosis is a chronic progressive systemic metabolic osteopathy characterized by a low bone mineral density (BMD). The bone microarchitecture of patients is damaged, and the bone fragility is aggravated. Patients with mild conditions in the early stage have no obvious symptom, and the diffuse pain or even systemic osteodynia can occur with the progress of disease. The incidence of fractures significantly increases [1, 2], which seriously affects the patients' quality of life. In recent years, with the aggravation of the population aging in China, the incidence of osteoporosis has increased, and the relevant data predict that the number of patients with osteoporotic fractures will reach 6 million by 2050 in China with the corresponding medical expenditure more than RMB 100 billion [3, 4]. Therefore, the deepening of clinical research on osteoporosis is beneficial for reducing the future medical burden in China and improving the prognosis of elderly patients with osteoporosis. At present, calcium is the main medicine for the treatment of osteoporosis, but the calcium treatment alone cannot exert an ideal prevention and control effect, and elderly patients with low calcium absorption rate in intestinal tract and 1α-hydrolase activity of kidney cannot benefit from it [5, 6]. In addition to calcium, bisphosphonates are also the first-line drug for the treatment of osteoporosis, which can

inhibit the bone remodeling, increase the BMD, improve the bone microarchitecture of patients, and reduce the possibility of fracture [7]. Since the bisphosphonates are prone to induce the adverse reactions, there are a few studies on the application of bisphosphonates in elderly patients with osteoporosis. Filippo et al. have found that zoledronic acid is the most likely to induce the adverse reactions, followed by pamidronate disodium and alendronate sodium [8]. This study did not compare the medication safety, which was the limitation of this study, but the safety of pamidronate disodium has been confirmed in various diseases. Pamidronate disodium has the same efficacy and the incidence of adverse reactions in alleviating and delaying the occurrence time of skeletal-related events in non-small-cell lung cancer with bone metastasis, and the use of zoledronic acid after ineffective treatment of pamidronate disodium can delay the occurrence time of skeletal-related events. Pamidronate disodium, as a new generation of bisphosphonates, can effectively inhibit the activity of osteoclasts, hinder the bone resorption mediated by osteoclasts, repair the osteolytic lesions, and slow down the rate of organismal bone resorption, thus exerting an impact on preventing the osteoporosis [9]. Most importantly, pamidronate disodium is often used in the treatment of bone metastasis of advanced malignant tumors. The medicine can inhibit the synthesis of osteoclasts and the release of nociceptive transmitters such as prostaglandin and reduce the symptoms of osteodynia, which plays an important role in improving the patients' quality of life. Most elderly patients with chronic diseases have the problem of low medication compliance, and low medication compliance is an important factor affecting the treatment effect of patients. Most literature shows that the compliance of elderly patients gradually decreases after leaving hospital; so, it is crucial to improve the medication compliance of patients. The mobile terminal platform for the Internet of Things can exert a monitoring role through multimode diagnosis and treatment, provide strong external support, and maintain medication compliance in elderly patients with osteoporosis. At present, there is no clinical research on the combined application of disodium pamidronate and calcium in the treatment of elderly osteoporosis. Based on the mobile terminal platform for the Internet of Things, in this study, the supervision and management of medication for elder patients with osteoporosis were strengthened, and the actual effects of pamidronate disodium combined with calcium in the treatment of elderly osteoporosis were explored. The reports are as follows.

2. Materials and Methods

2.1. Research Design. This retrospective study was conducted in our hospital from January 2019 to December 2020 to explore the effects of pamidronate disodium combined with calcium on BMD values and the severity of pain in elderly patients with osteoporosis based on the mobile terminal platform for the Internet of Things. The blind level of this study was double-blind. The study subjects and researchers did not understand the grouping of this experiment, and the research designers were responsible for arranging and controlling the experiment.

2.2. Inclusion and Exclusion Criteria. Inclusion criteria were as follows: (1) patients were diagnosed with primary osteoporosis according to the biochemical examination of bone metabolism in accordance with the diagnostic criteria of osteoporosis recommended by the International Society of Clinical Densitometry (ISCD) [10] and American college of radiology [11]. (2) Patients had the clinical manifestations with spontaneous pain in the whole body, waist, thorax, and back. (3) The BMD in patients measured by dual-energy absorptiometry was lower than 2.5 standard deviations below the mean in healthy people of the same age and sex. (4) Patients had not taken any drugs affecting the bone metabolism in the last three months. (5) The age of patients was more than 70 years old. (6) All patients were treated in our hospital during the whole process with the complete clinical information. (7) Patients were cooperative to complete the follow-up.

Exclusion criteria were as follows: (1) patients with secondary osteoporosis due to the endocrine metabolism, alimentary deficiency, and rheumatism; (2) patients who had taken drugs that might affect the bone metabolism in the last three months; (3) patients with the history of malignant tumor and cardiovascular disease or patients with the diseases that could affect the bone metabolism; (4) patients with the irrational drug use that might have the undefined treatment effects; (5) patients with the incomplete clinical information; (6) patients without complete follow-up; and (7) patients with psychiatric disorders and who could not communicate with others.

2.3. Procedures. In this study, 120 patients were divided into the experimental group ($n = 68$) and the control group ($n = 52$) according to the patients' condition and medication wills. All patients were given the chronic disease management based on the mobile terminals for the Internet of Things, and they received the treatment of bisphosphonates and calcium. On the day when the patients agreed to participate in the study, the study group collected the data of sociodemography and clinical manifestations. After the patients began to receive the treatment, they were given the follow-up for 1 year to investigate the changes of BMD and the pain perception.

2.4. Moral Consideration. This study was in line with the principles of Declaration of Helsinki (2013) [12], and patients signed the informed consent.

2.5. Standards of Withdrawing from Experiment. In the following conditions, the study group judged that patients were inappropriate for continuing the experiment, and the case record forms of patients were retained, but the data analysis was not performed: (1) patients with exacerbation during the experiment, (2) patients with severe comorbidities or complications, and (3) patients who requested the withdrawal from the clinical trials.

2.6. Methods. All patients were given the chronic disease management based on the mobile terminals for the Internet of Things, and the project of healthcare cloud was constructed. The integrated management system of osteoporosis

was consolidated into the cloud platform to build a remote monitoring platform for osteoporosis medication. Patients needed to register and report on the mobile terminal platform, and they were supervised and managed through the mobile terminal platform for the Internet of Things.

Control group was as follows: the control group was given the alendronate sodium (Beijing Wansheng Pharmaceutical Co., Ltd.; NMPA approval No. H20058996) once a week at a single dose of 70 mg with 300 ml of warm water on an empty stomach in the morning. Patients should keep standing or sitting within half an hour after taking the medicine and then take food. In addition, patients were given calcium (Huishi Pharmaceutical Co., Ltd.; NMPA approval No. H10950029) at a daily dose of 600 mg and 2 pellets of active vitamin D (Sinopharm Xingsha Pharmaceutical Co., Ltd.; NMPA approval No. H20173093).

The experimental group was as follows: The supplement of calcium and vitamin D in the experimental group was the same as those in the control group. In addition, the pamidronate disodium (Shenzhen Haiwang Pharmaceutical Co., Ltd.; NMPA approval No. H19980130) at a single dose of 30 mg diluted in 250 ml of 5% glucose once a day on 3 consecutive days was given by intravenous infusion three times a month.

2.7. Standards of Observation

(1) General information: the general information of patients such as gender, age, body mass, BMI, the course of disease, the severity of osteoporosis, education level, income level, payment of medical expenses, and the place of residence in the two groups were recorded

(2) BMD: the BMD values of patients were detected before treatment and at 6 months and 1 year after treatment using a dual energy X-ray absorptiometry (DTX-200; NMPA (I) 20113302208) by Osteometer MediTech, USA. Before the examination, the precision of instruments was calibrated by the model of lumbar vertebrae with the coefficient of variation (CV) as 0.40%. After the patients kept lying flat, the bone scan of lumbar vertebrae ($L_{2\text{-}4}$) in supine position was performed, and the hip was scanned in knee flexion position of both lower extremities. The BMD values of lumbar vertebrae, total hip, and femur neck were recorded

(3) Pain indexes: before treatment, and at 6 months and 1 year after treatment, the patients' severity of pain was evaluated with an 11-spot numeric rating scale (NRS). In the scale, the number of 0-10 on the straight line represented the severity of pain, and the patients chose the spot which was consistent with the severity of pain according to their own condition after visual estimation. 0 point represented the painlessness, 1-3 points represented the mild pain that did not interfere with sleep, 4-6 points represented the moderate pain, 7-9 points represented the severe pain that could not fall asleep or woke up from the pain during sleep, and 10 points represented the baryodynia

2.8. Statistical Treatment. In this study, the experimental data were processed by SPSS 20.0, and GraphPad Prism 7 (GraphPad software, San Diego, USA) was used to draw pictures of the data. The enumeration data and measurement data were tested by x^2 and t-test. When $p < 0.05$, the differences were considered to be statistically significant.

3. Results

3.1. Comparison of Patients' General Information. There was no significant difference in the general information between the two groups, see details in Table 1.

3.2. Comparison of Patients' BMD Values. The BMD values of the lumbar vertebrae $L_{2\text{-}4}$, total hip, and femur neck at 6 months and 1 year after treatment in the experimental group were significantly higher than those in the control group ($p < 0.001$), see details in Figure 1.

3.3. Comparison of Patients' Pain Indexes. There was no statistical difference in the pain scores between the experimental group and the control group before treatment (7.65 ± 0.64 vs. 7.65 ± 0.55, $p > 0.05$). The pain scores at 6 months and 1 year after treatment in the experimental group were significantly lower than those in the control group (4.24 ± 0.55 vs. 5.67 ± 0.61, 3.01 ± 0.44 vs. 4.13 ± 0.62, $p < 0.001$).

4. Discussion

Due to the existence of degenerative deformation during the senescence of the body, the calcium absorption rate in gastrointestinal tract and the sex hormone levels will decrease with age [13], so that age is a risk factor for osteoporosis, and higher age is associated with a higher incidence of osteoporosis [14]. Epidemiological data have shown that the number of elderly patients with osteoporosis is close to 100 million ranking third in chronic diseases among residents, and the incidence of osteoporotic fractures is as high as 7.5% in China. The rate of hip fracture in elderly patients increased by three times during 2012-2016, and the mortality of patients within one year is as high as 20.0%. In addition, this number will continue to rise further with the aggravation of the population aging in China [15–17]. Early measures of prevention and treatment can effectively improve the quality of life in elderly patients with osteoporosis and reduce the medical burden in China. At present, the calcium treatment is the basic treatment for senile osteoporosis. Calcium, as a key component of bone, plays an important role in reducing the osteoporosis. Some studies have shown that calcium can prevent the age-related calcium deficiency, thereby exerting the effect on prevention and treatment of senile osteoporosis [18]. However, the effect of calcium alone is limited, and it is necessary to cooperate with other therapeutic agents. At present, the common therapeutic agents used for osteoporosis also include bisphosphonates, calcium, and sex hormone supplementation. Bisphosphonates can maintain

Table 1: Comparison of patients' general information.

Groups	Experimental group ($n = 68$)	Control group ($n = 52$)	X^2/t	p
Gender			0.175	0.676
Male	34	28		
Female	34	24		
Age (years)	73.99 ± 3.16	74.44 ± 3.65	0.723	0.471
Body mass (kg)	62.65 ± 2.65	62.74 ± 2.40	0.192	0.848
BMI (kg/m^2)	22.11 ± 1.20	22.13 ± 1.24	0.089	0.929
Course of disease (years)	5.29 ± 1.94	4.98 ± 1.66	0.922	0.358
Severity degree			0.369	0.544
Moderate grade	48	34		
Severe grade	20	18		
Education level				
Primary school	30	26	0.410	0.522
Senior high school	28	20	0.091	0.764
University and above	10	6	0.256	0.613
Income level (yuan)			0.019	0.890
≥4000	41	32		
<4000	27	20		
Payment of medical expenses				
Medical insurance	30	22	0.039	0.843
Commercial insurance	24	18	0.006	0.938
Others	14	12	0.108	0.743
Place of residence			0.016	0.901
Town	40	30		
Countryside	28	22		

the effect on antiosteoporotic fracture for several years even after discontinuation, while the antifracture efficacy of other drugs decreases, indicating that bisphosphonates have a favorable value in long-term antiosteoporosis [19].

Scholars Tim et al. have found that the treatment with bisphosphonates for 4 years can reduce the risk of hip fracture by 50.0%. The annual growth rate of BMD value is 1.0% at a daily dose of 150 mg, and the densities of lumbar vertebrae and hip can increase continuously [20]. The results of this study showed that the densities of lumbar vertebrae, total hip, and femur neck in the two groups were increased after the treatment of bisphosphonates and calcium. However, the BMD values of lumbar vertebrae $L_{2\text{-}4}$, total hip, and femur neck in the experimental group at 6 months and 1 year after treatment were significantly higher than those in the control group ($p < 0.001$), suggesting that the intensity of pamidronate disodium by intravenous injection was higher than that of alendronate sodium by oral administration. Pamidronate disodium can fully adhere to the surface of trabecular bone by intravenous injection, which can directly inhibit the phagocytic factors of osteoclasts, hinder the effects of osteoclasts on dissolution and destruction of bone, and slow down the bone absorption, thereby preventing the bone dissolution [21]. Baroncelli et al. have believed that pamidronate disodium can promote the bone formation in patients with spontaneous juvenile osteoporosis, improve the BMD, reduce the incidence of fractures, and prevent the disability after fractures [22]. In addition, pamidronate disodium has the analgesic effect, especially in relieving the symptoms of bone pain. It can inhibit the premature maturation of osteoclasts, slow down the release frequencies of nociceptive transmitters such as prostaglandins and lactic acid and inflammatory transmitters, and relieve the osteolytic pain [23]. At present, pamidronate disodium is often used for analgesia in bone metastasis of malignant tumor. Some scholars have believed that the analgesic effect of this drug in osteoporosis is better than that in bone metastasis of malignant tumor [24]. This study showed that the pain scores at 6 months and 1 year after treatment in the experimental group were significantly lower than those in the control group ($p < 0.001$), indicating that pamidronate disodium has a definite analgesic effect in elderly patients with osteoporosis, which can effectively reduce the patients' severity of pain and has a great significance for improving the quality of life.

It is worth noting that the elderly patients with chronic diseases have the characteristic of poor medical compliance behavior [25], and patients with osteoporosis need long-term medication. In clinic, it is generally agreed that the treatment time of osteoporosis should be more than 1 year. Therefore, no matter what kind of drugs are used, attention should be paid to maintain the medication compliance of

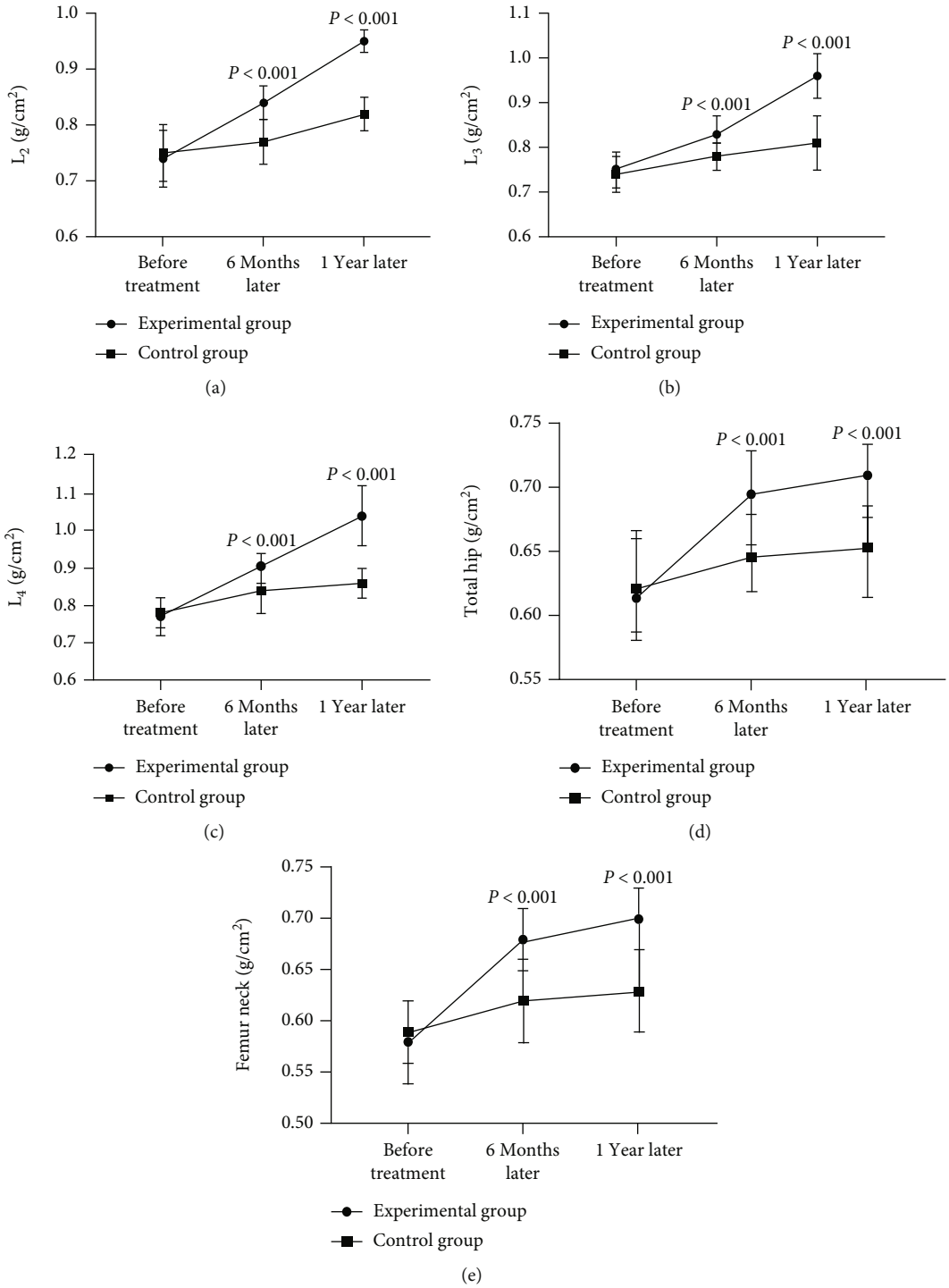

Figure 1: Comparison of patients' BMD values ($\bar{x} \pm s$, g/cm^2). Notes were as follows: Figure 1(a) shows the BMD value of L_2. Figure 1(b) shows the BMD value of L_3. Figure 1(c) shows the BMD value of L_4. Figure 1(d) shows the BMD value of total hip. Figure 1(e) shows the BMD value of femur neck. There was no statistical difference in the BMD values of lumbar vertebrae $L_{2\text{-}4}$, total hip, and femur neck between the experimental group and the control group before treatment (0.74 ± 0.05 vs. 0.75 ± 0.05, 0.75 ± 0.04 vs. 0.74 ± 0.04, 0.77 ± 0.05 vs. 0.78 ± 0.04, 0.62 ± 0.05 vs. 0.63 ± 0.05, 0.58 ± 0.04 vs. 0.59 ± 0.03, $p > 0.05$). The BMD values of lumbar vertebrae $L_{2\text{-}4}$, total hip, and femur neck in the experimental group at 6 months after treatment were significantly higher than those in the control group (0.84 ± 0.03 vs. 0.77 ± 0.04, 0.83 ± 0.04 vs. 0.78 ± 0.03, 0.90 ± 0.04 vs. 0.84 ± 0.06, 0.69 ± 0.04 vs. 0.64 ± 0.03, 0.68 ± 0.03 vs. 0.62 ± 0.04, $p < 0.001$). The BMD values of lumbar vertebrae $L_{2\text{-}4}$, total hip, and femur neck in the experimental group at 1 year after treatment were significantly higher than those in the control group (0.95 ± 0.02 vs. 0.82 ± 0.03, 0.96 ± 0.05 vs. 0.81 ± 0.06, 1.04 ± 0.08 vs. 0.86 ± 0.04, 0.71 ± 0.03 vs. 0.65 ± 0.04, 0.70 ± 0.03 vs. 0.63 ± 0.04, $p < 0.001$).

patients to ensure that drugs can play the best effect. Based on the mobile terminal platform for the Internet of Things, this study established a remote monitoring platform for elderly patients with osteoporosis and realized the continuous management of elderly patients, so that the medication effects of the two groups were better. With the development of aging society, the importance of information construction in elderly chronic diseases is increasingly prominent. It is beneficial for elderly patients with osteoporosis to accelerate the construction of the mobile terminal platform for the Internet of Things, and elderly patients with chronic diseases also benefit more.

In conclusion, the treatment of pamidronate disodium combined with calcium based on the mobile terminal platform for the Internet of Things can reduce the severity of pain in elderly patients with osteoporosis and improve the BMD, which has a generalization value.

Data Availability

Data to support the findings of this study is available on reasonable request from the corresponding author.

Conflicts of Interest

The authors do not have conflicts of interest to declare.

References

[1] H. Zhang, A. Wang, G. Shen et al., "Hepcidin-induced reduction in iron content and PGC-1β expression negatively regulates osteoclast differentiation to play a protective role in postmenopausal osteoporosis," *Aging*, vol. 13, no. 8, pp. 11296–11314, 2021.

[2] K. Ebina, M. Hirao, H. Tsuboi et al., "Effects of prior osteoporosis treatment on early treatment response of romosozumab in patients with postmenopausal osteoporosis," *Bone*, vol. 140, article 115574, 2020.

[3] Z. Fan, X. Li, X. Zhang, Y. Yang, Q. Fei, and A. Guo, "Comparison of OSTA, FRAX and BMI for predicting postmenopausal osteoporosis in a Han population in Beijing: a cross sectional study," *Clinical Interventions in Aging*, vol. 15, pp. 1171–1180, 2020.

[4] Y. R. Yang, C. W. Li, J. H. Wang et al., "Ubiquitylomes analysis of the whole blood in postmenopausal osteoporosis patients and healthy postmenopausal women," *Orthopaedic Surgery*, vol. 11, no. 6, pp. 1187–1200, 2019.

[5] Y. He, D. Chen, Q. Guo, P. Shi, C. You, and Y. Feng, "MicroRNA-151a-3p functions in the regulation of osteoclast differentiation: significance to postmenopausal osteoporosis," *Clinical Interventions in Aging*, vol. 16, pp. 1357–1366, 2021.

[6] K. Tomonori, M. Akiko, S. Makoto et al., "Denosumab versus romosozumab for postmenopausal osteoporosis treatment," *Scientific Reports*, vol. 11, no. 1, p. 11801, 2021.

[7] G. Yan, Y. Huang, H. Cao, J. Wu, N. Jiang, and X. Cao, "Association of breastfeeding and postmenopausal osteoporosis in Chinese women: a community-based retrospective study," *BMC Womens Health*, vol. 19, no. 1, p. 110, 2019.

[8] F. Migliorini, N. Maffulli, F. Spiezia, G. M. Peretti, M. Tingart, and R. Giorgino, "Potential of biomarkers during pharmacological therapy setting for postmenopausal osteoporosis: a systematic review," *Journal of Orthopaedic Surgery and Research*, vol. 16, no. 1, p. 351, 2021.

[9] C. Lin, S. Yu, R. Jin et al., "Circulating miR-338 cluster activities on osteoblast differentiation: potential diagnostic and therapeutic targets for postmenopausal osteoporosis," *Theranostics*, vol. 9, no. 13, pp. 3780–3797, 2019.

[10] V. Testini, M. T. Paparella, I. Gangai, and G. Guglielmi, "Postmenopausal osteoporosis: current status of bone densitometry," *Obstetrics and Gynecology*, vol. 73, no. 6, pp. 730–743, 2021.

[11] B. G. A. Stuckey, L. A. Mahoney, S. Dragovic, and S. J. Brown, "Celiac disease and bone health: is there a gap in the management of postmenopausal osteoporosis?," *Climacteric*, vol. 23, no. 6, pp. 559–565, 2020.

[12] World Medical Association, "World medical association declaration of Helsinki: ethical principles for medical research involving human subjects," *Journal of the American Medical Association*, vol. 310, no. 20, pp. 2191–2194, 2013.

[13] J. Xiaona, Z. Baozhen, and Z. Dangfeng, "Replication study confirms the association of the common rs1800629 variant of theTNFαGene with postmenopausal osteoporosis susceptibility in the Han Chinese population," *Genetic Testing and Molecular Biomarkers*, vol. 22, no. 4, pp. 246–251, 2018.

[14] Y. Kataoka, Y. Luo, A. Chaimani et al., "Cumulative network meta-analyses, practice guidelines, and actual prescriptions for postmenopausal osteoporosis: a meta-epidemiological study," *Archives of Osteoporosis*, vol. 15, no. 1, p. 21, 2020.

[15] X. Cai, X. Yi, Y. Zhang, D. Zhang, L. Zhi, and H. Liu, "Genetic susceptibility of postmenopausal osteoporosis on sulfide quinone reductase-like gene," *Osteoporosis International*, vol. 29, no. 9, pp. 2041–2047, 2018.

[16] B. Johnson, E. C. Lai, H. T. Ou, H. Li, and B. Stollenwerk, "Real-world cost-effectiveness of denosumab for the treatment of postmenopausal osteoporosis in Taiwan," *Archives of Osteoporosis*, vol. 16, no. 1, p. 155, 2021.

[17] A. Wawrzyniak, M. Skrzypczak-Zielinska, I. Krela-Kazmierczak et al., "Analysis of the tumor necrosis factor superfamily member 11 gene polymorphism with bone mineral density and bone fracture frequency in patients with postmenopausal osteoporosis," *Advances in Medical Sciences*, vol. 65, no. 2, pp. 291–297, 2020.

[18] S. Shetty, B. John, S. Mohan, and T. V. Paul, "Vertebral fracture assessment by dual-energy X-ray absorptiometry along with bone mineral density in the evaluation of postmenopausal osteoporosis," *Archives of Osteoporosis*, vol. 15, no. 1, p. 25, 2020.

[19] The North American Menopause Society (NAMS) and Management of osteoporosis in postmenopausal women: the, "Management of osteoporosis in postmenopausal women: the 2021 Position statement of the North American Menopause Society," *Menopause*, vol. 28, no. 9, pp. 973–997, 2021.

[20] T. Rolvien, P. Milovanovic, F. N. Schmidt et al., "Long-term immobilization in elderly females causes a specific pattern of cortical bone and osteocyte deterioration different from postmenopausal osteoporosis," *Journal of Bone and Mineral Research*, vol. 35, no. 7, pp. 1343–1351, 2020.

[21] P. Sawicki, M. Tałałaj, K. Życińska, W. S. Zgliczyński, and W. Wierzba, "Comparison of the characteristics of back pain in women with postmenopausal osteoporosis with and without vertebral compression fracture: a retrospective study at a single osteoporosis center in Poland," *Medical Science Monitor*, vol. 27, article e929853, 2021.

[22] G. I. Baroncelli, F. Vierucci, S. Bertelloni, P. Erba, E. Zampollo, and M. R. Giuca, "Pamidronate treatment stimulates the onset of recovery phase reducing fracture rate and skeletal deformities in patients with idiopathic juvenile osteoporosis: comparison with untreated patients," *Journal of Bone and Mineral Metabolism*, vol. 31, no. 5, pp. 533–543, 2013.

[23] N. Saleh, N. A. Nassef, M. K. Shawky, M. I. Elshishiny, and H. A. Saleh, "Novel approach for pathogenesis of osteoporosis in ovariectomized rats as a model of postmenopausal osteoporosis," *Experimental Gerontology*, vol. 137, article 110935, 2020.

[24] D. Aghamohammadi, N. Dolatkhah, S. K. Shakouri, P. Hermann, and F. Eslamian, "Ginger (Zingiber officinale) and turmeric (Curcuma longa L.) supplementation effects on quality of life, body composition, bone mineral density and osteoporosis related biomarkers and micro-RNAs in women with postmenopausal osteoporosis: a study protocol for a randomized controlled clinical trial," *Journal of Complementary and Integrative Medicine*, vol. 18, no. 1, pp. 131–137, 2020.

[25] W. Zhou, Y. Liu, X. Guo, H. Yang, Y. Xu, and D. Geng, "Effects of zoledronic acid on bone mineral density around prostheses and bone metabolism markers after primary total hip arthroplasty in females with postmenopausal osteoporosis," *Osteoporosis International*, vol. 30, no. 8, pp. 1581–1589, 2019.

Hindawi
Disease Markers
Volume 2022, Article ID 8692966, 8 pages
https://doi.org/10.1155/2022/8692966

Research Article

Effects of Lumbar Plexus Block Combined with Infiltration Anesthesia on Anesthesia Comfort Scores and Stress Responses in Elderly Patients Undergoing Hip Replacement

Jizheng Zhang, Yi Li, Xiaohua Sun, and Wanlu Ren

Department of Anesthesiology, Tianjin Hospital, 300211 Tianjin, China

Correspondence should be addressed to Wanlu Ren; renwanlu@tjorthop.org.cn

Received 24 June 2022; Revised 20 July 2022; Accepted 26 July 2022; Published 10 August 2022

Academic Editor: Jianxin Shi

Objective. To investigate the effects of lumbar plexus block combined with infiltration anesthesia on anesthesia comfort scores and stress responses in elderly patients undergoing hip replacement. *Methods.* The materials of 100 elderly patients undergoing hip replacement who were treated in our hospital (January 2020-January 2021) were retrospectively analyzed, and they were equalized into the experimental group ($n = 50$) and control group ($n = 50$) according to the anesthesia methods. The experimental group received lumbar plexus block combined with infiltration anesthesia, and the control group received combined spinal-epidural anesthesia combined with infiltration anesthesia. The patients' anesthesia comfort scores, stress responses, and postoperative pain indexes were compared between the two groups. *Results.* Compared with the control group, the experimental group achieved much lower scores of mood change, shivering response, and traction reaction ($P < 0.001$), indicating that the anesthesia comfort in the experimental group was higher. Compared with the control group, the experimental group had much better perioperative stress response indexes ($P < 0.05$) and eminently lower pain scores at 12 and 24 hours after surgery ($P < 0.05$). *Conclusion.* Lumbar plexus block combined with infiltration anesthesia can relieve the stress responses and postoperative pain of elderly patients undergoing hip replacement and increase their anesthesia comfort. Therefore, this anesthesia method is translational in clinic.

1. Introduction

With a larger aging population in China, the number of elderly patients undergoing hip replacement because of femoral neck fracture or femoral head necrosis is gradually increasing [1]. Although hip replacement can effectively reduce the disability rate, it has such disadvantages as large intraoperative blood loss and strong postoperative pain [2]. Especially for elderly patients who are complicated with cardiovascular, pulmonary, or respiratory diseases, their organ function declines to some extent, and their stress responses to anesthesia and surgery are more remarkable [3, 4]. Some patients resist early functional training due to pain and prolonged lying-bed period, which causes such complications as deep venous thrombosis and pressure ulcers [5]. These complications seriously affect the patients' postoperative recovery. Therefore, it is important to select appropriate anesthetic measures to enhance intraoperative comfort and reduce postoperative pain in elderly patients. According to previous studies, multimodal balanced analgesia has superior effects on elderly patients [6]. Multimodal balanced analgesia is not only the simple combination of different anesthetic drugs but also refers to the combined use of analgesic drugs or analgesic methods with different mechanisms of action. These drugs or methods have complementary effects due to different mechanisms of action, which can play an analgesic or synergistic effect. At the same time, the reduced dose of each drug can effectively alleviate side effects to meet the maximum ratio of effects to side effects and maintain a dynamic balance. This analgesia has been widely used in clinic in recent years. General anesthesia, lumbar plexus block analgesia, combined spinal-epidural anesthesia, local infiltration anesthesia, and patient-controlled analgesia pump are all common multimodal analgesic methods. General

anesthesia, as a traditional type of anesthesia, has the advantages of high comfort and mild stress response but is likely to suppress the patients' respiratory function. Combined spinal-epidural anesthesia can compensate for the disadvantages of general anesthesia but applying anticoagulant drugs in elderly patients during the perioperative period increases the risk of epidural analgesia. Lumbar plexus block analgesia only acts on the peripheral area of the nerves and does not affect the sympathetic nerve, so it is conducive to maintaining hemodynamic stability. However, when the range of hip replacement extends the lumbar plexus, it is needed to combine the lumbar plexus block analgesia with other types of anesthesia in practice [7, 8]. Local infiltration anesthesia refers to the stratified injection of local anesthetics along the surgical incision line to block the nerve endings in tissues. This anesthesia, with higher security and effectiveness, can effectively relieve the patients' early postoperative pain, decrease their dosage of opioids, and reduce the occurrence rate of complications [9]. At present, there are studies reporting the effect of the combination of local infiltration anesthesia, general anesthesia, and patient-controlled analgesia pump, but there is still a gap in the study on the application of local infiltration anesthesia combined with lumbar plexus block or combined spinal-epidural anesthesia in hip replacement. It is still unclear in academic circles which type of analgesia is more beneficial to reduce elderly patients' stress responses. Based on this, this paper investigates the effects of lumbar plexus block combined with infiltration anesthesia on elderly patients undergoing hip replacement, aimed at providing a theoretical basis for the clinical application of this anesthesia method.

2. Materials and Methods

2.1. Research Design. This was a retrospective study conducted in our hospital from January 2020 to January 2021, aimed at investigating the effects of lumbar plexus block combined with infiltration anesthesia on the anesthesia comfort scores and stress responses in elderly patients undergoing hip replacement. The study adopted the double-blind method, so neither the study subjects nor the investigators were aware of the trial grouping, and none of the subjects knew which group they belonged to, and the study designers were responsible for arranging and controlling all the trials.

2.2. General Data. This study included 100 patients, and they were equalized into experimental group and control group according to the anesthesia methods, with 50 patients in each group. The experimental group received lumbar plexus block combined with infiltration anesthesia, and the control group received combined spinal-epidural anesthesia combined with infiltration anesthesia.

Inclusion criteria are as follows: (1) Patients had received medical treatment, had no anesthesia contraindications and no allergic history to anesthetic drugs, and met the indications of hip surgery for elderly patients [10]; (2) patients had no history of hip replacement; (3) patients were over 60 years old; (4) patients were treated at our hospital for the whole course and had complete clinical data; (5) patients had no serious complications and all complications could be effectively controlled; and (6) patients were in the American Society of Anesthesiologists (ASA) [11] grades I-III.

Exclusion criteria are as follows: (1) Patients could not communicate with others because of hearing impairment, language handicap, unconsciousness, mental illness, or other factors; (2) patients had severe organic lesions or serious dysfunction of important organs; (3) patients were under 60 years old; (4) patients' clinical data were lack or lost; (5) patients had surgical contraindications; (6) patients had allergic history to anesthetic drugs; (7) patients suffered from the parasecretion of the adrenal cortex; (8) time from the happening of hip joint fracture to receiving hip replacement was more than 14 days; and (9) patients suffered from multiple fractures.

After collecting, analyzing, and comparing the patients' sociodemographic data and clinical data, no remarkable difference in general data between the two groups was found, and the patients in the two groups could be taken as the study objects, as illustrated in Table 1.

2.3. Moral Consideration. This study conformed with the principle of the *Declaration of Helsinki (2013)* [12]. The patients were informed of the contents, significance, purposes, and confidentiality of this study and signed the informed consent.

2.4. Methods. The experimental group received lumbar plexus block combined with infiltration anesthesia. (1) Lumbar plexus block: the diseased side was given the ultrasound-guided (GE Healthcare, Voluson P6, NMPA (I) 20152062178) lumbar plexus block by using the out-of-plane technology with the longitudinal scan. After positioning, the needle was inserted in the middle of the ultrasound probe. When the needle tip was observed to be beyond the transverse process, the anesthetist should confirm that there was no blood after pumpback. After that, 25 ml of anesthetic drugs, 0.5% ropivacaine (Guangdong Jiabo Pharmaceutical Co., Ltd., NMPA approval no. H20113381) and 1.0% lidocaine (Jumpcan Pharmaceutical Group Co., Ltd., NMPA approval no. H32023273), were injected. At first, 5 ml of anesthetic drugs were injected and the patients were observed for 3 minutes. Then, the remaining drug was injected around the lumbar plexus when the ultrasound showed no indication of arterial and venous blood flow next to the puncture needle and the patient had no adverse reaction. After successfully operating the nerve block, the patients received 0.5 μg/kg of dexmedetomidine (Jiangsu Hengrui Medicine Co., Ltd., NMPA approval no. H20090248) by intravenous infusion for 10 minutes. When the patients fell asleep, they inhaled sevoflurane through a laryngeal mask and continued to receive 0.3-0.5 μg/(kg·h) of dexmedetomidine by intravenous infusion until 0.5 hours before the end of surgery. (2) Infiltration anesthesia: after fitting the prosthesis, the patients were given 2.5 g (80 ml) of ropivacaine (containing 0.1 mg of epinephrine) by infiltration injecting around the articular capsule and incision before suturing the articular capsule. Then, the incision was closed

Table 1: Comparison of the general data.

Groups	Experimental group ($n = 50$)	Control group ($n = 50$)	χ^2/t	P
Male/female	30/20	28/22	0.164	0.685
Age (years old)	70.32 ± 5.28	70.76 ± 5.32	0.415	0.679
Body weight (kg)	64.65 ± 2.55	65.01 ± 2.47	0.717	0.475
BMI (kg/m^2)	22.68 ± 2.41	22.74 ± 2.68	0.118	0.907
ASA grades				
I	12	10	0.233	0.629
II	28	27	0.040	0.841
III	10	13	0.508	0.476
Complications				
Hypertension	20	18	0.170	0.680
Diabetes	15	16	0.047	0.829
Chronic obstructive pulmonary disease	8	10	0.271	0.603
Cerebral infarction	5	4	0.122	0.727
Others	8	10	0.271	0.603
Surgical approach			0.040	0.841
Internal fixation surgery	25	26		
Noninternal fixation surgery	25	24		
Month income (yuan)			0.041	0.839
≥4000	21	20		
<4000	29	30		
Education level			0.407	0.523
Senior high school and below	35	32		
College and higher	15	18		
Payment manner of medical expenses				
Medical insurance	18	20	0.170	0.680
Commercial insurance	20	22	0.164	0.685
Self-pay and others	12	8	1.000	0.317
Place of residence			0.040	0.841
Urban area	28	27		
Rural areas	22	23		

layer by layer after placing a plasma drainage tube in the anterior iliac region.

The control group received combined spinal-epidural anesthesia combined with infiltration anesthesia. The approaches of infiltration anesthesia were the same as those in the experimental group, and the steps of conducting combined spinal-epidural anesthesia were as follows. Half an hour before the surgery, the patients were given 10 mg of diazepam (Biozen Pharmaceutical Co., Ltd., NMPA approval no. H41023114) and 0.5 mg of atropine (Grandpharma (China) Co., Ltd., NMPA approval no. H42021922). The operating table was adjusted to a head-high and foot-low position, and the two-point puncture method was adopted to treat the patients with epidural puncture tubes and punctures in spinal subarachnoid space. Then, 2.0% lidocaine was injected at the puncture points of L_1-L_2 or T_{12}-L_1, and the mixed liquor of 1 ml of 100% glucose solution and 2 ml of 0.5% bupivacaine (Zizhu Pharmaceutical Co., Ltd., NMPA approval no. H11020426) were injected at the L_2-L_3 puncture points. After the anesthesia, the patients took the horizontal position and the anesthetic plane was adjusted accordingly. If the spinal anesthesia could not meet the requirement for the surgical anesthetic plane, the patients would receive epidural administration.

All the patients were fasted routinely before surgery and given routine monitoring and a nasal catheter to inhale oxygen when entering the operation room. When the blood pressure of the patients in the two groups elevated or decreased by more than 30.0% of the base value, they were intravenously injected with 0.5-2.0 μg/kg of nitroglycerin (Chuangchun Yishenkang Biopharmaceutical Co., Ltd., NMPA approval no. H22021894) and 1-2 μg/kg of dopamine (Second Pharma Co., Ltd., NMPA approval no. H11020137), respectively.

2.5. Observational Indexes

(1) The general data included patients' sex, age, body weight, body mass index (BMI), ASA grade, complications (hypertension, diabetes, chronic obstructive

pulmonary disease, cerebral infarction and others), surgical approach (internal fixation surgery and non-internal fixation surgery), monthly income, education level, payment manner of medical expenses, and place of residence

(2) The anesthesia comfort score was 0-10 points, with 0 as feeling comfortable and 10 as feeling the most uncomfortable. The patients' mood change (pain expression), shivering response, and traction reaction were observed, and the patients' anesthesia comfort was scored according to the scale of marks

(3) Stress responses: venous blood (5 ml) was collected from each patient before anesthesia (T_1), and at the end of surgery (T_2), and 12 hours after surgery (T_3). The blood glucose meter (Bayer Healthcare Company Limited, NMPA Certified No. 20092402599) was adopted to determine the patients' blood glucose levels. The enzyme-linked immunosorbent assay was adopted to determine the patients' cortisol levels and catecholamine levels, and the high-performance liquid chromatography electrochemical method was adopted to determine their norepinephrine levels. All the kits were bought from Beijing Kewei Clinical Diagnostic Reagent Inc., and the operations were conducted in strict accordance with the instructions

(4) Postoperative pain indexes: the numerical rating scale (NRS) [13] was adopted to evaluate the patients' pain indexes at 12 (T_3) and 24 hours after surgery (T_4). This scale used the numbers 1-10 to present pain degrees. Namely, a straight line was equally divided into 10 segments, and 1-10 points were plotted from low to high, with 0 as no pain and 10 as severe pain that makes the patients unable to fall asleep

2.6. Statistical Treatment. The statistical software SPSS 20.0 was adopted for data processing and GraphPad Prism 7 (GraphPad Software, San Diego, USA) was used to draw graphs of the data in this study. This study included count data and measurement data, which were tested by χ^2 and t. When $P < 0.05$, the differences were considered statistically significant.

3. Results

3.1. Comparison of the General Data. No statistical difference in patients' general data was found between the two groups ($P > 0.05$; Table 1).

3.2. Comparison of the Anesthesia Comfort Scores. Compared with the control group, the experimental group achieved much lower scores of mood change, shivering response, and traction reaction ($P < 0.001$), indicating that the anesthesia comfort in the experimental group was higher (Figure 1).

The experimental group achieved much lower scores of mood change, shivering response, and traction reaction compared with the control group (3.80 ± 0.72 vs. 6.76 ± 0.74, 3.76 ± 0.74 vs. 6.68 ± 0.68, and 3.74 ± 0.80 vs. 6.74 ± 0.77; $P < 0.001$).

3.3. Comparison of the Stress Responses. Compared with the control group, the experimental group had much better perioperative stress response indexes ($P < 0.05$; Figure 2).

No remarkable difference in blood sugar levels at T_1 between the experimental group and the control group was found (6.15 ± 0.45 vs. 6.18 ± 0.44, $P = 0.737$). The experimental group achieved much lower blood sugar level at T_2 compared with the control group (6.80 ± 0.54 vs. 8.67 ± 0.65, $P < 0.001$). The experimental group achieved much higher blood sugar level at T_3 compared with the control group (6.19 ± 0.54 vs. 6.01 ± 0.24, $P = 0.034$).

No remarkable difference in cortisol levels at T_1 between the experimental group and the control group was found (70.65 ± 2.14 vs. 70.67 ± 2.35, $P = 0.965$). The experimental group achieved much lower cortisol levels at T_2 and T_3 compared with the control group (74.65 ± 2.47 vs. 84.98 ± 2.58, 71.11 ± 2.65 vs. 74.68 ± 2.57; $P < 0.001$).

No remarkable difference in catecholamine levels at T_1 between the experimental group and the control group was found (349.65 ± 8.41 vs. 349.44 ± 8.65, $P = 0.902$). The experimental group achieved much lower catecholamine levels at T_2 and T_3 compared with the control group (370.65 ± 8.41 vs. 410.98 ± 8.74, 349.65 ± 8.74 vs. 355.94 ± 8.41; $P < 0.001$).

No remarkable difference in norepinephrine levels at T_1 between the experimental group and the control group was found (254.75 ± 4.68 vs. 254.80 ± 4.69, $P = 0.958$). The experimental group achieved much lower norepinephrine levels at T_2 and T_3 compared with the control group (370.65 ± 5.65 vs. 392.65 ± 5.74, 332.21 ± 5.98 vs. 369.65 ± 5.741; $P < 0.001$).

3.4. Comparison of Postoperative Pain Indexes. The experimental group had much lower pain scores at 12 (T_3) and 24 (T_4) hours after surgery compared with the control group (2.08 ± 0.72 vs. 2.50 ± 0.75, 1.22 ± 0.41 vs. 1.62 ± 0.69; $P = 0.005$ and 0.001).

4. Discussion

The World Health Organization lists pain as the fifth vital sign of the human body [14]. Intense pain seriously affects the patients' physical and mental health by inhibiting the normal function of many systems, like respiratory and cardiovascular systems. Clinical practice has shown that patients undergoing hip replacement feel moderate and severe pain after surgery [15]. Especially at 24 hours after the surgery, the patients feel more obvious pain. Besides, the surgery and anesthesia make them feel fearful, so they are loath to cooperate with the functional rehabilitation training, which is not conducive to their early recovery after surgery [16]. The compensatory capacity and organ function of elderly patients undergoing hip replacement have declined, and the noxious stimulation from anesthesia and surgery on such capacity and function is more obvious.

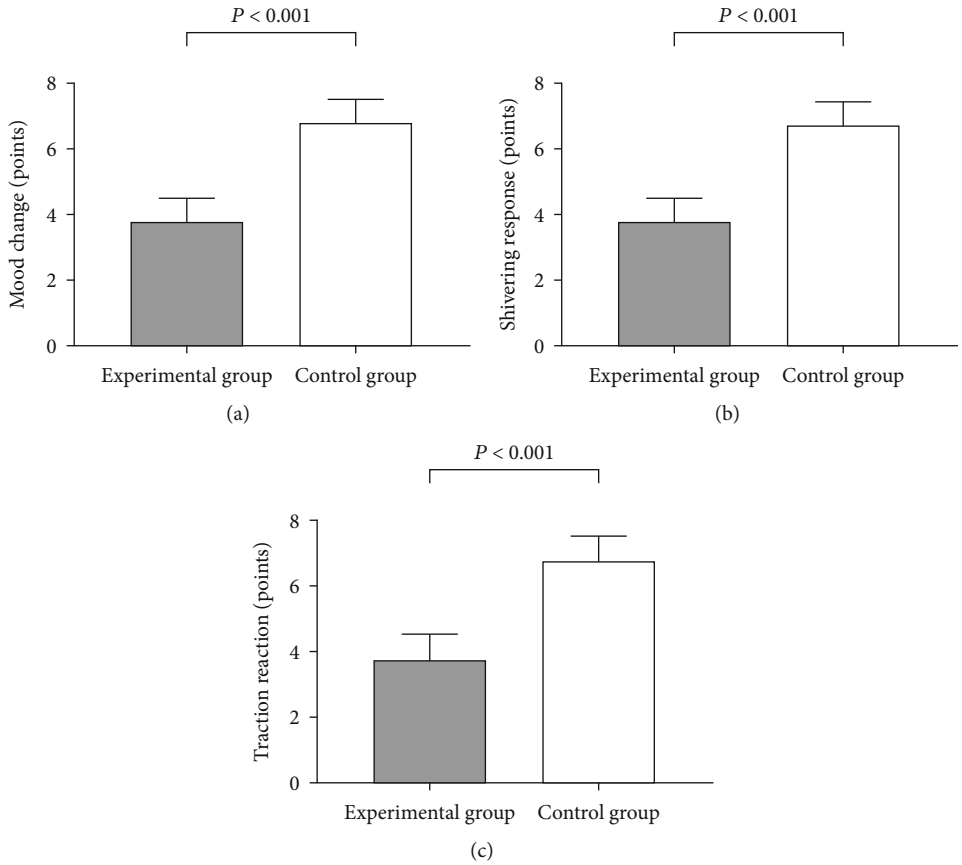

Figure 1: Comparison of the anesthesia comfort scores ($x \pm s$, points). Notes: (a) the comparison of mood changes, (b) the comparison of shivering responses, and (c) the comparison of traction reactions.

Besides, the intense stress response further increases the patients' physical and mental burden [17]. A stress response is a general adaptation syndrome that occurs when the organism is exposed to noxious stimulation. A moderate stress response is beneficial to maintain the stability of the intraoperative vital signs, while the excessive stress response can lead to the dysfunction of neurological, endocrine, and immune systems and cause serious complications. Therefore, reducing the stress responses of elderly patients undergoing hip replacement has important implications in relieving their postoperative pain and speeding up their recovery.

Anesthesia is a key element that affects the stress response, and different types of anesthesia and anesthetic drugs have different effects on the stress response [18, 19]. Multimodal balanced analgesia is a relatively advanced analgesic method, aimed at exerting comprehensive analgesic effects by adopting multiple types of anesthesia and anesthetic drugs. Multimodal balanced analgesia has been applied in hip replacement, but different routes of administration and drugs are used in patients, so the effects on reducing stress response are various [20, 21]. The lumbar plexus block selected in this study is a commonly used anesthetic method in hip replacement, and it is more conducive to reducing hemodynamic fluctuations and effectively maintaining the stability of elderly patients' signs compared with general anesthesia and intraspinal block. With the development of ultrasound technology in recent years, physicians have a better grasp of the structure of the target nerves and the routes of the puncture needle, so success rates of puncture and injection have increased substantially [22]. It is worth noting that hip surgery affects the areas beyond the lumbar plexus, so the lumbar plexus block alone is likely to cause discomfort and needs to be combined with sedation. However, elderly patients are likely to develop respiratory depression with excessive sedation [23], so the lumbar plexus block should be applied in combination with other more effective analgesia methods. This study combined dexmedetomidine with local infiltration anesthesia, which anesthetizes the injection site by local injection and is conducive to reducing postoperative incision pain. According to the study of scholars Brendan et al., the application of the multimodal analgesia regimen which takes the local infiltration anesthesia as the core in total hip replacement effectively reduces the dosage of opioids after surgery [24] and accelerates the patients' recovery.

According to this study, the local infiltration anesthesia with lumbar plexus block was more effective than the combination of combined spinal-epidural anesthesia and infiltration anesthesia, and the patients in the experimental group had better anesthesia comfort. The reasons for the above study result are as follows. For elderly patients, their

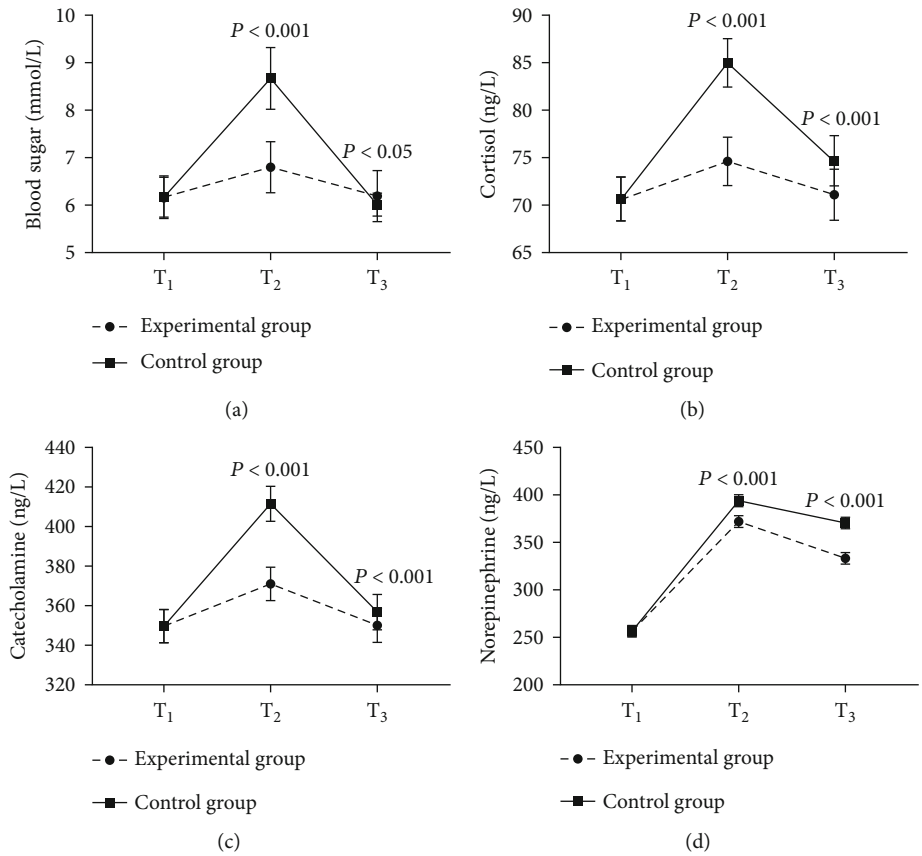

Figure 2: Comparison of the stress responses ($x \pm s$). Notes: (a) the comparison of blood sugar levels (mmol/l), (b) the comparison of cortisol levels (ng/l), (c) the comparison of catecholamine levels (ng/l), and (d) the comparison of norepinephrine levels (ng/l).

arachnoid villi are increased and their nerve roots are compressed, so the connective tissue proliferation leads to foraminal stenosis. As a result, it is difficult to control the upper bound of block levels of spinal anesthesia, and it is likely to have too high block levels. At the same time, the patients' blood vessels are dilated after anesthesia, and their hemodynamic changes are more obvious, which affects their respiratory and circulatory functions. Therefore, the patients receiving combined spinal-epidural anesthesia have lower comfort compared with the patients receiving lumbar plexus block. The single lumbar plexus block can block the affected limb and has less impact on the circulation, so the patient has fewer hemodynamic fluctuations and more stable signs. The catecholamine level is an important indicator of the body's hemodynamics and stress level. The experimental group had lighter stress responses, so the catecholamine levels in this group were lower. According to scholars Choi et al., elderly patients undergoing lower abdominal surgery who received lumbar plexus block had lower catecholamine levels compared with those who received general anesthesia, indicating that lumbar plexus block has positive effects on maintaining the signs of elderly patients [25]. In addition to catecholamine, blood glucose, cortisol, and norepinephrine also reflect the stress responses. In order to reduce the effect of time on cortin, this study scheduled the surgery for ten o'clock in the morning. It was found that the experimental group achieved remarkably better stress response indexes, indicating that the lumbar plexus block has a definite effect on reducing stress responses and can be applied in elderly patients undergoing hip replacement. This study also has some limitations. Firstly, it did not explore the incidence of adverse reactions in both groups. But in the related studies of elderly patients, anesthesia safety is a topic worthy of discussion. Secondly, this study has a small sample size possibly due to the restrains of patients' actual situation and geographical factors. Thirdly, since the study did not consider geographical factors, the research results may only reflect the situation of hip replacement in the region. Therefore, more subsequent studies should be conducted with an expanded sample size for deeper exploration.

In conclusion, lumbar plexus block combined with infiltration anesthesia can relieve the stress responses and postoperative pain of elderly patients undergoing hip replacement and increase their anesthesia comfort. Therefore, this anesthesia method is translational in clinic.

Data Availability

Data to support the findings of this study is available on reasonable request from the corresponding author.

Conflicts of Interest

The authors have no conflicts of interest to declare.

Authors' Contributions

Jizheng Zhang and Yi Li contributed equally to this work.

References

[1] M. D. Neuman, N. M. Elkassabany, J. Ochroch et al., "Nerve block use after hip fracture versus elective hip or knee arthroplasty: retrospective analysis," *Journal of the American Geriatrics Society*, vol. 68, no. 4, pp. 835–840, 2020.

[2] L. Xu, J. C. Leng, H. Elsharkawy et al., "Replacement of fascia iliaca catheters with continuous erector spinae plane blocks within a clinical pathway facilitates early ambulation after total hip arthroplasty," *Pain Medicine*, vol. 21, no. 10, pp. 2423–2429, 2020.

[3] T. J. Rajamäki, P. A. Puolakka, A. Hietaharju, T. Moilanen, and E. Jämsen, "Use of prescription analgesic drugs before and after hip or knee replacement in patients with osteoarthritis," *BMC Musculoskeletal Disorders*, vol. 20, no. 1, p. 427, 2019.

[4] S. Claude, "Enhanced recovery after posterior minimally invasive total hip arthroplasty with continuous intraarticular anaesthesia," *European Journal of Orthopaedic Surgery & Traumatology*, vol. 28, no. 5, pp. 761–769, 2018.

[5] V. Romano and J. Hou, "Implications of regional anesthesia in a patient with lymphangioleiomyomatosis (LAM) undergoing right total hip replacement," *Clinical Anesthesia*, vol. 58, pp. 107-108, 2019.

[6] L. P. Hunt, M. R. Whitehouse, P. W. Howard, Y. Ben-Shlomo, and A. W. Blom, "Using long term mortality to determine which perioperative risk factors of mortality following hip and knee replacement may be causal," *Scientific Reports*, vol. 8, article 15026, 2018.

[7] J. Song, Y. Qiao, Q. Zhou, and X. Zhang, "Fascia iliaca compartment block for analgesia in total hip replacement," *Medicine*, vol. 99, no. 37, article e22158, 2020.

[8] S. Panchal, A. D. Jogani, S. S. Mohanty, T. Rathod, P. Kamble, and S. A. Keny, "Is bilateral sequential total hip replacement as safe an option as staged replacement? A matched pair analysis of 108 cases at a tertiary care centre," *Indian Journal of Orthopaedics*, vol. 55, pp. 1250–1255, 2021.

[9] J. Maca, J. Neiser, L. Grasslova, M. Trlicova, D. Streitova, and R. Zoubkova, "Patient-controlled epidural analgesia versus conventional epidural analgesia after total hip replacement - a randomized trial," *Biomedical Papers*, vol. 164, no. 1, pp. 108–114, 2020.

[10] A. U. Katchy, U. E. Anyaehie, C. U. Nwadinigwe, and G. O. Eyichukwu, "Total hip replacement in sickle cell disorder: a preliminary report of challenges and early outcome of 21 consecutive patients," *Nigerian Journal of Clinical Practice*, vol. 21, no. 4, pp. 492–495, 2018.

[11] P. Poredos, A. Mavric, L. Leben, P. Poredos, and M. K. Jezovnik, "Total hip replacement provokes endothelial dysfunction," *Angiology*, vol. 69, no. 10, pp. 871–877, 2018.

[12] World Medical Association, "World Medical Association Declaration of Helsinki: ethical principles for medical research involving human subjects," *JAMA*, vol. 310, no. 20, pp. 2191–2194, 2013.

[13] M. C. Wyatt, J. W. Hozack, C. Frampton, A. Rothwell, and G. J. Hooper, "Is single-anaesthetic bilateral primary total hip replacement still safe? A 16-year cohort study from the New Zealand Joint Registry," *ANZ Journal of Surgery*, vol. 88, no. 12, pp. 1289–1293, 2018.

[14] C.-S. Oh, H. Y. Lim, H. J. Jeon et al., "Effect of deep neuromuscular blockade on serum cytokines and postoperative delirium in elderly patients undergoing total hip replacement," *European Journal of Anaesthesiology*, vol. 38, no. 1, pp. S58–S66, 2021.

[15] X. M. Xu, X. W. Hu, Y. Wu et al., "Effects of different BP management strategies on postoperative delirium in elderly patients undergoing hip replacement: a single center randomized controlled trial," *Journal of Clinical Anesthesia*, vol. 62, article 109730, 2020.

[16] J. B. Hou, X. Wan, B. Zhao, X. D. Wei, Z. Y. Xia, and Y. Wu, "Impact of combined nerve blocks on the outcome of hip replacement in elderly patients with acute cerebral infarction," *Zhonghua Yi Xue Za Zhi*, vol. 101, no. 25, pp. 1968–1972, 2021.

[17] H. Sharma, S. Mitra, J. Singh, S. Gupta, and S. Garg, "A randomized study comparing the efficacy of ultrasound guided lumbar plexus block and epidural anesthesia for postoperative analgesia in patients undergoing total hip replacement," *Asian Journal of Anesthesiology*, vol. 58, pp. 131–137, 2020.

[18] S. Matharu Gulraj, G. Cesar, R. Amar et al., "Does regional anesthesia reduce complications following total hip and knee replacement compared with general anesthesia? An analysis from the National Joint Registry for England, Wales, Northern Ireland and the Isle of Man," *The Journal of Arthroplasty*, vol. 35, no. 6, pp. 1521–1528.e5, 2020.

[19] T. W. Wainwright, M. Gill, D. A. McDonald et al., "Consensus statement for perioperative care in total hip replacement and total knee replacement surgery: enhanced recovery after surgery (ERAS®) society recommendations," *Acta Orthopaedica*, vol. 91, no. 1, pp. 3–19, 2020.

[20] M. Duque, M. P. Schnetz, A. J. Yates et al., "Impact of neuraxial versus general anesthesia on discharge destination in patients undergoing primary total hip and total knee replacement," *Anesthesia & Analgesia*, vol. 133, no. 6, pp. 1379–1386, 2021.

[21] B. S. Sharma, M. W. Swisher, C. N. Doan, B. Khatibi, and R. A. Gabriel, "Predicting patients requiring discharge to post-acute care facilities following primary total hip replacement: does anesthesia type play a role?," *Journal of Clinical Anesthesia*, vol. 51, pp. 32–36, 2018.

[22] S. G. Memtsoudis, C. Cozowicz, J. Bekeris et al., "Anaesthetic care of patients undergoing primary hip and knee arthroplasty: consensus recommendations from the International Consensus on Anaesthesia- Related Outcomes after Surgery group (ICAROS) based on a systematic review and meta-analysis," *British Journal of Anaesthesia*, vol. 123, no. 3, pp. 269–287, 2019.

[23] K. Donauer, H. Bomberg, S. Wagenpfeil, T. Volk, W. Meissner, and A. Wolf, "Regional vs. general anesthesia for total knee and hip replacement: an analysis of postoperative pain

perception from the International PAIN OUT Registry," *Pain Practice*, vol. 18, no. 8, pp. 1036–1047, 2018.

[24] B. Urvoy, C. Aveline, N. Belot, C. Catier, and H. Beloeil, "Opioid-free anaesthesia for anterior total hip replacement under general anaesthesia: the Observational Prospective Study of Opiate-free Anesthesia for Anterior Total Hip Replacement trial," *British Journal of Anaesthesia*, vol. 126, no. 4, pp. e136–e139, 2021.

[25] E.-J. Choi, Y. J. Choi, S. W. Lee et al., "Effect of anesthetic method on incidence of delirium after total hip replacement arthroplasty in South Korea: a population-based study using National Health Insurance claims data," *Korean Journal of Anesthesiology*, vol. 73, no. 1, pp. 36–43, 2020.

Hindawi
Disease Markers
Volume 2022, Article ID 7366576, 5 pages
https://doi.org/10.1155/2022/7366576

Research Article

Analysis of Bone Loss around Cemented and Biologic Prostheses after Hemiarthroplasty

Fan Zhang,[1] Chao Liu,[2] Haibo Xu,[1] Xiafen Zhang,[1] and Hanliang He[1]

[1]*The Department of Orthopedic Surgery, Dushu Lake Hospital Affiliated to Soochow University, Suzhou, 215028 Jiangsu, China*
[2]*The Department of Orthopedic Surgery, Suzhou BenQ Medical Center, The Affiliated BenQ Hospital of Nanjing Medical University, Suzhou, 215000 Jiangsu, China*

Correspondence should be addressed to Hanliang He; hehanliang@sdhmdp.org.cn

Received 9 June 2022; Accepted 24 July 2022; Published 5 August 2022

Academic Editor: Jun Yang

Objective. To perform hemiarthroplasty (HA) on elderly patients with femoral neck fractures using cemented and biologic prostheses and then compare the bone loss around the two types of prostheses after surgery. *Methods*. A total of 60 patients aged over 75 years (with a mean age of 83.5 years) and suffering from femoral neck fracture (Garden types III and IV) from January 2018 to December 2020 were selected; they were randomly divided into group A ($n = 30$, cemented prostheses) and group B ($n = 30$, biologic prostheses) and received HA. At 1 month, 6 months, and 12 months after surgery, Harris Hip Scale (HHS) was adopted for patient evaluation, and patients' bone mineral density (BMD) of the 7 Gruen zones around the prostheses was measured by dual-energy X-ray absorptiometry (DEXA scan). *Results*. Both groups achieved satisfactory results postoperatively, and the Harris scores of the hips increased gradually over time, which were better in group A than in group B. Gruen zones in group A showed a slower trend of decreasing BMD than group B, and the differences were significant at zones 2, 3, and 4 ($P < 0.05$). *Conclusion*. For elderly patients with femoral neck fractures, selecting cemented prosthesis for HA better recovers the hip function and has a low rate of bone loss around the prosthesis.

1. Introduction

Osteoporosis is increasingly recognized as the population ages. Patients with hip fracture caused by osteoporosis need long-term bed rest and have high rates of complications and mortality, resulting in great pressure on medical treatment and society. Currently, among the elderly hip fracture patients in China, the most common is femoral neck fracture, which accounts for 3.6% of all fractures and 45%-54% of hip fractures [1]. Osteoporosis prevention and treatment in elderly patients as well as performing bone mineral density (BMD) screening in a scientific and effective way has become the secondary prevention focus of orthopedics in China in recent years [2]. Currently, nondisplaced femoral neck fractures (Garden types I and II) can achieve satisfactory clinical results through internal fixation [3]; and although optimal treatment of displaced femoral neck fractures (Garden types III and IV) remains controversial, most choose hemiarthroplasty (HA) or total hip replacement. HA is technically simple; has short operation time, less blood loss, and low dislocation rate; and is suitable for elderly patients with displaced femoral neck fractures who have poor physical condition and less activity [4]. The cemented and biologic prostheses are two commonly used types, and the former case, as a mosaic agent, can firmly integrate the metal part of artificial joint with the patients' own bones, with the applied advantages of rapid postoperative recovery and small trauma, but the surgical procedures may damage the nerves, while the latter case with a short surgery time can reduce postoperative complications to a certain extent, but the probability of periprosthetic fracture is higher. Therefore, there is no consensus view on the choice of cemented or biologic prostheses. In this study, by adopting both cemented and biologic prostheses for HA in elderly patients with femoral neck fractures and recording postoperative improvement in hip function and changes in periprosthetic bone density, the clinical outcomes were evaluated.

2. Materials and Methods

2.1. Inclusion and Exclusion Criteria. Inclusion criteria were as follows: (1) the patients were over 75 years old and had femoral neck fractures (Garden types III and IV); and (2) before hospitalization, the patients could walk and carry out activities normally. Exclusion criteria were as follows: (1) the patients were complicated with a history of severe coxitis or rheumatoid arthritis; (2) the patients were complicated with a history of fractures at other sites; and (3) the patients had bone metabolic diseases.

2.2. General Data. A total of 60 patients with femoral neck fracture treated in our hospital from January 2018 to December 2020 were selected and randomly divided into group A ($n = 30$) and group B ($n = 30$); i.e., the samples were selected by the random number table. Experienced joint surgeons performed HA to patients in the two groups with the anesthesia method as tracheal intubation general anesthesia when patients were in lateral position by adopting the rear lateral approach and implanted the cemented and biologic prostheses according to the standard method [5]. After surgery, antibiotics were administered according to the clinical diagnosis and treatment code to prevent infection, deep vein thrombosis was prevented, and rehabilitation functional exercise was conducted. The CoCrMo alloy cemented femoral stem prostheses (morphologically matched type; specification: 127-933; NMPA approval No. 20173466557) were used in group A, and titanium alloy porous-coated cementless stem prostheses (tapered stem; specification: 1-4/129; NMPA approval No. 20203130412) were used in group B. The prostheses were provided by Zimmer (Shanghai) Medical International Trading Co., Ltd., and all patients were reviewed and approved by the Ethics Committee of BenQ Medical Center in Suzhou.

2.3. Evaluation Methods. The clinical data such as body mass index (BMI), surgery time, and hospitalization time were recorded, and the incidence of postoperative complications was counted. At 1 month, 6 months, and 12 months after surgery, follow-up visit was carried out, patients' Harris Hip Scale (HHS) scores were recorded, including four aspects of function, pain, malformation, and joint motion with a full score of 100 points in this scale and the score above 90 as excellent, 80-90 as better, 70-79 as acceptable, and less than 70 as poor, and patients' BMD of the 7 Gruen zones around the prostheses was measured by dual-energy X-ray absorptiometry (DEXA scan) for 3 times.

2.4. Statistical Analysis. Software SPSS 17.0 was used for data analysis, continuous variables were expressed as mean ± standard deviation, quantitative data that conformed to normal distribution were assessed by paired sample t-test, and those that have skewed distribution were assessed by Mann–Whitney U test at the test level $\alpha = 0.05$, and differences were considered statistically significant at $P < 0.05$.

3. Results

3.1. Comparison of General Data. The patients' BMI and age were not statistically different between the two groups (see Table 1). The mean surgery time of group A was 70.13 ± 3.50 min, which was obviously higher than that of group B (52.52 ± 3.60 min, $P < 0.001$). No statistically significant difference on the mean hospitalization time between the two groups was observed ($P = 0.443$). A total of 5 patients had postoperative complications, 2 of them were in group A (1 with postoperative lower-extremity deep vein thrombosis and 1 with lung infection), and 3 of them were in group B (1 with postoperative lower-extremity deep vein thrombosis and 2 with urinary tract infection). All complications were cured after active treatment.

3.2. Postoperative Evaluation of Hip Joint Function. At 1 month, 6 months, and 12 months after surgery, the Harris scores of the hips increased gradually over time in the two groups. At postoperative 1 month, the Harris scores of patients in group A and group B were, respectively, 65.74 ± 5.32 points and 63.43 ± 5.76 points, presenting no statistical difference ($P = 0.112$), and at postoperative 6 months and 12 months, the Harris scores were better in group A than in group B. At postoperative 12 months, the Harris scores of group A and group B were, respectively, 84.56 ± 6.70 points and 80.29 ± 7.08 points, which reached a satisfied level (see Table 2).

3.3. Comparison of DEXA Analysis Results. Periprosthetic BMD loss was measured on 3 consecutive DEXA scans in all 7 Gruen zones, with group B specifically showing the highest degree of BMD loss in zone 7. The change in mean periprosthetic BMD values was different between groups A and B, with a slower trend towards lower BMD values in the Gruen zones in group A compared to group B using biologic prostheses. Such difference was statistically significant in zones 2, 3, and 4 ($P < 0.05$, see Table 3).

4. Discussion

Femoral neck fracture is a common type of fracture, and the pathogenic factors include osteoporosis, trauma, and femoral neck bone cyst. At present, there is a certain consensus on the application of HA in elderly patients with femoral neck fractures. The surgery can make patients achieve early ambulation, better solve the symptoms of hip joint pain and claudication caused by femoral head necrosis, avoid related complications caused by long-term bed rest, improve patients' QOL, and reduce family burden [5]. The controversy lies in the choice of the type of prosthesis in the surgical treatment of HA in elderly patients with femoral neck fractures. Periprosthetic stability is a key factor in the recovery and maintenance of postoperative hip function, and aseptic loosening of the bone-prosthesis interface is an important cause of postoperative pain, prosthesis loosening, and even periprosthetic fracture [6], and such loosening may be associated with periprosthetic bone loss. Bone loss after trauma and fracture surgery has been a research hotspot, and the rate of bone loss is influenced not only by friction-mediated osteolysis and stress shielding but also by the

Table 1: Between-group comparison of patients' general data.

Group	N (cases)	Age (years)	BMI (kg/m^2)	Surgery time (min)	Hospitalization time (d)
A	30	77.41 ± 5.65	22.64 ± 4.32	70.13 ± 3.50	8.82 ± 1.25
B	30	78.32 ± 4.73	21.37 ± 3.53	52.52 ± 3.60	8.52 ± 1.72
t	—	0.676	1.247	19.210	0.773
P	—	0.501	0.217	<0.001	0.443

Table 2: Between-group comparison of patients' postoperative Harris scores.

Postoperative Harris score	Group A	Group B	t	p
1 month	65.74 ± 5.32	63.43 ± 5.76	1.614	0.112
6 months	72.45 ± 6.53	67.23 ± 5.41	3.372	0.001
12 months	84.56 ± 6.70	80.29 ± 7.08	2.399	0.020

Table 3: Changes in mean BMD in the Gruen zones between the two groups at postoperative 1, 6, and 12 months.

Gruen zone	Group	1 month after surgery			6 months after surgery			12 months after surgery		
		(g/cm^2)	t	P	(g/cm^2)	t	P	(g/cm^2)	t	P
R1	A	0.633 ± 0.110	0.407	0.685	0.595 ± 0.098	1.464	0.149	0.583 ± 0.001	1.962	0.071
	B	0.621 ± 0.118			0.557 ± 0.103			0.547 ± 0.021		
R2	A	1.417 ± 0.120	1.751	0.086	1.388 ± 0.125	2.649	0.01	1.305 ± 0.129	2.958	0.040
	B	1.351 ± 0.168			1.278 ± 0.190			1.194 ± 0.160		
R3	A	1.488 ± 0.126	2.284	0.026	1.456 ± 0.097	3.050	0.003	1.403 ± 0.114	3.679	0.001
	B	1.406 ± 0.151			1.347 ± 0.170			1.277 ± 0.149		
R4	A	1.615 ± 0.101	4.192	0.026	1.574 ± 0.106	3.765	<0.001	1.521 ± 0.136	4.146	<0.001
	B	1.489 ± 0.130			1.456 ± 0.135			1.377 ± 0.133		
R5	A	1.578 ± 0.128	0.335	0.738	1.555 ± 0.125	0.031	0.976	1.482 ± 0.136	0.339	0.736
	B	1.589 ± 0.126			1.556 ± 0.128			1.470 ± 0.138		
R6	A	1.364 ± 0.137	0.302	0.764	1.332 ± 0.130	0.406	0.686	1.275 ± 0.140	1.030	0.307
	B	1.375 ± 0.145			1.317 ± 0.155			1.234 ± 0.167		
R7	A	0.698 ± 0.134	1.550	0.127	0.676 ± 0.138	0.291	0.772	0.584 ± 0.112	1.245	0.218
	B	0.746 ± 0.104			0.666 ± 0.128			0.545 ± 0.130		

induction of osteoporosis with posttraumatic physiological alterations, thereby causing implant loosening [7]. Relevant studies have shown that the severity of trauma, intraoperatively excessive periosteal and vascular injury, and the level of functional recovery of the limb after surgery directly affect the extent of bone loss. In this study, 60 elderly patients with femoral neck fracture in our hospital were included as the study subjects, and all patients were treated with HA. The clinical application value of cemented and biologic prostheses was comprehensively evaluated by estimating the hip joint function and BMD values of two groups. By analyzing Table 1, it is found that there was no significant difference in clinical data such as age and BMI values between the two groups in addition to the surgery time ($P > 0.05$), which laid the foundation for the subsequent studies. In this study, trauma and surgical injuries were more similar between the two groups, but follow-up revealed some differences in patients' functional recovery outcomes, which might be associated with periprosthetic bone loss. The implanted biologic prosthesis was relatively unstable, possibly leading to postoperative pain, hindering patients' weight-bearing activity, and then affecting bone repair and resulting in low bone mass [8]. As Knutsen et al. reported [9], after total hip replacement surgery for patients with osteoarthritis of the hip using cemented and biologic prostheses, the degree of periprosthetic bone loss was different, which was obviously higher in biologic prostheses than in cemented prostheses, and the result was consistent with the study herein. In another study, quantitative computed tomography (QCT) measurements of BMD were performed after surgery in patients with femoral neck fractures of Garden types III and IV and hip osteoarthritis, and the Harris score was

significantly lower, and bone loss was more obvious in the femoral neck fracture group compared with the hip osteoarthritis group. According to the study by Sinaki et al. [10], patients with femoral neck fracture more easily have bone mass loss after surgery, and such difference in bone mass loss is mainly caused by different functional recovery after surgery. Weight-bearing is an important driving force for bone formation, while dysfunction and non-weight-bearing are closely related to bone resorption. Good filling of the medullary cavity is an important factor for optimal weight-bearing stability of the prosthesis, whereas tight press-fit and solid initial fixations are essential requirements for achieving good long-term outcomes of the prosthesis, and long-term follow-up studies have found that patients achieve initial press-fit fixation by bone ingrowth or fibrous stable fixation in the proximal femur and isthmus [11]. The initial stability is very important, and the precise preparation of the femoral medullary cavity is an important factor to ensure the long-term stability of cementless prostheses. Elderly patients have osteoporosis with thinner femoral cortical and enlarged volume of the medullary cavity, it is not advisable to increase the template model blindly and sequentially during surgery, and C-arm X-ray fluoroscopy should be used to understand the filling rate of the prosthesis in the femoral medullary cavity when necessary. In addition, precise reaming helps to prevent the occurrence of anterior femoral fracture at the insertion of prosthesis and guarantees close contact between bone and prosthesis. Intraoperatively, when a suitable femoral template is punched to achieve a defined depth, C-arm X-ray fluoroscopy is performed to understand its position, depth, and fill rate in the medullary cavity, thus ensuring a good position and fill rate in the medullary cavity after prosthesis implantation. Cemented prostheses can be strongly bonded at the bone-prosthesis interface, offering a better biomechanical stabilization [12].

The cemented prosthesis can form the tiny noose with the surrounding residual cancellous bone and then firmly fix the prosthesis, which is helpful to maintain the initial stability of this prosthesis, with a relatively low risk of splitting in proximal femur during the implantation of prosthesis, and it can be completely filled with the marrow cavity to prevent the violent injury of the femoral stem prosthesis during the implantation. In addition, the biologic prosthesis can also carry out the coverage of bone cement according to the patients' anatomical structure of femur and leg length to make the prosthesis in the best position, but it cannot completely match the femur, so the effect of cemented prosthesis is better. In this study, Harris hip scores increased gradually in both groups at three follow-up visits after surgery, but the scores of the cemented prosthesis group were significantly higher than those of the biologic prosthesis group. Compared with the cemented prosthesis group, the reduction in BMD in the biologic prosthesis group was greater in all zones, with the most significant reductions in zones 2, 3, and 4. This difference may be because patients who underwent HA using cemented prostheses were able to achieve better functional recovery and weight-bearing exercises. Naturally, there are also disadvantages of using cemented prostheses for elderly patients, such as high risk of cardiopulmonary complications, long operation time, high technical requirements for surgery, and difficulties in secondary revision surgery [13]. And during the procedure, the use of cemented prosthesis implantation may increase the occurrence of periprosthetic fracture, air embolism, hypotension, and other complications [14]. Recently, studies have shown that with the advancement of medical devices as well as the improvement of surgical techniques, the incidence of the above complications has significantly decreased [15]. Compared with the use of biological prostheses in this study, the use of cemented prostheses increased surgery time by an average of 18 minutes, but the mean time of hospitalization and the incidence of postoperative related complications did not differ significantly between the two groups. Cemented prostheses have previously been documented to be preferred for the treatment of osteoporotic femoral neck fractures, but no further studies were performed [16]. Through the quantitative measurement of BMD, it is believed that cemented prostheses can provide early stabilization of the prosthesis-bone interface, which is good for functional recovery and reducing periprosthetic bone mass loss. Despite the constant progress of medical technology, there are still many difficulties in the treatment of femoral neck fractures, so that more efficient diagnosis and intervention modes need to be explored constantly by medical workers to provide more reliable basis for the treatment of femoral neck fractures. The contributions of this study were as follows. The application of the two types of prosthesis in HA was deeply understood by comparing the cemented and biologic prostheses, with a major progress and development in clinic and an extensive guiding significance in orthopedic treatment, which undoubtedly becomes the development direction of future medicine.

However, this study also has shortcomings that would affect the study results, such as the relatively small sample size, the differences in individual samples and prosthetic factors (the type of fracture, the preoperative osteoporosis condition, the impact of prosthetic model and geometry on stress shielding, etc.), and the differences in the surgical approach among the surgeons. Therefore, more prospective controlled studies are needed in the future.

Data Availability

Data to support the findings of this study is available on reasonable request from the corresponding author.

Conflicts of Interest

The authors do not have conflicts of interest to declare.

Acknowledgments

This research was funded by 2021 Suzhou Science and Technology Development Plan (medical and health science and technology innovation-Applied Basic Research), grant number SKJY2021027. This research was funded by Open project of National Local Joint Engineering Laboratory for New Functional Polymers in 2021, grant number SDGC2113.

References

[1] Y. Z. Zhang, *Clinical Epidemiology of Orthopedic Trauma*, People's Medical Publishing House, Beijing, 2014.

[2] The Chinese medical association of osteoporosis and bone mineral disease, "Chinese," *Journal of Practical Internal Medicine*, vol. 2018, no. 2, pp. 127–150, 2017.

[3] C. R. Schwartsmann, H. M. Lammerhirt, L. D. F. Spinelli, and A. S. Ungaretti Neto, "Treatment of displaced femoral neck fractures in young patients with DHS and its association to osteonecrosis," *Revista Brasileira de Ortopedia*, vol. 53, no. 1, pp. 82–87, 2018.

[4] T. Yagura, K. Oe, M. Paku et al., "A Possible Protective Effect of the'Cam Deformity'on Femoral Neck Fracture: The Relationship between Hip Morphology and the Types of Hip Fracture," *Acta Medica Okayama*, vol. 74, no. 3, pp. 221–227, 2020.

[5] R. Russo, A. Cozzolino, A. Guastafierro et al., "Use of 3D planning and patient-specific guides for proximal humerus corrective osteotomy associated with shoulder prosthesis implantation in proximal humeral varus malunion," *Techniques in Hand & Upper Extremity Surgery*, vol. 26, no. 2, pp. 131–138, 2022.

[6] D. Vidovic, A. Matejcic, M. Punda et al., "Periprosthetic bone loss following hemiarthroplasty: a comparison between cemented and cementless hip prosthesis," *Injury*, vol. 44, pp. S62–S66, 2013.

[7] B. Cortet, A.-M. Schott, G. Désaméricq et al., "Trends in postmenopausal osteoporosis treatment in France during the period 2007-2016: A nationwide claims database analysis," *Bone*, pp. 154–116255, 2022.

[8] H. T. Aro, S. Nazari-Farsani, M. Vuopio, E. Löyttyniemi, and K. Mattila, "Effect of denosumab on femoral periprosthetic BMD and early femoral stem subsidence in postmenopausal women undergoing cementless total hip arthroplasty," *JBMR Plus*, vol. 3, no. 10, article e10217, 2019.

[9] A. R. Knutsen, N. Lau, D. B. Longjohn, E. Ebramzadeh, and S. N. Sangiorgio, "Periprosthetic femoral bone loss in total hip arthroplasty: systematic analysis of the effect of stem design," *Hip International*, vol. 27, no. 1, pp. 26–34, 2017.

[10] M. Sinaki, M. Pfeifer, E. Preisinger et al., "The role of exercise in the treatment of osteoporosis," *Current Osteoporosis Reports*, vol. 8, no. 3, pp. 138–144, 2010.

[11] Q. Cui, Y. S. Liu, D. F. Li et al., "Cemented hip hemiarthroplasty clinical observations on unstable intertrochanteric fracture in elderlies," *European Journal of Trauma and Emergency Surgery*, vol. 42, no. 5, pp. 651–656, 2016.

[12] E. Langslet, F. Frihagen, V. Opland, J. E. Madsen, L. Nordsletten, and W. Figved, "Cemented versus uncemented hemiarthroplasty for displaced femoral neck fractures: 5-year followup of a randomized trial," *Clinical Orthopaedics and Related Research*, vol. 472, no. 4, pp. 1291–1299, 2014.

[13] M. Q. Guan, Z. X. Zhu, and G. M. Zhou, "Cemented versus cementless hemiarthroplasty for femoral neck fractures in the elderly," *Chinese Journal of Tissue Engineering Research*, vol. 22, no. 7, pp. 991–996, 2018.

[14] A. Klasan, M. Bäumlein, C. Bliemel et al., "Cementing of the hip arthroplasty stem increases load-to-failure force: a cadaveric study," *Acta Orthopaedica*, vol. 90, no. 5, pp. 445–449, 2019.

[15] Y. Okutani, K. Goto, Y. Kuroda et al., "Long-term outcome of cemented total hip arthroplasty with the Charnley-type femoral stem made of titanium alloy," *Journal of Orthopaedic Science*, vol. 24, no. 6, pp. 1047–1052, 2019.

[16] P. Prochor and E. Sajewicz, "A comparative analysis of internal bone remodelling concepts in a novel implant for direct skeletal attachment of limb prosthesis evaluation: A finite element analysis," *Proceedings of the Institution of Mechanical Engineers, Part H: Journal of Engineering in Medicine*, vol. 232, no. 3, pp. 289–298, 2018.

Hindawi
Disease Markers
Volume 2022, Article ID 7294358, 6 pages
https://doi.org/10.1155/2022/7294358

Research Article

Clinical Value of Total Intravenous Anesthesia with Sufentanil and Propofol in Radical Mastectomy

Lingyan Qu[1] and Xiaoqing Wu[2]

[1]*Department of Anesthesiology, Yantaishan Hospital, Yantai, 264000 Shandong, China*
[2]*Department of Radiotherapy, Central Hospital Affiliated to Shandong First Medical University, Jinan, 250013 Shandong, China*

Correspondence should be addressed to Xiaoqing Wu; wuxiaoqing@jnzxhospital.cn

Received 21 June 2022; Revised 15 July 2022; Accepted 19 July 2022; Published 5 August 2022

Academic Editor: Jianxin Shi

Objective. To investigate the clinical value of sufentanil combined with propofol for total intravenous anesthesia (TIVA) in radical mastectomy. *Methods*. The data of 120 patients undergoing radical mastectomy of breast cancer in our hospital from February 2020 to February 2021 were retrospectively analyzed, and they were randomly assigned to the experimental group (EXG) ($n = 60$) and the control group (COG) ($n = 60$). The anesthesia maintenance scheme was 0.01–0.03 μg/(kg·min) of sufentanil + 80–100 μg/(kg·min) of propofol in EXG and 3 μg/(kg·h) of fentanyl + 80–100 μg/(kg·min) of propofol in COG. The hemodynamic indices, stress indexes, postoperative pain scores, and incidence of adverse reactions were compared between EXG and COG. *Results*. The heart rates (HR) and mean arterial pressure (MAP) after tracheal intubation (T_2) and at separation of deep tissues (T_3), tracheal extubation (T_4), and the end of surgery (T_5) were markedly lower in EXG than in COG ($P < 0.001$). The stress indexes and postoperative pain scores at 1 h (T_6), 6 h (T_7), and 12 h (T_8) after surgery were lower in EXG than in COG ($P < 0.001$). The incidence of dizziness, headache, pruritus, and emergence agitation in EXG was lower compared with that in COG ($P < 0.05$). *Conclusion*. Sufentanil combined with propofol for TIVA can stabilize intraoperative hemodynamic indices of patients undergoing radical mastectomy, alleviate perioperative stress response, and reduce pain perception. Therefore, this anesthesia method is safe and merits clinical promotion.

1. Introduction

Breast cancer (BC) is a type of cancer caused by the uncontrolled proliferation of mammary epithelial cells, and its incidence ranks first among female tumors worldwide [1], with 52.9% occurring in developing countries [2]. As the most populous developing country, China has the highest number of new BC patients in the world each year and the number of patients needing radical mastectomy increases yearly [3, 4]. Since radical mastectomy is a body surface surgery with significant trauma and has a major impact on the respiratory system and circulatory system of patients, there is a clinical need for highly effective anesthesia modalities with good analgesic effects, such as total intravenous anesthesia [5]. Total intravenous anesthesia (TIVA) refers to the combination of multiple intravenous anesthetics after intravenous anesthesia induction to maintain anesthesia by intravenous injection. Propofol is one of the most common TIVA drugs [6, 7], with significant advantages such as rapid onset, rapid postoperative recovery, complete recovery of various system functions, and a low incidence of adverse reactions such as nausea and vomiting. Moreover, its combined use with other anesthetics can further improve the analgesic function and enhance the anesthetic effects. At present, opioids are often combined with propofol in thoracic surgery and neurosurgery, such as fentanyl, sufentanil, and remifentanil [8], in which remifentanil has a strong inhibitory effect on the respiratory system and its comprehensive anesthesia effect is inferior to sufentanil [9]. Fentanyl is an early opioid analgesic with strong analgesic effects and can reduce postoperative delirium [10]. However, not much is known about the combined use of sufentanil and propofol for TIVA and the comparison results of effects between fentanyl and sufentanil remain unclear. Based on

this, this study will explore the application effects of fentanyl combined with propofol and sufentanil combined with propofol for TIVA, trying to provide a reference for clinical practice.

2. Materials and Methods

2.1. Study Design. This retrospective study was conducted in our hospital from February 2020 to February 2021 to explore the clinical application value of sufentanil combined with propofol for TIVA in radical mastectomy of breast cancer.

2.2. General Information. The data of 120 female patients undergoing radical mastectomy in our hospital from February 2020 to February 2021 were retrospectively analyzed, and they were randomly assigned to the experimental group (EXG) ($n = 60$) and the control group (COG) ($n = 60$). The clinical data of both groups were shown in Table 1. No notable differences were found in the general data between EXG and COG ($P > 0.05$).

Inclusion criteria are as follows: (1) patients were diagnosed with BC by pathological examination [11], (2) patients had indications for radical mastectomy, (3) patients were treated in our hospital throughout the whole process and had complete clinical data, and (4) patients were aged ≥18 years old.

Exclusion criteria are as follows: (1) Patients who were unable to communicate with others due to factors such as hearing disorders, language disorders, unclear consciousness, or mental illness; (2) patients with dysfunctions in important organs such as the heart, lung, liver, and kidney; (3) patients allergic to drugs involved in the study; (4) patients with long-term administration of analgesics or sedatives; (5) patients with severe anemia; (6) patients with a history of acute and chronic respiratory diseases; and (7) those in pregnancy or lactation.

2.3. Moral Considerations. This study was in accordance with the principles of the Declaration of Helsinki (2013) [12]. Patients knew the purpose, significance, content, and confidentiality of the study and signed the informed consent.

2.4. Methods. All patients were routinely fasted and prohibited from drinking before surgery. After entering the operating room, the upper limb vein access was opened and 8–10 ml/(kg·min) of ringer lactate solution (Sichuan Kelun Pharmaceutical Co. Ltd.; NMPA approval no. H20055488) was intravenously dripped. ECG and blood oxygen saturation were routinely monitored during surgery, while the bispectral index (BIS) and muscle relaxation were also monitored. In EXG, 1–2 mg/kg of propofol (Shenyang First Pharmaceutical Co. Ltd. of Northeast Pharmaceutical Group; NMPA approval no. H20031358), 0.1–0.2 μg/kg of sufentanil (Yichang Humanwell Pharmaceutical Co. Ltd.; NMPA approval no. H20054171), 0.3 mg/kg of midazolam (Jiangsu NHWA Pharmaceutical Co. Ltd.; NMPA approval no. H10980026), and 0.1 mg/kg of vecuronium bromide (Zhejiang Xianju Pharmaceutical Co. Ltd.; NMPA approval no. H19991172) were intravenously injected for anesthesia induction. When TOFT4/T1 = 0 was monitored by a muscle relaxation monitor, the direct vision orotracheal intubation was carried out. During surgery, 0.01–0.03 μg/(kg·min) of sufentanil and 80–100 μg/(kg·min) of propofol were used for anesthesia maintenance. The infusion of sufentanil was stopped at 30 min before the end of the surgery, and propofol was stopped at 10 min before the end of the surgery. The anesthesia method in COG was the same as that in EXG. In COG, 1–2 mg/kg of propofol, 2 μg/kg of fentanyl (Yichang Humanwell Pharmaceutical Co. Ltd.; NMPA approval no. H42022076), 0.3 mg/kg of midazolam, and 0.1 mg/kg of vecuronium were intravenously injected for anesthesia induction. The anesthesia maintenance scheme was 3 μg/(kg·h) of fentanyl combined with 80–100 μg/(kg·min) of propofol. The infusion of fentanyl was stopped at 30 min before the end of the surgery, and propofol was stopped at 10 min before the end of the surgery.

Table 1: Comparison of clinical data between the two groups.

Items	EXG ($n = 60$)	COG ($n = 60$)	X^2/t	P
Average age ($\bar{x} \pm s$, yrs)	52.28 ± 5.20	52.32 ± 5.21	0.042	0.967
Body weight ($\bar{x} \pm s$, kg)	62.65 ± 3.21	62.87 ± 3.20	0.376	0.708
BMI ($\bar{x} \pm s$, kg/m^2)	22.35 ± 1.21	22.41 ± 1.23	0.269	0.788
ASA classification			0.135	0.714
I	32	34		
II	28	26		

BMI: body mass index; ASA: American Society of Anesthesiologists.

Both groups received pump infusion of atracurium (Shanghai Hengrui Pharmaceutical Co. Ltd.; NMPA approval no. H20061298) to maintain muscle relaxation. The pumping was stopped at 30 min before the end of the surgery, and TOFT4/T1 < 15% and 40–60 BIS were maintained during surgery. After surgery, 0.3–0.6 mg/kg of neostigmine (Shanghai Zhongxi Sunve Pharmaceutical Co. Ltd.; NMPA approval no. H31020217) and 0.1–0.3 mg/kg of atropine (Tianjin Huajin Pharmaceutical Co. Ltd.; NMPA approval no. H12020417) were intravenously injected to antagonize residual muscle relaxants.

2.5. Observation Criteria

2.5.1. Hemodynamic Indices. The noninvasive anesthesia depth detector (Sichuan Intelligent Electronics Industry Co. Ltd.; Sichuan Medical Products Administration Approval no. 20062210024) was connected with the monitoring electrode placed in the middle of the forehead and the left mastoid and the reference electrode placed in the left forehead. After wearing the headphones, auditory stimulation was performed at 70 dB and 6.9 Hz. The heart rate (HR) and mean arterial pressure (MAP) of both groups were observed before anesthesia (T_1), after tracheal intubation (T_2), and at separation of deep tissues (T3), tracheal extubation (T_4), and the end of surgery (T_5).

2.5.2. Stress Indexes. The radial artery blood (5 ml) of patients was collected before anesthesia (T_1), and at 1 h (T_6), 6 h (T_7), and 12 h (T8) after surgery. After

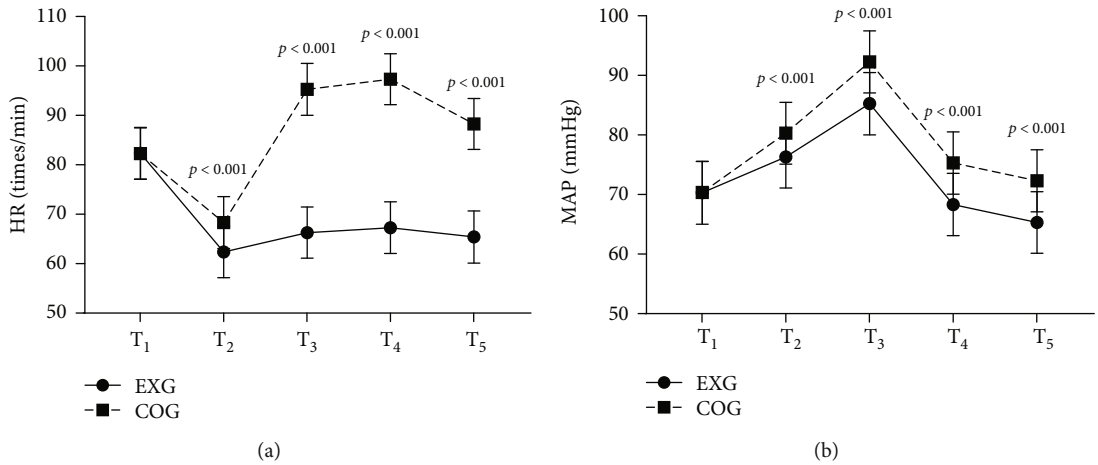

Figure 1: Comparison of hemodynamic indexes ($\bar{x} \pm s$). (a) showed the heart rate (HR) (times/min); (b) showed mean arterial pressure (MAP) (mmHg).

centrifugation, the upper plasma was taken. The concentrations of epinephrine (E) and norepinephrine (NE) were determined by the modified fluorimetric method (Chuzhou Ruigu Biotechnology Co. Ltd.; Anhui Medical Products Administration Approval no. 20202400353), and the cortisol (COR) levels were determined by the chemiluminescence method (Beckman Coulter Co. Ltd. (America); NMPA (I) 20082403092).

2.5.3. Postoperative Pain Scores. The verbal rating scale (VRS) [13] was used to evaluate the pain degree of both groups at 1 h (T_6), 6 h (T_7), and 12 h (T_8) after surgery. VRS was composed of a group of adjectives to describe pain from the lightest to the heaviest grading 1–4 points. The higher the score, the more severe the pain.

2.5.4. Incidence of Adverse Reactions. The types of adverse reactions in both groups were recorded and the incidence of adverse reactions was calculated. Adverse reactions referred to harmful reactions unrelated to the purpose of treatment in the course of prevention, diagnosis, or treatment of diseases by normal usage and dosage of drugs.

2.6. Statistical Treatment. The data were processed by Software SPSS20.0 and graphed by GraphPad Prism 7 (GraphPad Software, San Diego, USA). The data in the study comprised enumeration data and measurement data, tested by X^2 and t-test. The differences were statistically significant at $P < 0.05$.

3. Results

3.1. Comparison of Hemodynamic Indexes. The heart rates (HRs) and mean arterial pressure (MAP) at T_2, T_3, T_4, and T_5 were markedly lower in EXG than in COG ($P < 0.001$), as presented in Figure 1.

No obvious differences were shown in HR at T_1 between EXG and COG (82.35 ± 5.23 vs 82.28 ± 5.19; $P = 0.942$). The HRs at T_2, T_3, T_4, and T_5 in EXG were markedly lower than those in COG (62.38 ± 5.19 vs 68.33 ± 5.27, 66.30 ± 5.18 vs 95.27 ± 5.23, 67.30 ± 5.24 vs 97.33 ± 5.16, and 65.40 ± 5.27 vs 88.28 ± 5.16; $P < 0.001$).

No obvious differences were shown in MAP at T_1 between EXG and COG (70.30 ± 5.26 vs 70.35 ± 5.22, $P = 0.958$). The MAP at T_2, T_3, T_4, and T_5 in EXG was markedly lower than that in COG (76.32 ± 5.20 vs 80.30 ± 5.18, 85.25 ± 5.23 vs 92.28 ± 5.20, 68.33 ± 5.23 vs 75.30 ± 5.24, and 65.32 ± 5.16 vs 72.33 ± 5.21; $P < 0.001$).

3.2. Comparison of Stress Indexes. The stress indexes at T_6, T_7, and T_8 were notably lower in EXG than in COG ($P < 0.001$), as shown in Figure 2.

No obvious differences were shown in the E levels at T_1 between EXG and COG (50.21 ± 5.22 vs 50.29 ± 5.24, $P = 0.933$). The E levels at T_6, T_7, and T_8 in EXG were markedly lower than those in COG (53.66 ± 5.10 vs 57.88 ± 5.20, 55.98 ± 4.50 vs 59.65 ± 4.27, and 68.98 ± 5.16 vs 81.55 ± 6.21; $P < 0.001$).

No obvious differences were shown in the NE levels at T_1 between EXG and COG (272.65 ± 8.55 vs 273.10 ± 8.47; $P = 0.773$). The NE levels at T_6, T_7, and T_8 in EXG were markedly lower than those in COG (318.65 ± 7.88 vs 330.98 ± 7.80, 385.65 ± 8.54 vs 468.98 ± 9.41, and 341.65 ± 4.77 vs 412.58 ± 7.52; $P < 0.001$).

No obvious differences were shown in the COR levels at T_1 between EXG and COG (74.55 ± 2.65 vs 74.58 ± 2.47; $P = 0.949$). The COR levels at T_6, T_7, and T_8 in EXG were markedly lower than those in COG (119.65 ± 4.21 vs 140.65 ± 5.47, 210.65 ± 5.88 vs 257.98 ± 4.56, and 149.65 ± 5.74 vs 190.65 ± 6.41; $P < 0.001$).

3.3. Comparison of Postoperative Pain Scores. The pain scores at T_6, T_7, and T_8 in EXG were markedly lower than those in COG (1.70 ± 0.53 vs 3.32 ± 0.50, 1.63 ± 0.48 vs 2.67 ± 0.51, and 1.47 ± 0.53 vs 1.93 ± 0.48; $P < 0.001$).

3.4. Comparison of Incidence of Adverse Reactions. The incidence of dizziness, headache, pruritus, and emergence agitation in EXG was lower compared with that in COG ($P < 0.05$), as demonstrated in Table 2.

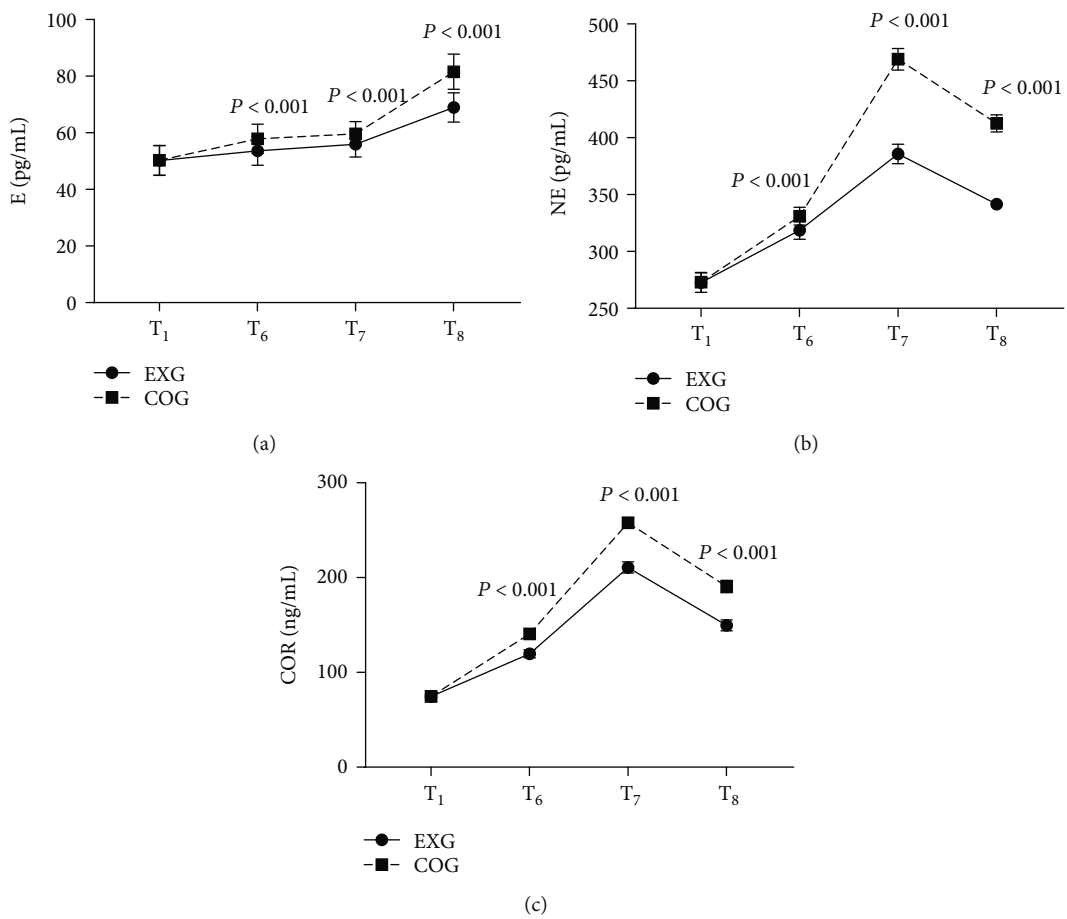

Figure 2: Comparison of stress indexes ($\bar{x} \pm s$). (a) Showed epinephrine (E) levels (pg/ml); (b) showed norepinephrine (NE) levels (pg/mL); (c) showed cortisol (COR) levels (ng/ml).

Table 2: Comparison of incidence of adverse reactions [n(%)].

Group	n	Nausea and vomiting	Dizziness and headache	Drowsiness	Palpitation	Intolerance of cold	Pruritus	Abdominal distension	Emergence agitation
EXG	60	4(6.7)	1(1.7)	3(5.0)	1(1.7)	1(1.7)	0(0.0)	2(3.3)	0(0.0)
COG	60	9(15.0)	8(13.3)	3(5.0)	2(3.3)	1(1.7)	4(6.7)	6(10.0)	10(11.7)
X^2		2.157	5.886	0.000	0.342	0.000	4.138	2.143	10.909
P		0.142	0.015	1.000	0.559	1.000	0.042	0.143	0.001

4. Discussion

Due to the short duration of radical mastectomy and low requirements for muscle relaxation, fast-track anesthesia is often applied in clinic, such as total intravenous anesthesia (TIVA) [14]. TIVA refers to the general anesthesia by intravenous injection of anesthetic drugs that act on the central nervous system through blood circulation. In order to ensure the stability of anesthesia and alleviate physiological disturbance, TIVA is generally achieved by a combination of drugs. However, the efficacy of the combined drugs cannot be accurately predicted because the combination may have synergistic and additive effects as well as antagonistic effects, leading to pharmacodynamic changes. Therefore, the compound effects of different drugs need to be analyzed one by one to clarify the drug efficacy of their combination [15–17]. This study combined two drugs (fentanyl and sufentanil) with propofol. Since fentanyl is rarely involved in previous studies, there is a lack of a large number of control studies to evaluate its application effect. Zhang et al. [18] believed that there was a synergistic effect between fentanyl and propofol. From their point of view, when propofol was used alone, 3.3 μg/ml and 27.4 μg/ml of steady-state blood concentrations were required to make 50% of patients unresponsive to oral commands and skin incision, while 3.26 ng/ml and 4.17 ng/ml of steady-state blood concentrations were required for patients without movement and endocrine disorders when propofol combined with fentanyl was used. This shows that the combination of fentanyl and propofol can improve the analgesic and sedative effects. However,

excessive application of fentanyl can lead to reactions such as drowsiness, nausea, and vomiting, and even death due to respiratory depression in severe cases [19, 20]. Therefore, dosage control of fentanyl is required, which has always been the key and difficult content of TIVA.

Compared with fentanyl, sufentanil has faster clearance and does not accumulate in patients due to its smaller volume of distribution, shorter half-life, and shorter terminal clearance period, with fewer postoperative adverse reactions, so it is easier to achieve the controllable amount of anesthesia [21, 22]. Moreover, sufentanil is a thienyl derivative at the N-4 position of fentanyl and its receptor affinity is about 7–10 times that of fentanyl. Therefore, sufentanil has a stronger inhibitory effect on the stress response induced by noxious stimuli [7]. The clinical manifestations of stress response include increased blood pressure, accelerated heart rate (HR), and increased cardiac oxygen consumption. Therefore, the HR and MAP in EXG were more stable and the stress response indexes at T_6, T_7, and T_8 were lower in EXG than in COG ($P < 0.001$). It is worth noting that the mechanism of sufentanil stabilizing HR is to stabilize peripheral vascular resistance, excite the central vagus nerve nucleus, and block the sympathetic nerve. Therefore, patients with bradycardia should be closely watched and treated with atropine if necessary [23].

The analysis by Seokha et al. [24] showed that sufentanil, the most effective fentanyl family drug at present, could not only maintain intraoperative analgesia, but also have good postoperative analgesic effects. The application of sufentanil combined with propofol for TIVA in laparoscopic appendectomy prolongs the analgesic time and has better effects, especially for short-term postoperative analgesia and sedation, with greater postoperative comfort for patients. This study found that the postoperative pain scores at T_6, T_7 and T_8 in EXG were lower compared with COG ($P < 0.001$), which was consistent with the study of Seokha et al. In addition, clinical reports have shown that adverse drug reactions of sufentanil are mostly the same as those of fentanyl, mainly including respiratory depression, skeletal muscle stiffness, tachycardia, arrhythmia, and pruritus. With no respiratory depression in this study, the main adverse reactions of patients included nausea and vomiting, dizziness and headache, and abdominal distension. The incidence of dizziness, headache, pruritus, and emergence agitation in EXG was lower compared with that in COG ($P < 0.05$), suggesting that sufentanil had faster clearance and better safety, which is conducive to the better quality of the recovery period.

In conclusion, sufentanil combined with propofol for TIVA can stabilize intraoperative hemodynamic indices of patients undergoing radical mastectomy, alleviate perioperative stress response, and reduce pain perception. Therefore, this anesthesia method is safe and merits clinical promotion.

Data Availability

Data to support the findings of this study is available upon reasonable request from the corresponding author.

Conflicts of Interest

The authors have no conflicts of interest to declare.

References

[1] O. Aghamelu, P. Buggy, G. Smith, R. Inzitari, T. Wall, and D. J. Buggy, "Serum NETosis expression and recurrence risk after regional or volatile anaesthesia during breast cancer surgery: a pilot, prospective, randomised single-blind clinical trial," *Acta Anaesthesiologica Scandinavica*, vol. 65, no. 3, pp. 313–319, 2021.

[2] A. Clairoux, M. Soucy-Proulx, F. Pretto et al., "Intrapandemic regional anesthesia as practice: a historical cohort study in patients undergoing breast cancer surgery," *Canadian Journal of Anaesthesia*, vol. 69, no. 4, pp. 485–493, 2022.

[3] D. I. Sessler, L. Pei, Y. Huang et al., "Recurrence of breast cancer after regional or general anaesthesia: a randomised controlled trial," *Lancet*, vol. 394, no. 10211, pp. 1807–1815, 2019.

[4] Y. J. Lee, C. S. Oh, J. M. Choi, S. Park, and S. H. Kim, "mu-opioid receptor polymorphisms and breast cancer recurrence in adult Korean women undergoing breast cancer surgery: a retrospective study," *International Journal of Medical Sciences*, vol. 17, no. 18, pp. 2941–2946, 2020.

[5] A. Ní Eochagáin, D. Burns, B. Riedel, D. I. Sessler, and D. J. Buggy, "The effect of anaesthetic technique during primary breast cancer surgery on neutrophil–lymphocyte ratio, platelet–lymphocyte ratio and return to intended oncological therapy," *Anaesthesia*, vol. 73, no. 5, pp. 603–611, 2018.

[6] M. Nadeem and A. Sahu, "Ultrasound guided surgery under dilutional local anaesthesia and no sedation in breast cancer patients," *The Surgeon*, vol. 18, no. 2, pp. 91–94, 2020.

[7] E. Kujawa, A. Blau, and L. Rametta, "Anesthesia related to breast cancer recurrence and chronic pain: a review of current research," *AANA Journal*, vol. 89, no. 4, pp. 291–298, 2021.

[8] Y. H. Huang, M. S. Lee, Y. S. Lou et al., "Propofol-based total intravenous anesthesia did not improve survival compared to desflurane anesthesia in breast cancer surgery," *PLoS One*, vol. 14, no. 11, article e0224728, 2019.

[9] A. Chhabra, A. R. Chowdhury, H. Prabhakar et al., "Paravertebral anaesthesia with or without sedation versus general anaesthesia for women undergoing breast cancer surgery," *Cochrane Database of Systematic Reviews*, vol. 2021, no. 2, p. CD012968, 2021.

[10] M. Enlund, A. Berglund, R. Ahlstrand et al., "Survival after primary breast cancer surgery following propofol or sevoflurane general anesthesia-a retrospective, multicenter, database analysis of 6305 Swedish patients," *Acta Anaesthesiologica Scandinavica*, vol. 64, no. 8, pp. 1048–1054, 2020.

[11] A. Raigon-Ponferrada, M. E. D. Recio, J. L. Guerrero-Orriach et al., "Breast cancer and anesthesia," *Current Pharmaceutical Design*, vol. 25, no. 28, pp. 2998–3004, 2019.

[12] World Medical Association, "World Medical Association Declaration of Helsinki," *Journal of the American Medical Association*, vol. 310, no. 20, pp. 2191–2194, 2013.

[13] T. Konishi, M. Fujiogi, N. Michihata et al., "Impact of body mass index on outcomes after breast cancer surgery: nationwide inpatient database study in Japan," *Clinical Breast Cancer*, vol. 20, no. 6, pp. e663–e674, 2020.

[14] T. Morita, M. Yamamoto, and A. Sakamoto, "Factors associated with postoperative nausea and vomiting after breast

cancer surgery with inhalation anesthesia," *Journal of Nippon Medical School*, vol. 88, no. 5, pp. 418–422, 2021.

[15] V. Lukoseviciene, R. Tikuisis, A. Dulskas, P. Miliauskas, and V. Ostapenko, "Surgery for triple-negative breast cancer- does the type of anaesthesia have an influence on oxidative stress, inflammation, molecular regulators, and outcomes of disease?," *Journal of BUON*, vol. 23, no. 2, pp. 290–295, 2018.

[16] T. Yan, G. H. Zhang, B. N. Wang, L. Sun, and H. Zheng, "Effects of propofol/remifentanil-based total intravenous anesthesia versus sevoflurane-based inhalational anesthesia on the release of VEGF-C and TGF-β and prognosis after breast cancer surgery: a prospective, randomized and controlled study," *BMC Anesthesiology*, vol. 18, no. 1, p. 131, 2018.

[17] A. Raigon Ponferrada, J. L. Guerrero Orriach, J. C. Molina Ruiz, S. Romero Molina, A. Gómez Luque, and J. Cruz Mañas, "Breast cancer and anaesthesia: genetic influence," *International Journal of Molecular Sciences*, vol. 22, no. 14, p. 7653, 2021.

[18] J. Zhang, C. L. Chang, C. Y. Lu, H. M. Chen, and S. Y. Wu, "Paravertebral block in regional anesthesia with propofol sedation reduces locoregional recurrence in patients with breast cancer receiving breast conservative surgery compared with volatile inhalational without propofol in general anesthesia," *Biomedicine & Pharmacotherapy*, vol. 142, p. 111991, 2021.

[19] J. W. Ji, Y. Liu, Z. Q. Liu, and Y. Wang, "Effect of thoracic paravertebral block on intraoperative hypotension and postoperative pain in patients undergoing breast cancer surgery under general anesthesia: a retrospective study," *Annals of Palliative Medicine*, vol. 10, no. 8, pp. 8930–8938, 2021.

[20] W. Tang, G. Luo, Y. Lu, C. Chen, H. Liu, and Y. Li, "Application of a new serratus anterior plane block in modified radical mastectomy under ultrasound guidance: a prospective, randomized controlled trial," *Journal of Clinical Anesthesia*, vol. 74, p. 110377, 2021.

[21] B. Hong, S. Lee, Y. Kim et al., "Anesthetics and long-term survival after cancer surgery-total intravenous versus volatile anesthesia: a retrospective study," *BMC Anesthesiology*, vol. 19, no. 1, p. 233, 2019.

[22] A. Yap, M. A. Lopez-Olivo, J. Dubowitz et al., "Anesthetic technique and cancer outcomes: a meta-analysis of total intravenous versus volatile anesthesia," *Canadian Journal of Anaesthesia*, vol. 66, no. 5, pp. 546–561, 2019.

[23] R. Kim, A. Kawai, M. Wakisaka, and T. Kin, "Current status and prospects of anesthesia and breast cancer: does anesthetic technique affect recurrence and survival rates in breast cancer surgery?," *Frontiers in Oncology*, vol. 12, p. 795864, 2022.

[24] S. Yoo, H. B. Lee, W. Han et al., "Total intravenous AnesthesiaversusInhalation anesthesia for breast cancer surgery," *Anesthesiology*, vol. 130, no. 1, pp. 31–40, 2019.